2009

Functionalization of mesoporous silica nanoparticles and their applications in organo-, metallic and organometallic catalysis

Yulin Huang
Iowa State University

Functionalization of mesoporous silica nanoparticles and their applications in organo-, metallic and organometallic catalysis

by

Yulin Huang

A dissertation submitted to the graduate faculty

in partial fulfillment of the requirements for the degree of

DOCTOR OF PHILOSOPHY

Major: Chemistry

Program of Study Committee:
Victor S.-Y. Lin, Major Professor
Amy H. Andreotti
Nikki L. Pohl
Marek Pruski
Aaron D. Sadow

Iowa State University

Ames, Iowa

2009

TABLE OF CONTENTS

ABSTRACT

Mesoporous silica nanoparticles (MSN) with high surface area, tunable pore size and very narrow pore size distribution were functionalized by organic acid, organic base, metallic nanoparticles and organometallic complexes through co-condensation methods and/or post-synthesis grafting methods. And these surface-functionalized mesoporous materials were applied as heterogeneous catalysts in organocatalysis, metallic catalysis and organometallic catalysis.

Organocatalysis. First, Brønsted acid and base were confined into the mesoporous channels of MSN and they could co-exist as compatible catalysts for one-pot reaction cascades without neutralizing each other because they were confined in different MSN particles' channels. Brönsted acid and base also were site-separated by MSN's internal surface and external surface through co-condensation method to functionalize MSN's internal surface followed by grafting method to functionalize MSN's external surface. These internal and external surface-separated Brönsted acid and base could co-exist as compatible catalysts too.

Metallic catalysis. Water-soluble rhodium nanoparticles with well defined particle size were synthesized and immobilized on MSN during *in situ* MSN's synthesis. The obtained material (MSNRhNPs) had homogeneous rhodium nanoparticle size, homogeneous rhodium nanoparticle distribution in MSN, typical MSN's highly ordered structure and surface area and narrow pore size distribution as well. After MSNRhNPs were modified by manganese oxide, it could catalyze the hydrogenation of CO to produce the renewable energy alternative - ethanol with high selectivity and high activity. Additionally, after MSNRhNPs were functionalized by some chiral agents such as (-)-cinchonidine, it can used as a solid chiral catalyst which can be recycled and reused without any loss of reactivity and enantioselectivity.

Organometallic catalysis. Wilkinson-type rhodium phosphine complex was homogeneously immobilized on MSN surface by co-condensation method. This MSN-immobilized rhodium-phosphine complex (RhPMSN) had a new and total different catalytic

performance: RhPMSN could enantioselectively catalyze the hydrogenation of pyruvate when (-)-cinchonidine was adsorbed on RhPMSN surface. However, $RhCl(TPP)_3$ (TPP: triphenylphosphine) and (-)-cinchonidine could not enantioselectively catalyze the same reaction in homogeneous system.

An in-depth solid-state NMR study of RhPMSN has been presented. Functionalization of the ligand was confirmed by the presence of T sites in the ^{29}Si CPMASNMR spectrum and quantification of these sites was achieved via integration of the ^{29}Si DPMAS NMR spectrum. Both 1D and 2D SSNMR experiments showed that covalent attachment of the rhodium– phosphine ligand to the MSN surfaces was successful. Both ^{13}C–^{1}H and ^{31}P–^{1}H idHETCOR experiments provided structural details of oxidized and non-oxidized phosphine ligands, otherwise indiscernible in a conventional 1D CPMAS NMR experiments.

Organometallic complex (salen)Cr on MSN was synthesized and applied in the oxidation of tetramethylbenzidine (TMB) with iodosobenzene. MSN-(salen)Cr^{III} as a heterogeneous catalyst exhibited both similarities and differences with the analogous (salen)$Cr^{III}(H_2O)^+$ as catalyst in aqueous acetonitrile (10% H_2O). It was shown that the covalently attached catalyst in mesoporous channels of MSN was still easily accessible to the reactants without diffusion problem.

Aminopropyl-functionalized MSN was synthesized and applied in the selective sequestration of carboxylic acids from biomass fermentation. Aminopropyl-functionalized MSN with a designed loading of functional groups could have a very high selectivity for carboxylic acid instead for ethanol, glucose, and protein. The regeneration of aminopropyl-functionalized MSN could be done easily by increasing pH to 10.5 because the adsorption reaction between carboxylic acids and aminopropyl-functionalized MSN was pH-dependent. And the regenerated aminopropyl-functionalized MSN showed adsorption capacity equivalent to the original.

CHAPTER 1. GENERAL INTRODUCTION OF FUNCTIONALIZATION OF MESOPOROUS SILICATE

DISSERTATION ORGANIZATION

This dissertation includes ten chapters: a general introduction (Chapter 1), followed by eight chapters for scientific results (Chapter 2 – 9) and general conclusions (Chapter 10).

Chapter 1 describes the general introduction of mesoporous silicates, including the synthesis, mechanism, functionalization and applications in catalysis.

Chapter 2 describes the confinements of Brönsted acid and base in the mesoporous channels of different mesoporous silica nanoparticles and their successful applications as compatible catalysts for one-pot reaction cascades.

Chapter 3 extends the successful functionalization of individual mesoporous silica nanoparticle with both Brönsted acid and base by co-condensation methods followed by post-synthesis grafting methods. As a result of this ideal site-isolation, reaction cascades requiring two or more catalysts which are incompatible in one solution system could be done by these new internal and external surface bifunctionalized one-particle.

Chapter 4 shows the new MSN-supported manganese-modified rhodium nanoparticle catalyst (MSNRhNPsMN) could suppress the formation of by-product methanol efficiently therefore has very high selectivity to the ideal C_2 oxygenates in CO hydrogenation. In MSNRhNPsMn, the well-defined rhodium nanoparticles were distributed homogeneously through the whole mesoporous silica and modified by promoters during the formation of mesoporous silica.

Chapter 5 describes the immobilizations of both well defined rhodium nanoparticles and chiral reagent cinchonidine on mesoporous silica nanoparticle surface by co-condensation method. In the enantioselective hydrogenation of ethyl pyruvate, reactivity and enantioselectivity could be retained very well during the catalyst recycling without any additional chiral reagent supplement.

Chapter 6 presents that the enantioselectivity of the hydrogenation of ethyl pyruvate catalyzed by the achiral RhPMSN (rhodium phosphine complex immobilized on MSN surface) material could be induced and tuned by introducing a surface-adsorbed chiral agent ((-)-cinchonidine), although its counterpart, $RhCl(TPP)_3$ and (-)-cinchonidine, could not enantioselectively catalyze the same reaction in homogeneous system.

Chapter 7 describes an in-depth solid-state NMR study of RhPMSN. Functionalization of MSN by 2-(diphenylphosphino)ethyl groups was confirmed by the presence of T sites in the ^{29}Si CPMAS NMR spectrum and quantification of these sites was achieved via integration of the ^{29}Si DPMAS NMR spectrum. Both 1D and 2D SSNMR experiments showed that covalent attachment of the rhodium– phosphine ligand to the MSN surfaces was successful. Both ^{13}C–^{1}H and ^{31}P–^{1}H idHETCOR experiments provided structural details of oxidized and non-oxidized phosphine ligands, otherwise indiscernible in a conventional 1D CPMAS NMR experiments. It was found that oxidation of the attached 2-(diphenylphosphino)ethyl groups and detachment of Rh was enhanced at higher temperature even under CO and H_2.

Chapter 8 describes the synthesis of MSN-supported organometallic complex $(salen)Cr^{III}$ and its application in the oxidation of tetramethylbenzidine (TMB) with iodosobenzene. And the reaction using MSN-$(salen)Cr^{III}$ as a heterogeneous catalyst exhibited both similarities and differences with the analogous homogeneous reaction using $(salen)Cr^{III}(H_2O)^{+}$ as catalyst in aqueous acetonitrile (10% H_2O).

Chapter 9 shows that the aminopropyl-functionalized MSN could serve as an efficient adsorbent for selective sequestration of carboxylic acids. Aminopropyl-functionalized MSN with a designed loading of functional groups had a very high selectivity for carboxylic acid instead of ethanol, glucose, and protein. Because the adsorption reaction between carboxylic acids and aminopropyl-functionalized MSN was pH-dependent, the regeneration of aminopropyl-functionalized MSN could be done successfully by increasing pH to 10.5. It was demonstrated that the regenerated aminopropyl-functionalized MSN showed adsorption capacity equivalent to the original.

Chapter 10 includes the summary of my research work and future directions of study.

LITERATURE REVIEW OF FUNCTIONALIZATION OF MESOPOROUS SILICATES

Introduction

Because of their high surface areas and large pore volumes, many porous materials are widely used as adsorbents, catalysts and catalyst supports. Depending on the predominant pore size, the International Union of Pure and Applied Chemistry (IUPAC) classified porous materials into the following three categories in 1985:[1]

1) **Microporous**: with pore diameter less than 2 nm;
2) **Mesoporous**: with pore diameter between 2 nm and 50 nm;
3) **Macroporous**: with pore diameter larger than 50 nm.

Well known members of the microporous materials are the zeolites[2] which have the pore sizes in the range of 0.2-1.0 nm. They provide excellent catalytic properties by virtue of their crystalline aluminosilicate network. It's also well-known from the beginning that their applications are limited by the relatively small pore sizes. Thus, mesoporous materials with larger pores and well-defined pore structure remain an active and attractive research area for many researchers in chemistry, materials and chemical engineering.

However, before the early 1990s, there seemed to be a limitation for the artificially synthetic porous materials, including zeolites and sol-gel materials,[2,3] which usually had a pore or channel diameter less than 2.0 nm with a wide pore size distribution because the individual quaternary directing agents with small alkyl chain length were used as templates (Figure 1-1).[4]

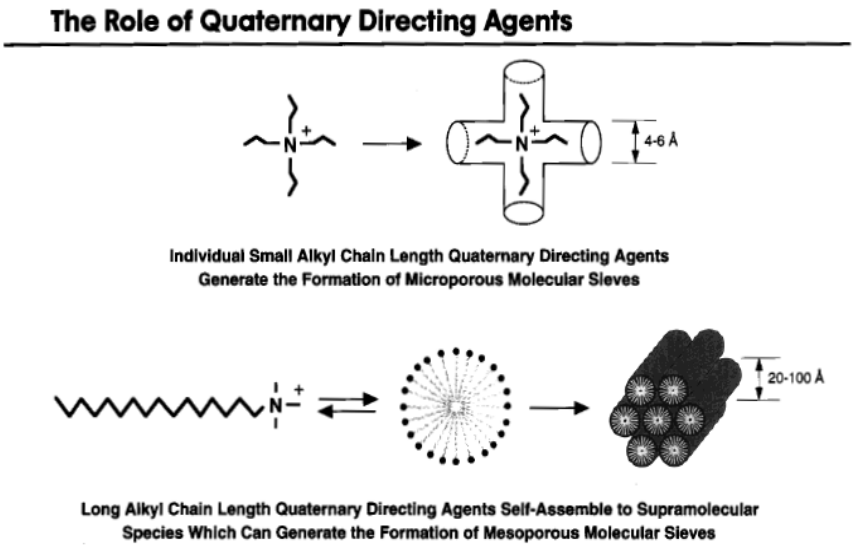

Figure 1-1. The formation of microporous molecular sieves using individual small alkyl chain length quaternary directing agents (top) and the formation of mesoporous molecular sieves using long alkyl chain length quaternary directing agents (bottom).[4]

Discovery and Synthesis of Mesoporous Materials

In the early 1990s the discovery of the MCM-41 and the M41S family of mesoporous materials using the cooperative assembly of surfactant with silicates,[5-9] opened a new era to

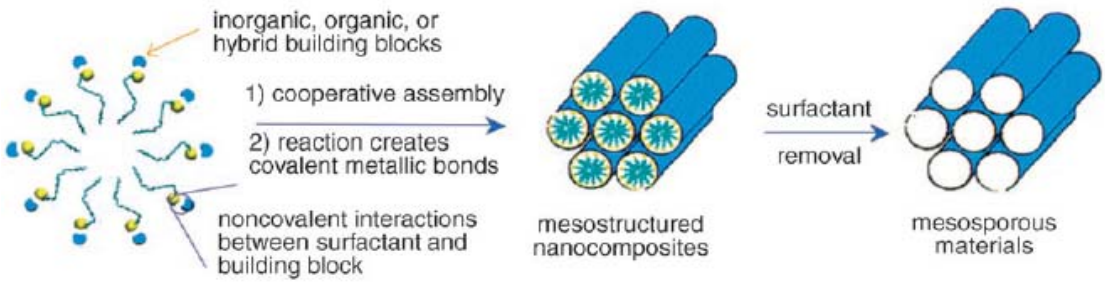

Figure 1-2. Surfactant-directed formation of mesoporous materials from inorganic, hybrid, or organic building blocks. [9,10]

exceed the pore size limit of zeolites (Figure 1-1). This discovery sparked extensive research on surfactant-directed assembly, using surfactant to direct and assembly building blocks into mesoscopically ordered structures. More specially, noncovalent interactions between the surfactant and the building blocks drive the building blocks to organize around supramolecular surfactant structures first (Figure 1-2).[9,10] Simultaneously or subsequently, chemical reactions, such as a condensation / co-condensation of inorganic clusters or electrochemical reduction, create covalent or metallic bonds among building blocks, resulting in mesostructured nanocomposites containing liquid-crystalline surfactant. The removal of the surfactant by calcination or solvent extraction creates a mesoporous material with a templated pore structure.

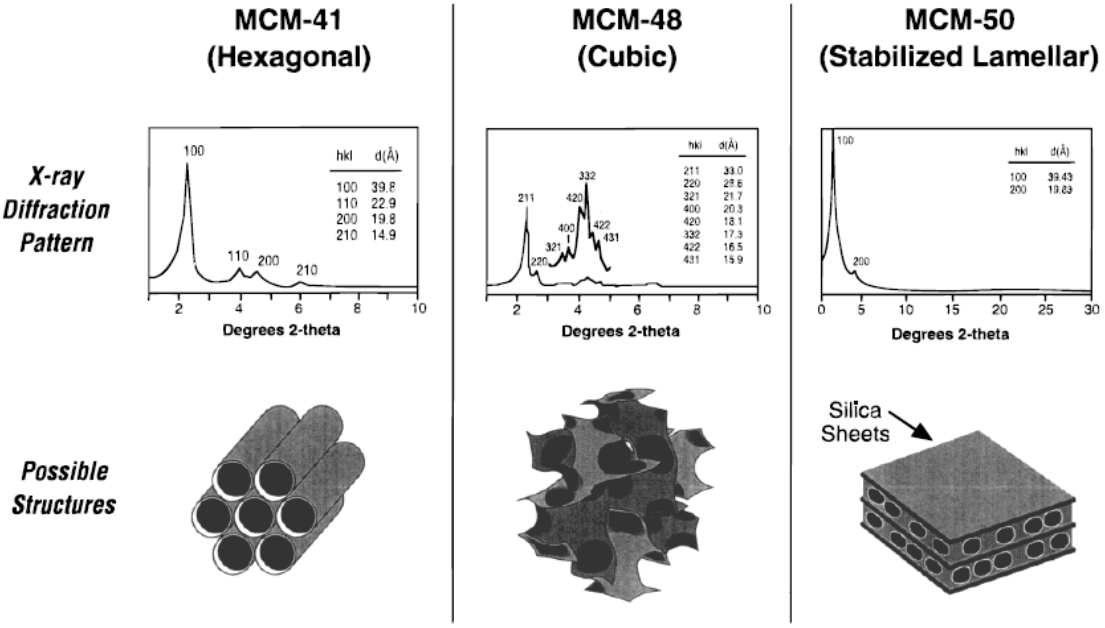

Figure 1-3. The X-ray diffraction patterns and proposed structures of MCM-41, MCM-48, and MCM-50.[4]

The size, shape, and intermolecular interactions of the mesoporous material can be tuned to produce hexagonal (MCM-41, SBA-15[11]), cubic (MCM-48), lamellar (MCM-50), and other random arranged mesostructures (Figure 1-3).[4] All of these mesoporous materials were characterized and show high surface area, large pore volume and narrow pore size distributions compared to microporous materials. When these mesoporous materials are used

as catalyst supports, surface area and large pore volume are very important to catalyst activity and tunable narrow pore size distribution plays a key role in selectivity controlling.

In the synthesis of the hexagonal MCM-41 and cubic MCM-48, usually a quarternary ammonium surfactant as an ionic template, such as cetyltrimethylammonium bromide (CTAB), was used as a template to make the pore size around 2 to 10 nm.[6-9] Charge-matching has been recognized as the most critical factor in governing the final phases and stability. Liquid-crystal templating (LCT) mechanism was proposed by Beck et al.[6] to explain the formation mechanism of MCM-41 (Figure 1-4).

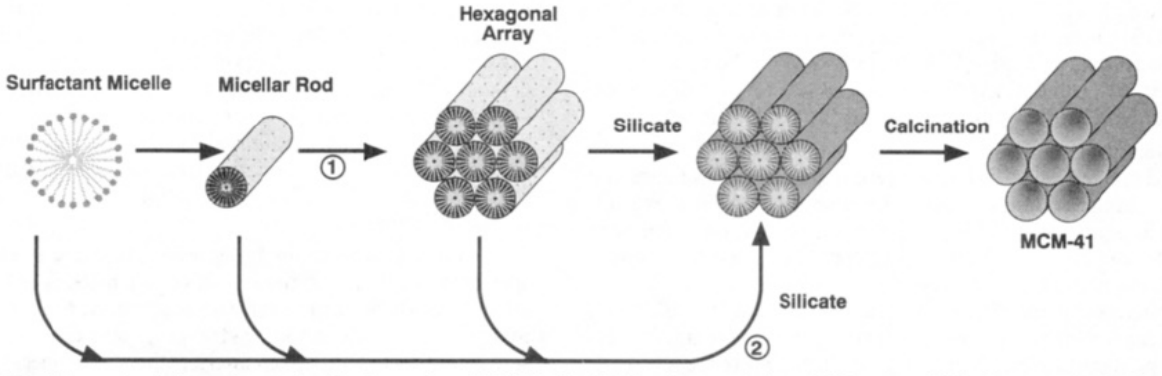

Figure 1-4. Possible mechanistic pathways for the formation of MCM-41: (1) liquid crystal phase initiated and (2) silicate anion initiated.[6]

Since then, many synthetic routes and strategies have been developed to yield a wide diversity of materials of various frameworks with different chemical compositions and pore structures.[11-41] Stucky *et al.* introduced nonionic surfactants in acidic condition to produce thick-wall large pore size (4-6 nm in diameter) hexagonal mesoporous silicates SBA-15.[11,21,22] And SBA-15 usually has mesopores and micropores together evidenced by BET isotherm and TEM study.[42] In general, almost every organic molecule can be used as a soft template to lead hard inorganic porous materials in solution state. One is able to freely alter the pore organization (hexagonal, cubic or lamellar) and a pore size as well. Disordered mesostructured siliceous or nonsiliceous materials were also synthesized by Pinnavaia *et al.* through a neutral amine templating.[14]

These mesoporous materials already sparkled an extensive study on their applications in catalysis,[43-53] biology,[38,54-60] drug delivery,[61-74] remediation of toxic compounds[75-80] and material synthesis by replication.[35,36,81,82]

Functionalization of Mesoporous Silicates

In many cases where mesoporous materials were involved, further functionalization of these materials on their surface was done usually in order to improve their chemical and physical properties. My thesis will focus on catalysis on mesoporous silicates, therefore functionalization of mesoporous silicates will be described here.

As mentioned before, mesoporous silicates usually have very high surface and their surfaces are covered by silanol groups, which makes the functionalization of the pore surface of the mesoporous materials adjustable. Additionally, the surface functionalization of mesoporous silicates could change the chemical and physical properties of these materials dramatically. Therefore, the surface functionalization of mesoporous silicates has been intensively investigated.[83] There are two major ways to functionalize the surface of mesoporous silicates by organic functional groups, named as post-synthesis grafting and co-condensation. Each of these two functionalization methods has certain advantages, which will be described below.

Grafting Methods

Grafting is a post-synthesis method to modify a pre-fabricated inorganic mesoporous material surface by attachment of functional groups to the surface of material, usually after surfactant removal (Fig. 1-5).[83] In the process of grafting mesoporous silicates, the surface silanol groups (Si-OH), which can be present in high concentration, act as convenient anchoring points for organic functionalization.

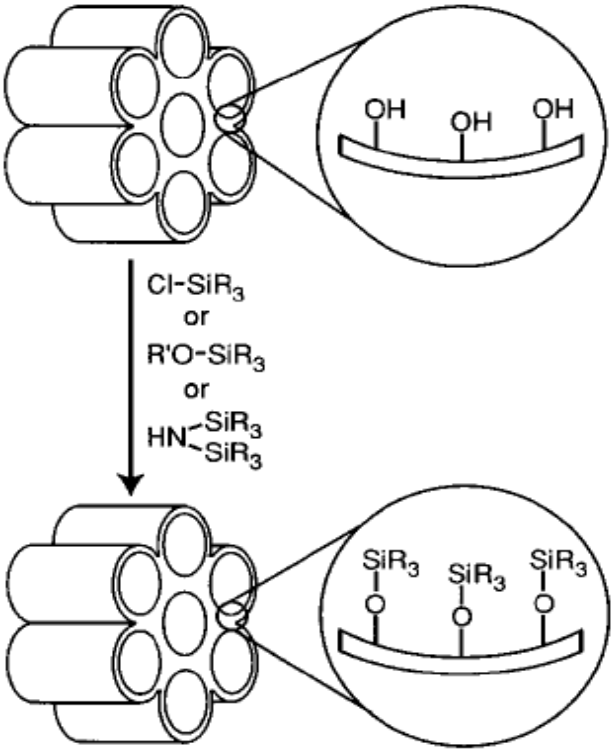

Figure 1-5. Functionalization of mesoporous silicates by grafting.[83]

Surface functionalization with organic groups by grafting is most commonly carried out by silylation, which is accomplished by one of the three procedures (Eq. (1) to (3)).[84]

$$\equiv Si-OH + Cl-SiR_3 \xrightarrow{\text{base, } 25\,^{\circ}C} \equiv Si-OSiR_3 + HCl \cdot \text{base} \quad (1)$$

$$\equiv Si-OH + R'O-SiR_3 \xrightarrow{100\,^{\circ}C} \equiv Si-OSiR_3 + HOR' \quad (2)$$

$$2 \equiv Si-OH + HN(SiR_3)_2 \xrightarrow{25\,^{\circ}C} 2 \equiv Si-OSiR_3 + NH_3 \quad (3)$$

Silylation occurs on free (≡Si-OH) and geminal silanol (=Si(OH)2) groups, but hydrogen-bonded silanol groups are less accessible to modification because they form hydrophilic networks among themselves.[85] The original structure of the mesoporous support is generally maintained after grafting.

As we know, mesoporous silicates have two 'different' surfaces, the internal surface in the mesopores and the external surface. In the grafting which was mentioned before, the external surface is more accessible and is functionalized predominantly over the internal mesopore surface.[86] The functional groups on the external surface are also more accessible in subsequent reactions, leading to reduced selectivities in processes that benefit from pore confinement. To minimize involvement of the external surface in reaction processes and to optimize selectivity, it is possible to passivate these surfaces first, before functionalizing the internal silanol groups. Controlled dual functionalization has been achieved by two different site-selective grafting methods (Fig. 1-6).

Johnson et al.[87] assumed that silanol groups on the external surface of a calcined MCM-41 sample are kinetically more accessible for functionalization. Calcined MCM-41 was modified first with Ph_2SiCl_2 to passivate the external surface and then with $(MeO)_3SiCH_2CH_2CH_2NH_2$ as an anchor for a redox-active ruthenium cluster catalyst. This cluster acted as a stain in high-resolution transmission electron microscopy (HRTEM) by which the authors concluded that the amine tethers were present almost entirely on the internal surface of MCM-41. De Juan and Ruiz-Hitzky[88] employed an alternate approach for selective functionalization of external and internal MCM-41 surfaces. The first (external) grafting step was carried out with the as-synthesized mesoporous sieve whose pores were still filled with the surfactant template. Exposure of this support to a solution of trimethylsilyl chloride resulted in functionalization mainly of the external surface due to steric restrictions in the surfactant-filled mesochannels. The template was then extracted and the internal pore surfaces were functionalized with phenylpropyldimethylchlorosilane.

Co-condensation Methods

Co-condensation method is another strategy to functionalize mesoporous silicates' surface by sol-gel chemistry between tetraalkoxysilane and one or more organoalkoxy-silanes with Si-C bonds (Figure S1-7).

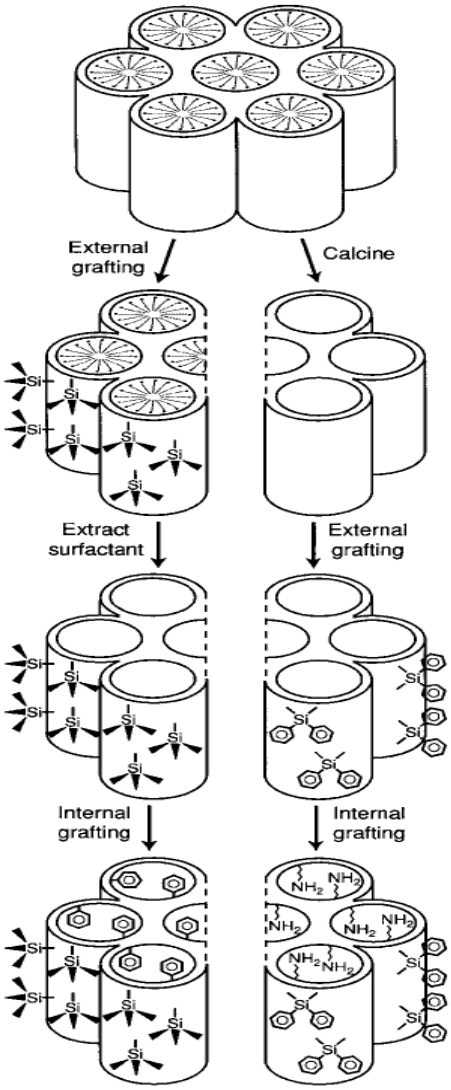

Figure 1-6. Methods of selective grafting on external and internal surfaces of mesoporous silicates.[83]

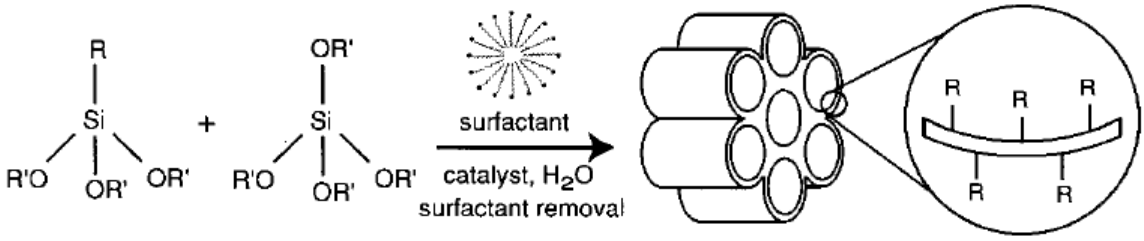

Figure 1-7. Co-condensation between tetraalkoxysilane and organoalkoxysilanes with Si-C bonds to synthesize hybrid inorganic-organic mesoporous silicates.[83]

Compared with the post-grafting method in which the distribution of functional groups often tends to be inhomogeneous, the co-condensation is able to give homogeneously distributed organic groups on the entire inner pore surfaces and no pore-blockage or shrinkage problems have been reported. Even though bulky organoalkoxysilane precursors often perturb the original textural properties of the systems, some new methods already developed to decorate the surface wall efficiently while maintaining the mesoporous structure.[89-91] Another advantage of co-condensation over post-synthesis grafting is to control the particle morphology of final mesoporous silicate very easily,[30,92] which is closely related to the biomineralization process in nature, for example the complex forms of diatoms.[16,93]

Comparison between Grafting and Co-condensation Methods

Lim and Stein[86] compared the relative distribution of surface groups in vinyl-functionalized MCM-41 samples prepared by either a post-synthesis grafting process or a direct co-condensation synthesis. Based on powder X-ray diffraction (XRD), X-ray photoelectron spectroscopy (XPS), and bromination kinetics data, the vinyl groups appeared to be non-uniformly distributed in samples prepared by the grafting process, with a large proportion of vinyl groups on the external surface of the crystallites or inside channels but near the channel openings. In products from a direct co-condensation reaction, the vinyl groups appeared to be more uniformly distributed throughout the channels.

Each of the two functionalization methods has certain advantages. If uniform surface coverage with organic groups is desired in a single step synthesis, the direct method may be the first choice. It also provides better control over the amount of organic groups incorporated in the structure.

Applications of Functionalized Mesoporous Silicates in Catalysis[83]

Because of their high surface area and large pore size, mesostructured materials are frequently used as support for immobilizing precious metal catalysts.[94-100]

During the last two decades, hybrid mesoporous solids have been considered for a wide range of heterogeneous catalysis reactions.[43-50,58,59,101-115] Immobilization of active centers can improve the overall efficiency of the catalytic processes because: 1) it is easier to retain the solid catalyst in the reactor or to separate it from the liquid process stream by filtration (compared to extraction or distillation requirements for homogeneous processes); 2) often the catalyst can be regenerated and recycled; 3) confinement of the catalyst within mesopores provides a means of introducing size and/or shape selectivity and thus greater specificity for a reaction. In contrast to organic polymers, mesoporous silicates used in organic solvents do not swell or dissolve. If functional groups are covalently attached to the surface, leaching is minimized.

It has been noted that mesoporous catalysts differ significantly in many respects from their post-functionalized, amorphous silica counterparts.[116-118] In several investigations, confinement of the catalyst in the mesoporous solid improved the activity compared to attachment to amorphous or non-porous silica, either due to enhanced selectivity in a sterically homogeneous environment or due to higher catalyst turnover brought about by stabilization of the catalyst within the channels. Other advantages exist: for example, mesoporous silicates with highly acidic surface groups are relatively safe to handle, since most of the acidic groups are confined within the channels.

In this dissertation, by integrating the advantages of mesoporous silica nanoparticles, the advantages of co-condensation methods, the advantages of post-synthesis grafting methods and the advantages of heterogeneous catalysis, several mesoporous silica nanoparticle(MSN)-based catalytic systems will be designed and applied in organocatalysis, metallic catalysis and organomeallic catalysis as well.[43,44,49,102]

References

(1) Sing, K. S. W.; Everett, D. H.; Haul, R. A. W.; Moscou, L.; Pierotti, R. A.; Rouquerol, J.; Siemieniewska, T. *Pure Appl. Chem.* **1985**, *57*, 603-19.

(2) Brinker, C. J.; Scherer, G. W. *Sol-gel science: the physics and chemistry of sol-gel processing*; Academic Press, 1990.

(3) *Introduction to Zeolite Molecular Sieves*; 3rd ed.; Cejka, J.; Bekkum, H. v.; Corma, A.; Schueth, F., Eds.; Elsevier, 2007.

(4) Barton, T. J.; Bull, L. M.; Klemperer, W. G.; Loy, D. A.; McEnaney, B.; Misono, M.; Monson, P. A.; Pez, G.; Scherer, G. W.; Vartuli, J. C.; Yaghi, O. M. *Chem. Mater.* **1999**, *11*, 2633-2656.

(5) Kresge, C. T.; Leonowicz, M. E.; Roth, W. J.; Vartuli, J. C.; Beck, J. S. *Nature (London, United Kingdom)* **1992**, *359*, 710-712.

(6) Beck, J. S.; Vartuli, J. C.; Roth, W. J.; Leonowicz, M. E.; Kresge, C. T.; Schmitt, K. D.; Chu, C. T. W.; Olson, D. H.; Sheppard, E. W.; et al. *J. Am. Chem. Soc.* **1992**, *114*, 10834-43.

(7) Yanagisawa, T.; Shimizu, T.; Kuroda, K.; Kato, C. *Bull. Chem. Soc. Jpn.* **1990**, *63*, 1535-7.

(8) Yanagisawa, T.; Shimizu, T.; Kuroda, K.; Kato, C. *Bull. Chem. Soc. Jpn.* **1990**, *63*, 988-92.

(9) Inagaki, S.; Fukushima, Y.; Kuroda, K. *J. Chem. Soc., Chem. Commun.* **1993**, 680-2.

(10) Lu, Y. *Angew. Chem. Int. Ed.* **2006**, *45*, 7664-7667.

(11) Zhao, D.; Feng, J.; Huo, Q.; Melosh, N.; Frederickson, G. H.; Chmelka, B. F.; Stucky, G. D. *Science (Washington, D. C.)* **1998**, *279*, 548-552.

(12) Wu, C. G.; Bein, T. *Science (Washington, DC, United States)* **1994**, *264*, 1757-9.

(13) Wu, C.-G.; Bein, T. *Science (Washington, D. C.)* **1994**, *266*, 1013-15.

(14) Bagshaw, S. A.; Prouzet, E.; Pinnavaia, T. J. *Science (Washington, D. C.)* **1995**, *269*, 1242-4.

(15) Lin, H.-P.; Mou, C.-Y. *Science (Washington, D. C.)* **1996**, *273*, 765-768.

(16) Mann, S.; Ozin, G. *Nature (London)* **1996**, *382*, 313-318.

(17) Davis, S. A.; Burkett, S. L.; Mendelson, N. H.; Mann, S. *Nature (London)* **1997**, *385*, 420-423.

(18) Gruen, M.; Lauer, I.; Unger, K. K. *Adv. Mater.* **1997**, *9*, 254-257.

(19) Lu, Y.; Ganguli, R.; Drewien, C. A.; Anderson, M. T.; Brinker, C. J.; Gong, W.; Guo, Y.; Soyez, H.; Dunn, B.; Huang, M. H.; Zink, J. I. *Nature (London)* **1997**, *389*, 364-368.

(20) Kim, S. S.; Zhang, W.; Pinnavaia, T. J. *Science (Washington, D. C.)* **1998**, *282*, 1302-1305.

(21) Yang, P.; Deng, T.; Zhao, D.; Feng, P.; Pine, D.; Chmelka, B. F.; Whitesides, G. M.; Stucky, G. D. *Science (Washington, D. C.)* **1998**, *282*, 2244-2247.

(22) Yang, P.; Zhao, D.; Chmelka, B. F.; Stucky, G. D. *Chem. Mater.* **1998**, *10*, 2033-2036.

(23) Yang, P.; Zhao, D.; Margolese, D. I.; Chmelka, B. F.; Stucky, G. D. *Nature (London)* **1998**, *396*, 152-155.

(24) Zhao, D.; Huo, Q.; Feng, J.; Chmelka, B. F.; Stucky, G. D. *J. Am. Chem. Soc.* **1998**, *120*, 6024-6036.

(25) Asefa, T.; MacLachlan, M. J.; Coombs, N.; Ozin, G. A. *Nature (London)* **1999**, *402*, 867-871.

(26) Ciesla, U.; Schuth, F. *Micropor. Mesopor. Mater.* **1999**, *27*, 131-149.

(27) Melde, B. J.; Holland, B. T.; Blanford, C. F.; Stein, A. *Chem. Mater.* **1999**, *11*, 3302-3308.

(28) Schmidt-Winkel, P.; Yang, P.; Margolese, D. I.; Chmelka, B. F.; Stucky, G. D. *Adv. Mater.* **1999**, *11*, 303-307.

(29) Kimura, T.; Kamata, T.; Fuziwara, M.; Takano, Y.; Kaneda, M.; Sakamoto, Y.; Terqasaki, O.; Sugahara, Y.; Kuroda, K. *Angew. Chem. Int. Ed.* **2000**, *39*, 3855-3859.

(30) Ozin, G. A. *Chem. Commun.* **2000**, 419-432.

(31) Fowler, C. E.; Khushalani, D.; Lebeau, B.; Mann, S. *Adv. Mater.* **2001**, *13*, 649-652.

(32) Miyata, H.; Kuroda, K. *Adv. Mater.* **2001**, *13*, 558-561.

(33) Mokaya, R. *Chem. Commun.* **2001**, 933-934.

(34) Pauwels, B.; Van Tendeloo, G.; Thoelen, C.; Van Rhijn, W.; Jacobs, P. A. *Adv. Mater.* **2001**, *13*, 1317-1320.

(35) Ryoo, R.; Joo, S. H.; Kruk, M.; Jaroniec, M. *Adv. Mater.* **2001**, *13*, 677-681.

(36) Lee, J.-S.; Joo Sang, H.; Ryoo, R. *J. Am. Chem. Soc.* **2002**, *124*, 1156-7.

(37) Che, S.; Garcia-Bennett, A. E.; Liu, X.; Hodgkins, R. P.; Wright, P. A.; Zhao, D.; Terasaki, O.; Tatsumi, T. *Angew. Chem. Int. Ed.* **2003**, *42*, 3930-3934.

(38) Fan, J.; Yu, C.; Gao, F.; Lei, J.; Tian, B.; Wang, L.; Luo, Q.; Tu, B.; Zhou, W.; Zhao, D. *Angew. Chem. Int. Ed.* **2003**, *42*, 3146-3150.

(39) Pai, R. A.; Humayun, R.; Schulberg, M. T.; Sengupta, A.; Sun, J.-N.; Watkins, J. J. *Science (Washington, DC, United States)* **2004**, *303*, 507-511.

(40) Trewyn, B. G.; Whitman, C. M.; Lin, V. S.-Y. *Nano Lett.* **2004**, *4*, 2139-2143.

(41) Wang, S.-G.; Wu, C.-W.; Chen, K.; Lin, V. S.-Y. *Chem.--Asian J.* **2009**, *4*, 658-661.

(42) Fan, J.; Yu, C.; Wang, L.; Tu, B.; Zhao, D.; Sakamoto, Y.; Terasaki, O. *J. Am. Chem. Soc.* **2001**, *123*, 12113-12114.

(43) Lin, V. S.-Y.; Huang, Y.; Cai, Y. *Prepr. Symp. - Am. Chem. Soc., Div. Fuel Chem.* **2008**, *53*, 192-193.

(44) Huang, Y.; Trewyn, B. G.; Chen, H.-T.; Lin, V. S.-Y. *New J. Chem.* **2008**, *32*, 1311-1313.

(45) Huh, S.; Chen, H.-T.; Wiench, J. W.; Pruski, M.; Lin, V. S.-Y. *J. Am. Chem. Soc.* **2004**, *126*, 1010-1011.

(46) Huh, S.; Chen, H.-T.; Wiench, J. W.; Pruski, M.; Lin, V. S.-Y. *Angew. Chem. Int. Ed.* **2005**, *44*, 1826-1830.

(47) Cai, Y.; Kumar, R.; Huang, W.; Trewyn, B. G.; Wiench, J. W.; Pruski, M.; Lin, V. S.-Y. *J. Phys. Chem. C* **2007**, *111*, 1480-1486.

(48) Chen, H.-T.; Huh, S.; Wiench, J. W.; Pruski, M.; Lin, V. S.-Y. *J. Am. Chem. Soc.* **2005**, *127*, 13305-13311.

(49) Szajna-Fuller, E.; Huang, Y.; Rapp Jennifer, L.; Chaka, G.; Lin Victor, S. Y.; Pruski, M.; Bakac, A. *Dalton Trans* **2009**, 3237-46.

(50) Zorn, D.; Lin, V. S.-Y.; Pruski, M.; Gordon, M. S. *J. Phys. Chem. A* **2008**, *112*, 10635-10649.

(51) Zorn, D.; Lin, V. S.-Y.; Pruski, M.; Gordon, M. S. *J. Phys. Chem. B* **2008**, *112*, 12753-12760.

(52) Tanev, P. T.; Chibwe, M.; Pinnavaia, T. J. *Nature (London, United Kingdom)* **1994**, *368*, 321-3.

(53) Xia, Y.; Mokaya, R. *Angew. Chem. Int. Ed.* **2003**, *42*, 2639-2644.

(54) Torney, F.; Trewyn, B. G.; Lin, V. S.-Y.; Wang, K. *Nat. Nanotechnol.* **2007**, *2*, 295-300.

(55) Radu, D. R.; Lai, C.-Y.; Jeftinija, K.; Rowe, E. W.; Jeftinija, S.; Lin, V. S.-Y. *J. Am. Chem. Soc.* **2004**, *126*, 13216-13217.

(56) Mortera, R.; Vivero-Escoto, J.; Slowing, I. I.; Garrone, E.; Onida, B.; Lin, V. S.-Y. *Chem. Commun. (Cambridge, U. K.)* **2009**, 3219-3221.

(57) Lin, V. S.-Y.; Lai, C.-Y.; Huang, J.; Song, S.-A.; Xu, S. *J. Am. Chem. Soc.* **2001**, *123*, 11510-11511.

(58) Lin, V. S.-Y.; Radu, D. R.; Han, M.-K.; Deng, W.; Kuroki, S.; Shanks, B. H.; Pruski, M. *J. Am. Chem. Soc.* **2002**, *124*, 9040-9041.

(59) Mbaraka, I. K.; Radu, D. R.; Lin, V. S.-Y.; Shanks, B. H. *J. Catal.* **2003**, *219*, 329-336.

(60) Lei, C.; Shin, Y.; Liu, J.; Ackerman Eric, J. *J. Am. Chem. Soc.* **2002**, *124*, 11242-3.

(61) Radu, D. R.; Lai, C.-Y.; Wiench, J. W.; Pruski, M.; Lin, V. S.-Y. *J. Am. Chem. Soc.* **2004**, *126*, 1640-1641.

(62) Determan, A. S.; Trewyn, B. G.; Lin, V. S.-Y.; Nilsen-Hamilton, M.; Narasimhan, B. *J. Controlled Release* **2004**, *100*, 97-109.

(63) Giri, S.; Trewyn, B. G.; Stellmaker, M. P.; Lin, V. S.-Y. *Angew. Chem. Int. Ed.* **2005**, *44*, 5038-5044.

(64) Lai, C.-Y.; Trewyn, B. G.; Jeftinija, D. M.; Jeftinija, K.; Xu, S.; Jeftinija, S.; Lin, V. S.-Y. *J. Am. Chem. Soc.* **2003**, *125*, 4451-4459.

(65) Lin, V. S.-Y. *Nat. Mater.* **2009**, *8*, 252-253.

(66) Slowing, I. I.; Trewyn, B. G.; Giri, S.; Lin, V. S.-Y. *Adv. Funct. Mater.* **2007**, *17*, 1225-1236.

(67) Slowing, I. I.; Trewyn, B. G.; Lin, V. S.-Y. *J. Am. Chem. Soc.* **2007**, *129*, 8845-8849.

(68) Slowing, I. I.; Vivero-Escoto, J. L.; Wu, C.-W.; Lin, V. S.-Y. *Adv. Drug Delivery Rev.* **2008**, *60*, 1278-1288.

(69) Trewyn, B. G.; Giri, S.; Slowing, I. I.; Lin, V. S.-Y. *Chem. Commun. (Cambridge, U. K.)* **2007**, 3236-3245.

(70) Trewyn, B. G.; Nieweg, J. A.; Zhao, Y.; Lin, V. S.-Y. *Chem. Eng. J. (Amsterdam, Neth.)* **2008**, *137*, 23-29.

(71) Trewyn, B. G.; Slowing, I. I.; Giri, S.; Chen, H.-T.; Lin, V. S.-Y. *Acc. Chem. Res.* **2007**, *40*, 846-853.

(72) Vivero-Escoto, J. L.; Slowing, I. I.; Wu, C.-W.; Lin, V. S.-Y. *J. Am. Chem. Soc.* **2009**, *131*, 3462-3463.

(73) Zhao, Y.; Trewyn, B. G.; Slowing, I. I.; Lin, V. S.-Y. *J. Am. Chem. Soc.* **2009**, *131*, 8398-8400.

(74) Han, Y.-J.; Stucky, G. D.; Butler, A. *J. Am. Chem. Soc.* **1999**, *121*, 9897-9898.

(75) Jang, M.; Park, J. K.; Shin, E. W. *Microporous Mesoporous Mater.* **2004**, *75*, 159-168.

(76) Algarra, M.; Jimenez, M. V.; Rodriguez-Castellon, E.; Jimenez-Lopez, A.; Jimenez-Jimenez, J. *Chemosphere* **2005**, *59*, 779-786.

(77) Jang, M.; Shin, E. W.; Park, J. K.; Choi, S. I. *Environ. Sci. Technol.* **2003**, *37*, 5062-5070.

(78) Feng, X.; Fryxell, G. E.; Wang, L. Q.; Kim, A. Y.; Liu, J.; Kemner, K. M. *Science (Washington, D. C.)* **1997**, *276*, 923-926.

(79) Yoshitake, H.; Yokoi, T.; Tatsumi, T. *Chem. Mater.* **2002**, *14*, 4603-4610.

(80) Yoshitake, H.; Yokoi, T.; Tatsumi, T. *Chem. Mater.* **2003**, *15*, 1713-1721.

(81) Kim, T.-W.; Chung, P.-W.; Slowing, I. I.; Tsunoda, M.; Yeung, E. S.; Lin, V. S.-Y. *Nano Lett.* **2008**, *8*, 3724-3727.

(82) Joo, S. H.; Choi, S. J.; Oh, I.; Kwak, J.; Liu, Z.; Terasaki, O.; Ryoo, R. *Nature (London, United Kingdom)* **2001**, *414*, 470.

(83) Stein, A.; Melde, B. J.; Schroden, R. C. *Adv. Mater.* **2000**, *12*, 1403-1419.

(84) Anwander, R.; Palm, C.; Stelzer, J.; Groeger, O.; Engelhardt, G. *Stud. Surf. Sci. Catal.* **1998**, *117*, 135-142.

(85) Zhao, X. S.; Lu, G. Q. *J. Phys. Chem. B* **1998**, *102*, 1556-1561.

(86) Lim, M. H.; Stein, A. *Chem. Mater.* **1999**, *11*, 3285-3295.

(87) Shephard, D. S.; Zhou, W.; Maschmeyer, T.; Matters, J. M.; Roper, C. L.; Parsons, S.; Johnson, B. F. G.; Duer, M. J. *Angew. Chem. Int. Ed.* **1998**, *37*, 2719-2723.

(88) De Juan, F.; Ruiz-Hitzky, E. *Adv. Mater.* **2000**, *12*, 430-432.

(89) Huh, S.; Wiench, J. W.; Trewyn, B. G.; Song, S.; Pruski, M.; Lin, V. S.-Y. *Chem. Commun.* **2003**, 2364-2365.

(90) Huh, S.; Wiench, J. W.; Yoo, J.-C.; Pruski, M.; Lin, V. S.-Y. *Chem. Mater.* **2003**, *15*, 4247-4256.

(91) Chen, H.-T., Huh, S., Wiench, J. W., Pruski, M., Lin, V. S.-Y. *J. Am. Chem. Soc.* **2005**, *127*, 13305-13311.

(92) Yang, H.; Coombs, N.; Ozin, G. A. *Nature (London)* **1997**, *386*, 692-695.

(93) Bradbury, J. *PLoS Biol.* **2004**, *2*, 1512-1515.

(94) *Handbook of Heterogeneous Catalysis*; Ertl, G.; Knozinger, H.; Weitkamp, J., Eds.; Wiley-VCH: New York, Weinheim, 1997.

(95) Thomas, J. M.; Thomas, W. J. *Principles and Practice of Heterogeneous Catalysis*; Wiley-VCH: Weinheim, 1997.

(96) *Chiral Catalysis Immobilization and Recycling*; Vos, D. E. D.; Vankelecom, I. F. J.; Jacobs, P. A., Eds.; Wiley-VCH: Weinheim, 2000.

(97) A.Taguchi; Schuth, F. *Micropor. Mesopor. Mater.* **2005**, *77*, 1-45.

(98) Murzin, D. Y.; Maki-Arvela, P.; Toukoniitty, E.; Salmi, T. *Catal. Rev.* **2005**, *47*, 175-256.

(99) Cormaa, A.; Garciaa, H. *Adv. Synth. Catal.* **2006**, *348*, 1391-1412.

(100) Heitbaum, M.; Glorius, F.; Escher, I. *Angew. Chem. Int. Ed.* **2006**, *45*, 4732-4762.

(101) Clark, J. H.; Macquarrie, D. J. *Chem. Commun.* **1998**, 853-860.

(102) Rapp, J. L.; Huang, Y.; Natella, M.; Cai, Y.; Lin, V. S.-Y.; Pruski, M. *Solid State Nucl. Magn. Reson.* **2009**, *35*, 82-86.

(103) Liu, D.-J.; Chen, H.-T.; Lin, V. S.-Y.; Evans, J. W. *Phys. Rev. E: Stat., Nonlinear, Soft Matter Phys.* **2009**, *80*, 011801/1-011801/9.

(104) Nieweg, J. A.; Kern, C.; Trewyn, B. G.; Wiench, J. W.; Pruski, M.; Lin, V. S.-Y. *Prepr. - Am. Chem. Soc., Div. Pet. Chem.* **2007**, *52*, 89-90.

(105) Lin, V. S.-Y.; Nieweg, J. A.; Kern, C.; Trewyn, B. G.; Wiench, J. W.; Pruski, M. *Prepr. Symp. - Am. Chem. Soc., Div. Fuel Chem.* **2006**, *51*, 426-427.

(106) Nieweg, J. A.; Lemma, K.; Trewyn, B. G.; Lin, V. S.-Y.; Bakac, A. *Inorg. Chem.* **2005**, *44*, 5641-5648.

(107) Lin, V. S.-Y.; Radu, D. R.; Chen, H.-T. *Prepr. Symp. - Am. Chem. Soc., Div. Fuel Chem.* **2005**, *50*, 306-307.

(108) Sharma, K. K.; Buckley, R. P.; Asefa, T. *Langmuir* **2008**, *24*, 14306-14320.

(109) Sharma, K. K.; Asefa, T. *Angew. Chem. Int. Ed.* **2007**, *46*, 2879-2882.

(110) Anan, A.; Sharma, K. K.; Asefa, T. *J. Mol. Catal. A* **2008**, *288*, 1-13.

(111) Anan, A.; Vathyam, R.; Sharma, K. K.; Asefa, T. *Catal. Lett.* **2008**, *126*, 142-148.

(112) Sharma, K. K.; Anan, A.; Buckley, R. P.; Ouellette, W.; Asefa, T. *J. Am. Chem. Soc.* **2008**, *130*, 218-228.

(113) Mishler, R. E., II; Biradar, A. V.; Duncan, C. T.; Schiff, E. A.; Asefa, T. *Chem. Commun.* **2009**, 6201-6203.

(114) Tao, Z.; Wang, G.; Goodisman, J.; Asefa, T. *Langmuir* **2009**, *25*, 10183-10188.

(115) Xie, Y.; Sharma, K. K.; Anan, A.; Wang, G.; Biradar, A. V.; Asefa, T. *J. Catal.* **2009**, *265*, 131-140.

(116) Macquarrie, D. J.; Jackson, D. B. *Chem. Commun.* **1997**, 1771-1772.

(117) Thomas, J. M.; Raja, R. *Acc. Chem. Res.* **2008**, *41*, 708-720.

(118) Jones, M. D.; Raja, R.; Thomas, J. M.; Johnson, B. F. G.; Lewis, D. W.; Rouzaud, J.; Harris, K. D. M. *Angew. Chem. Int. Ed.* **2003**, *42*, 4326-4331.

CHAPTER 2. ONE-POT REACTION CASCADES CATALYZED BY BASE- AND ACID-FUNCTIONALIZED MESOPOROUS SILICA NANOPARTICLES

A paper published in the *New Journal of Chemistry*, **2008**, 32, 1311-1313.

Yulin Huang, Brian G. Trewyn, Hung-Ting Chen, Victor S.-Y. Lin*

Department of Chemistry, U.S. Department of Energy Ames Laboratory, Iowa State University, Ames, Iowa 50011-3111

**Corresponding author.*

Abstract

Mesoporous silica nanoparticles (MSNs) containing base (primary amine) and sulfonic acid inside the MCM-41 type porous channels were used as compatible catalysts for one-pot reaction cascades successfully.

Introduction

Nature's strategy of employing multistep reaction cascades for the synthesis of complex and bioactive organic molecules in living systems has long been a goal for designing artificial catalysts. While recent advancements in supramolecular chemistry, nanomaterial synthesis, and catalyst design have significantly improved our ability in mimicking this ingenious strategy of biocatalysis, the progress in constructing compatible multifunctional catalytic system that can operate synergistically in one-pot sequential

reactions is still relatively limited. Nonetheless, the recently developed "site isolation" concept for synthesizing surface-supported catalysts with multiple functionalities has led to many efficient biomimetic catalysts. In these systems, the different and often incompatible catalytic functionalities, such as acidic and basic groups, are separatively isolated within the supporting matrices. The spatial separation of these chemical species that react avidly with each other in solution prevents the undesired self destruction of catalytic capability. A few recent literature reports have highlighted the success of this approach. For example, Cohen and co-workers first developed a "wolf and lamb" two-stage reaction system, where a soluble reagent reacts first with one polymeric reagent and the product with the second polymeric reagent.[1] Blum and Avnir further developed "wolf and lamb" type one-pot reactions by encapsulating opposing catalysts in sol-gel.[2-6] More recent investigations on using soluble star polymers[7] and other polymers[8] as site-isolating matrices also led to effective catalytic systems for one-pot reaction cascades.

Ever since the discovery of MCM-41 mesoporous silica,[9] these structurally ordered materials have been regarded as the ideal solid support for various catalysts due to their high surface areas (> 800 m^2/g) and tunable pore sizes (2-20 nm). Several recent reports on the multifunctionalization of mesoporous silica materials have rendered several interesting systems for cooperative catalysis.[10-13] Given that Blum and Avnir have pioneerly demonstrated that sol-gel silica can serve as an effective matrix for entraping opposing catalysts for one-pot reaction cascades,[2-6] we are interested in taking advantage of the unique properties, i.e., homogeneous mesoporous structure and tunable particle size and pore diameter, of the MCM-type of mesoporous silicas for the site isolation of opposing catalytic reagents as well as the pore size discrimination that can regulate the mass-transport

properties of a given reaction. By "hiding" one kind of functional groups inside the mesopores of a mesoporous silica particle, while ensuring the other opposing reagent is situated inside another mesoporous silica material with different particle and pore sizes, the reaction kinetics could foreseeably be further manipulated. To achieve this goal, a key prerequisite is to functionalize the interior mesoporous surface with homogeneously distributed, high concentrations of functional groups, along with precise morphology control. We have recently developed an interfacial designed co-condensation method under low surfactant concentration condition for the synthesis of a series of organically functionalized mesoporous silica nanoparticle (MSN) materials.[13-18] Herein, we report on the synthesis and characterization of two MCM-41 type MSN materials that are functionalized with a 4-ethylphenylsulfonic acid (SAMSN) and an aminopropyl-functionality (APMSN) as depicted in Figure 1-1. We demonstrated that SAMSN and APMSN could serve as acid and base catalysts, respectively, for the wolf-and-lamb type of one-pot reaction cascades. As a proof of principle, we examined the catalytic conversion of 4-nitrobenzaldehyde dimethyl acetal (Compound A) to (*E*)-1-nitro-4-(2-nitrovinyl)benzene (Compound C), which involved two separate reactions, i.e., an acid-catalyzed deprotection to yield the 4-nitrobenzaldehyde denoted as Compound B, followed by a base-catalyzed Henry reaction in nitromethane to generate the final product (*E*)-1-nitro-4-(2-nitrovinyl)benzene (Table 1-1).

Results and Discussions

The SAMSN and APMSN materials were synthesized via the previously described co-condensation of tetraethyl orthosilicate (TEOS) and 4-chlorosulfonophneylethylene-

trimethoxysilane (CSTMOS) (or 3-aminopropyl-trimethoxysilane (APTMOS)) in the presence of cetyltrimethylammonium bromide (CTAB) as template under basic conditions as detailed in the Supporting Information. The CTAB-removed SAMSN and APMSN materials were characterized with nitrogen sorption analysis, powder X-ray diffraction (XRD), scanning electron microscopy (SEM), transimission electron microscopy (TEM), and the ^{13}C and ^{29}Si solid-state NMR. The TEM (Figure 1a and b) and SEM (Figure S1 of the Supporting Information) images of SAMSN and APMSN showed that both materials have the typical MCM-41 type, highly ordered parallel channel-like porous structure packed in a hexagonal symmetry. The XRD diffraction patterns (Figure S3) further confirmed the MCM-41 type mesoporous structure with the d_{100} = 42.5 Å and 40.9 Å (SAMSN and APMSN, respectively). As illustrated in Figure S4, the N_2 surface sorption analysis showed very high total surface areas (SAMSN: 827.9 m^2/g; APMSN: 789.0 m^2/g) and narrow pore diameter distributions (SAMSN: 25.4 Å; APMSN: 22.3 Å).

The ^{29}Si solid-state crossed polarization magic angle spining (CP-MAS) NMR (Figure S5 and S6) of these materials confirmed the covalent linkage between the organic functional groups to the silica surfaces as indicated by the T^2 and T^3 peaks, which are derived from $(\equiv SiO)_2\mathbf{Si}(OH)R$ and $(\equiv SiO)_3\mathbf{Si}R$, respectively.[19-21] Furthermore, the presence and chemical structures of the desired organic acid and base functionalities were quantatively verified by the ^{13}C solid-state CP-MAS NMR spectra (Figure 1-2). The loading of sulfonic acid was determined to be 0.32 mmol/g of SAMSN, whereas the loading of amine was 0.40 mmol/g of APMSN.

In order to test the compatibility of these mesopore-confined acid and base solids in catalyzing the one-pot reaction cascade, different molar ratios of SAMSN/APMSN were

applied to the chemical transformation of 4-nitrobenzaldehyde dimethyl acetal(Compound A) to (*E*)-1-nitro-4-(2-nitrovinyl)benzene (Compound C). Reactions without any catalysts, with either free acid or free base, and with non-functionalized MSN were also performed as control experiments (Table 1-1).

As shown in entries 1–4 in Table 1-1, the acid-catalyzed deprotection of **A,** which is the first step of this two-step cascade reaction, was completed within 24 h in the presence of SAMSN (1.0 mol%) and APMSN (1.0–6.0 mol%). The result suggested that the sulfonic acid functionality of SAMSN was not affected by the presence of APMSN. Interestingly, the conversion of **B** to the final product **C** of the second Henry reaction was significantly enhanced from 43.5 to 97.7 % as the amount of base-catalyst (APMSN) increased from 1.0 to 6.0 mol%. Also, different amounts of compound **B** (56.4–2.3 %) were isolated at the end of 24 h in these reactions (entries 1–4) of various quantities of APMSN. Apparently, the more APMSN introduced to the reaction mixture, the faster kinetics could be achieved in the Henry reaction.

Furthermore, the desired Henry adduct **C** did not form in entries 5–6, where only one of the two MSN catalysts was present in the reaction. In entries 7 and 8, a molecular base (*tert*-butylamine) and an acid (*para*-toluenesulfonic acid) that are structurally similar to the corresponding organic groups immobilized in APMSN and SAMSN, respectively, were used to replace the solid catalysts. As predicted, these molecular substitutes could freely diffuse into the mesopores of APMSN (or SAMSN) and reacted to the surface-anchored acidic/basic functional groups. The deactivated solids no longer could catalyze the reaction cascade. This homogeneous acid-base neutralization-induced destruction was confirmed by mixing both *tert*-butylamine and *para*-toluenesulfonic in the reaction solution (entry 9).

Conclusions

We have demonstrated that by confining organic acid and base inside of mesoporous silica nanoparticles, these opposing reagents can be isolated and serve as effective catalysts for a one-pot reaction cascade that requires incompatible catalysts. We envision that this approach can be further developed into a general design principle for mimicking biological systems, in which a series of reactions are catalyzed by different enzymes in a precise sequence.

Acknowledgement

The authors thank the Office of Basic Energy Sciences of the U.S. Department of Energy (DOE) under Contract No. DE-AC02-07CH11358 for providing financial support of this research.

Supplementary Information, including synthesis of APMSN and SAMSN, nitrogen adsorption/desorption isotherms and pore size distributions, powder small angle XRD, SEM images, TEM images, ^{29}Si solid state NMR spectra of APMSN and SAMSN, was attached.

References

1. B. J. Cohen, M. A. Kraus and A. Patchornik, *J. Am. Chem. Soc.*, 1981, **103**, 7620-7629.

2. F. Gelman, J. Blum and D. Avnir, *J. Am. Chem. Soc.,* 2000, **122**, 11999-12000.

3. F. Gelman, J. Blum and D. Avnir, *Angew. Chem. Int. Ed.*, 2001, **40**, 3647-3649.

4. F. Gelman, J. Blum and D. Avnir, *J. Am. Chem. Soc.*, 2002, **124**, 14460-14463.

5. F. Gelman, J. Blum and D. Avnir, *New J. Chem.*, 2003, **27**, 205-207.

6. F. Gelman, J. Blum, H. Schumann and D. Avnir, *J. Sol-Gel Sci. Technol.*, 2003, **26**, 43-46.

7. B. Helms, S. J. Guillaudeu, Y. Xie, M. McMurdo, C. J. Hawker and J. M. J. Frechet, *Angew. Chem. Int. Ed.*, 2005, **44**, 6384-6387.

8. N. T. S. Phan, C. S. Gill, J. V. Nguyen, Z. J. Zhang and C. W. Jones, *Angew. Chem. Int. Ed.*, 2006, **45**, 2209-2212.

9. C. T. Kresge, Leonowicz, M. E., Roth, W. J., Vartuli, J. C., Beck, J. S., *Nature* 1992, **359**, 710-712.

10. J. Alauzun, A. Mehdi, C. Reye and R. J. P. Corriu, *J. Am. Chem. Soc.* 2006, **128**, 8718-8719.

11. R. K. Zeidan and M. E. Davis, *J. Catal.*, 2007, **247**, 379-382.

12. R. K. Zeidan, S.-J. Hwang and M. E. Davis, *Angew. Chem. Int. Ed.,* 2006, **45**, 6332-6335.

13. S. Huh, H.-T. Chen, J. W. Wiench, M. Pruski and V. S.-Y. Lin, *Angew. Chem. Int. Ed.*, 2005, **44**, 1826-1830.

14. S. Huh, J. W. Wiench, B. G. Trewyn, S. Song, M. Pruski and V. S.-Y. Lin, *Chem. Commun.*, 2003, 2364-2365.

15. S. Huh, J. W. Wiench, J.-C. Yoo, M. Pruski and V. S.-Y. Lin, *Chem. Mater.*, 2003, **15**, 4247-4256.

16. S. C. Huh, H.-T. Chen, J. W. Wiench, M. Pruski, V. S.-Y. Lin, *J. Am. Chem. Soc.*, 2004, **126**, 1010-1011.

17. D. R. Radu, C.-Y. Lai, J. Huang, X. Shu and V. S.-Y. Lin, *Chem. Commun.*, **2005**, 1264-1266.

18. B. G. Trewyn, C. M. Whitman and V. S.-Y. Lin, *Nano Lett.,* 2004, **4**, 2139-2143.

19. J. Trebosc, J. W. Wiench, S. Huh, V. S.-Y. Lin and M. Pruski, *J. Am. Chem. Soc.*, 2005, **127**, 7587-7593.

20. J. Trebosc, J. W. Wiench, S. Huh, V. S.-Y. Lin and M. Pruski, *J. Am. Chem. Soc.*, 2005, **127**, 3057-3068.

21. J. W. Wiench, C. E. Bronnimann, V. S.-Y. Lin and M. Pruski, *J. Am. Chem. Soc.*, 2007, **129**, 12076-12077.

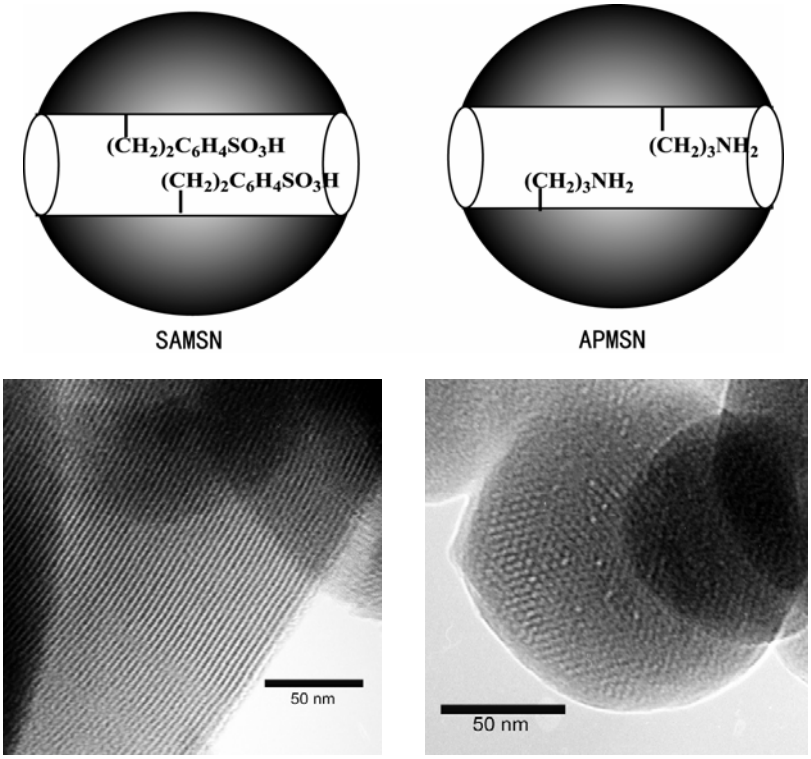

Figure 1-1. Mesoporous silica nanoparticles functionalized with an ethylphenylsulfonic acid (SAMSN) and an aminopropyl group (APMSN). The transmission electron micrographs (TEM) of SAMSN **(a)** and APMSN **(b)**. Scale bar = 50 nm.

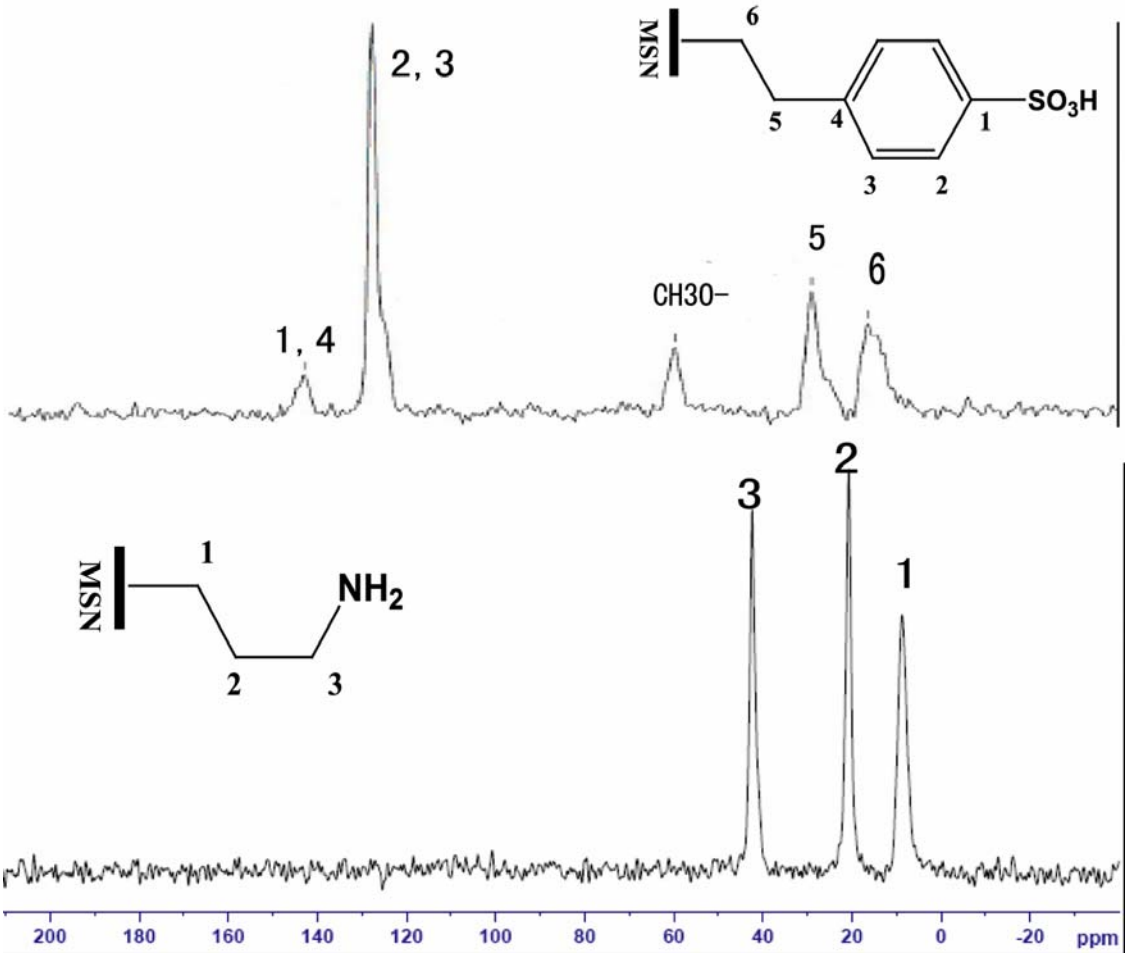

Figure 1-2. ^{13}C CP-MAS spectra of SAMSN (above) and APMSN (bottom).

Table 1-1. One-pot reaction cascade catalyzed by SAMSN and APMSN.

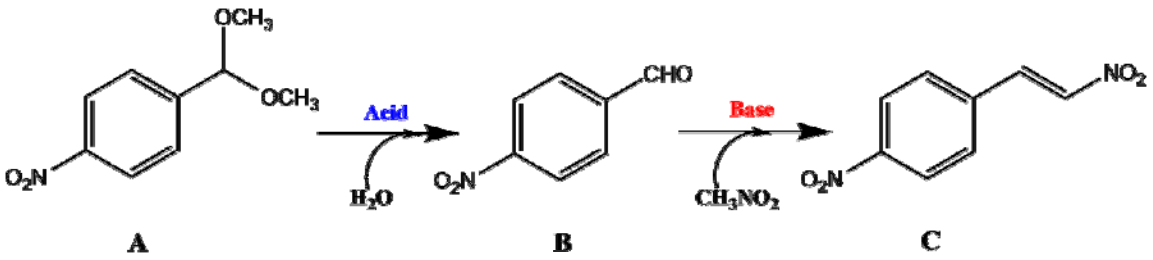

Entry	SAMSN (mol %)	APMSN (mol %)	Conversion of A (%)	Yield of B (%)	Yield of C (%)
1	1.0	1.0	99.9	56.4	43.5
2	1.0	2.0	100	22.0	78.0
3	1.0	4.0	100	5.0	95.0
4	1.0	6.0	100	2.3	97.7
5	1.0	0	98.1	98.1	0
6	0	1.0	0	0	0
7	1.0	1.0 (tert-butylamine)	0	0	0
8	1.0 (para-toluenesulfonic acid)	1.0	0	0	0
9	1.0 (para-toluenesulfonic acid)	1.0 (tert-butylamine)	0	0	0
10	Pure MSN	Pure MSN	0	0	0

Supporting Information

1. Synthesis of mesoporous silica nanosphere (MSN) containing organic acid confined inside pores (SAMSN) and MSN containing organic base confined inside pores (APMSN)

SAMSN and APMSN were synthesized via the co-condensation reaction from our group.[1 – 3] A typical procedure is as following: A mixture of cetyltrimethylammonium bromide (CTAB, 5.49 mmol), 2.0 mol / L of aqueous NaOH (7 mL, 14 mmol) and water (480 mL, 26.67 mol) was heated at 80 ^{o}C for 30 min. Into this clear solution, tetraethylorthosilicate (TEOS, 10 mL, 51.40 mmol) and 1.0 mmol of 2-(4-chlorosulfonylphenyl)ethyltrimethoxysilane for SAMSN (or 3-aminopropyltrimethoxysilane for APMSN) were added rapidly and sequentially via injection with vigorous stirring. Within few minutes, the white solid precipitate was observed. After 2 hours, the as-synthesized material was separated by hot filtration, washed with copious amount of methanol, dried under vacuum overnight. The surfactant (CTAB) was removed b y acid extraction at 60 ^{o}C with vigorous stirring by placing 1.0 gram of as-made solid in 100 mL methanol including 1.0 mL concentrated hydrochloride acid for 6 hours. The resulted surfactant-removed solid SAMSN (or APMSN) was collected by hot filtration, washed with copious amount of water and methanol, dried at 90 ^{o}C under vacuum overnight.

2. Characterization of MSB-acid and APMSN

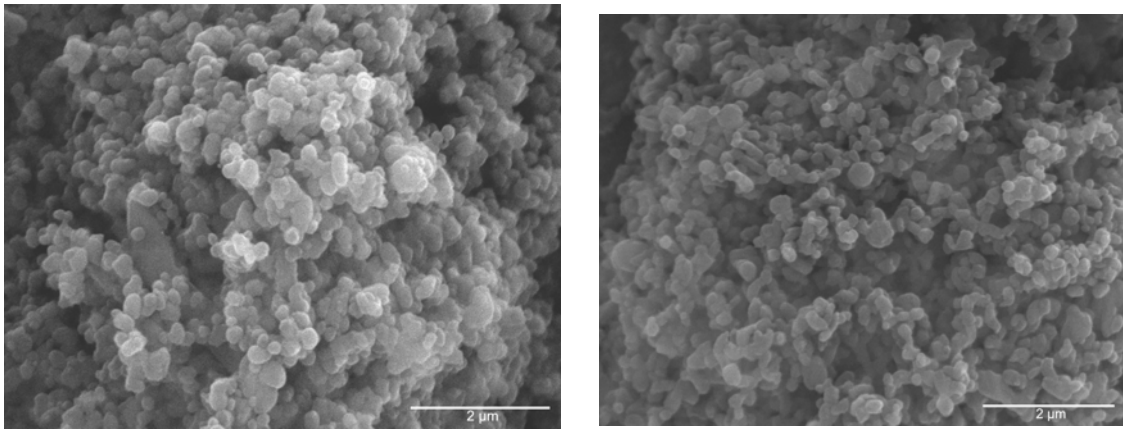

(a) **(b)**

Figure S1-1. Scanning electron microscopy (SEM) of SAMSN (a) and APMSN (b).

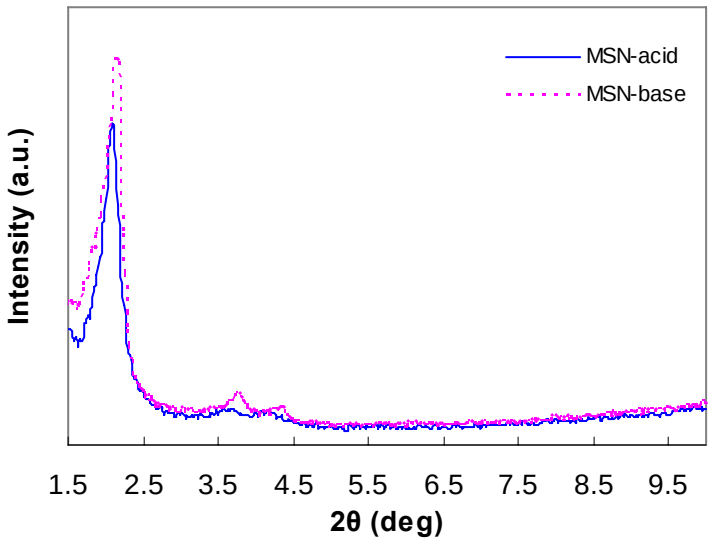

Figure S1-2. Powder XRD data of SAMSN and APMSN.

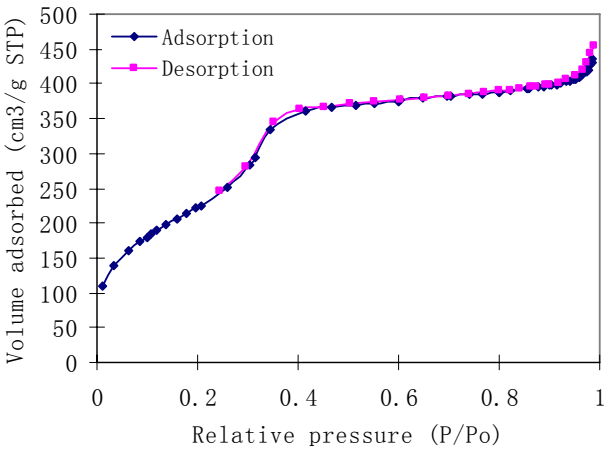

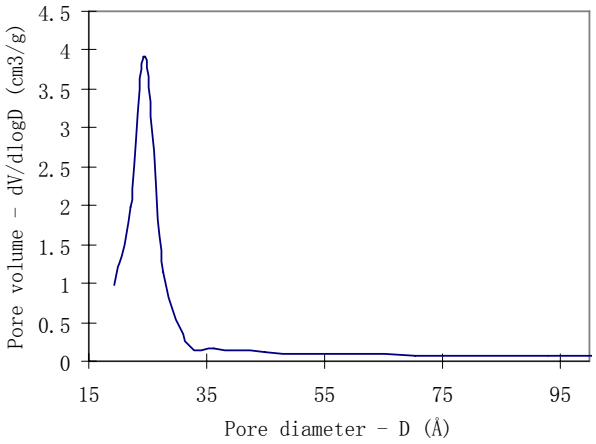

(a) SAMSN

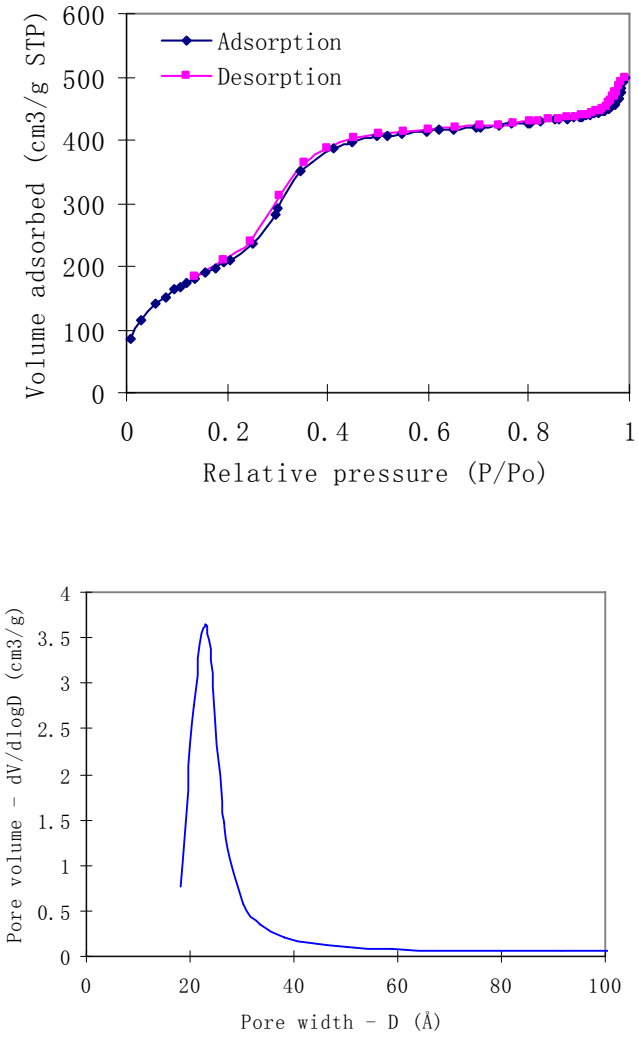

(b) APMSN

Figure S1-3. BET isotherms and BJH pore diameter distribution curves of SAMSN and APMSN.

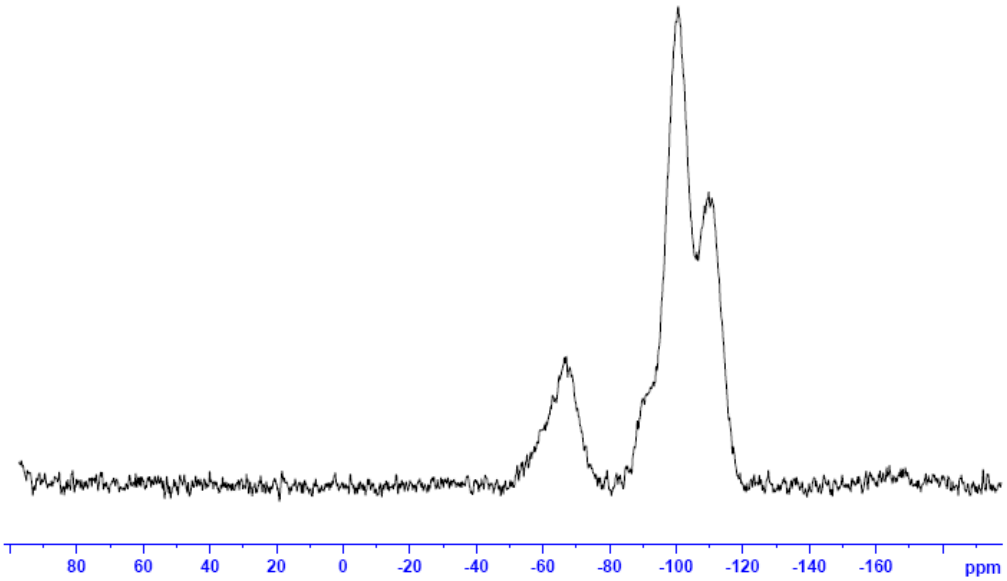

Figure S1-4. ^{29}Si solid state NMR spectrum of SAMSN (T^2: -59 ppm; T^3: -68 ppm; Q^2: -90 ppm; Q^3: -100 ppm; Q^4: -110 ppm).

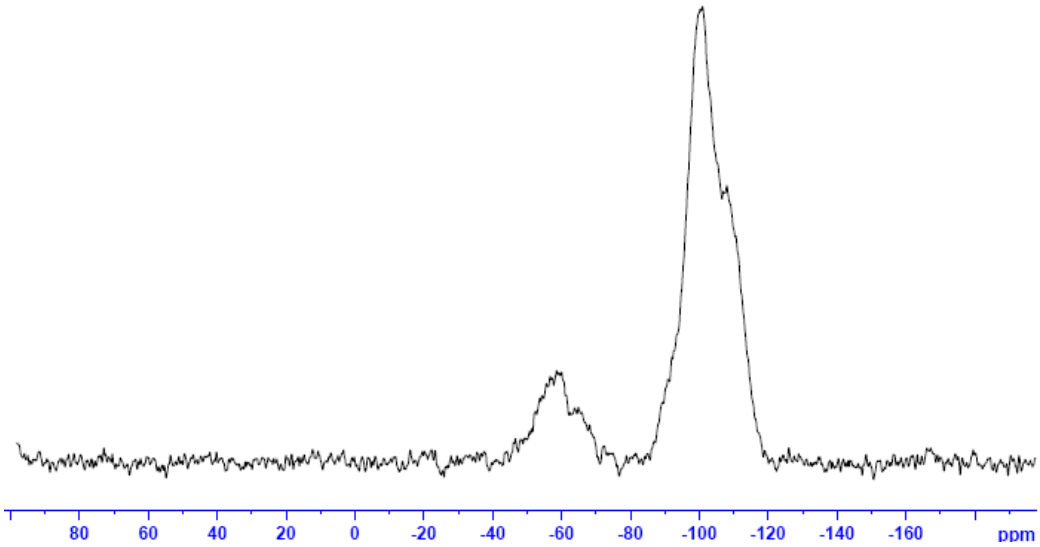

Figure S1-5. ^{29}Si solid state NMR spectrum of APMSN (T^2: -59 ppm; T^3: -68 ppm; Q^2: -90 ppm; Q^3: -100 ppm; Q^4: -110 ppm).

Table S1-1. Structural data of SAMSN and APMSN.[a]

Samples	d_{100} (Å)	S_{BET} (m^2/g)	V_p (cm^3/g)	D_{BJH} (Å)
SAMSN	42.5	827.9	0.67	25.4
APMSN	40.9	789.0	0.74	22.3

[a] The BET surface area (S_{BET}), the mesopore volume (V_p), and the mean mesopore diameter (D_{BJH}) were obtained from the nitrogen absorption / desorption data in Figure S3. The d_{100} data represent the d-spacing corresponding to the (100) peaks in XRD (Figure S2).

3. One-pot reaction cascades

4-nitrobenzaldehyde dimethyl acetal (0.75 mmol) and water (0.75 mmol) were mixed with SAMSN (or free acid, and the acid quantity is decided by the reaction conditions) and APMSN (or free base, and the base quantity is decided by the reaction conditions) at room temperature under N_2 and sealed in a glass vessel. The as-made slurry was heated to 80 ^oC with vigorous stirring. After 24 hours, the reaction was stopped by cooling to room temperature. The product was analyzed by GC-MS with capillary column (HP-5, 30 m x 0.319 mm x 0.25 μm).

(1) Huh, S.; Wiench, J.W.; Yoo, J.C.; Pruski, M.; Lin, V.S.Y. *Chem. Mater.* **2003**, 15, 4247–4256.

(2) Huh, S.; Wiench, J.W.; Trewyn, B.G.; Song, S.; Pruski, M.; Lin, V.S.Y. *Chem. Commun.* **2003**, 2364-2365.

(3) Radu, D.R.; Lai, C.Y.; Huang, J.; Xu, S.; Lin, V.S.Y. *Chem. Commun.* **2005**, 1265–1266.

CHAPTER 3. BIFUNCTIONALIZED MESOPOROUS MATERIALS WITH SITE-SEPARATED BRØNSTED ACID AND BASE AS SUCCESSFUL COHABITATING CATALYSTS

A paper to be submitted to *Angew. Chem. Int. Ed.*

Yulin Huang, Shu Xu, Victor S.-Y. Lin*

Department of Chemistry, U.S. Department of Energy Ames Laboratory, Iowa State University, Ames, Iowa 50011-3111

**Corresponding author.*

Abstract

Brønsted acid and base were site-separated on the different surfaces of mesoporous silica nanoparticle through cocondensation to functionalize the internal surface and post-synthesis grafting to functionalize the external surface. As a result of this ideal site-isolation, reaction cascades requiring two or more catalysts which are incompatible in one solution system could be done by these new internal and external surface-bifunctionalized particle.

Introduction

Mesoporous silica have been regarded as ideal supports for heterogeneous catalysts due to their high surface area, tunable pore size since the discovery of ordered mesoporous material MCM-41,[1] which opened a wide range of possibilities for the chemical design of novel heterogeneous catalysts.[2] Based on the rapid development of immobilized organo-catalysis, one of the major research interests about mesoporous silica in catalysis is surface functionalization with organic functional groups, which are potential immobilized organo-catalysts, by either post-synthesis grafting or co-condensation.[3-27] Wherein, the design and synthesis of bi- or multi-functionalized mesoporous silica containing multiple types of active centers has attracted a lot of attention, because these functional groups might be used as catalysts in several steps in a reaction sequence with a cooperative or independent catalytic

performance.[3,7,9-14,16,28] Actually, in biological system, there are many interesting examples of multifunctional catalysts -- enzymes, such as α-amylases,[29] as they can catalyze different reactions using different or incompatible catalytic active sites.

There are many examples of bifunctional mesoporous material catalysts in which attention has been focused on combinations of different organic functional groups, such as amines with silanols,[16,30] amine with thiols,[31,32] amines with ureas,[3,7] sulfonic acid with thiols,[9,11,14] and adjacent sulfonic acid functional groups,[28] where all of these two incorporated organic groups are compatible with each other. Recently different and incompatible catalytic centers (Brönsted acid and base) on separated and different mesoporous silica nanoparticles have been investigated.[33] As a matter of fact, many enzymes can immobilize mutually incompatible catalytic groups, including Brönsted acid and base, on one molecule, but all catalytic groups maintain their independent abilities to catalyze multistep reactions sequentially with full functionalities because they are well site-separated by 3-D folding of the enzyme. Up to now, there are only few examples of mesoporous materials with two functional groups which cannot coexist in solution. For example, Davis and his coworkers[10] reported sulfonic acid and amine functionalized SBA-15 with limited amount of acid and base groups to neutralize each other during the one-pot synthesis of material; Mehdi and his coworkers[23] reported another bifunctionalized mesoporous silica material with sulfonic acid groups in its framework and basic groups in its channel pores, but sulfonic acid groups in its framework were not so accessible for reactants. However, there is no report on selective dual-functionalization of single mesoporous silica nanoparticle with Brönsted acid and base on mesoporous silica external surface and internal surface separately, presumably due to the incompatibility of these groups and the difficulty to control reactions on external surface and internal surface individually.[34-42]

Here we report two mesoporous silica nanoparticles (MSNs) that were functionalized by both Brönsted acid and base, in which one of Brönsted acid and base was tethered on MSN external surface by post-synthesis grafting and the other was located on MSN internal surface through co-condensation independently. These functional groups on one MSN particle can catalyze multistep reactions sequentially, such as sulfonic acid-catalyzed hydrolysis of 4-nitrobenzaldehyde dimethyl acetal and the following amine-catalyzed Henry

reaction of 4-nitrobenaldehyde with nitromethane, which cannot be achieved with these same groups in one-pot homogeneous solution system. These novel materials were synthesized by co-condensation of tetraethyl orthosilicate (TEOS) and 3-aminopropyltrimethoxysilane (APTMOS) (or 3-mecaptotrimethoxysilane (STMOS)) in the presence of cetyltrimethylammonium bromide (CTAB) as template under basic medium, which was followed by post-treatment to grafting another functional group onto its external surface.

Results and Discussions

Typically, these bifunctional mesoporous materials were synthesized by co-condensation of one of the two functional groups in its internal channel[4] followed by grafting another on its external surface with template in its mesoporous channels[41,42]. In the synthesis procedure of bifunctional mesoporous silica nanoparticles with sulfonic acid on internal surface and amine groups on external surface, 2.0 g of CTAB and 7.0 mL of aqueous sodium hydroxide (2.0 mol/L) was dissolved into 480 mL of water at 80 ^{o}C with stirring (pH = 11.8); 10.0 mL of TEOS (44.0 mmol) and 190.6 μL (1.0 mmol) of STMOS were injected into the solution with vigorous stirring; After 2 h stirring, solid was separated by hot filtration, washed with excess water, dried at 120 ^{o}C under vacuum overnight; the as-made solid with CTAB inside mesoporous channels was stirred with 180.0 μL (1.0 mmol) of APTMOS in toluene at 120 ^{o}C for 6 h before being filtrated and washed with excess solvent and dried at 120 ^{o}C under vacuum overnight; In order to convert thiol groups to sulfonic acids, the as-gotten solid was stirred in acetic acid (10.0 mL) with 30 % H_2O_2 (20.0 mL) at 100 ^{o}C for 6 h; The surfactant was removed by extraction with methanol for 24 h and then washed with excess water and heated at 150 ^{o}C overnight in order to recover the amino groups.[43] The obtained white powder was termed as SAMSN-AP (Figure 3-1). Another bifunctional mesoporous silica nanoparticle with amine groups on its internal surface and sulfonic acid groups on its external surface, termed as APMSN-SA, was synthesized by the similar method (Figure S3-1).

The N_2 adsorption-desorption measurements for SAMSN-AP and APMSN-SA showed type IV isotherms with very clear H_1-hysteresis loops at relative high pressure, characteristic of mesoporous materials with BET surface areas over 853 m^2/g for SAMSN-

AP, 934 m^2/g for APMSN-SA, total pore volumes of 0.8 cm^3/g for SAMSN-AP, 0.9 cm^3/g for APMSN-SA, and very narrow pore size distribution centered at 2.8 nm for SAMSN-AP, 2.6 nm for APMSN-SA (Figure S3-2, S3-3 and Table S3-1). Small-angle X-ray scattering patterns of SAMSN-AP and APMSN-SA indicated highly ordered structures with corresponding d_{100} as 4.1 nm and 4.2 nm respectively (Figure S3-4 and Table S3-1). TEM images in Figure S3-6 confirmed their mesoporous structures with parallel channels as well as uniform pore size.

These materials were also analyzed by ^{29}Si and ^{13}C solid-state NMR spectroscopies. T^2 and T^3 peaks in ^{29}Si NMR spectra (Figure 3-2 and S3-7) indicated the incorporation of sulfonic acid and amine groups. ^{13}C NMR spectra (Figure 3-3 and S3-8) indicated the presence of the intact organic functional groups and the removal of most of surfactant. And the elemental analysis of both SAMSN-AP and APMSN-SA showed they have 0.35 mmol/g of sulfur and 0.35 mmol/g of nitrogen, which means the concentration of sulfonic acid is equal to that of amine on MSN with S/N ratio around 1.0.

Activities of these immobilized bifunctional catalysts were tested in a reaction cascade which was the hydrolysis of acetal followed by Henry reaction in one-pot reaction system, in which the first step in the cascade could only be catalyzed by acid and the second step in the cascade could merely be catalyzed by base catalyst (Scheme 3-1).

In all experiments, the amount of amine and/or sulfonic acid functional groups was kept at 4.0 mol %. As shown in Table 3-1, after the two step reaction cascade, the conversion of starting material is 100 %. In the final product, more than 97% was C when the bifunctionalized MSN (SAMSN-AP and APMSN-SA) was used as catalyst (Table 3-1, entry 1 and 2), which matched the result in entry 3 where amine and sulfonic acid were trapped in two different mesoporous silica nanoparticles, SAMSN and APMSN, individually. However, neither SAMSN nor APMSN could show any conversion of the reactant A to the final product C (Table 3-1, entry 4 and 5) although SAMSN could catalyze the first step of this two-step cascade. Interestingly, no conversion of the starting materials into final product was observed when either of the homogeneous analogues of the sulfonic acid and amine was used with the bifunctionalized MSN (SAMSN-AP or APMSN-SA) (Table 3-1, entry 6 -9),

apparently because these functionalities neutralize each other. The pure support MSN alone, as an experimental control, caused no conversion (Table 3-1, entry 10).

These bifunctionalized MSNs (SAMSN-AP and APMSN-SA) can be recycled easily by filtration after reactions without any detectable catalytic activity decrease up to several times (Table S3-2), which further confirmed that these two functional groups were quite stable and well site-separated on MSN.

Whilst the one-pot reaction cascades including hydrolysis and Henry reactions was studied to establish proof of our site-separation of Brönsted acid and base on one mesoporous silica nanoparticle, in order to compare with our earlier results,[33] kinetics of these acid and base catalysts were investigated and shown in Figure 3-4. Turnover frequency of both acid and base decreased along the reaction time due to the decreased reactant concentration. Although silanol groups on the external surface of MCM-41 were more kineticly accessible than that on the internal surface,[37,44,45] both acid and base on MSN's internal surface show higher reactivity or turnover frequency (TOF) than their counterparts which were on the external surface of MSN.

These kinetic results indicate that 1) there is no diffusion limitation in our MSN-based catalysts and 2) reactivity of acid and base might be related to the dispersion or surface coverage of catalytic sites. In order to investigate the relationship between reactivity and catalyst surface coverage or dispersion, a series of Henry reactions catalyzed by five aminopropyl functionalized MSNs (APMSN) with different amine concentration on their surfaces (Figure S3-9, S3-10 and S3-11) were investigated (Scheme 3-2) and results were shown in Figure 3-5. From the fitted curve of catalytic activities (TOF) vs the concentration of base on the surface (mmol amine per square meters surface), catalytic activity (TOF) did decrease dramatically when the surface coverage of catalyst was increased, which was consistent with the results when we changed the reaction time (from Figure S3-12 to S3-15).

Conclusions

Combining cocondensation to functionalize MSN internal surface and post-synthesis grafting to functionalize its external surface, we have shown that site-separation of Brönsted acid and base on one mesoporous silica nanoparticle was successful. As a result of this ideal

site-isolation, reaction cascades requiring two or more catalysts which are incompatible in free-moving states could be done by our new bifunctionalized one-particle, which can be a good model for biological systems in which a series of reactions catalyzed by only one multifunctional enzyme. At the same time, we also demonstrated that the activity of catalyst on the surface mesoporous silica nanoparticle was closely related to the coverage of catalyst on MSN surface, therefore we have a better understanding about the catalysis on MSN surface and can envision a better adjustment on the kinetics and efficiency of catalyst by changing the quantity of catalytic sites on a unit surface area.

Acknowledgement

This research was supported at Ames Laboratory by the U.S. DOE, office of BES, under contract DE-AC02-07CH11358.

Supporting Information, including experimental details, N_2 adsorption-desorption measurements including BET surface area and BJH pore size distributions, XRD spectra, SEM images, TEM images, ^{29}Si and ^{13}C solid NMR are attached.

References

(1) Kresge, C. T., Leonowicz, M. E., Roth, W. J., Vartuli, J. C., Beck, J. S. Nature 1992, 359, 710-712.

(2) Thomas, J. M.; Raja, R. Acc. Chem. Res. 2008, 41, 708-720.

(3) Huh, S.; Chen, H.-T.; Wiench, J. W.; Pruski, M.; Lin, V. S.-Y. J. Am. Chem. Soc. 2004, 126, 1010-1011.

(4) Huh, S.; Wiench, J. W.; Yoo, J.-C.; Pruski, M.; Lin, V. S.-Y. Chem. Mater. 2003, 15, 4247-4256.

(5) Huh, S.; Wiench, J. W.; Trewyn, B. G.; Song, S.; Pruski, M.; Lin, V. S.-Y. Chem. Commun. 2003, 2364-2365.

(6) Chen, H.-T., Huh, S., Wiench, J. W., Pruski, M., Lin, V. S.-Y. J. Am. Chem. Soc. 2005, 127, 13305-13311.

(7) Huh, S.; Chen, H.-T.; Wiench, J. W.; Pruski, M.; Lin, V. S.-Y. Angew. Chem. Int. Ed. 2005, 44, 1826-1830.

(8) Radu, D. R.; Lai, C.-Y.; Huang, J.; Shu, X.; Lin, V. S.-Y. Chem. Commun. 2005, 1264-1266.

(9) Zeidan, R. K.; Dufaud, V.; Davis, M. E. J. Catal. 2006, 239, 299-306.

(10) Zeidan, R. K.; Hwang, S.-J.; Davis, M. E. Angew. Chem. Int. Ed. 2006, 45, 6332-6335.

(11) Margelefsky, E. L.; Zeidan, R. K.; Dufaud, V.; Davis, M. E. J. Am. Chem. Soc. 2007, 129, 13691-13697.

(12) Zeidan, R. K.; Davis, M. E. J. Catal. 2007, 247, 379-382.

(13) Margelefsky, E. L.; Zeidan, R. K.; Davis, M. E. Chem. Soc. Rev. 2008, 37, 1118-1126.

(14) Margelefsky, E. L.; Bendjeriou, A.; Zeidan, R. K.; Dufaud, V.; Davis, M. E. J. Am. Chem. Soc. 2008, 130, 13442-13449.

(15) Liu, D.; Lei, J.-H.; Guo, L.-P.; Du, X.-D.; Zeng, K. Micro. Meso. Mater. 2009, 117, 67-74.

(16) Sharma, K. K.; Buckley, R. P.; Asefa, T. Langmuir 2008, 24, 14306-14320.

(17) Notestein, J. M.; Katz, A. Chem. Eu. J. 2006, 12, 3954-3965.

(18) Wight, A. P.; Davis, M. E. Chem. Rev. 2002, 102, 3589-3613.

(19) Alauzun, J.; Mehdi, A.; Reye, C.; Corriu, R. J. P. J. Mater. Chem. 2007, 17, 349-356.

(20) Alauzun, J.; Mehdi, A.; Reye, C.; Corriu, R. New J. Chem. 2007, 31, 911-915.

(21) Mouawia, R.; Mehdi, A.; Reye, C.; Corriu, R. New J. Chem. 2006, 30, 1077-1082.

(22) Mehdi, A.; Mutin, P. H. J. Mater. Chem. 2006, 16, 1606-1607.

(23) Alauzun, J.; Mehdi, A.; Reye, C.; Corriu, R. J. P. J. Am. Chem. Soc. 2006, 128, 8718-8719.

(24) Mehdi, A.; Reye, C.; Brandes, S.; Guilard, R.; Corriu, R. J. P. New J. Chem. 2005, 29, 965-968.

(25) Besson, E.; Mehdi, A.; Matsura, V.; Guari, Y.; Reye, C.; Corriu, R. J. P. Chem. Commun. 2005, 1775-1777.

(26) Corriu, R. J. P.; Mehdi, A.; Reye, C.; Thieuleux, C. Chem. Commun. 2002, 1382-1383.

(27) Corriu, R. J. P.; Guari, Y.; Mehdi, A.; Reye, C.; Thieuleux, C.; Datas, L. Chem. Commun. 2001, 763-764.

(28) Dufaud, V.; Davis, M. E. J. Am. Chem. Soc. 2003, 125, 9403-9413.

(29) Matsuura, Y. Biologia (Bratislava, Slovakia) 2002, 57, 21-27.

(30) Bass, J. D.; Solovyov, A.; Pascall, A. J.; Katz, A. J. Am. Chem. Soc. 2006, 128, 3737-3747.

(31) Bass, J. D.; Katz, A. Chem. Mater. 2006, 18, 1611-1620.

(32) Coutinho, D.; Madhugiri, S.; Balkus, K. J., Jr. J. Porous Mater. 2004, 11, 239-254.

(33) Huang, Y.; Trewyn, B. G.; Chen, H.-T.; Lin, V. S.-Y. New J. Chem. 2008, 32, 1311-1313.

(34) Rosenholm, J. M.; Duchanoy, A.; Linden, M. Chem. Mater., 2008, 20, 1126-1133.

(35) Kecht, J.; Schlossbauer, A.; Bein, T. Chem. Mater. 2008, 20, 7207-7214.

(36) Kilian, K. A.; Bocking, T.; Gaus, K.; Gooding, J. J. Angew. Chem. Int. Ed. 2008, 47, 2697-2699.

(37) Shephard, D. S.; Zhou, W.; Maschmeyer, T.; Matters, J. M.; Roper, C. L.; Parsons, S.; Johnson, B. F. G.; Duer, M. J. Angew. Chem. Int. Ed. 1998, 37, 2719-2723.

(38) Raja, R.; Thomas, J. M.; Jones, M. D.; Johnson, B. F. G.; Vaughan, D. E. W. J. Am. Chem. Soc. 2003, 125, 14982-14983.

(39) Jones, M. D.; Raja, R.; Thomas, J. M.; Johnson, B. F. G.; Lewis, D. W.; Rouzaud, J.; Harris, K. D. M. Angew. Chem. Int. Ed. 2003, 42, 4326-4331.

(40) Jones, M. D.; Raja, R.; Meurig Thomas, J.; Johnson, B. F. G. Topics in Catalysis 2003, 25, 71-79.

(41) De Juan, F.; Ruiz-Hitzky, E. Adv. Mater. 2000, 12, 430-432.

(42) Cheng, K.; Landry, C. C. J. Am. Chem. Soc. 2007, 129, 9674-9685.

(43) Olszak-Humienik, M. Thermochimica Acta 2001, 378, 107-112.

(44) Johnson, B. F. G.; Raynor, S. A.; Shephard, D. S.; Mashmeyer, T.; Thomas, J. M.; Sankar, G.; Bromley, S.; Oldroyd, R.; Gladden, L.; Mantle, M. D. Chem. Commun. 1999, 1167-1168.

(45) Raynor, S. A.; Thomas, J. M.; Raja, R.; Johnson, B. F. G.; Bell, R. G.; Mantle, M. D. Chem. Commun. 2000, 1925-1926.

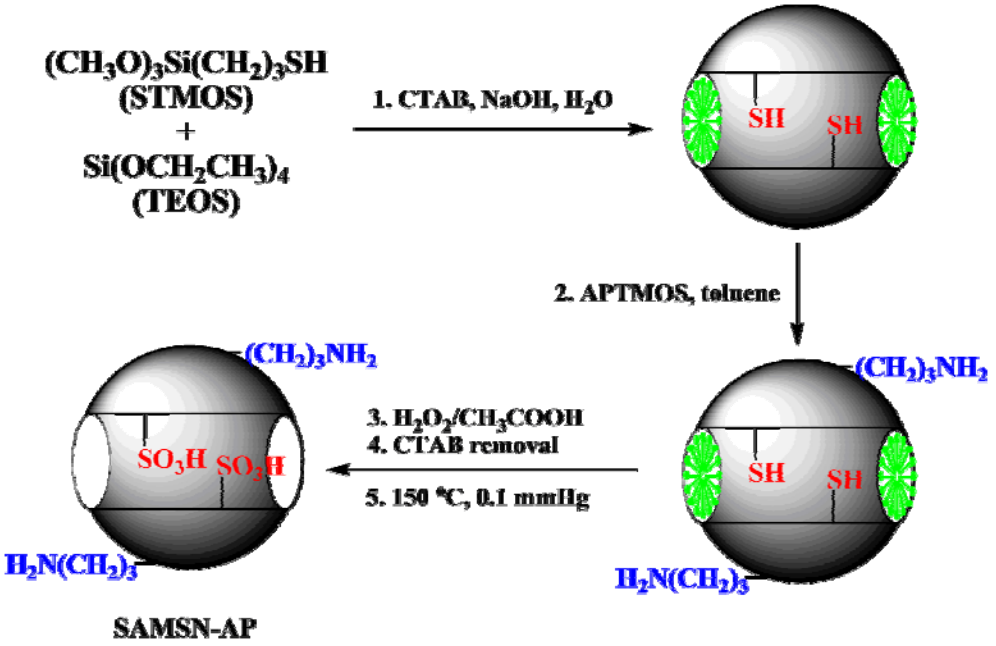

Figure 3-1. Synthesis of mesoporous silica nanoparticles which were bifunctionalized by sulfonic acid groups on internal surface and organic amine groups on external surface independently.

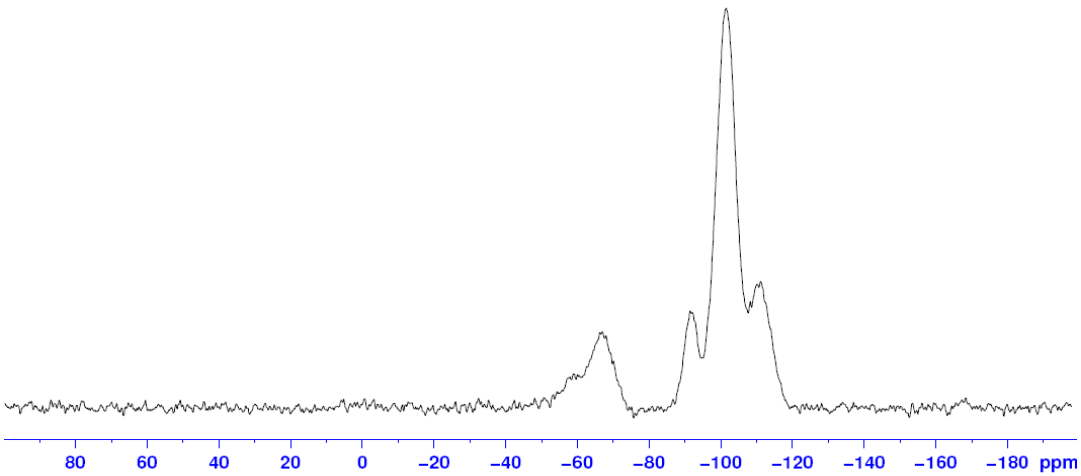

Figure 3-2. ^{29}Si solid-sate NMR spectra of SAMSN-AP (T^2: -59 ppm; T^3: -68 ppm; Q^2: -90 ppm; Q^3: -100 ppm; Q^4: -110 ppm).

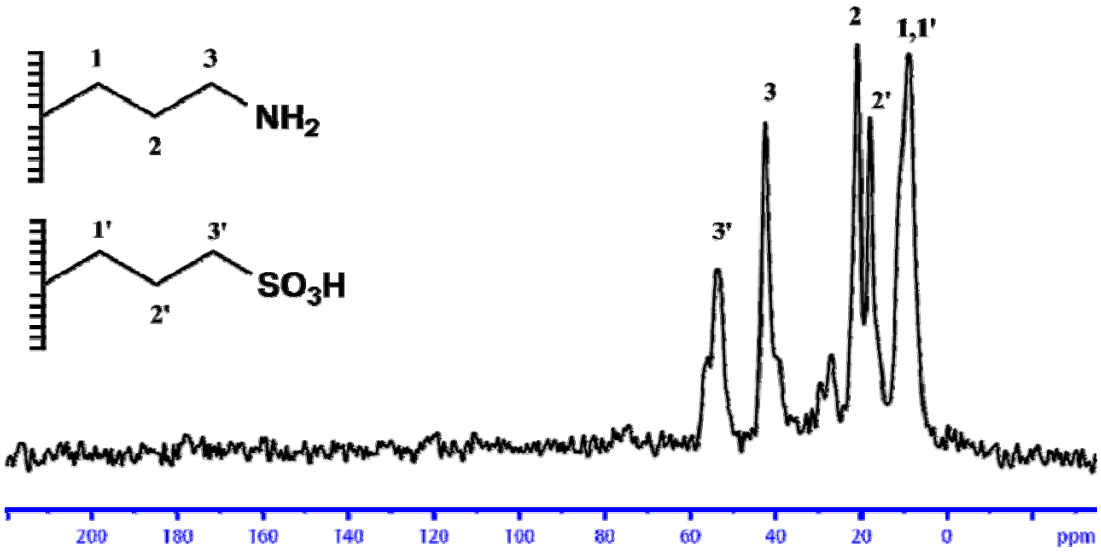

Figure 3-3. ^{13}C solid-sate NMR spectra of SAMSN-AP. (Chemical shift at 29.5 ppm was from CTAB; Chemical shift at 26.0 ppm was from starting material 3-mecaptopropyl group.)

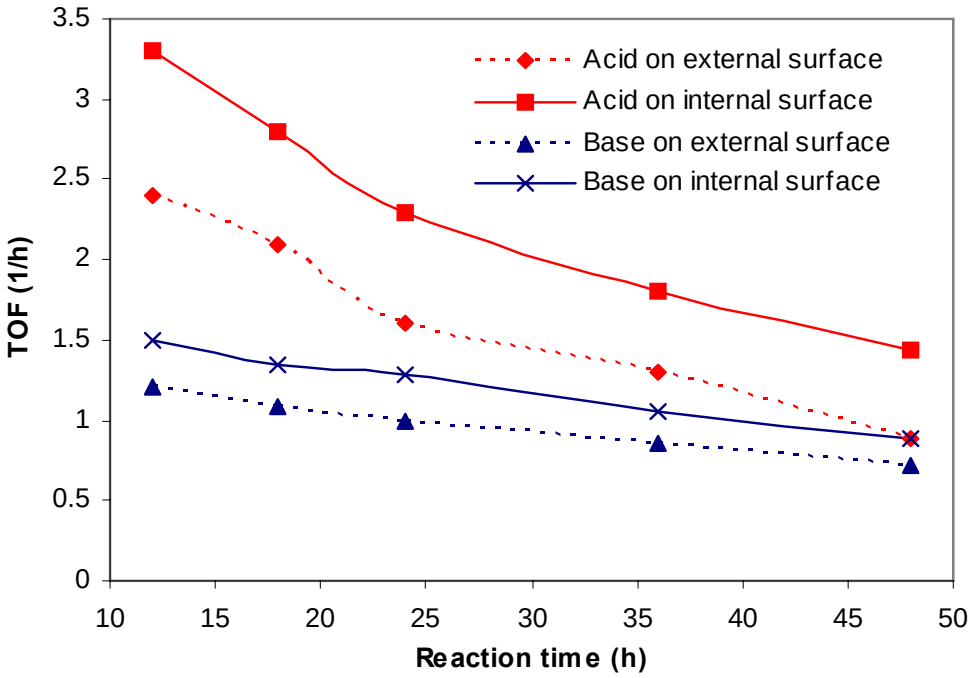

Figure 3-4. Turnover frequency of acid and base catalysts on either internal or external surface of SAMSN-AP and APMSN-SA.

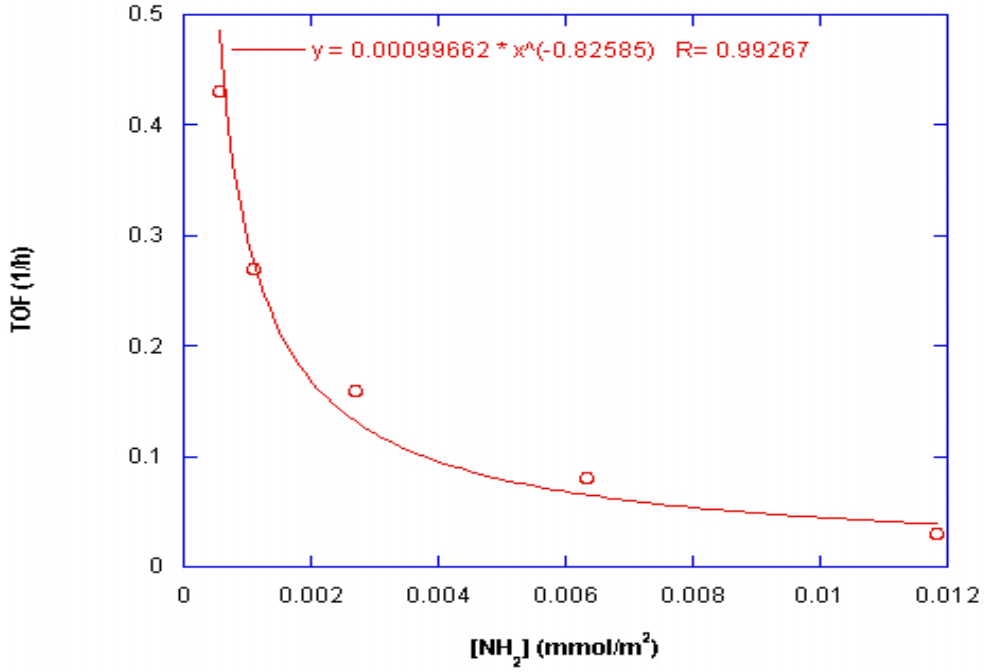

Figure 3- 5. Fitted curve of base activity vs base concentration on MSN surface (Reaction conditions were the same as that in Table 3-1).

Table 3-1. One-pot reaction cascades composed of acid-catalyzed hydrolysis and base-catalyzed Henry reaction

Entry	Catalyst	B (%)	C (%)	Conv. of A(%)
1	SAMSN-AP	2.3	97.7	100
2	APMSN-SA	1.9	98.1	100
3	SAMSN/APMSN	4.5	95.5	100
4	SAMSN	100	0	100
5	APMSN	0	0	0
6	SAMSN-AP/AP	0	0	0
7	SAMSN-AP/PTSA	100	0	100
8	APMSN-SA/AP	0	0	0
9	APMSN-SA/PTSA	100	0	100
10	MSN	0	0	0

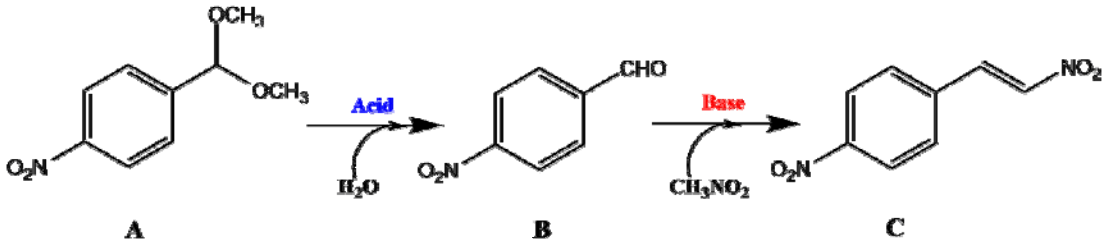

Scheme 3-1. One-pot reaction cascade involving sequential acid-catalyzed acetal hydrolysis followed by the amine-catalyzed Henry reaction.

Scheme 3-2. Henry reaction catalyzed by APMSN.

Supporting Information

1. Synthesis of bifunctional mesoporous materials with sulfonic acid on its external surface and amine groups on its internal surface (APMSN-SA)

In order to locate one of the final two functional groups homogeneously on the internal surface of mesoporous silica, first co-condensation method from our group was used.[1-5] 2.0 g of cetyltrimethylammonium bromide (CTAB) and 7.0 mL of sodium hydroxide aqueous solution(2.0 mol/L) was dissolved into 480 mL of deionized water at 80 ^{o}C with vigorous stirring (pH = 11.8); 10.0 mL of tetraethyl orthosilicate (TEOS) (44.0 mmol) and 180.0 μL (1.0 mmol) of 3-aminopropyltrimethoxysilane (APTMOS) were injected into the solution with vigorous stirring; After 2 h stirring, the white solid was separated by hot filtration, washed with excess water, dried at 120 ^{o}C under vacuum

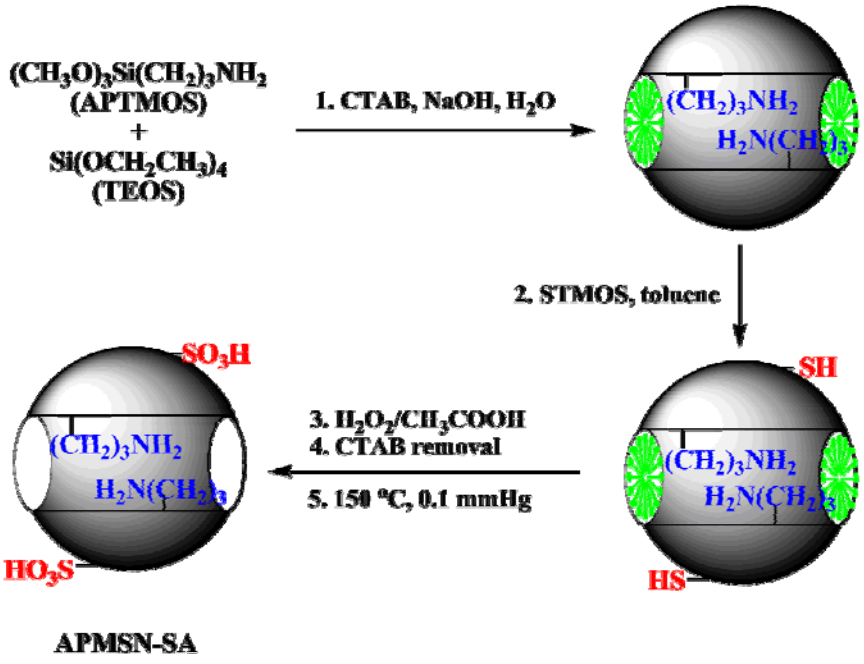

Figure S3-1. Synthesis of mesoporous silica nanoparticles which were bifunctionalized by organic amine groups on external surface and sulfonic acid groups on internal surface independently.

overnight. In order to selectively functionalize mesoporous silica external surface,[6,7] the as-made solid with template CTAB inside mesoporous channels was stirred with 190.6 μL (1.0 mmol) of 3-mecaptotrimethoxysilane (STMOS) in toluene at 120 ^{o}C for 6 h before being filtrated and washed with excess solvent and dried at 120 ^{o}C under vacuum overnight; In order to convert thiol groups to sulfonic acids, the as-gotten solid was stirred in acetic acid (10.0 mL) with 30 % H_2O_2 (20.0 mL) at 100 ^{o}C for 6 h; The surfactant was removed by extraction with methanol for 24 h and then washed with excess water and heated at 150 ^{o}C overnight in order to recover the amino groups.[8] The obtained white powder was termed **APMSN-SA**.

The highly ordered mesoporous structures of these two bifunctional mesoporous materials were characterized by nitrogen sorption isotherms (Figure S3-1 and S3-2), powder X-ray diffraction (XRD) (Figure S3-3), scanning electron microscopy (SEM) (Figure S3-4), and transmission electron microscopy (TEM) (Figure S3-5). Structural data of SAMSN-AP and APMSN-SA were summarized in Table S1. ^{29}Si solid-state NMR in Figure S3-6 gave us T^3 and T^2 sites as well as Q^4, Q^3 and Q^2 sites for both SAMSN-AP and APMSN-SA, which indicated that both SAMSN-AP and APMSN-SA were organic functionalized mesoporous silica. ^{13}C solid-state NMR (Figure S3-7) confirmed the intact chemical structures of sulfonic acid and amine on these two materials.

2. One-pot reaction cascades catalyzed by APMSN-SA or SAMSN-AP

Nitromethane (1.0 mL), 4-nitrobenzaldehyde dimethyl acetal (0.75 mmol) and water (0.75 mmol) were mixed with SAMSN-AP or APMSN-SA (100 mg) at room temperature under N_2 and sealed in a glass vessel. The as-made slurry was heated to 80 ^{o}C with vigorous stirring. After 48 hours, the reaction was stopped by cooling to room temperature with ice-water bath. The product was analyzed by a GC (Varian 3900) with capillary column (HP-5, 30 m x 0.319 mm x 0.25 μm).

For catalysts recycling, catalysts were separated by filtration after reaction, washed with excess tetrahydrofuran and dried at 120 ^{o}C under high vacuum overnight before being used for another test. Results for catalyst recycling were listed in Table S3-2.

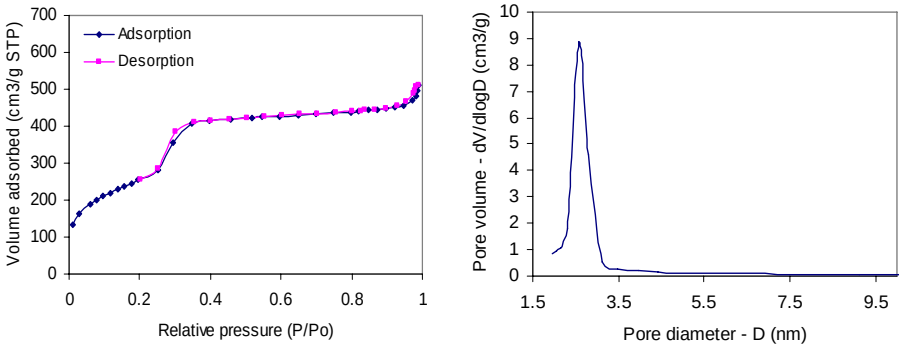

Figure S3-2. BET isotherms and BJH pore size distribution curve of **SAMSN-AP**.

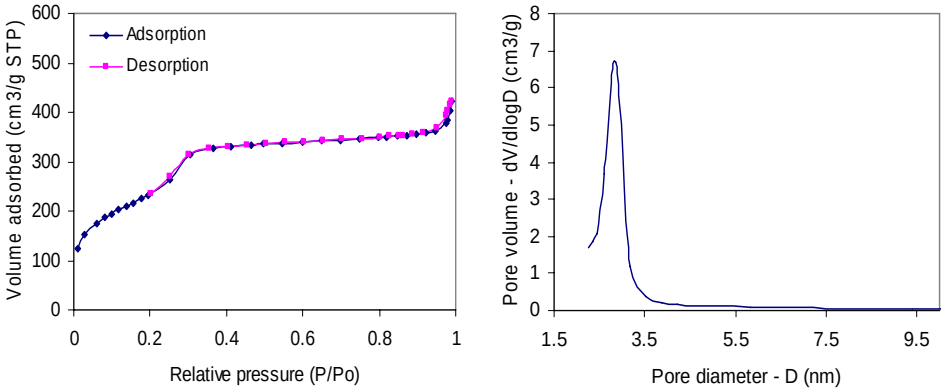

Figure S3-3. BET isotherms and BJH pore size distribution curve of **APMSN-SA**.

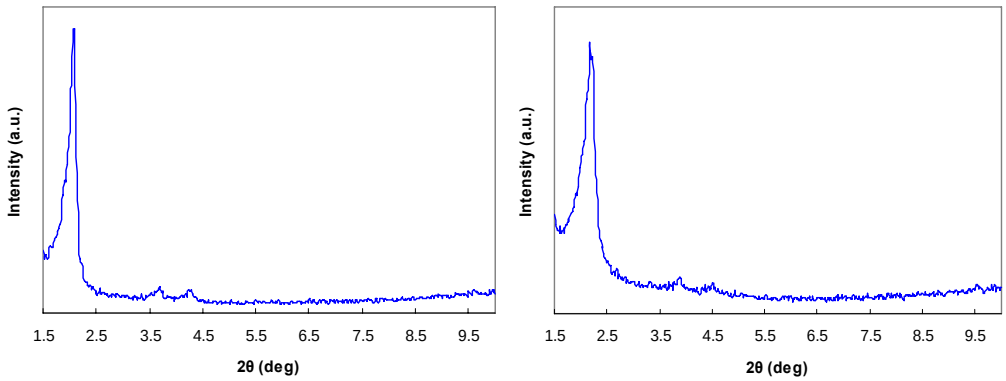

Figure S3-4. XRD of **SAMSN-AP**(left) and **APMSN-SA**(right).

Table S3-1. Structural data of SAMSN-AP and APMSN-SA.[a]

Samples	d_{100} (Å)	S_{BET} (m^2/g)	V_p (cm^3/g)	D_{BJH} (Å)
SAMSN-AP	41	853	0.8	29
APMSN-SA	42	934	0.9	26

[a] The BET surface area (S_{BET}), the mesopore volume (V_p), and the mean mesopore diameter (D_{BJH}) were obtained from the nitrogen absorption / desorption data in Figure S3-1 and S3-2. The d_{100} data represent the d-spacing corresponding to the (100) peaks in XRD (Figure S3-3).

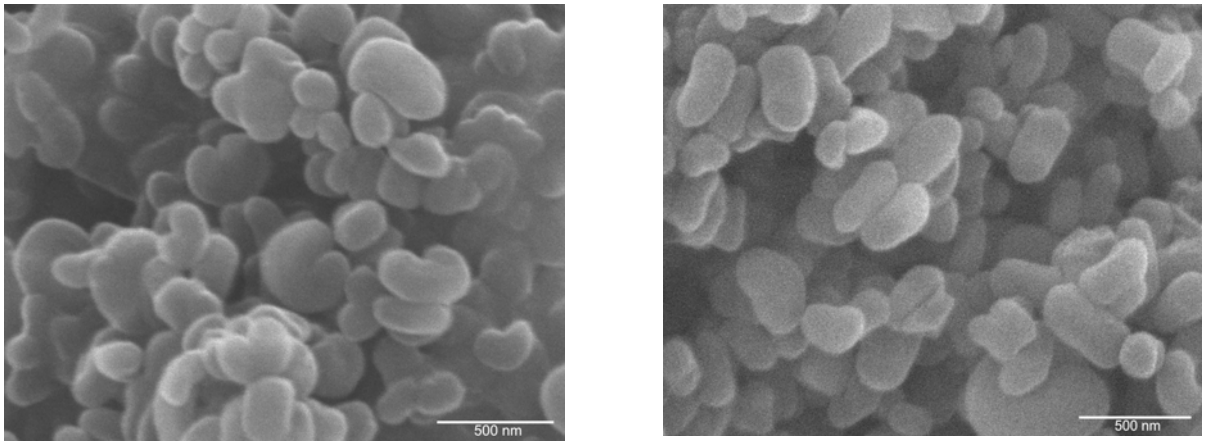

(a) (b)

Figure S3-5. SEM images of **SAMSN-AP**(a) and **APMSN-SA**(b).

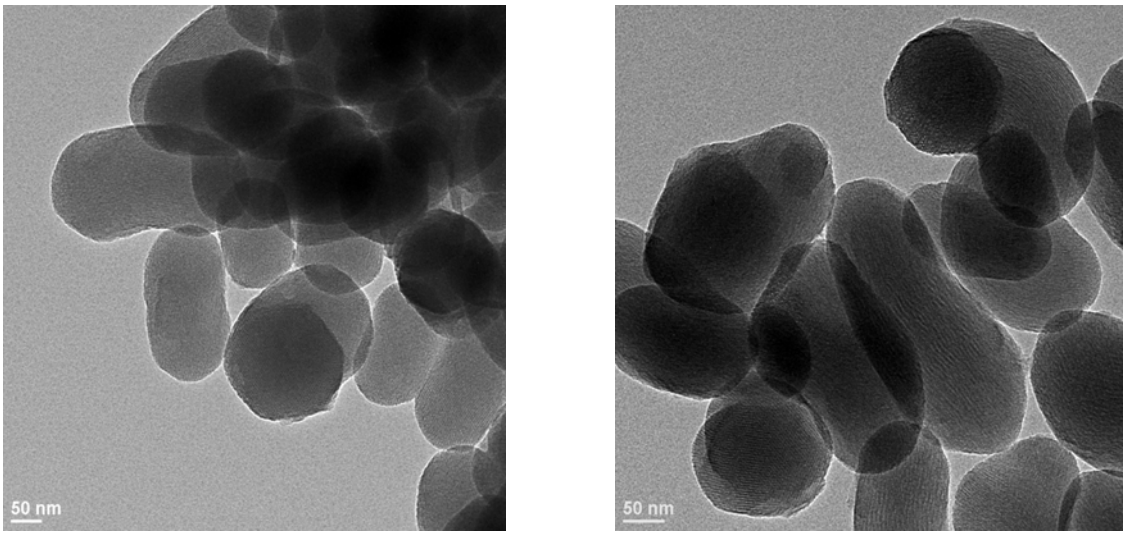

(a) (b)

Figure S3-6. TEM images of **SAMSN-AP**(a) and **APMSN-SA**(b).

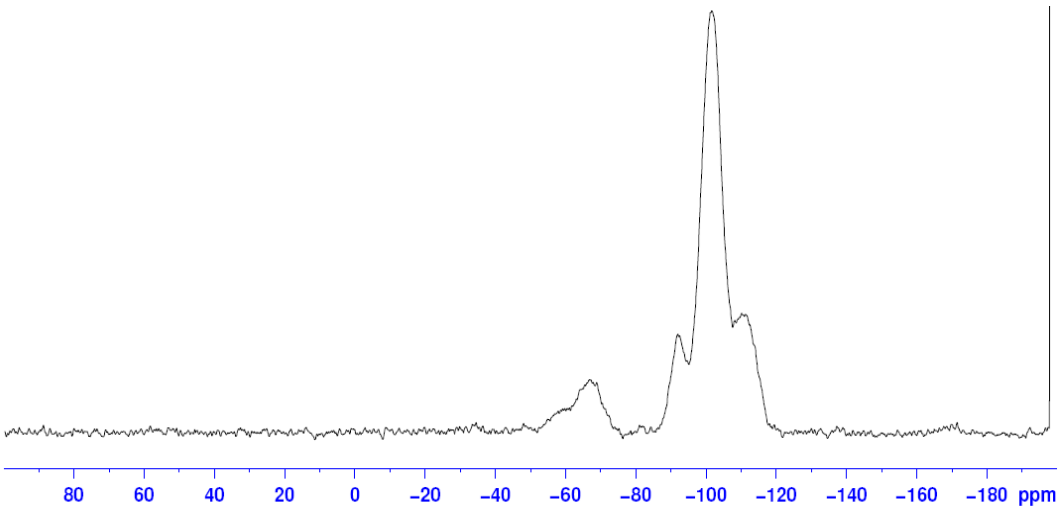

Figure S3-7. ^{29}Si solid-sate NMR spectra of and **APMSN-SA** (T^2: -59 ppm; T^3: -68 ppm; Q^2: -90 ppm; Q^3: -100 ppm; Q^4: -110 ppm).

3. Synthesis of aminopropyl-functionalized mesoporous silica with homogeneously distributed amine groups on its surface

In order to distribute the amine functional groups homogeneously on the surface of mesoporous silica nanoparticles, co-condensation method from our group was used.[1-5] Typically, 2.0 g of cetyltrimethylammonium bromide (CTAB) and 7.0 mL of sodium hydroxide aqueous solution(2.0 mol/L) was dissolved into 480 mL of deionized water at 80 ^{o}C with vigorous stirring (pH = 11.8); 10.0 mL of tetraethyl orthosilicate (TEOS) (44.0 mmol) and different quantity of 3-aminopropyltrimethoxysilane (APTMOS) were injected into the solution with vigorous stirring; After stirring for 2 h, the white solid was separated by hot filtration, washed with excess water, dried at 120 ^{o}C under vacuum overnight. The surfactant was removed by extraction with methanol for 24 h and then washed with excess water and heated at 150 ^{o}C overnight in order to recover the amino groups.

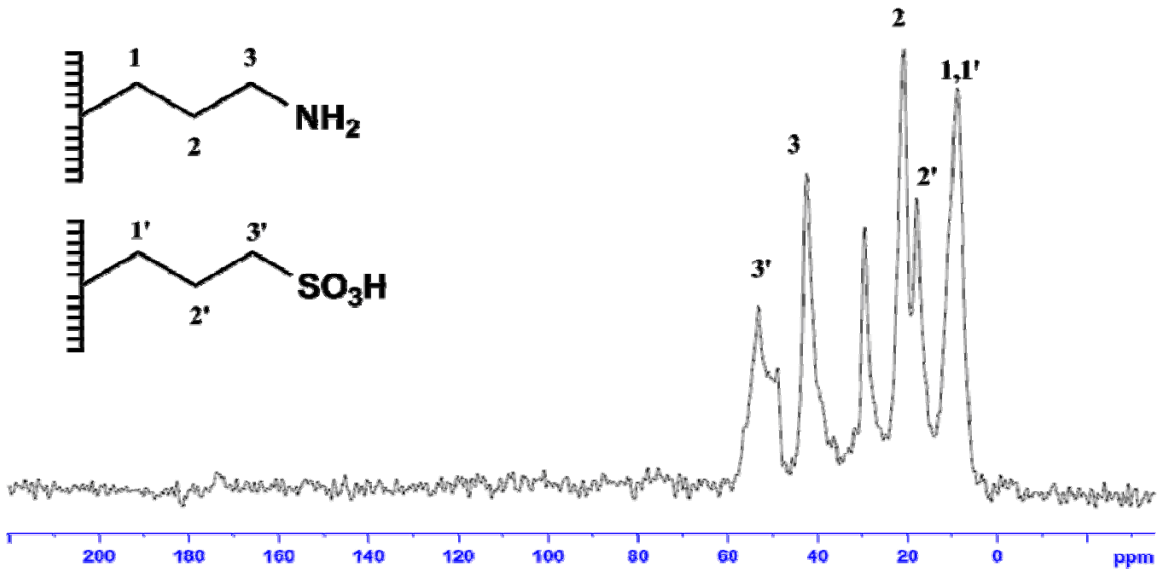

Figure S3-8. ^{13}C solid-sate NMR spectra of **APMSN-SA**. (Chemical shift at 29.5 ppm was from CTAB; Chemical shift at 26.0 ppm was from starting material 3-mecaptopropyl group.)

Table S3-2. One-pot reaction cascades composed of acid-catalyzed hydrolysis and base-catalyzed Henry reaction

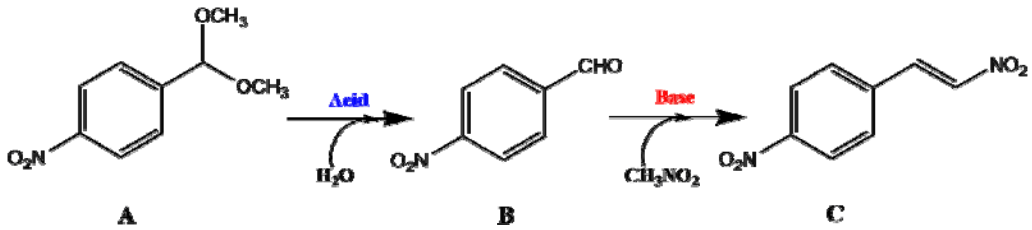

A B C

Recycle	Catalyst	B (%)	C (%)	Conv. (%)
0	SAMSN-AP	2.3	97.7	100
1	SAMSN-AP	2.0	98.0	100
2	SAMSN-AP	2.8	97.2	100
3	SAMSN-AP	3.0	97.0	100
4	SAMSN-AP	4.0	96.0	100
5	SAMSN-AP	3.2	96.8	100
0	APMSN-SA	1.9	98.1	100
1	APMSN-SA	4.3	95.7	100
2	APMSN-SA	2.5	97.5	100
3	APMSN-SA	3.0	97.0	100
4	APMSN-SA	3.3	96.7	100
5	APMSN-SA	2.8	97.2	100

Reaction conditions: $[\mathbf{A}]_0$ = 7.5 M in CH_3NO_2 (1.0 mL) with 1.0 equivalent H_2O was stirred at 80 ^oC in a sealed vials for 48 h. Conversion and yields were based on the GC data. AP: 1-aminopropane, PTSA: p-toluenesulfonic acid.

These materials were analyzed by N_2 adsorption-desorption measurements (Figure S3-9) and they all show type IV isotherms with very clear H_1-hysteresis loops at relative high pressure and narrow pore size distributions, characteristic of mesoporous materials and Small-angle X-ray scattering patterns of these materials (Figure S3-10) indicated highly ordered structures. T^2 and T^3 peaks in ^{29}Si solid NMR (Figure S3-11) show that there were organic functional groups on these five materials and the concentration of organic groups on these five materials were different. Elemental analysis was used to determine the accurate concentration of amino group on the surface.

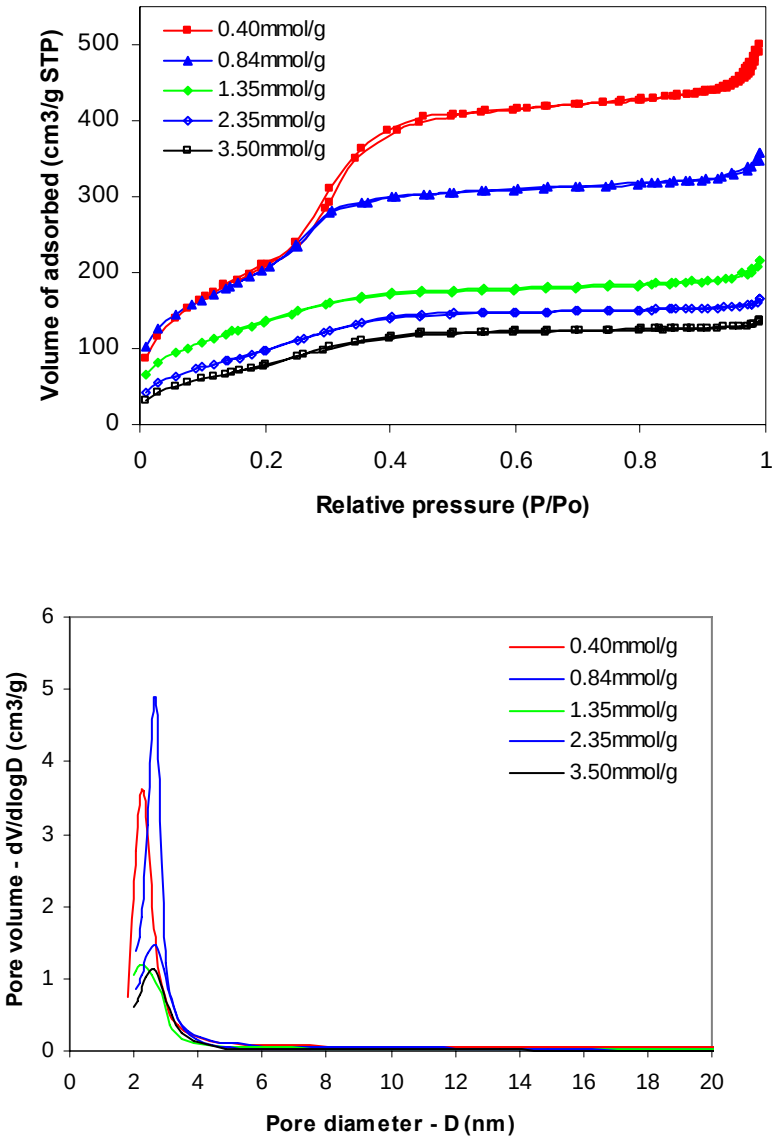

Figure S3-9. BET isotherms and BJH pore size distribution curves of APMSNs with different aminopropyl group loading.

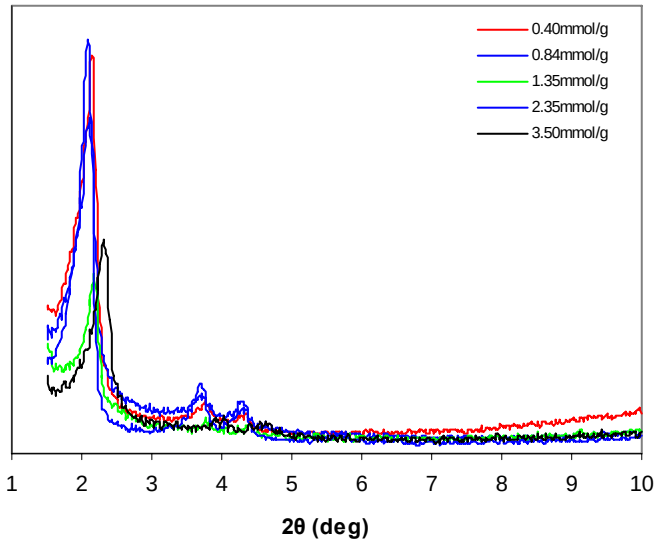

Figure S3-10. XRD of APMSNs with different aminopropyl group loading.

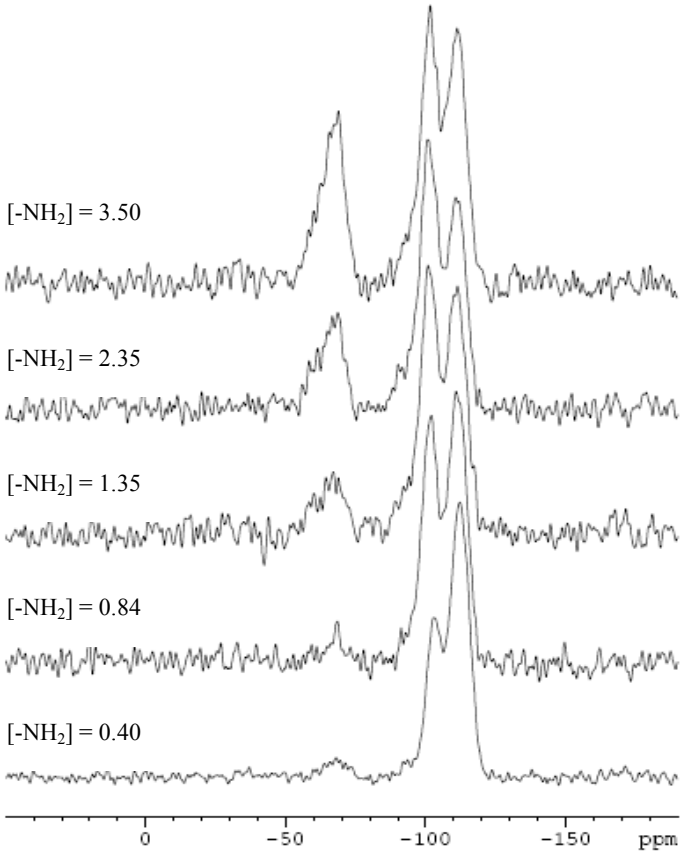

Figure S3-11. ^{29}Si solid NMR of APMSNs with different aminopropyl group loading.

4. Henry reactions catalyzed by APMSN

4-nitrobenzaldehyde (1.0 mmol) was mixed with APMSN (100 mg) in 1.0 mL nitromethane at room temperature under N_2 and sealed in a glass vessel. The as-made slurry was heated to 80 ^oC with vigorous stirring. After the designed reaction time, the reaction was stopped by cooling to room temperature with ice-water bath. The product was analyzed by GC-MS with capillary column (HP-5, 30 m x 0.319 mm x 0.25 μm).

Turnover frequency (TOF, 1/h) of catalyst was determined by mole of product per mole of catalyst per hour. Catalyst concentration here (mmol/m^2) was calculated by the loading of catalyst (mmol/g) of material divided by the surface area of the materials (m^2/g). The relationship between TOF and catalyst concentration were shown in Fig. S12. The TOF of catalyst always decreased with the increased catalyst concentration. The fitted curves of TOF vs catalyst surface coverage, shown in Figure S13, S14 and S15, indicated TOF could decrease dramatically when we increased the catalyst coverage on MSN surface, which indicates the decrease of catalyst efficiency. In order to design a MSN-based catalyst with a better catalytic performance, the catalyst surface coverage must be considered as an important parameter.

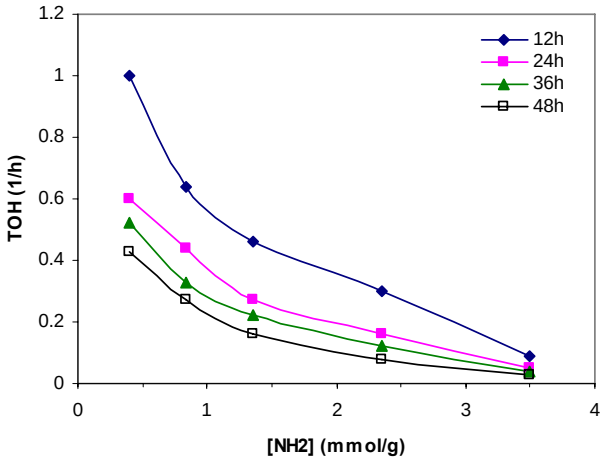

Figure S3-12. Turnover frequency vs the concentration of aminopropyl group of APMSN.

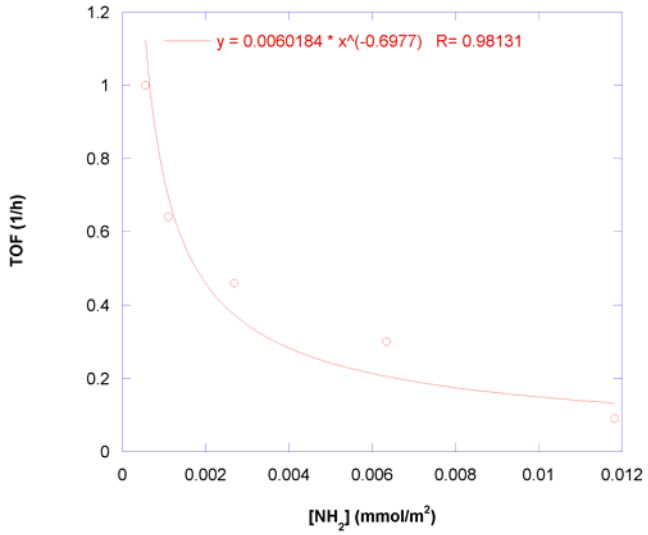

Figure S3-13. Fitted curve of base activity (12 h) vs base concentration on MSN surface.

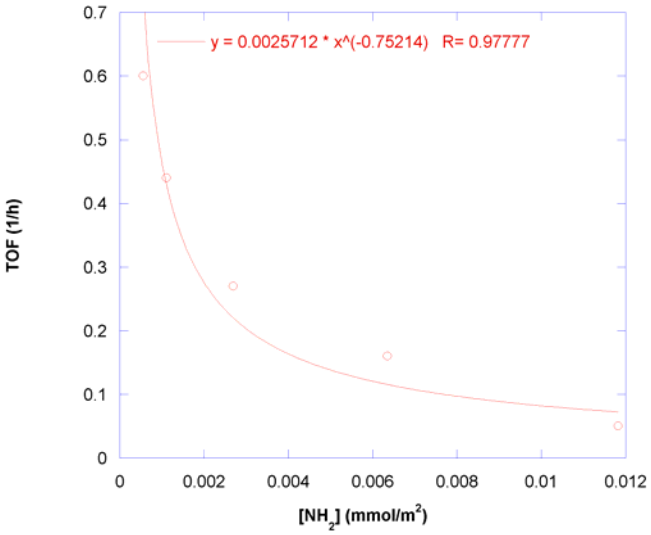

Figure S3-14. Fitted curve of base activity (24 h) vs base concentration on MSN surface.

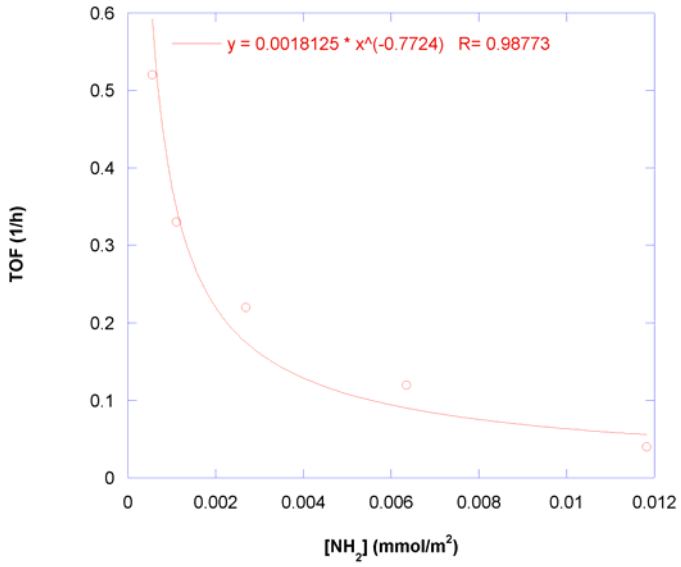

Figure S3-15. Fitted curve of base activity (36 h) vs base concentration on MSN surface.

(1) Huh, S.; Chen, H.-T.; Wiench, J. W.; Pruski, M.; Lin, V. S.-Y. *Angew. Chem. Int. Ed.* **2005**, *44*, 1826-1830.

(2) Chen, H.-T., Huh, S., Wiench, J. W., Pruski, M., Lin, V. S.-Y. *J. Am. Chem. Soc.* **2005**, *127*, 13305-13311.

(3) Huh, S.; Wiench, J. W.; Yoo, J.-C.; Pruski, M.; Lin, V. S.-Y. *Chem. Mater.* **2003**, *15*, 4247-4256.

(4) Huh, S.; Wiench, J. W.; Trewyn, B. G.; Song, S.; Pruski, M.; Lin, V. S.-Y. *Chem. Commun.* **2003**, 2364-2365.

(5) Huh, S.; Chen, H.-T.; Wiench, J. W.; Pruski, M.; Lin, V. S.-Y. *J. Am. Chem. So.* **2004**, *126*, 1010-1011.

(6) Shephard, D. S.; Zhou, W.; Maschmeyer, T.; Matters, J. M.; Roper, C. L.; Parsons, S.; Johnson, B. F. G.; Duer, M. J. *Angew. Chem. Int. Ed.* **1998**, *37*, 2719-2723.

(7) De Juan, F.; Ruiz-Hitzky, E. *Adv. Mater.* **2000**, *12*, 430-432.

(8) Olszak-Humienik, M. *Thermochimica Acta* **2001**, *378*, 107-112.

CHAPTER 4. MN-MODIFIED AND WELL-DEFINED RH NANOPARTICLES SUPPORTED ON MESOPOROUS SILICA NANOPARTICLES: HIGHLY-SELECTIVE SYNTHESIS OF ETHANOL FROM SYNGAS

A paper to be submitted to *Nano Letters*

Yulin Huang,[1] Weihua Deng,[2] Enruo Guo,[1] Senniang Chen,[1] Po-Wen Chung,[1] Brian G. Trewyn,[1] Victor S.-Y. Lin[1,*]

1. Department of Chemistry and Ames Laboratary-U.S. Department of Energy, Iowa State University, Ames, IA 50011, 2. Center for Sustainable Environmental Technologies, Iowa State University, Ames, IA 5001

**Corresponding author.*

ABSTRACT

Well-defined and monodispersed rhodium (Rh) nanoparticles as small as ~2 nm were synthesized with polyvinylpyrrolidone (PVP) polymer in ethanol. And the as-made PVP-stabilized Rh nanoparticles were dispersed and encapsulated in mesoporous silica nanoparticles *in situ* during the synthesis of this high-surface-area mesoporous silica nanoparticle (MSN) support. Catalytic performance of the MSN-supported Rh nanoparticles (MSNRhNPs) was modified by manganese oxides and studied with CO hydrogenation. MSNRhNPs were active for the CO hydrogenation and the selectivity to C2 oxygenates reached the highest point without formation of by-product methanol after the Rh nanoparticles were modified by manganese oxide during the formation of MSN.

Introduction

It is well known that higher alcohols synthesized from natural gas, coal, or biomass can be used as a renewable energy alternative, such as additives to gasoline and an easily transportable source of hydrogen.[1-4] Because ethanol could not only decrease the dependence

on imported cruel oil but also would have a positive environmental impact, synthesis of ethanol selectively from syngas (CO and H_2), which can be made from coal or biomass pyrolysis, has been a topic of growing interesting from both industrial and academic points of views. In the catalytic synthesis of ethanol since the 1980s,[5] rhodium-based catalysts have been known for decades to be the most selective catalysts for the synthesis of C_{2+} oxygenates, including ethanol, acetaldehyde and acetic acid, due to the unique CO adsorption behavior on Rh surface,[6,7] although some other transition metal catalysts were reported.[2,8-15] Most of the attention on Rh-based catalysts for ethanol synthesis from syngas was and is still on the influences of catalyst precursors,[16-21] supports[6,22-28] and promoters or additives[16,21,22,24,29-43] on the activity and selectivity. And most of these Rh-based heterogeneous catalysts were made from impregnation of rhodium salt solution which then was followed by calcinations of the as-made solid at high temperature and reduction of rhodium oxides to metallic rhodium particles by hydrogen gas.[44-46] Usually rhodium particles from this process, including impregnation, calcination and reduction, have a very broad size distribution and vary a lot from batch to batch, because the control of particle size distribution especially on support surface is still very challenging especially at the required high temperature.[13] And that might be the reason there are only few studies on the size controlling of Rh particles in CO hydrogenation.[47] But, for CO hydrogenation or any other reactions catalyzed by immobilized Rh catalysts, Rh particle size controlling should be a very important to adjust the percentage of surface metal atoms that are the only accessible to the reactants.[48,49] Therefore downsizing Rh particles, especially to nanometer scale, should be an efficient strategy to increase the reactivity and probably improve the selectivity, due to the dramatically increased percentage of surface metal atoms.

For downsizing metal catalyst particle, colloidal chemistry could be adopted to synthesize mono-dispersed metal nanoparticle with well-defined particle size in solution. After metal nanoparticle was made in colloidal solution, nanoparticle's dispersion on porous supports by impregnation is required. Mesoporous silica structures have been regarded as ideal catalyst supports due to their high surface area, tunable pore size and highly ordered alignment since its discovery at the beginning of 1990s.[27,50-52] However, in this method, in addition to the difficulty of controlling the homogeneous distribution of metal particles on

porous supports surface, rhodium particle growing is still challenging for both chemists and chemical engineer, due to 1) the weak interaction (or physical adsorption) between metal nanoparticle and support surface and 2) the inevitable growth or sintering of catalyst particles.

Here we reported the successful synthesis of ~2.0 nm Rh particles (RhNPs) in alcoholic solution using a polymer, polyvinylpyrrolidone (PVP), as a nanoparticle stabilizer and subsequent encapsulate the as-made RhNPs in the framework of mesoporous silica nanoparticle (MSN) during *in situ* of the forming of MSN (Scheme 4-1). Comparing with commonly used MSN-supported Rh catalyst from incipient wetness impregnation of aqueous $RhCl_3$ solution (MSNRh), RhNPs encapsulated in MSN framework (MSNRhNPs) not only have a higher reactivity in CO hydrogenation but have also better selectivity to the desired product ethanol. The reactivity of MSNRhNPs in CO hydrogenation and especially the selectivity to ethanol were further improved after it was modified by manganese oxide.

Results and Discussions

Synthesis of PVP-stabilized Rh Nanoparticles and Mesoporous Silica Nanoparticle Framework Encapsulated Rh Nanoparticles. Metal nanoparticles less than 10 nm that were well-defined and monodispersed with controlled shape have been synthesized by colloid chemistry in recent years.[53-55] For the synthesis of Rh nanoparticles less than 2.0 nm, there are a few reported methods.[48,49,56,57] Because PVP is a water soluble polymer, PVP stabilized rhodium nanoparticles can be dispersed homogeneously in water which can be homogeneously distributed in aqueous solution for MSN synthesis. PVP-stabilized RhNPs were synthesized as reported with minor modifications.[48,49] PVP (Typical M_w = 29,000) was purchased from Sigma-Aldrich as the nanoparticle stabilizer. A 7.9 mmol/L PVP solution was prepared by dissolving the polymer into anhydrate ethanol. The PVP ethanolic solution was mixed with 7.1 mmol/L aqueous $RhCl_3$ (Rh, 38-40% from Strem Chemicals, Inc.) solution at room temperature, where the mole ratio between PVP and Rh^{3+} was 10.0. After reduction of rhodium in ethanol, solvent was evaporated by rotavap at 40 ^oC and the as-made Rh nanoparticles (RhNPs) were characterized by transmission electronic

miscroscopy (TEM). TEM image (Figure 4-1a) shows that the Rh particles are well-defined and mono-dispersed spheres with ~2.0 nm in diameter and HRTEM image (Figure 4-1b) combining with diffraction pattern indicates that these tiny RhNPs have the crystalline structures.

The as-made RhNPs (480.0 mg, including 40.0 mg Rh) were re-dissolved into water (10.0 mL, 0.6 mol) and mixed with water (470 mL, 26.1 mol), cetyltrimethylammonium bromide (CTAB, 2.0 g, 5.5 mmol), NaOH (7.0 mL x 2.0 mol/L, 14.0 mmol) at room temperature prior to the hydrolysis of tetraethoxyl orthosilicate (TEOS, 10.0 mL, 44.8 mmol) at 80 ^{o}C for 2.0 hours. After the hydrolysis, the grey solid was filtrated and dried under vacuum overnight. The catalytic material MSNRhNPs was made and ready for catalyst characterization, analysis and catalytic tests after the removal of template CTAB and PVP at 350 ^{o}C in air for 5 hours. Before reaction, MSNRhNPs was reduced in continuous H_2 flow (10 mL/min) at 310 ^{o}C with 450 psi pressure for at least 2 h. N_2 adsorption and desorption isotherms (Figure S4-1) show that MSNRhNPs still had a typical mesoporous structure of MSN with a narrow pore size distribution as diameter was around 2.4 nm, surface area at 947 m^2/g and pore volume at 1.0 mL. X-ray powder diffraction (XRD, Figure S4-2) indicated that MSNRhNPs were still full of highly ordered parallel channels, which could be seen clearly from Transmission Electron Microscopy (TEM) images (Figure 4-2a). In TEM image, a lot of tiny black spots could be seen in addition to the highly ordered parallel channels and these were RhNPs, which was further confirmed by Scanning Transmission Electron Microscopy (STEM) image in Figure 4-2b. From STEM images of MSNRhNPs, it is clear that 1) RhNPs were well-distributed over the mesoporous silica nanoparticle and 2) the supported RhNPs was almost the same size, around 2.0 nm in diameter, as unsupported RhNPs (as shown in Figure 4-1), although it is very difficult to accurately measure the size of small nanoparticles on mesoporous supports because TEM images taken from nanoparticles supported on mesoporous supports often suffer from low contrast due to the decrease of the supporting material's electron transparency, and this behavior is magnified as particle size decreases, and nanoparticles on mesoporous silica are also in different focal planes during TEM imaging. Energy Dispersive X-ray (EDX) was used to determine the loading of Rh on

MSNRhNPs and 1.6 wt% of Rh in this material was obtained basing on the atomic ratio between Si and Rh (Figure S4-4).

Synthesis of Rh-MSN and Mn^{n+} Modified Rh Catalysts through Impregnation Methods. MSNRhNPs' counterparts, Rh-MSN with 1.6 wt% of Rh loading, from traditional incipient wet-chemistry, impregnation methods, were synthesized (see supporting information) in order to compare their catalytic properties in CO hydrogenation reactions. For Rh catalysts in CO hydrogenation, many promoters were used to improve selectivity to C_2 (including ethanol and acetaldehyde) or C_{2+} oxygenates,[2-4] and among these reported promoters, Mn_xO_y was a very good candidate.[34-36,58,59] (Here, the oxidation states of Mn species usually could not be accurate and it will be addressed in the flowing studies in this paper.) Therefore, in order to improve the selectivities of MSNRhNPs and Rh-MSN to C_2 oxygnates, Mn^{n+} modified MSNRhNPs (MSNRhNPs-Mn) and Mn^{n+} modified Rh-MSN (Rh-Mn-MSN) were both synthesized by impregnation methods using $Mn(NO_3)_2$ (see supporting information).

Modification of RhNPs by Mn^{n+} during *in situ* formation of MSN.

It's a well-known challenge to control the distribution of metal ions on solid surface. Therefore, many catalysts, even with the same chemical composition, have different catalytic performances if they are from different companies or different research groups. For the bimetallic or multimetallic catalysts, the situation was even worse due to the difficulty to adjust the interaction between these different metals. In catalyst MSNRhNPs, RhNPs were distributed homogeneously in MSN particles as we can see from Figure 4-3. However, during the Mn^{n+} modification procedure, the distribution of Mn^{n+} and the interaction between RhNPs and Mn^{n+} are still out of control due to the innate disadvantage of impregnation method. In order to achieve a homogeneous distribution of Mn^{n+} around RhNPs and the interaction between RhNPs and Mn^{n+}, we, for the first time, modify RhNPs by Mn^{n+} right during the formation of MSN as shown in Scheme 4-2.

Typically, the as-made RhNPs (480.0 mg, including 40.0 mg Rh) were re-dissolved into water (10.0 mL, 0.6 mol) and mixed with water (470 mL, 26.1 mol), CTAB (2.0 g, 5.5 mmol), NaOH (7.0 mL x 2.0 mol/L, 14.0 mmol) at room temperature prior to the adding of $Mn(NO_3)_2 \cdot xH_2O$ (104.7mg, including 20.0 mg Mn) and the hydrolysis of TEOS (10.0 mL,

44.8 mmol) at 80 ^{o}C for 2.0 hours. After the hydrolysis of TEOS, the black solid was filtrated and dried under vacuum overnight. The catalytic material MSNRhNPsMn was made and ready for the catalyst characterization after the calcination at 350 ^{o}C in air for 5 hours. Before reaction, MSNRhNPsMn was also reduced in continuous H_2 flow as other catalysts. N_2 adsorption and desorption isotherms (Figure S4-12), XRD (Figure S4-13) show that MSNRhNPsMn still has the typical highly ordered MSN parallel channel structure with high surface area (S_{BET} = 878 m^2/g), very narrow pore size distribution (d_{BJH} = 2.5 nm). TEM and STEM images (Figure 4-3) of MSNRhNPsMn show that RhNPs are distributed homogeneously through the whole structure of MSN and the particle size is still around 2.0 nm without change after modification with Mn^{n+}. EDX was used to determine the loading of Rh and Mn on MSNRhNPsMn and 1.6 wt% of Rh and 0.8 wt% of Mn in this material were found, which makes the ratio between Rh and Mn around 2.0.

X-ray Photoelectron Spectroscopy (XPS) Study. XPS was used to characterize the oxidation states of Rh and Mn in our catalysts on a Perkin-Elmer PHI 5500 XPS spectrometer with a position-sensitive detector, a hemispherical energy analyzer in an ion-pumped chamber (evacuated to 2 x 10^{-9} Torr), and a Al Kα (BE = 1486.6 eV) X-ray source at 300 W with 15 kV acceleration voltage. For all of our experiments, the binding energy of silicon was forced to be 104.5 eV which was used as an internal standard for other elements' binding energy. Figure 4-4 shows the XPS results of RhNPs and MSNRhNPs. Before calcination (Figure 4-4a and 4-4b), the Rh $3d_{5/2}$ peak (~308 eV) could be fit by two peaks with bonding energies of 307.3 eV and 308.9 eV, corresponding to the metallic Rh (0) and the oxidized Rh (+3) respectively. As shown in Figure 4-4a, RhNPs was very stable in air at room temperature with 88 % of metallic Rh(0) and 12 % of oxidized Rh(+3). After being encapsulated in MSN, there is still 30 % of metallic Rh(0) as shown in Figure 4-4b. After calcinations in air at 350 ^{o}C for 5 h, from XPS spectroscopy, Si, Mn, Rh and O are the only four detectable elements in all of our catalysts reported here, which indicates that template CTAB and PVP were removed completely from MSNRhNPs surface. With calcination, Rh was oxidized almost completely to Rh_2O_3 (Figure 4-4c) which can be reduced back to metallic Rh(0) by H_2 easily during the reaction(Figure 4-4d). So the XPS data might indicate that all of Rh atoms in RhNPs could be accessible to at least O_2 and H_2 and might be

accessible to CO as well under our reaction conditions. In any XPS spectroscopy of Mn^{n+} modified catalysts, Mn^{n+} was found. However, the oxidation states of Mn species could not be solved because of its lower intensity and the relatively small difference between binding energies of Mn^{2+}, Mn^{3+} and Mn^{4+} (Figure S4-15), which decreases the reliability of fitting theoretically. Therefore, it is better to use Mn^{n+} instead of other Mn species with defined oxidation states here.

Carbon Monoxide Hydrogenation Catalyzed by Rh Catalysts. Here a laboratory scale flow and tubular reactor (Figure S4-16) was used for the CO hydrogenation with low surface area SiC as catalyst diluting reagent. Temperature was controlled by a Parr controller (4843) and two type-K thermocouples. Gas flows (CO and H_2 were all from Praxair and UHP) were regulated by two calibrated mass flow system (Parr mass flow system with Brooks mass flow controllers). Before syngas was charged to the reactor, catalyst was reduced with 10 mL/min H_2 flow at 450 psi and 632 K for two hours. Deionized water was charged into the condenser in order to dissolve most of alcohols from the reaction. Tail gas right after the tubular reactor from the reaction was analyzed on an on-line GC (Varian 3900 with CP-Molsieve 5A (10 m x 0.32 mm x 10 μm) and CP-PoraBOND Q (50 m x 0.53 mm x 10 μm)), and a thermal conductivity detector (TCD)) with 5 wt% Ar as an internal reference gas. Liquid samples were analyzed on another Varian 3900GC but with flame ionization detector (FID) and a CP-PoraBOND Q (50 m x 0.32 mm x 5 μm) column.

We found that MSN encapsulated RhNPs catalysts (MSNRhNPs) has higher activity (CO conversion) and better selectivity to C_2 oxygenates than that of Rh-MSN made from impregnation methods in CO hydrogenation (Entry 1 and 2 in Table 4-1). And these trends were kept very well at different reaction temperatures (Figure S4-17). Since catalytic activity comparison was based on assuming 100% dispersion for every catalyst, the difference of reactivity was most likely due to the difference between Rh particles sizes. After reaction at 573 K for 24 h, TEM images showed that the Rh particles on Rh-MSN (Figure 4-5a) from impregnation methods grew much faster and had a much broader particle distribution (Most of them were larger than 5.0 nm and some of them even were around 20 nm in diameter) compared to that of MSNRhNPs (Figure 4-5b) where most of RhNPs were still less than 5 nm in diameter. The larger Rh particle in Rh-MSN made CO and H_2 accessible surface Rh

atoms less than that in MSNRhNPs with smaller particle size. The higher selectivity to C_2 oxygenates of MSNRhNPs might be related to both Rh particle size and the special interaction between MSN matrix and RhNPs, which is still under investigated in our lab.

After being modified with promoter Mn^{n+}, as shown in Figure S4-18, MSNRhNPs-Mn had the highest selectivity (32.4 %) to ethanol and lowest selectivity (3.7 %) to methanol. And both MSNRhNPs-Mn and Rh-Mn-MSN have higher catalytic activities after being modified with Mn^{n+} than that of their unmodified counterparts MSNRhNPs and Rh-MSN respectively (Entry 3 and 4 in Table 4-1). That indicates that manganese oxides not only can improve the selectivity of Rh catalysts to C2 oxygenates but also can accelerate the CO hydrogenation. In another words, Mn^{n+} not only help to tilt the adsorbed CO from Rh to Mn which is helpful to synthesize ethanol and acetaldehyde according to Bao et. al.,[58] but also participate the hydrogenation of CO to HCO which was thought to be the rate limiting step in CO hydrogenation to ethanol according to the density functional theory.[60] Although the mechanism of Mn effects on CO hydrogenation is still under investigation, it is clear that the close interaction between Rh and Mn is necessary for a better catalytic performance of Rh catalyst in CO hydrogenation, which was further proved by our catalytic tests over MSNRhNPsMn.

As listed in Table 4-1 (Entry 4 and 5), the catalytic activity of MSNRhNPsMn was almost the same as that of MSNRhNPs-Mn, which is because the same RhNPs were used as the catalytic sites in both cases. Although the selectivities to gas product methane were close to each other for MSNRhNPsMn and MSNRhNPs-Mn, interestingly, the selectivity of MSNRhNPsMn to ethanol is much higher than that of MSNRhNPs-Mn as shown in Figure 4-6. Methanol, which usually is one of the main liquid by-products in CO hydrogenation, was kept at very low level through our tests when MSNRhNPsMn was used as catalyst. In the mean time, CO_2 production is under GC's detection limitation even at 593 K for MSNRhNPsMn as well. These results indicate that the closer or stronger interaction between promoter Mn and catalytic site Rh is necessary to synthesize the ideal product C2 oxygenates such as ethanol and suppress the formation of by-product methanol. As shown in Figure 4-6, the selectivity of ethanol in tested temperature range from 523 K to 573 K reached its highest

point and the selectivity of methane touched its lowest point although the CO conversion is only around 9.8 % which is lower than 24.2 % at 543 K.

Conclusions

In summary, we have designed a new Rh-based catalyst in which well-defined rhodium nanoparticles were distributed homogeneously through the whole mesoporous silica particle and could be easily modified by promoters during *in situ* of the formation of mesoporous silica. The resulting catalyst possesses a high surface area and narrow pore size distribution as normal MSN does. The new manganese modified rhodium catalyst could suppress the formation of by-product methanol efficiently therefore has very high selectivity to the ideal C_2 oxygenates in CO hydrogenation. With the demonstrated better thermostability and better catalytic performance of MSN-encapsulated and Mn-modified rhodium nanoparticles, we defined a novel synthesis and modification method for metallic heterogeneous catalysts.

Acknowledgement

This research was supported at Ames Laboratory by the U.S. DOE, office of BES, under contract DE-AC02-07CH11358.

References

(1) Farrell, A. E.; Plevin, R. J.; Turner, B. T.; Jones, A. D.; O'Hare, M.; Kammen, D. M. *Science (Washington, DC, U. S.)* **2006**, *311*, 506-508.

(2) Fang, K.; Li, D.; Lin, M.; Xiang, M.; Wei, W.; Sun, Y. *Catal. Today* **2009**, *147*, 133-138.

(3) Subramani, V.; Gangwal, S. K. *Energy Fuels* **2008**, *22*, 814-839.

(4) Spivey James, J.; Egbebi, A. *Chem. Soc Rev* **2007**, *36*, 1514-1528.

(5) Takeuchi, K.; Matsuzaki, T.; Arakawa, H.; Sugi, Y. *Appl. Catal.* **1985**, *18*, 325-334.

(6) Bhasin, M. M.; Bartley, W. J.; Ellgen, P. C.; Wilson, T. P. *J. Catal.* **1978**, *54*, 120-128.

(7) Chuang, S. S. C.; Stevens, R. W., Jr.; Khatri, R. *Top. Catal.* **2005**, *32*, 225-232.

(8) Takeuchi, K.; Matsuzaki, T.; Arakawa, H.; Hanaoka, T.; Sugi, Y. *Appl. Catal.* **1989**, *48*, 149-157.

(9) Sugi, Y.; Takeuchi, K.; Matsuzaki, T.; Arakawa, H. *Chem. Lett.* **1985**, 1315-1318.

(10) Kintaichi, Y.; Kuwahara, Y.; Hamada, H.; Ito, T.; Wakabayashi, K. *Chem. Lett.* **1985**, 1305-1306.

(11) Zaman, S. F.; Smith, K. J. *Catal. Commun.* **2009**, *10*, 468-471.

(12) Subramanian, N. D.; Balaji, G.; Kumar, C. S. S. R.; Spivey, J. J. *Catal. Today* **2009**, *147*, 100-106.

(13) Spivey, J. J.; Egbebi, A. A.; Subramanian, N.; Kumar, N.; Gupta, M. *Prepr. Symp. - Am. Chem. Soc., Div. Fuel Chem.* **2009**, *54*, 127-128.

(14) Shi, X.-R.; Jiao, H.; Hermann, K.; Wang, J. *J. Mol. Catal. A: Chem.* **2009**, *312*, 7-17.

(15) Gupta, M.; Spivey, J. J. *Catal. Today* **2009**, *147*, 126-132.

(16) Jiang, D.; Ding, Y.; Pan, Z.; Li, X.; Jiao, G.; Li, J.; Chen, W.; Luo, H. *Appl. Catal., A* **2007**, *331*, 70-77.

(17) Budge, J. R.; Gates, B. C. **1982**, *1*, 204-207.

(18) Terreros, P.; Fandos, R.; Granados, M. L.; Otero, A.; Rojas, S.; Vivar-Cerrato, M. A. *Stud. Surf. Sci. Catal.* **2000**, *130D*, 3891-3896.

(19) Hanaoka, T.; Kim, W.-Y.; Kishida, M.; Nagata, H.; Wakabayashi, K. *Chem. Lett.* **1997**, 645-646.

(20) Ito, S.-i.; Chibana, C.; Nagashima, K.; Kameoka, S.; Tomishige, K.; Kunimori, K. *Appl. Catal., A* **2002**, *236*, 113-120.

(21) Burch, R.; Hayes, M. J. *J. Catal.* **1997**, *165*, 249-261.

(22) Jiang, D.; Ding, Y.; Pan, Z.; Chen, W.; Luo, H. *Catal. Lett.* **2008**, *121*, 241-246.

(23) Pan, X.; Fan, Z.; Chen, W.; Ding, Y.; Luo, H.; Bao, X. *Nat. Mater.* **2007**, *6*, 507-511.

(24) Bastein, A. G. T. M.; Van der Boogert, W. J.; Van der Lee, G.; Luo, H.; Schuller, B.; Ponec, V. *Appl. Catal.* **1987**, *29*, 243-260.

(25) Van der Lee, G.; Ponec, V. *J. Catal.* **1986**, *99*, 511-512.

(26) Panpranot, J.; Goodwin, J. G., Jr.; Sayari, A. *J. Catal.* **2002**, *211*, 530-539.

(27) Martinez, A.; Prieto, G. *Top. Catal.* **2009**, *52*, 75-90.

(28) Ma, H.; Yuan, Z.; Wang, Y.; Bao, X. *Surf. Interface Anal.* **2001**, *32*, 224-227.

(29) Mo, X.; Gao, J.; Goodwin, J. G. *Catal. Today* **2009**, *147*, 139-149.

(30) Haider, M. A.; Gogate, M. R.; Davis, R. J. *J. Catal.* **2009**, *261*, 9-16.

(31) Subramanian, N.; Spivey, J. J.; Gao, J.; Mo, X.; Goodwin, J. G.; Torres, W., Jr. *Proc. - Annu. Int. Pittsburgh Coal Conf.* **2008**, *25th*, 182/1-182/7.

(32) Chen, W.; Ding, Y.; Jiang, D.; Pan, Z.; Luo, H. *J. Nat. Gas Chem.* **2005**, *14*, 199-206.

(33) Yin, H. M.; Ding, Y. J.; Luo, H. Y.; Chen, W. M.; Lin, L. W. *Stud. Surf. Sci. Catal.* **2004**, *147*, 421-426.

(34) Ojeda, M.; Granados, M. L.; Rojas, S.; Terreros, P.; Garcia-Garcia, F. J.; Fierro, J. L. G. *Appl. Catal., A* **2004**, *261*, 47-55.

(35) Yin, H.; Ding, Y.; Luo, H.; Zhu, H.; He, D.; Xiong, J.; Lin, L. *Appl. Catal., A* **2003**, *243*, 155-164.

(36) Yin, H.; Ding, Y.; Luo, H.; Yan, L.; Wang, T.; Lin, L. *Energy Fuels* **2003**, *17*, 1401-1406.

(37) Luo, H. Y.; Zhang, W.; Zhou, H. W.; Huang, S. Y.; Lin, P. Z.; Ding, Y. J.; Lin, L. W. *Appl. Catal., A* **2001**, *214*, 161-166.

(38) Luo, H.; Zhou, H.; Lin, L.; Liang, D.; Li, C.; Fu, D.; Xin, Q. *J. Catal.* **1994**, *145*, 232-234.

(39) Gallaher, G. R.; Goodwin, J. G., Jr.; Huang, C. S.; Houalla, M. *J. Catal.* **1993**, *140*, 453-463.

(40) Gallaher, G. R.; Goodwin, J. G., Jr.; Guczi, L. *Appl. Catal.* **1991**, *73*, 1-15.

(41) Gallaher, G.; Goodwin, J. G., Jr.; Huang, C. S.; Houalla, M. *J. Catal.* **1991**, *127*, 719-731.

(42) Chuang, S. S. C.; Pien, S. I.; Narayanan, R. *Appl. Catal.* **1990**, *57*, 241-251.

(43) Van der Lee, G.; Schuller, B.; Post, H.; Favre, T. L. F.; Ponec, V. *J. Catal.* **1986**, *98*, 522-529.

(44) Thomas, J. M.; Thomas, J. W.; Editors *Principles and Practice of Heterogeneous Catalysis*, 1996.

(45) Satterfield, C. N. *Heterogeneous Catalysis in Industrial Practice. 2nd Ed*, 1991.

(46) Le Page, J. F. *Applied Heterogeneous Catalysis: Design, Manufacture, Use of Solid Catalysts*, 1987.

(47) Zhou, S.; Zhao, H.; Ma, D.; Miao, S.; Cheng, M.; Bao, X. *Z. Phys. Chem. (Muenchen, Ger.)* **2005**, *219*, 949-961.

(48) Huang, Y.; Li, Y.; Hu, J.; Cheng, P.; Chen, H.; Li, R.; Li, X.; Yip, C. W.; Chan, A. S. C. *J. Mol. Catal. A: Chem.* **2002**, *189*, 219-224.

(49) Huang, Y.; Chen, J.; Chen, H.; Li, R.; Li, Y.; Min, L. e.; Li, X. *J. Mol. Catal. A: Chem.* **2001**, *170*, 143-146.

(50) Beck, J. S.; Vartuli, J. C.; Roth, W. J.; Leonowicz, M. E.; Kresge, C. T.; Schmitt, K. D.; Chu, C. T. W.; Olson, D. H.; Sheppard, E. W.; et al. *J. Am. Chem. Soc.* **1992**, *114*, 10834-10843.

(51) Kresge, C. T.; Leonowicz, M. E.; Roth, W. J.; Vartuli, J. C.; Beck, J. S. *Nature (London)* **1992**, *359*, 710-712.

(52) Song, H.; Rioux, R. M.; Hoefelmeyer, J. D.; Komor, R.; Niesz, K.; Grass, M.; Yang, P.; Somorjai, G. A. *J. Am. Chem. Soc.* **2006**, *128*, 3027-3037.

(53) Ferrando, R.; Jellinek, J.; Johnston, R. L. *Chem. Rev. (Washington, DC, U. S.)* **2008**, *108*, 845-910.

(54) Crooks, R. M.; Lemon, B. I., III; Sun, L.; Yeung, L. K.; Zhao, M. *Top. Curr. Chem.* **2001**, *212*, 81-135.

(55) Crooks, R. M.; Zhao, M.; Sun, L.; Chechik, V.; Yeung, L. K. *Acc. Chem. Res.* **2001**, *34*, 181-190.

(56) Grass, M. E.; Joo, S. H.; Zhang, Y.; Somorjai, G. A. *J. Phys. Chem. C* **2009**, *113*, 8616-8623.

(57) Huang, W.; Kuhn, J. N.; Tsung, C.-K.; Zhang, Y.; Habas, S. E.; Yang, P.; Somorjai, G. A. *Nano Lett.* **2008**, *8*, 2027-2034.

(58) Wang, Y.; Luo, H.; Liang, D.; Bao, X. *J. Catal.* **2000**, *196*, 46-55.

(59) Hu, J.; Wang, Y.; Cao, C.; Elliott, D. C.; Stevens, D. J.; White, J. F. *Catal. Today* **2006**, *120*, 90-95.

(60) Choi, Y. M.; Liu, P. *J. Am. Chem. Soc.* **2009**, *131*, 13054-13061.

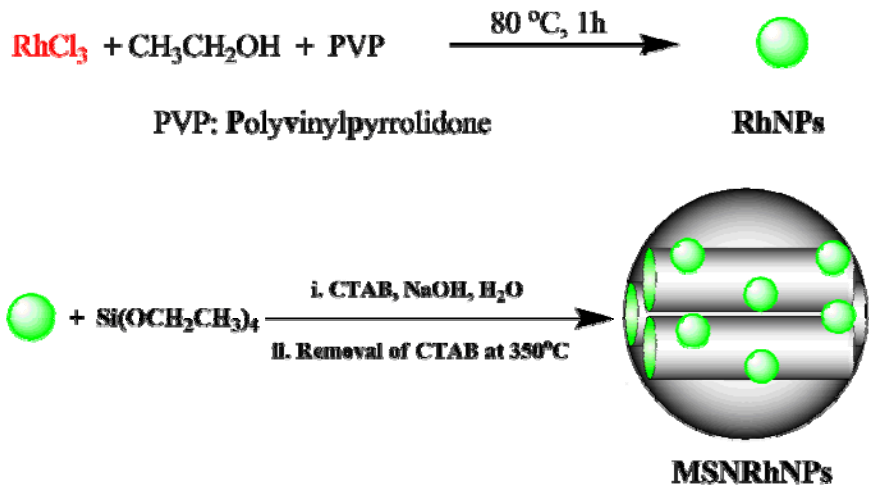

Scheme 4-1. Synthesis of PVP-stabilized Rhodium Nanoparticles and the Subsequent Encapsulation of the RhodiumNanoparticle in the Framework of Mesoporous Silica Nanoparticles.

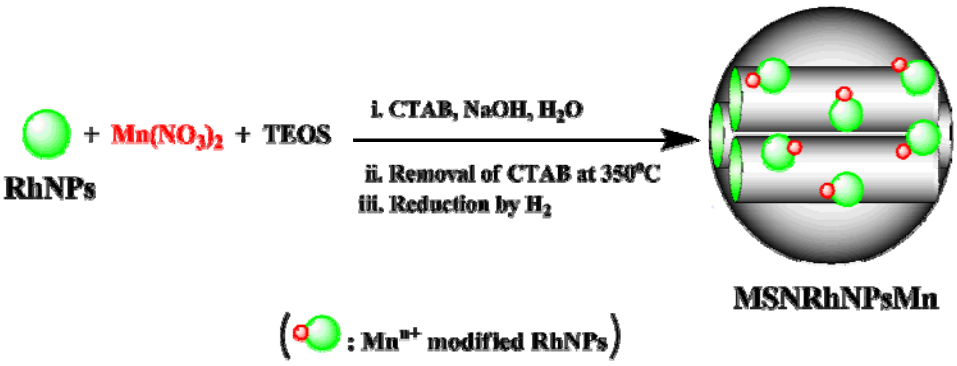

Scheme 4-2. Synthesis of MSNRhNPsMn by co-condensation of $Mn(NO)_2$, RhNPs with TEOS.

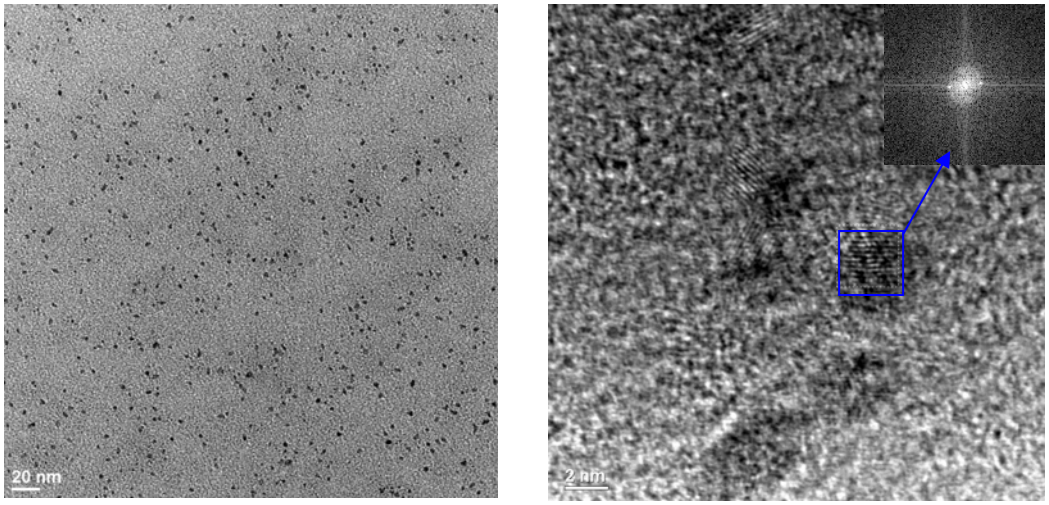

(a) (b)

Figure 4-1. TEM image (a) and HRTEM image (b) of RhNPs.

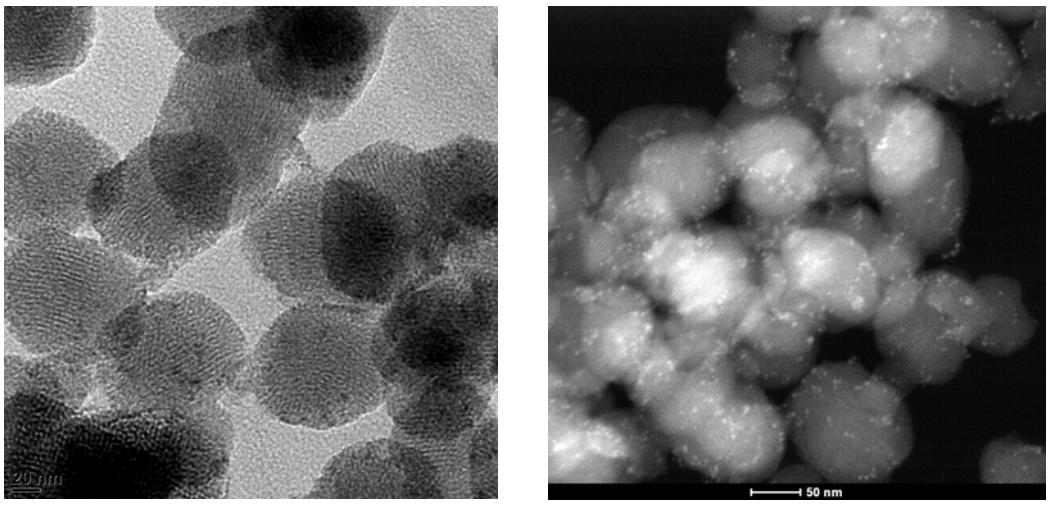

(a) **(b)**

Figure 4-2. TEM image (a) and STEM image (b) of MSNRhNPs.

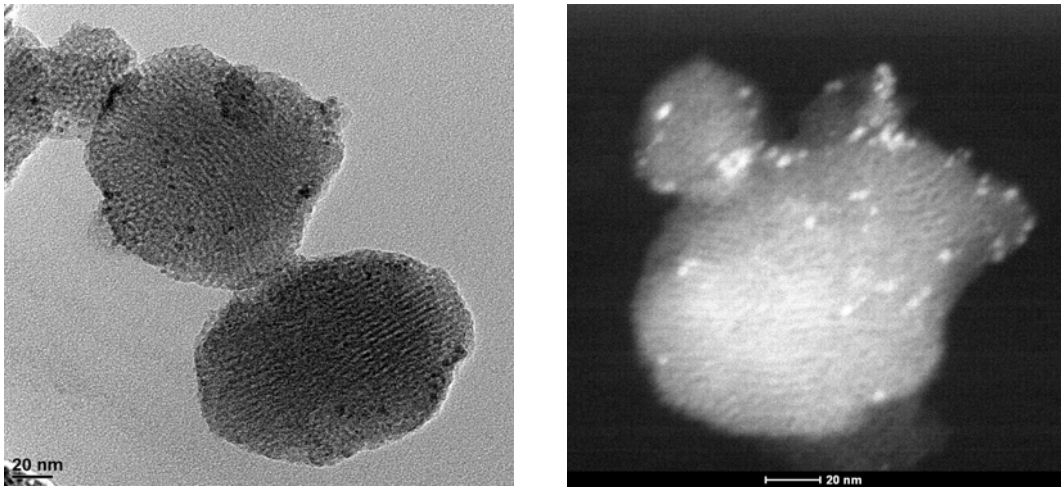

(a) **(b)**

Figure 4-3. TEM (a) of STEM (b) images of MSNRhNPsMn.

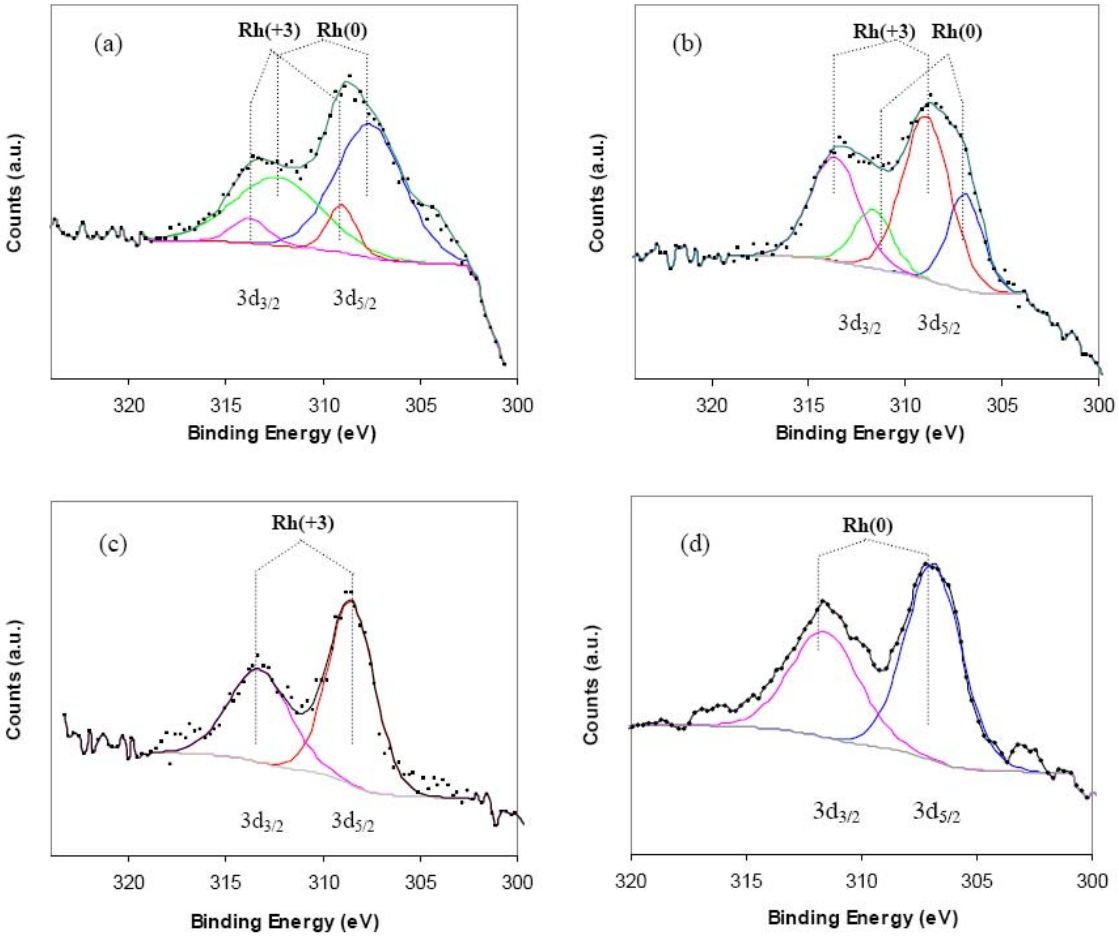

Figure 4-4. XPS of RhNPs (a) and MSNRhNPs (b: before calcination, c: after calcination, d: after reaction.

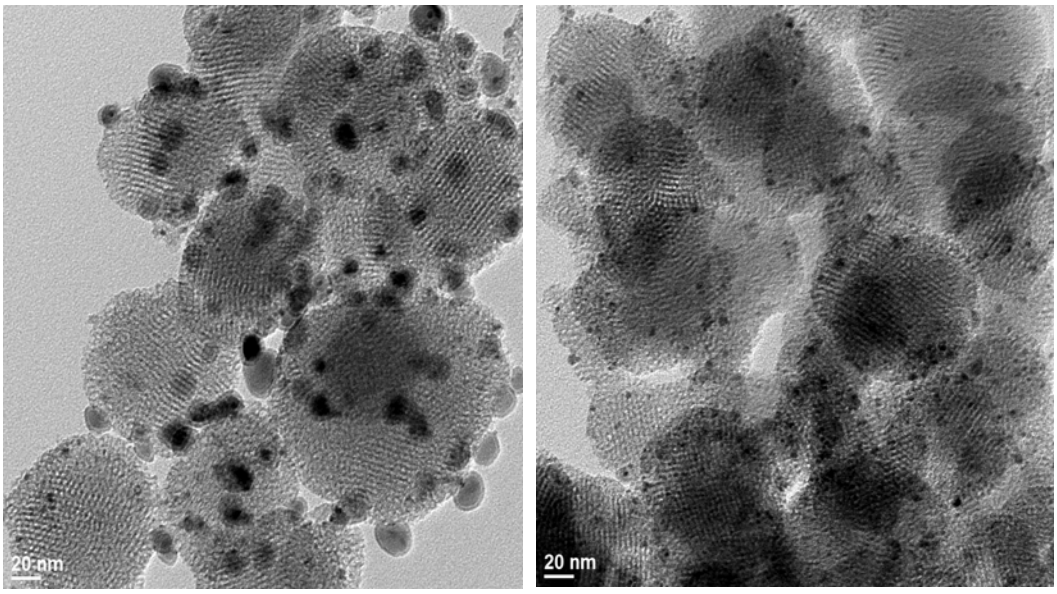

(a)

Figure 4-5. TEM images of Rh-MSN (a) and MSNRhNPs (b) both after reaction at 300 ^{o}C for 24h.

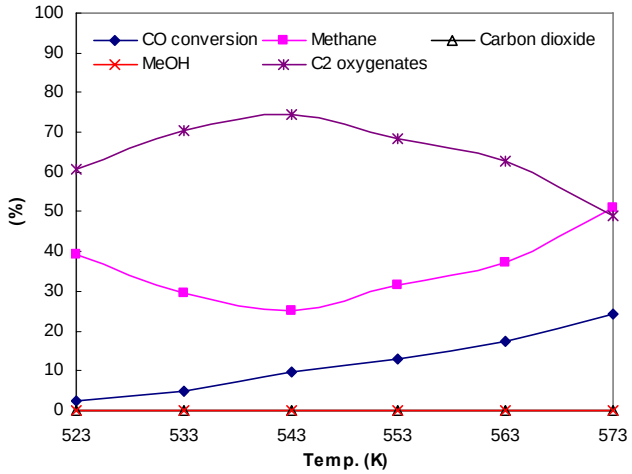

Figure 4-6. Effect of temperature on CO hydrogenation catalyzed by MSNRhNPsMn.

Table 4-1. Catalytic data of Rh-based catalysts in CO hydrogenation*

		CO conversion (%)	Selectivity (%)				
			CH_4	CO_2	CH_3OH	C_2	C_{2+}
1	Rh-MSN	2.7	40.8	0	24.4	33.0	34.8
2	MSNRhNPs	4.8	27.2	0	17.8	53.0	55.0
3	Rh-Mn-MSN	13.7	63.0	1.6	3.8	24.3	31.6
4	MSNRhNPs-Mn	20.2	47.0	2.5	3.7	42.2	46.8
5	MSNRhNPsMn	24.2	51.2	0	0	40.3	48.8

* All data were collected at the same conditions (0.3 g of catalyst with 3.0 g SiC, 300 ^oC, 450 psi, 11 mL/min of CO, 22 mL/min of H_2).

Supporting Information

1. Characterization of Catalysts MSNRhNPs

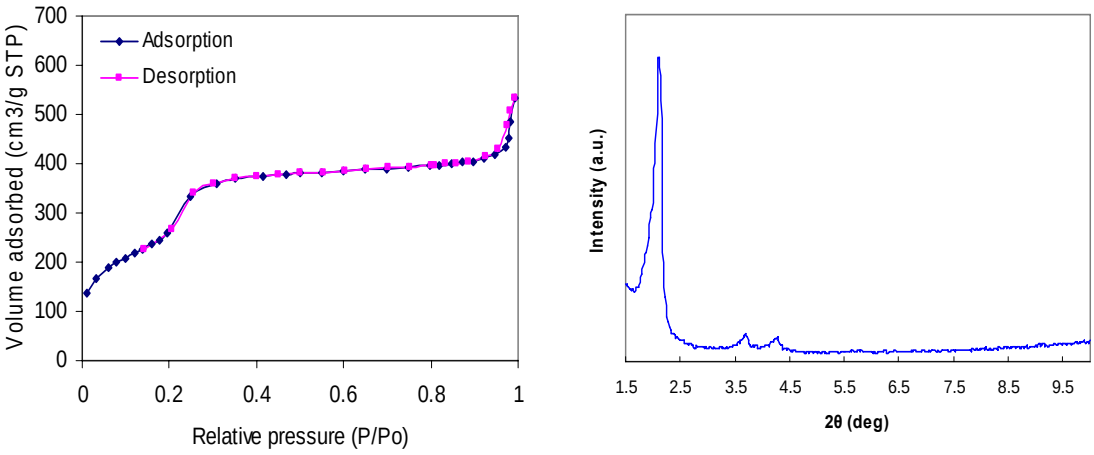

Figure S4-1. BET isotherms and BJH pore size distribution curve of MSNRhNPs.

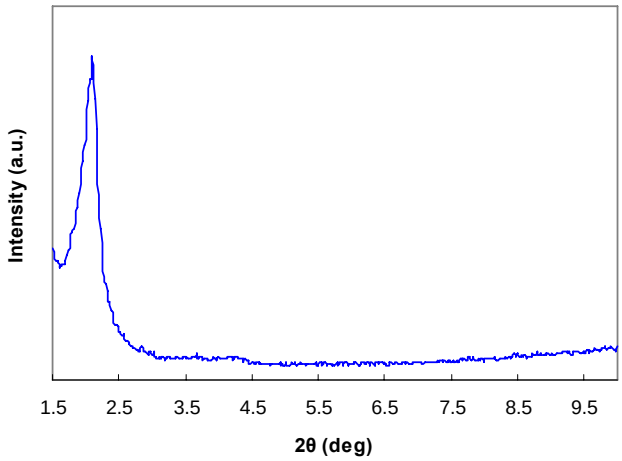

Figure S4-2. XRD of MSNRhNPs.

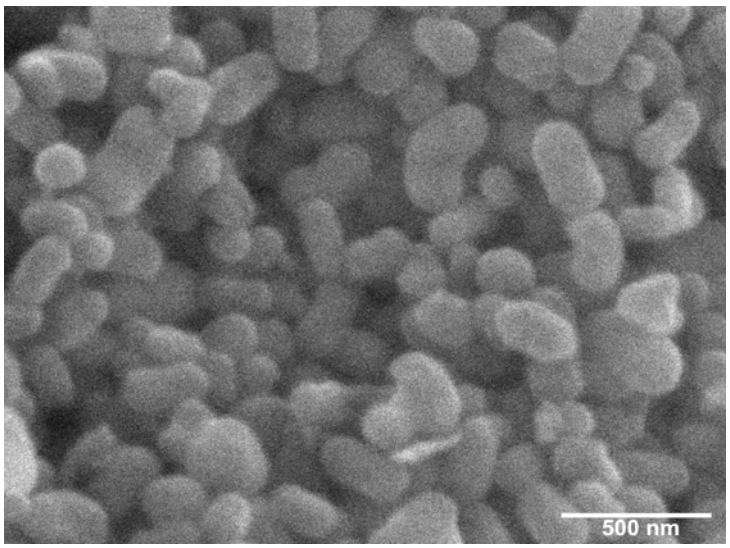

Figure S4-3. SEM image of MSNRhNPs.

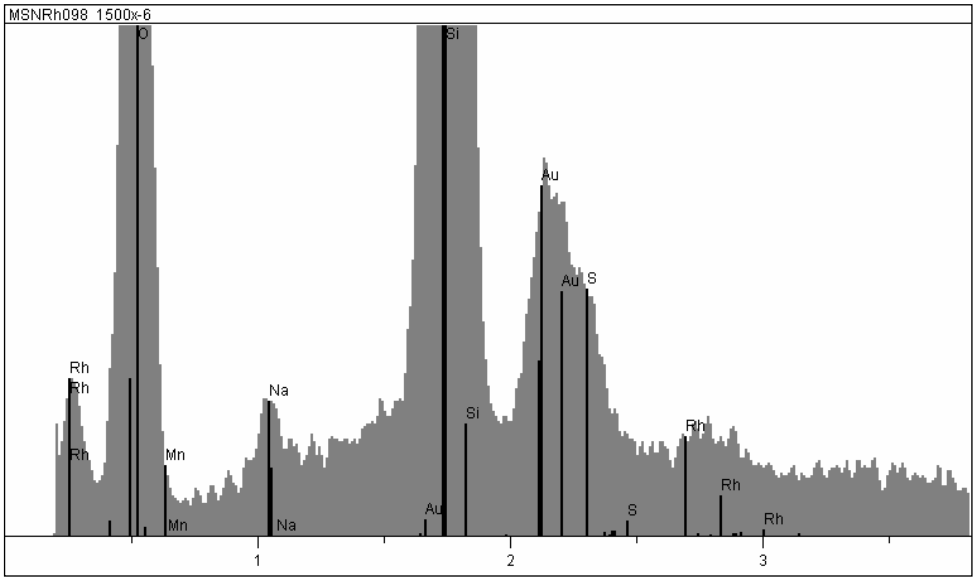

Figure S4-4. EDX spectroscopy of MSNRhNPs.

2. Synthesis of catalyst Rh-MSN with 1.6 wt % Rh by impregnation

$RhCl_3 \cdot H_2O$ (42.5 mg, including ~16 mg Rh) was dissolved into 2.0 mL H_2O at room temperature and then mixed with 1.0 g pure MSN with vigorous stirring for 24 hours. The solid was collected by filtration and dried in an oven at 100 ^oC overnight. Then the catalyst was calcinated at 350 ^oC in air for 5 hours. Before reaction, the catalyst was reduced in continuous H_2 flow (10 mL/min) at 310 ^oC with 450 psi pressure for at least 2 h and MSN-Rh was made. N_2 adsorption and desorption isotherms (Figure S4-5) show that MSNRhNPs still had a typical mesoporous structure of MSN with a narrow pore size distribution as diameter was around 2.4 nm, surface area at 855 m^2/g and pore volume at 0.8 mL. X-ray powder

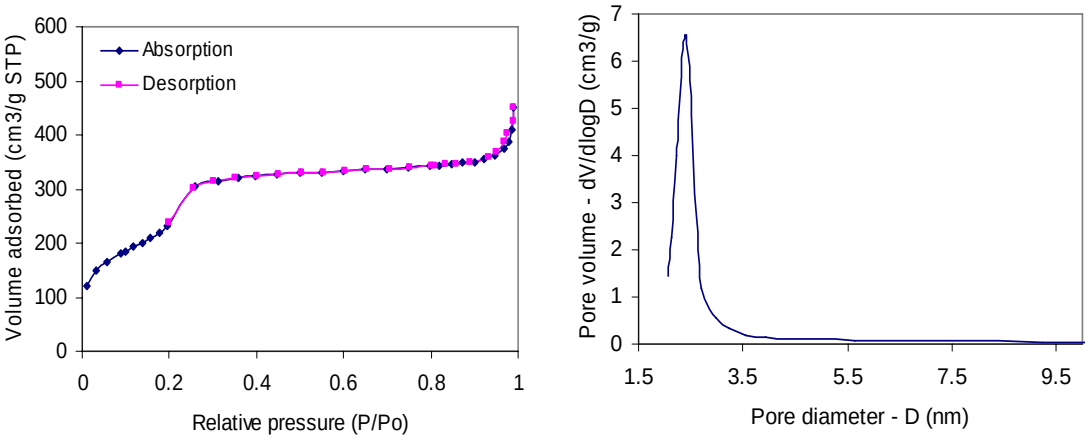

Figure S4-5. BET isotherms and BJH pore size distribution curve of MSN-Rh.

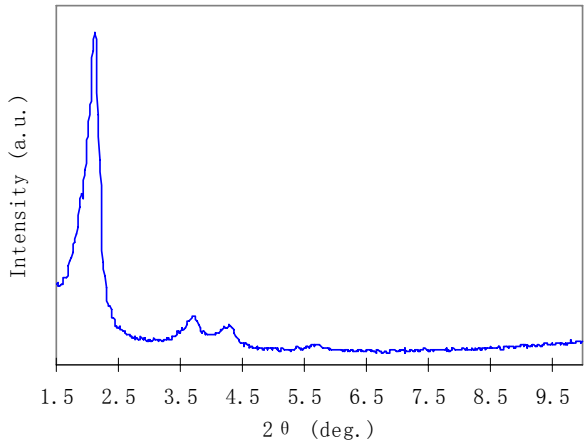

Figure S4-6. XRD of catalyst MSN-Rh.

diffraction (XRD, Figure S4-6) indicated that MSN-Rh were still full of highly ordered parallel channels, which could be seen clearly from Transmission Electron Microscopy (TEM) images (Figure S4-7).

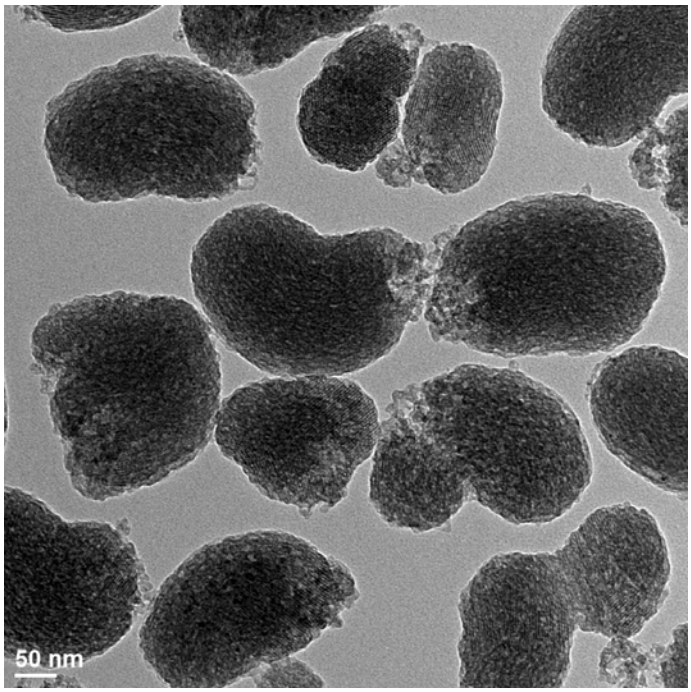

Figure S4-7. TEM images of MSN-Rh.

3. Synthesis of MSNRhNPs-Mn and Rh-Mn-MSN

$Mn(NO_3)_2 \cdot 6H_2O$ (83.7 mg, including ~16 mg Mn) was dissolved into 2.0 mL H_2O at room temperature and then mixed with 1.0 g Rh-MSN (or MSNRhNPs) with vigorous stirring for 24 hours. The solid was collected by filtration and dried in an oven at 100 ^oC overnight. Then the catalyst was calcinated at 350 ^oC in air for 5 hours. Before reaction, the catalyst was reduced in continuous H_2 flow (10 mL/min) at 310 ^oC with 450 psi pressure for at least 2 h and MSN-Rh-Mn (or MSNRhNPs-Mn) was made. N_2 adsorption and desorption isotherms (Figure S4-8 or S4-9) show that MSN-Rh-Mn (or MSNRhNPs-Mn) still had the same mesoporous structure of MSN-Rh (or MSNRhNPs) with a narrow pore size distribution as diameter was around 2.4 nm (or 2.5 nm), surface area at 765 m^2/g (or 890 m^2/g) and pore volume at 0.8 mL (or 0.7 mL). XRD (Figure S4-10 and S4-11) indicated that MSN-Rh-Mn

and MSNRhNPs-Mn were still full of highly ordered parallel channels, which could be seen clearly from TEM images (Figure S4-12 and S4-13).

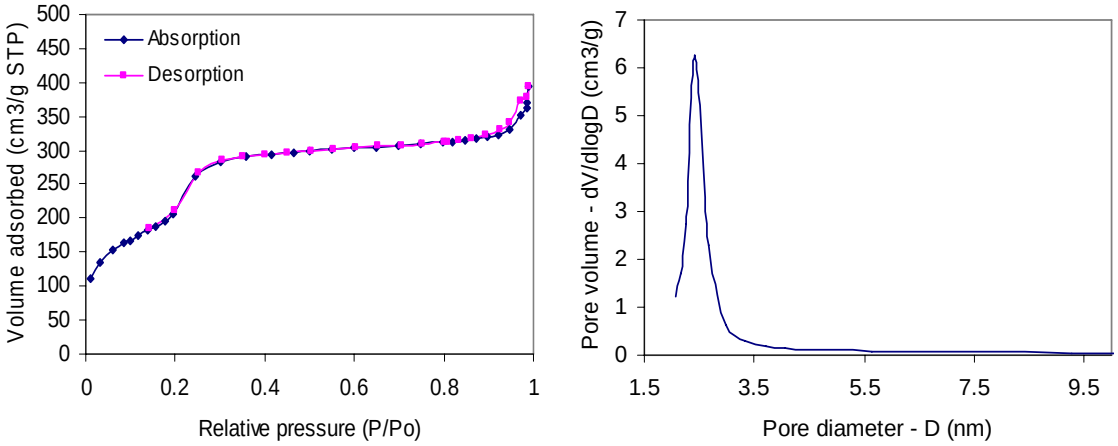

Figure S4-8. BET isotherms and BJH pore size distribution curve of MSN-Rh-Mn.

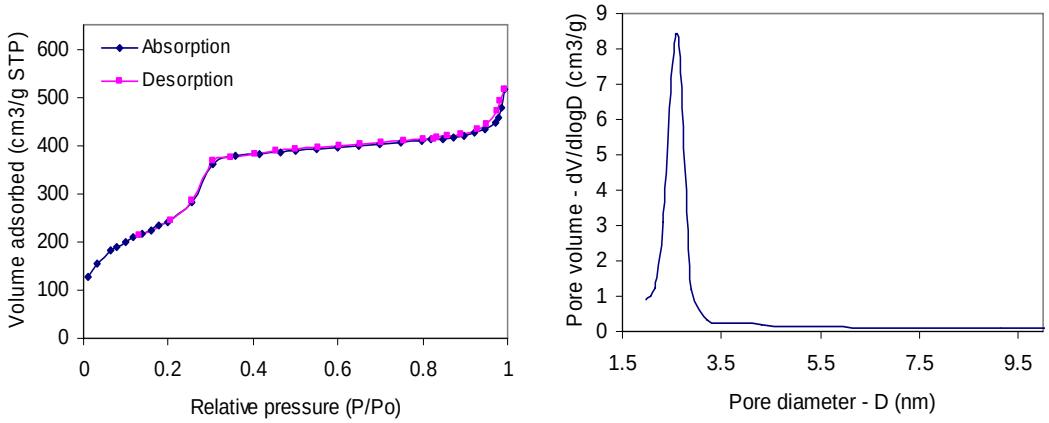

Figure S4-9. BET isotherms and BJH pore size distribution curve of MSNRhNPs-Mn.

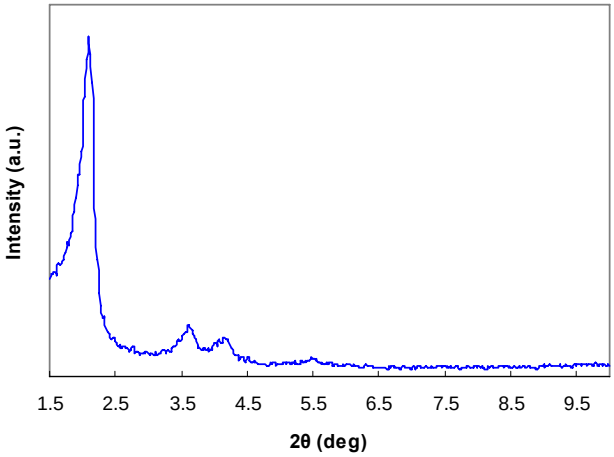

Figure S4-10. XRD of MSN-Rh-Mn.

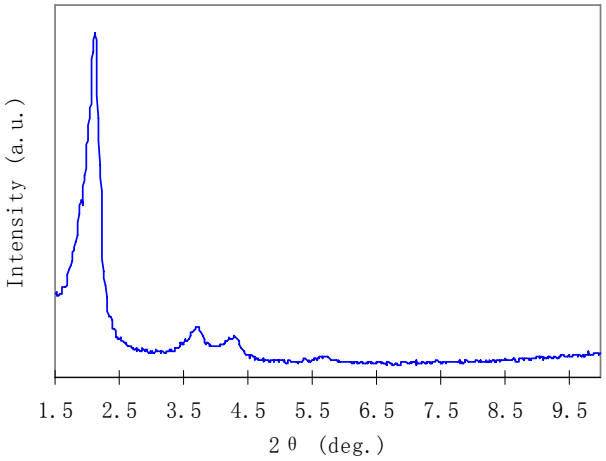

Figure S4-11. XRD of MSNRhNPs-Mn.

4. Characterization of Catalysts MSNRhNPsMn

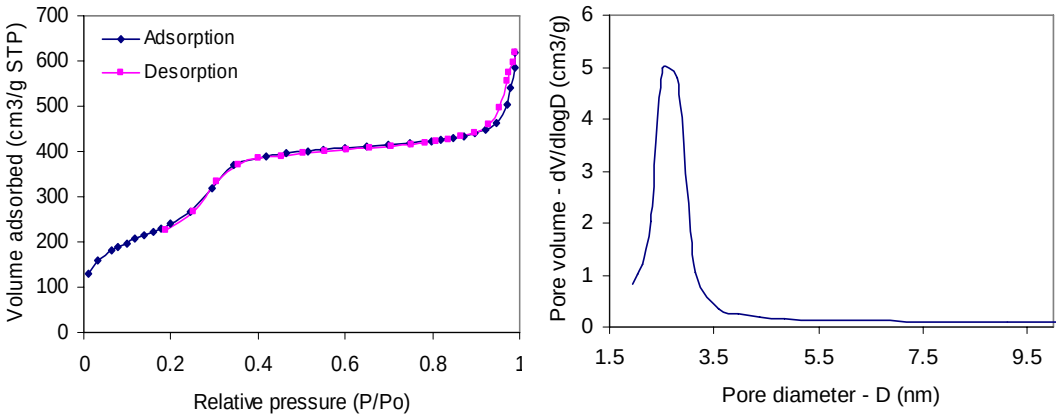

Figure S4-12. BET isotherms and BJH pore size distribution curve of MSNRhNPsMn.

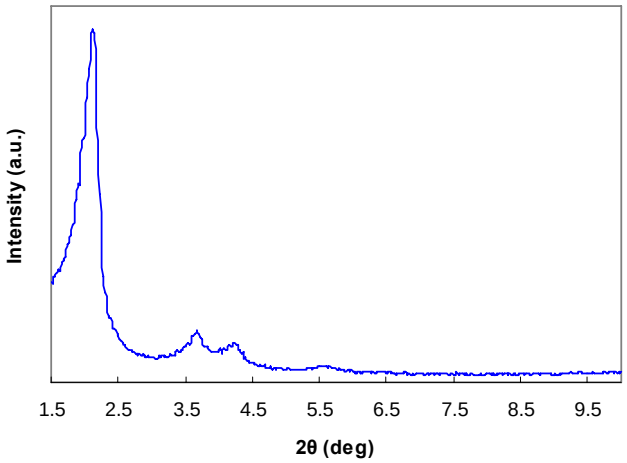

Figure S4-13. XRD of MSNRhNPsMn.

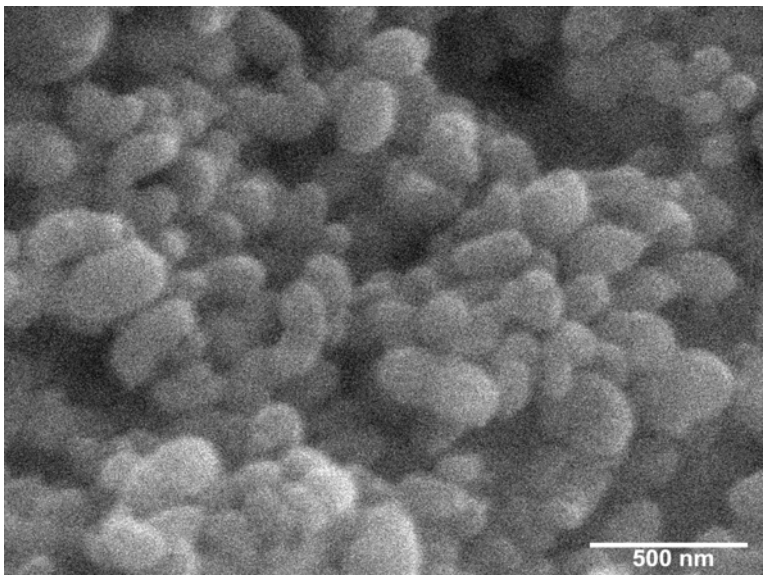

Figure S4-14. SEM image of MSNRhNPsMn.

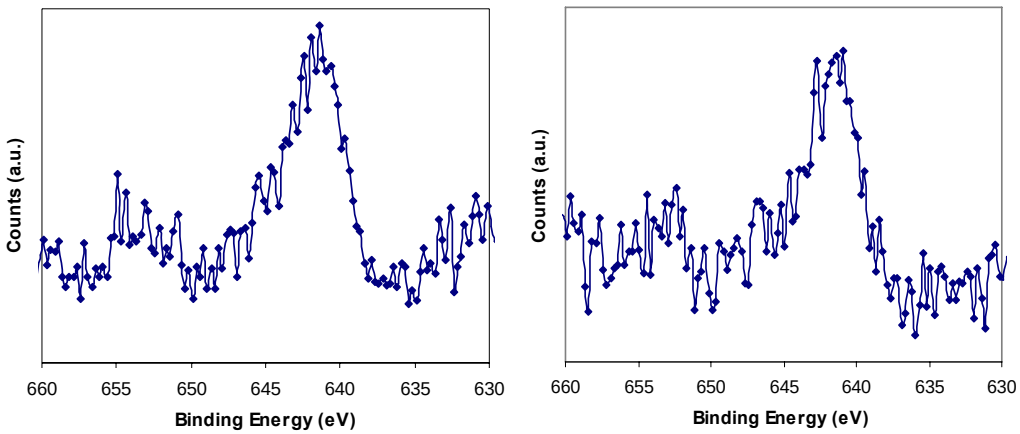

(a) Before reaction (b) After reaction

Figure S4-15. Manganese XPS spectra of MSNRhNPs-Mn (or MSNRhNPsMn) (Mn_3O_4: 640.9 eV, MnO: 641 eV, Mn_2O_3: 641 eV, MnO_2: 641.6 eV).

5. CO hydrogenation over Rh-based catalysts

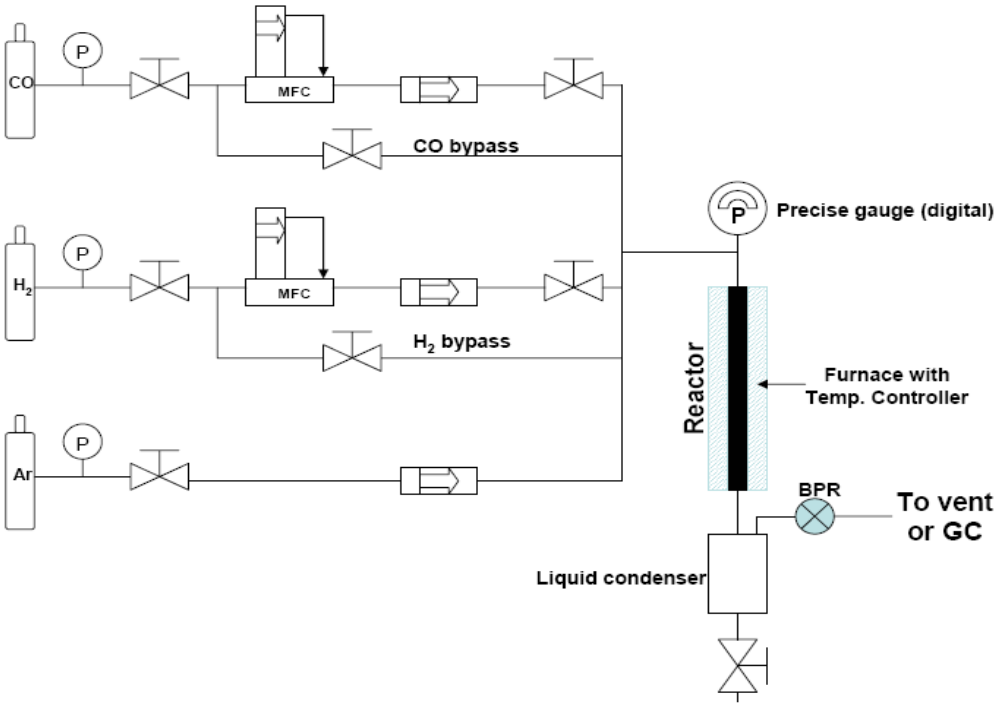

Figure S4-16. Scheme of the fixed-bed reactor system.

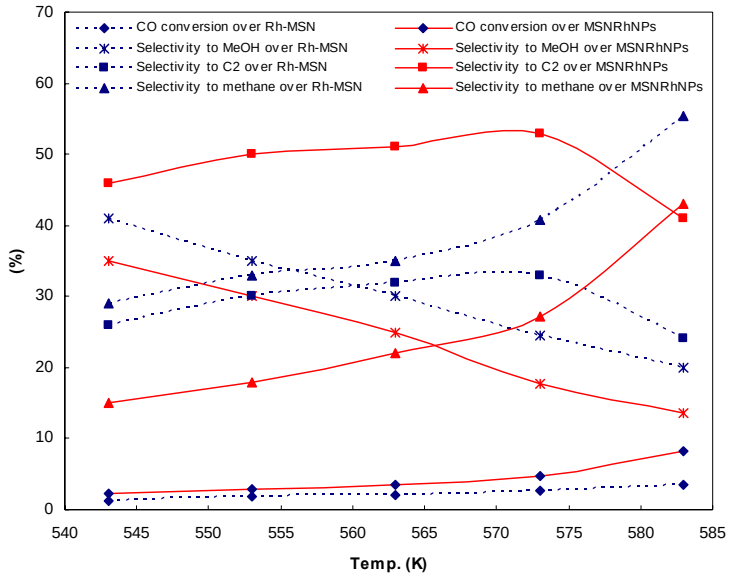

Figure S4-17. Effect of temperature on CO hydrogenation catalyzed by MSN-Rh and MSNRhNPs.

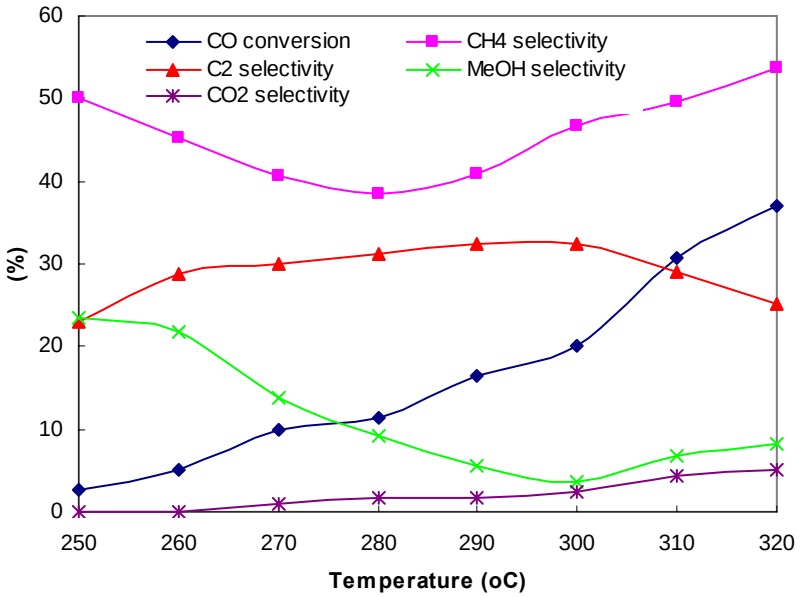

Figure S4-18. Effect of temperature on CO hydrogenation catalyzed by MSNRhNPs-Mn.

CHAPTER 5. NEW STRATEGY FOR ENANTIOSELECTIVE HETEROGENEOUS CATALYSIS: IMMOBLIZATION OF BOTH METAL NANOPARTICLES AND CHIRAL MODIFIERS IN MESOPOROUS SILICA

A paper to be submitted to *Angew. Chem. Int. Ed.*

Yulin Huang, Victor S.-Y. Lin*

Department of Chemistry and Ames Laboratory-U.S. Department of Energy, Iowa State University, Ames, IA50011

**Corresponding author.*

ABSTRACT

By co-condensation method, well defined rhodium nanoparticles and chiral reagent cinchonidine were immobilized and stabilized on mesoporous silica nanoparticle surface. In the enantioselective hydrogenation of ethyl pyruvate, reactivity and enantioselectivity could be retained very well during the catalyst recycling without any additional chiral reagent supplement.

Introduction

Due to the well-known potential advantages of heterogeneous catalysis, such as easy separation, efficient recycling, minimization of metal traces in the product, an improved handling and process control, overall low costs,[1,2] enormous progress has been resulted recently in interdisciplinary studies on stereoselective heterogeneous catalysis. Among asymmetric heterogeneous catalysts, some heterogenized homogeneous complexes[3-5] and chirally modified metals[4,6,7] seem most promising. And chirally modified nickel[8], platinum[9-11], palladium[12], rhodium[13-17] have emerged as effective heterogeneous asymmetrical catalysts for enantioselective hydrogenation of some specific substrates. Up to now, several methods

have been developed to immobilize metal particles on porous inorganic supports.[18,19] The best, also simplest method is incipient wetness and ion exchange, in which the porous oxide support is impregnated with metal precursors in solution phase, followed by thermal treatment and/or reduction with hydrogen to form metal nanoparticles.[20-23] However the size and size-distribution of metal nanoparticles formed on the support typically lack uniformity in size and shape, and the degree of dispersion on the support also usually could not be well controlled. In comparison, the more controllable formation of transition metal nanoparticles[14,15,24-28] for enantioselective heterogeneous catalysis has been achieved by wet-chemistry approach during the past decade.

Traditionally, these metal nanoparticles could be deposited on the surface of porous supports through mechanical mixing followed by evaporation. The immobilized metal nanoparticles could be used as asymmetrically heterogeneous catalysts after being modified by some chiral agents (usually cinchona alkaloids) through physical adsorption. As a result, the metal nanoparticles are not homogeneously dispersed on the support surface and the physically-adsorbed chiral modifiers will be washed away when the product was separated from the reaction system, which causes the loss of both reactivity and enantioselectivity. In order to improve the performance of heterogeneous metal nanoparticle, either different immobilization methods for metal nanoparticles on different supports[15,24-26,29] or various chiral modifiers[30-36] have been developed. However, enantioselectively heterogeneous catalysis, both having the homogenous distribution of metal nanoparticles and stabilized chiral modifiers on the catalyst surface, is still challenging. Herein, for the first time, we report a new strategy for enantioselective heterogeneous catalysis that can stabilize the well defined metal nanoparticle catalyst in mesoporous silica nanoparticle (MSN) framework during *in situ* MSN's growth and simultaneously immobilize its chiral modifier through cocondensation methods[37-42] followed by a post-synthesis coupling (Figure 5-1). Furthermore, we can decrease the amount of chiral modifier for enantioselective reactions.

Results and Discussions

We synthesized rhodium nanoparticles (RhNPs), which were well defined with an approximate diameter of 2.0 nm (Figure S5-1), as the real catalytic sites for our designed

reactions. Because these rhodium nanoparticles are protected by water-soluble polymer, polyvinylpyrrolidone (PVP), these metal nanoparticles can be partially encapsulated in mesoporous silica nanoparticles' framework and homogeneously distributed in mesoporous silica supports during *in situ* the synthesis of mesoporous silica materials. At the same time, thiol group as a linker for the following reaction was covalently bonded on mesoporous silica surface during *in situ* the formation of mesoporous silica through cocondensation of 3-mercaptopropyltrimethoxysilane (STMOS) and tetraethyl orthosilicate (TEOS). After the removal of template cetyltrimethylammonium bromide(CTAB), chiral reagent, (-)-cinchonidine, was coupled with the thiol group on mesoporous silica surface and immobilized around rhodium nanoparticles therefore to modify rhodium surface to be chiral environment for the coming reactants (Figure 5-1).

This material (**MSNRhNPsCD**) was analyzed by ^{13}C and ^{29}Si CP/MAS solid state NMR spectroscopy, small angle X-ray diffraction (XRD), N_2 adsorption/desorption, thermogravimetric analysis (TGA) (see Supporting Information). The N_2 adsorption/desorption isotherms (Figure S5-2) show that the rhodium nanoparticle and cinchonidine functionalized MSN has high surface area (S_{BET} = 604 m^2/g) with a very narrow pore size distribution (D_{BJH} = 2.3 nm). Powder small angle XRD pattern (Figure S5-3) shows MSNRhNPsCD is full of highly ordered hexagonally parallel channels as pure MSN does, which was further proved by Transmission Electronic Microscopy (TEM) (Figure 5-2a). In TEM image, beside the parallel channels, some black spots could be seen allover the materials and the diameter of black spot was around 2.0 nm. STEM image of this material (Figure 5-2b), where RhNPs were shinning spots, indicates that RhNPs were distributed homogeneously through MSNRhNPsCD material and the size of RhNPs was not changed during the synthesis of material. Energy Dispersive X-ray (EDX) was used to determine the loading of Rh on MSNRhNPsCD and 1.0wt% (0.10 mmol/g) of Rh in this material was obtained basing on the atomic ratio between Si and Rh. As shown in X-ray Photoelectron Spectroscopy (XPS) (Figure 5-3a), the Rh $3d_{5/2}$ peaks (308 eV) could be fit by two peaks with bonding energies of 307.2 eV and 308.9 eV, corresponding to the metallic Rh (0) and the oxidized Rh (+3) respectively. As shown in Figure 5-3a, 88% of rhodium atoms were still metallic Rh(0) and only 12% was oxidized to Rh(+3) in the as-made MSNRhNPsCD, which

means RhNPs was quite stable through our synthesis procedure. And the oxidized Rh(+3) could be reduced by hydrogenation at room temperature easily back to metallic Rh(0) as shown in Figure 5-3b, which will be used as the catalyst in this study.

T^2 and T^3 peaks in ^{29}Si solid NMR (Figure 5-4a) indicate the incorporation of covalent linked organic functional groups in MSNRhNPsCD and the ^{13}C solid NMR (Figure 5-4b) indicates the presence of both organic functional groups and the complete removal of template-CTAB although there still has trace amount of PVP (Chemical shift at 178 ppm came from PVP's carbonyl group). Immobilized CD loading on MSNRhNPsCD was around 4.6wt% (15.5×10^{-2} mmol/g) basing on TGA results, which makes the mole ratio between CD and Rh to be 1.55.

MSNRhNPsCD was tested in the enantioselective hydrogenation of ethyl pyruvate (Scheme 5-1) which is the best prochiral substrate for metallic Rh(0) catalysts.[17,43] In order to compare the catalytic performance of MSN encapsulated RhNPs in enantioselective hydrogenation, MSNRhNPs without CD (Figure S5-5 – S5-8) and three other MSNRhNPsCDs with different CD loadings were synthesized. As shown in Figure 5-5, the chemical bound CD could increase the reactivity (TOF: turnover frequency) of RhNPs dramatically and the enantioselectivity of RhNPs quickly reach to a plateau with e.e. value around 58.0%. And these results are quite similar to that when MSNRhNPs were modified by physically adsorbed CD (Figure S5-9). And these results also suggested that the chiral modification capability of CD on Rh surface was the same after it was chemically bound MSN surface. More interestingly, in the case of MSNRhNPsCD, CD (molar ratio of CD/Rh was around 1.6) needed to reach the same enantioselectivity was less than that in the case of MSNRhNPs where molar ratio of CD/Rh was about 4.2, which prove that only adsorbed CD on Rh surface plays a role for the enantioselectivity instead of the free CD in bulk solution. As shown in Figure 5-6, both the activity and enantioselectivity of MSNRhNPsCD could be retained very well even after being recycled for more than ten times in the enantioselective hydrogenation of ethyl pyruvate, which indicated that both RhNPs and CD were very stable in MSNRhNPsCD without any leaching.

Conclusions

In summary, we have demonstrated that both metal nanoparticles and chiral modifier or reagent could be immobilized on mesoporous silica nanoparticles without losing the reactivity and enantioselectivity of the catalyst, and the catalyst could be recycled or reused with the same reactivity and selectivity as the fresh catalyst does without any additional chiral reagent supplement. Therefore, we envision that our study could serve as a new catalyst design principle for enantioselective heterogeneous catalysis of various asymmetric reactions catalyzed by metallic catalysts modified with chiral reagents.

Experimental Section

Synthesis of catalysts: Rh nanoparticles were synthesized according to reported methods with minor modification.[14,15] Typically, A 7.9 mmol/L PVP (M_w = 29,000 from Sigma-Aldrich) solution was prepared by dissolving the polymer into anhydrate ethanol. The PVP ethanolic solution was mixed with 7.1 mmol/L aqueous $RhCl_3$ (Rh, 38-40% from Strem Chemicals, Inc.) solution at room temperature, where the mole ratio between PVP and Rh^{3+} was 10.0. After reducing rhodium in ethanol, solvent was evaporated by Rotavap at 40 ^oC. The obtained black powder is named as RhNPs and its size was found around 2.0 nm with homogeneous distribution and clear crystalline structure (Figure S5-1). Under Ar, the as-made RhNPs (480.0 mg, including 40.0 mg Rh) were re-dissolved into water (10.0 mL, 0.6 mol) and mixed with water (470 mL, 26.1 mol), cetyltrimethylammonium bromide (CTAB, 2.0 g, 5.5 mmol), NaOH (7.0 mL x 2.0 mol/L, 14.0 mmol) at room temperature prior to the hydrolysis of mercaptopropyltrimethoxysilane (STMOS, 0.4 mL, 2.2 mmol) and tetraethoxyl orthosilicate (TEOS, 10.0 mL, 44.8 mmol) at 80 ^oC for 2.0 hours. After the hydrolysis, the grey solid was filtrated and dried under vacuum overnight at room temperature. Template CTAB and PVP in the as-made material were removed by methanol (300 mL) at 60 ^oC with concentrated HCl (3.0 mL) for 2 hours under Ar, followed by filtration at room temperature and washing with copious water and methanol. About 2.3 g solid material was made after it was dried at 70 ^oC under vacuum overnight. The obtained solid was stirred with excess CD

(1200 mg, 4.1 mmol) and azobisisobutyronitrile (AIBN, 50 mg) in 100 mL dry chloroform under Ar for 24 hours after it was dried at 110 ^{o}C under vacuum for 12 hours. The solid was filtrated after being cooled under to room temperature and washed with methanol until no CD can be detected by Uv-vis spectrometer. The final solid, MSNRhNPsCD with 1.0wt% Rh (including 0.1 mmol Rh/g) and 4.6wt% CD (1.55 x 10^{-2} mmol/g), was reduced by H_2 (500 psi) at room temperature in THF for 1.0 hour before the reaction. Other materials with different CD concentrations were synthesized with the same method except that different initial STMOS were used properly.

Characterizations of catalysts: Powder X-ray diffraction patterns were gotten from a Scintag XDS-2000 powder diffractometer using Cu Kα irradiation. N_2 adsorption/desorption was done with a Micromeritics ASAP 2000 sorptometer. Particle morphology was observed by using a JEOL 840A scanning electron microscope (SEM) with a 10 kV acceleration voltage. TEM images were taken on a Tecnai G2 F20 transmission electron microscope with a 200 kV acceleration voltage. EDX data was collected from IXRF EDS2004 system installed on the JEOL 840A SEM. Thermal analysis was provided with a TA Instruments (formerly DuPont) thermal analysis system with Thermo-gravimetric analysis (TGA) module. XPS was used to characterize the rhodium nanoparticles in our catalysts on a Perkin-Elmer PHI 5500 XPS spectrometer with a position-sensitive detector, a hemispherical energy analyzer in an ion-pumped chamber (evacuated to 2 x 10^{-9} Torr), and a Al Kα (BE = 1486.6 eV) X-ray source at 300 W with 15 kV acceleration voltage. For all of our experiments, the binding energy of silicon was forced to be 304.5 eV which was used as an internal standard for other elements' binding energy.

Enantioselective hydrogenation of ethyl pyruvate catalyzed by MSNRhNPsCD: MSNRhNPsCD (50 mg, including 5.0 x 10^{-3} mmol Rh) and 5.0 mL THF were charged into a 25 mL autoclave. After purged several times with hydrogen, the autoclave was pressurized to 500 psi with H_2. After 1.0 hours at room temperature with stirring, reduction of Rh was finished. 0.5 mL (5.0 mmol) ethyl pyruvate was added into the autoclave under Ar and the hydrogen was recharged into the reactor again until the pressure reached 900 psi. The reaction was started with the vigorous stirring. After 10 min, the reaction was stopped and the solution was separated by filtration and centrifuge before the supernatant was analyzed

by Varian 3900 GC with chiral capillary column (CP-ChiralSil-Dex CB, 25 m × 0.25 mm × 0.25 μm). The turnover frequency (TOF) was equal to the moles of substrates that one mole rhodium can convert to product in one minute. The enantiomeric excess is obtained as: e.e.(%) = 100 x (R-S) / (R+S).

Acknowledgment

This research was supported at Ames Laboratory by the U.S. DOE, office of BES, under contract No. DE-FG26-0NT08854.

References

(1) Heitbaum, M.; Glorius, F.; Escher, I. Angew. Chem. Int. Ed. 2006, 45, 4732-4762.
(2) Thomas, J. M.; Thomas, W. J. Principles and Practice of Heterogeneous Catalysis; Wiley-VCH: Weinheim, 1997.
(3) Chiral Reactions in Heterogeneous Catalysis; Jannes, G.; Dubois, V., Eds.; Plenum Press: New York, 1995.
(4) Chiral Catalysis Immobilization and Recycling; Vos, D. E. D.; Vankelecom, I. F. J.; Jacobs, P. A., Eds.; Wiley-VCH: Weinheim, 2000.
(5) Murzin, D. Y.; Maki-Arvela, P.; Toukoniitty, E.; Salmi, T. Catal. Rev. 2005, 47, 175-256.
(6) Baiker, A. Curr. Opin. Solid State Mater. Sci. 1998, 3, 86-93.
(7) Bein, T. Curr. Opin. Solid State Mater. Sci. 1999, 4, 85-96.
(8) Osawa, T.; Harada, T.; Takayasu, O. Top. Catal. 2000, 13, 155-168.
(9) Studer, M.; Blaser, H.-U.; Exner, C. Adv. Synth. Catal. 2003, 345, 45-65.
(10) Baiker, A. J. Mol. Catal. A 2000, 163, 205-220.
(11) Baiker, A. J. Mol. Catal. A 1997, 115, 473-493.
(12) Sípos, É.; Tungler, A.; Fogassy, G. J. Mol. Catal. A 2004, 216, 171-180.

(13) Blaser, H. U.; Jalett, H. P.; Monti, D. M.; reber, J. F.; Wehrli, J. T. Stud. Surf. Sci. Catal. 1988, 41.

(14) Huang, Y.; Chen, J.; Chen, H.; Li, R.; Li, Y.; Min, L.; Li, X. J. Mol. Catal. A 2001, 170, 143-146.

(15) Huang, Y.; Li, Y.; Hu, J.; Cheng, P.; Li, R.; Li, X.; Yip, C. W.; Chan, A. S. C. J. Mol. Catal. A 2002, 189, 219-224.

(16) Hess, R.; Krumeich, F.; Mallat, T.; Baiker, A. J. Mol. Catal. A 2004, 212, 205-209.

(17) Sonderegger, O. J.; Ho, G. M.-W.; Burgi, T.; Baiker, A. J. Catal. 2005, 230, 499-506.

(18) Handbook of Heterogeneous Catalysis; Ertl, G.; Knozinger, H.; Weitkamp, J., Eds.; Wiley-VCH: New York, Weinheim, 1997.

(19) Geus, J. W.; Ween, J. A. R. v. In Catalysis: An Integrated Approach to Homogeneous, Heterogeneous and Industrial Catalysis; Moulijn, J. A., Leeuwen, P. W. N. M. v., Santen, R. A. v., Eds.; Elsevier: Amsterdam, 1993, p Chapter 9.

(20) Hayek, K.; Kramer, R.; Paal, Z. Appl. Catal. A 1997, 162, 1.

(21) Fukuoka, A.; Higashimoto, N.; Sakamoto, Y.; Inagaki, S.; Fukushima, Y.; Ichikawa, M. Top. Catal. 2002, 18, 73.

(22) Yang, C.-M.; Liu, P.-H.; Chiu, C.-Y.; Chao, K.-J. Chem. Mater. 2003, 15, 275-280.

(23) Dekany, G. S. A. M. A. K. I. J. Mater. Chem. 2005, 15, 2462-2469.

(24) Zuo, X.; Liu, H.; Liu, M. Tetrahedron Lett. 1998, 39, 1941-1944.

(25) Zuo, X.; Liu, H.; Guo, D.; Yang, X. Tetrahedron 1999, 55, 7787-7804.

(26) Zuo, X.; Liu, H.; Tian, J. J. Mol. Catal. A 2000, 157, 217-224.

(27) Collier, P. J. I., Jonathan A.; Whyman, Robin; Hall, Tracey J.; Iggo, Jonathan A.; Johnston, Peter; Anton Slipszenko, J.; Wells, Peter B. Chem. Commun. 1998, 1451-1452.

(28) Collier, P. J. I., Jonathan A.; Whyman, Robin J. Mol. Catal. A 1999, 146, 149-157.

(29) Song, H.; Rioux, R. M.; Hoefelmeyer, J. D.; Komor, R.; Niesz, K.; Grass, M.; Yang, P.; Somorjai, G. A. J. Am. Chem. Soc. 2006, 128, 3027 - 3037.

(30) Tungler, A.; Máthé, T.; Fodor, K.; Sheldon, R. A.; Gallezot, P. J. Mol. Catal. A 1996, 108, 145-151.

(31) Schürch, M.; Thomas Heinz; Aeschimann, R.; Mallat, T.; Pfaltz, A.; Baiker, A. J. Catal. 1998, 173, 187-195.

(32) Diezi, S.; Mallat, T.; Szabo, A.; Baiker, A. J. Catal. 2004, 228, 162-173.

(33) Orglmeister, E.; Mallat, T.; Baiker, A. J. Catal. 2005, 233, 333-341.

(34) Heinz, T.; Wang, G.; Pfaltz, A.; Minder, B.; Schürch, M.; Mallat, T.; Baiker, A. J. Chem. Soc., Chem. Commun. 1995, 1421-1422.

(35) Solladié-Cavallo, A.; Marsol, C.; Garin, F. Tetrahedron Lett. 2002, 43, 4733-4735.

(36) Orglmeister, E.; Mallat, T.; Baiker, A. Adv. Synth. Catal. 2005, 347, 78-86.

(37) Chen, H.-T., Huh, S., Wiench, J. W., Pruski, M., Lin, V. S.-Y. J. Am. Chem. Soc. 2005, 127, 13305-13311.

(38) Huh, S.; Chen, H.-T.; Wiench, J. W.; Pruski, M.; Lin, V. S.-Y. Angew. Chem. Int. Ed. 2005, 44, 1826-1830.

(39) Huh, S.; Wiench, J. W.; Yoo, J.-C.; Pruski, M.; Lin, V. S.-Y. Chem. Mater. 2003, 15, 4247-4256.

(40) Huh, S.; Chen, H.-T.; Wiench, J. W.; Pruski, M.; Lin, V. S.-Y. J. Am. Chem. Soc. 2004, 126, 1010-1011.

(41) Lin, V. S.-Y.; Radu, D. R.; Han, M.-K.; Deng, W.; Kuroki, S.; Shanks, B. H.; Pruski, M. J. Am. Chem. Soc. 2002, 124, 9040-9041.

(42) Radu, D. R.; Lai, C.-Y.; Huang, J.; Shu, X.; Lin, V. S.-Y. Chem. Commun. 2005, 1264-1266.

(43) Mallat, T.; Orglmeister, E.; Baiker, A. Chem. Rev. 2007, 107, 4803-4890.

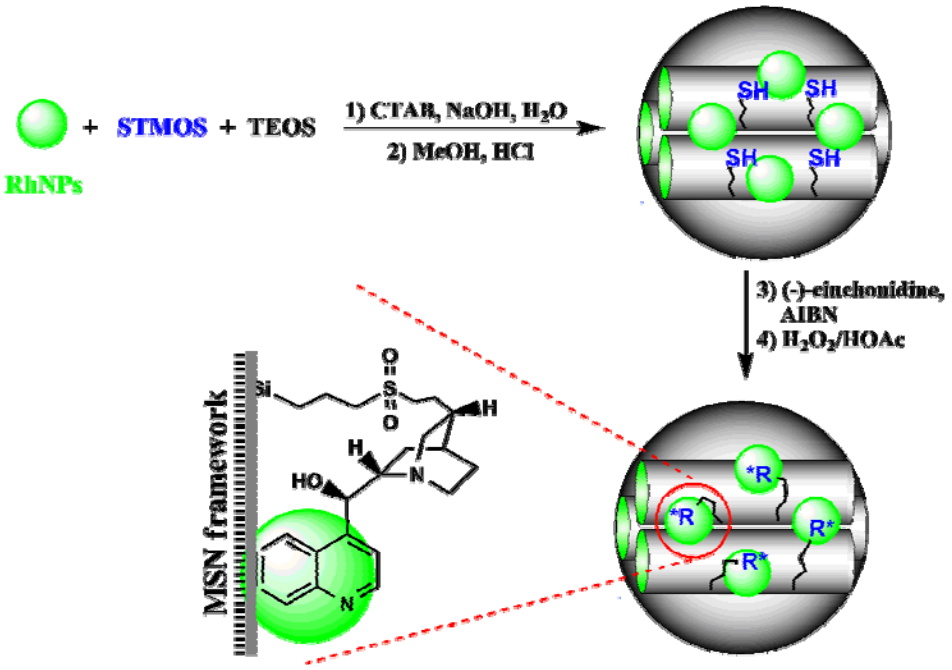

Figure 5-1. Synthesis of mesoporous silica nanoparticles which was functionalized by monodispersed rhodium nanoparticles and tethered (-)-cinchonidine (**MSNRhNPsCD**).

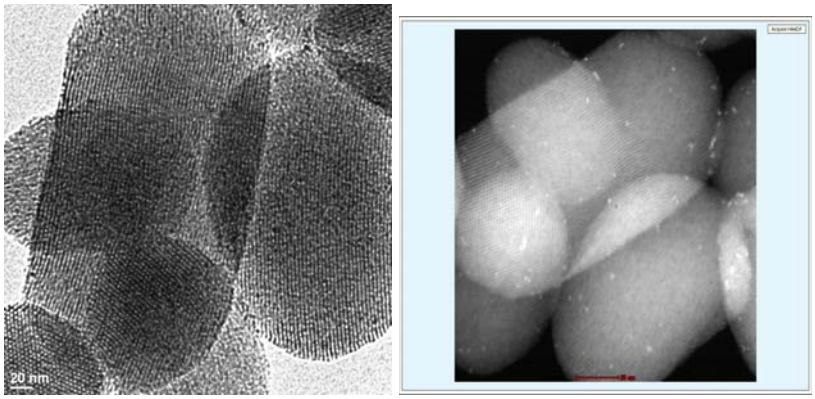

(a) (b)

Figure 5-2. TEM image (a) and STEM image (b) of MSNRhNPsCD.

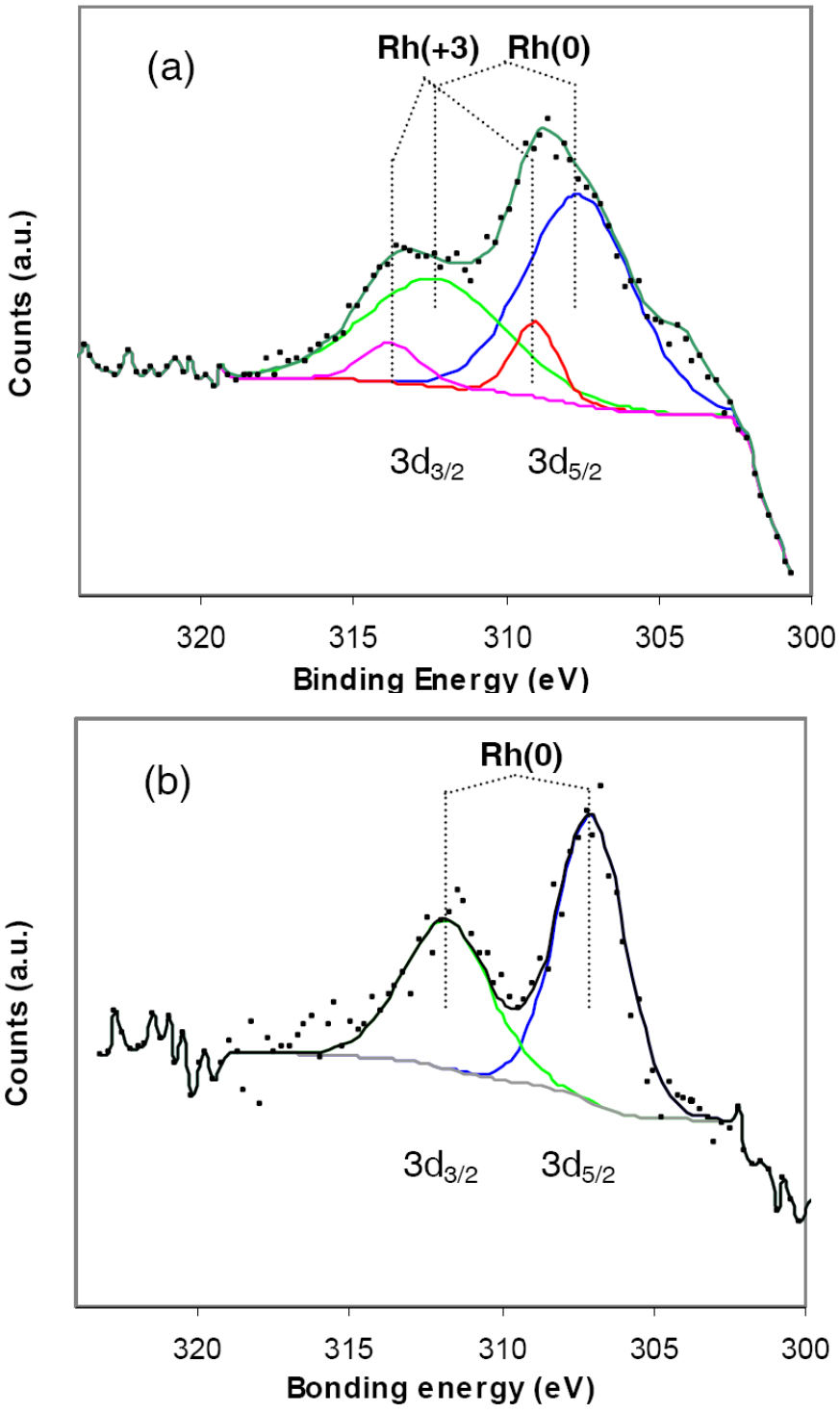

Figure 5-3. XPS of as-made MSNRhNPsCD (a) and reduced MSNRhNPsCD (b).

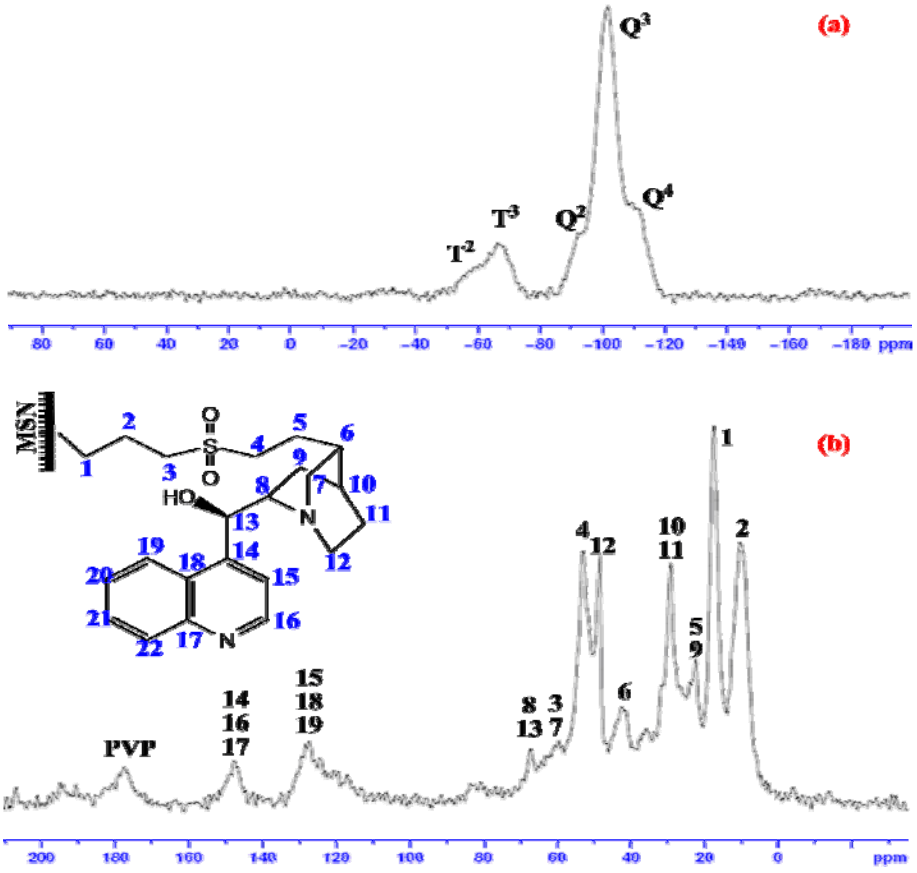

Figure 5-4. ^{29}Si (a) and ^{13}C (b) solid state NMR spectra of MSNRhNPsCD.

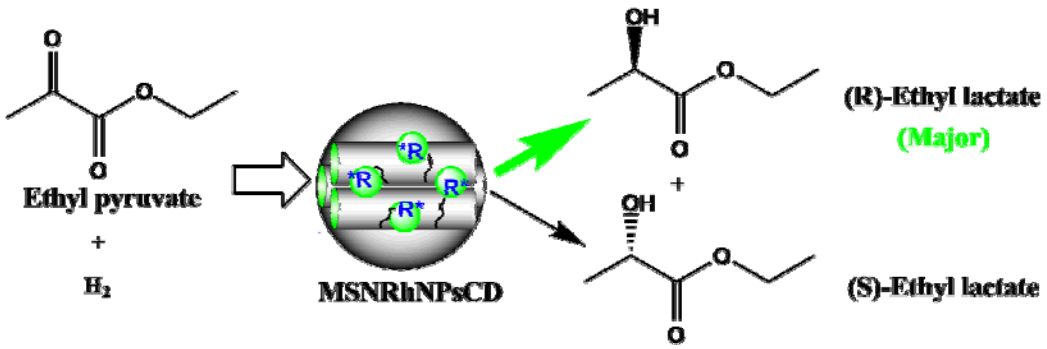

Scheme 5-1. Enantioselective hydrogenation of ethyl pyruvate catalyzed by MSNRhNPsCD.

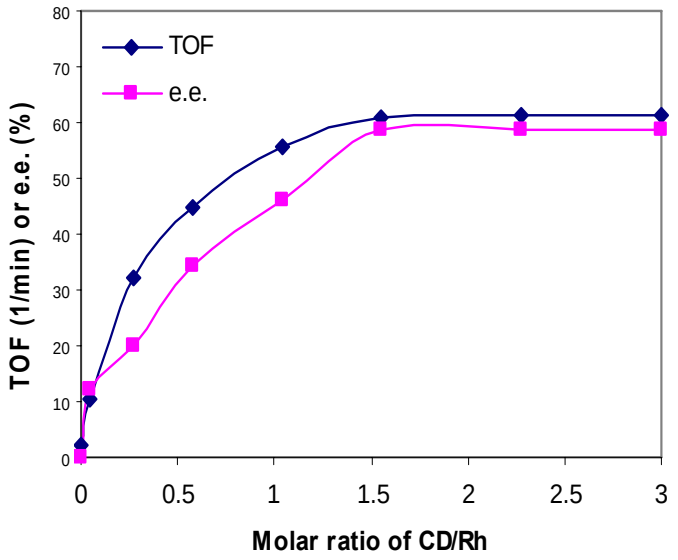

Figure 5-5. Effect of molar ratio between CD and Rh on enantioselective hydrogenation of ethyl pyruvate catalyzed by MSNRhNPsCD with different CD loading.

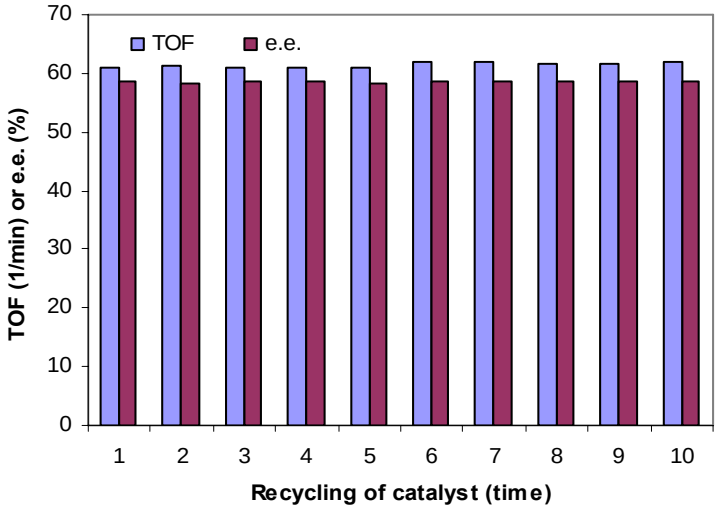

Figure 5-6. Recycling of MSNRhNPsCD in enantioselective hydrogenation of ethyl pyruvate.

Supporting Information

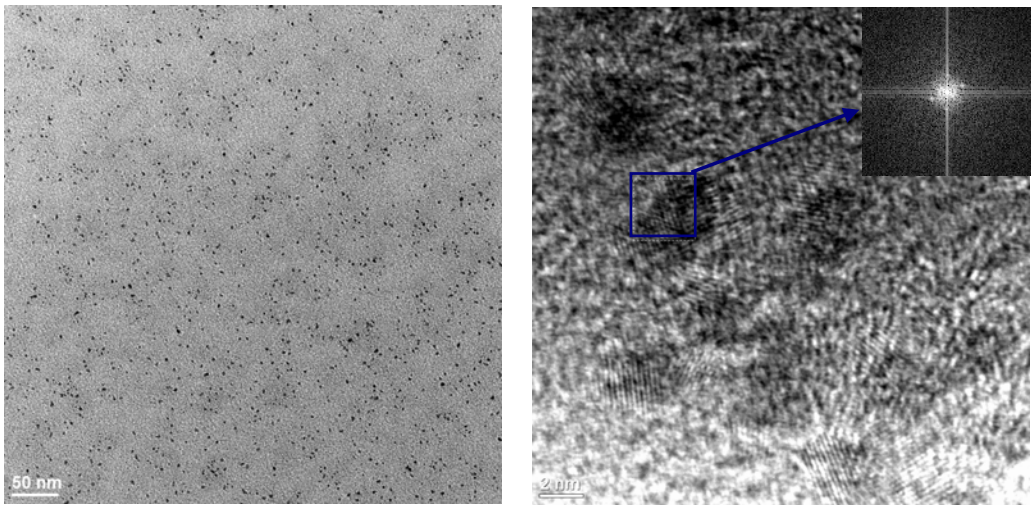

(a) (b)

Figure S5-1. TEM image (a) and HRTEM image (b) of rhodium nanoparticles (RhNPs).

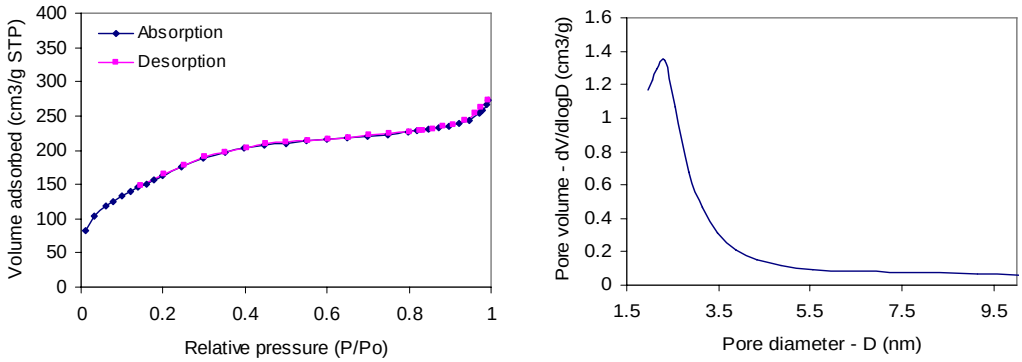

Figure S5-2. BET isotherms and BJH pore size distribution curve of MSNRhNPsCD.

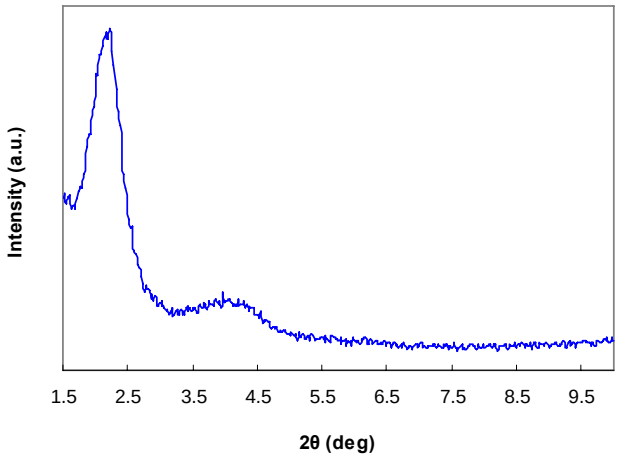

Figure S5-3. XRD of MSNRhNPsCD.

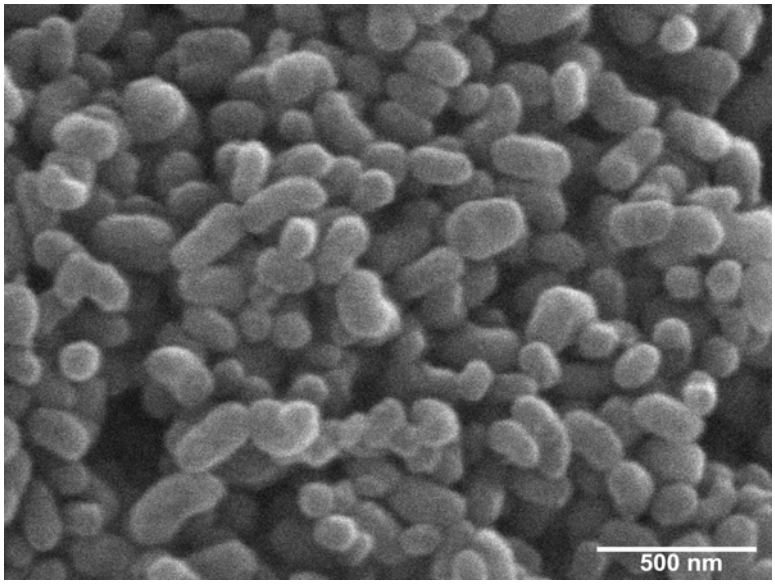

Figure S5-4. SEM image of MSNRhNPsCD.

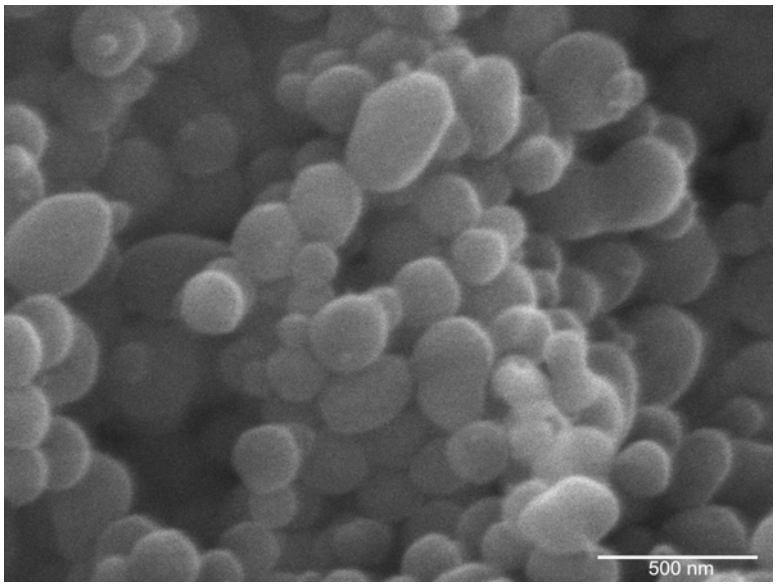

Figure S5-5. SEM image of MSNRhNPs.

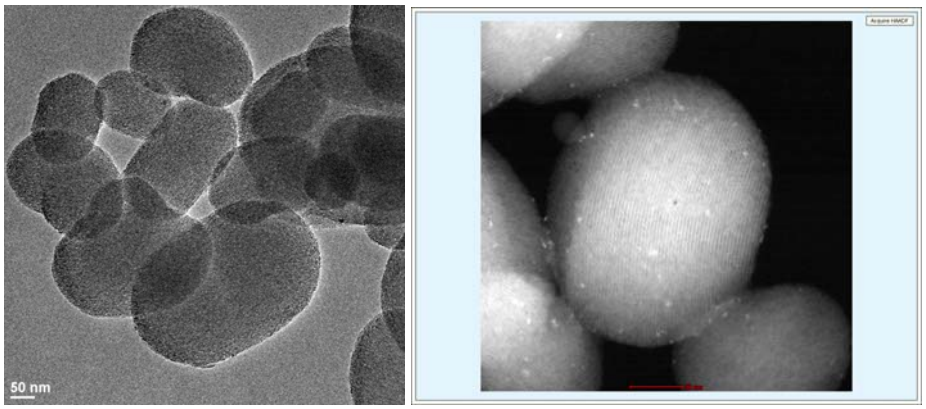

Figure S5-6. TEM image(left) and STEM image (right) of MSNRhNPs.

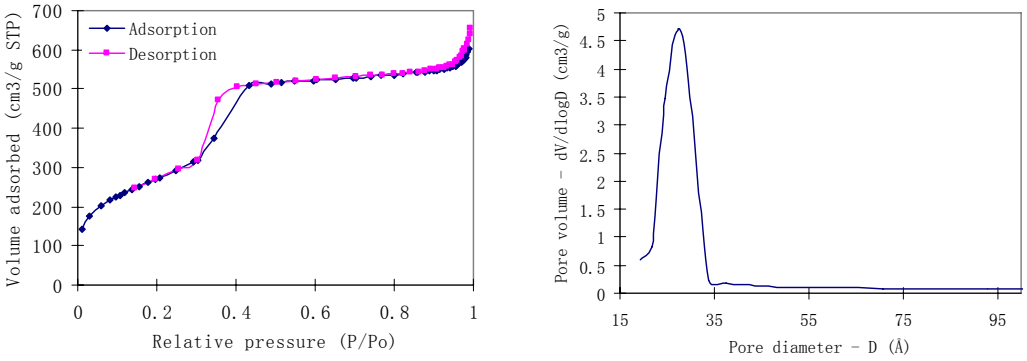

Figure S5-7. BET isotherms and BJH pore size distribution curve of MSNRhNPs (S_{BET} = 990 m^2/g, D_{BJH} = 2.5nm).

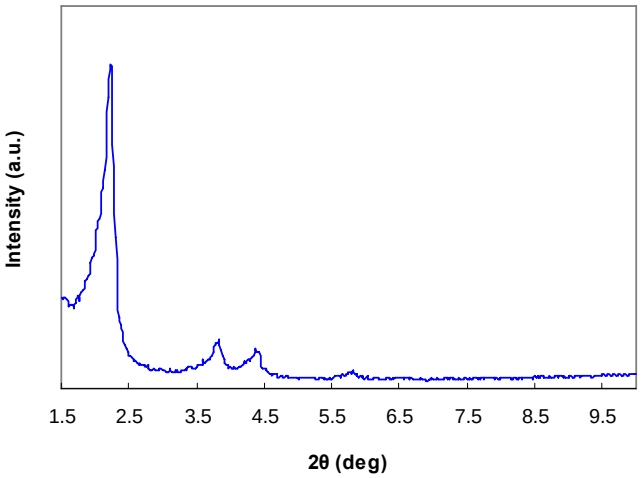

Figure S5-8. XRD of MSNRhNPs.

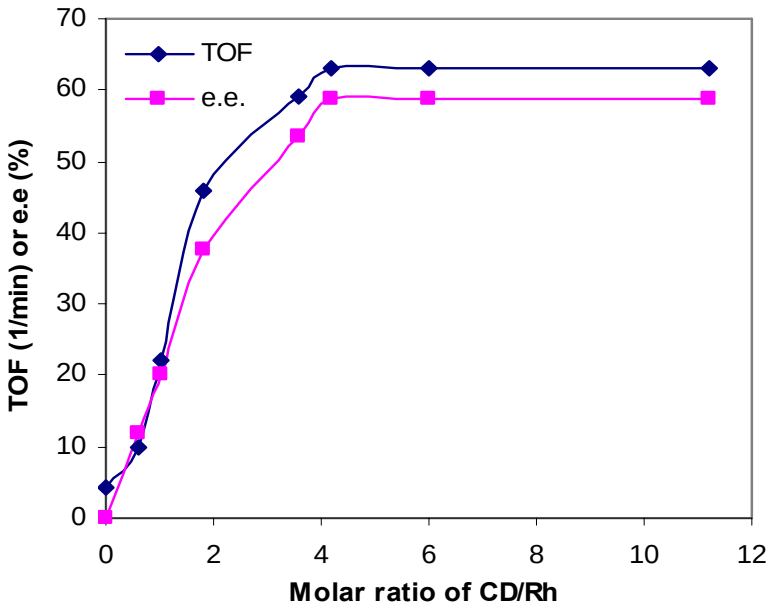

Figure S5-9. CD/Rh effects on enantioselective hydrogenation of ethyl pyruvate catalyzed by MSNRhNPs materials with adsorbed CD.

CHAPTER 6. ASYMMMETRIC HYDROGENATION CATALYZED BY A WILKINSON TYPE OF ACHIRAL RHODIUM CATALYST SUPPORTED ON AN ORGANICALLY FUNCTIONALIZED MESOPOROUS SILICA NANOPARTICLE

A paper submitted to *Chemical Communications*

Yulin Huang, Jennifer L. Rapp, Shu Xu, Marek Pruski, Victor S.-Y. Lin*

Department of Chemistry, U.S. Department of Energy Ames Laboratory, Iowa State University, Ames, Iowa 50011-3111

**Corresponding author.*

Abstract

A Wilkinson-type achiral rhodium(I)-phosphine complex was covalently tethered on the surface of highly ordered, MCM-41 type mesoporous silica nanoparticles surface to yield a RhPMSN material. Interestingly, we discovered that these achiral RhPMSN particles could serve as efficient heterogeneous catalysts for the asymmetric hydrogenation of ethyl pyruvate to ethyl lactate. We demonstrated that the enantioselectivity of this reaction could be induced and tuned by introducing different concentrations of a chiral molecule, (-)-cinchonidine (CD), to the mesopores of RhPMSN in THF. The RhPMSN/CD catalytic system gave rise to a turnover frequency (TOF) of 37 h^{-1} and 50% enantiomeric excess (e.e.) for the (*R*)-ethyl lactate product in the presence of only 1.6 mM of CD. In contrast, the homogeneous counterpart, $RhCl(TPP)_3$, yielded a TOF of 31 h^{-1} with no enantioselectivity even when a high concentration (21 mM) of CD introduced to the THF solution. To investigate whether this unprecedented chiral induction effect depends on the structural uniformity of MSN solid support, we immobilized the same rhodium-phosphine catalyst on the surface of an amorphous silica material (RhPNPS). Under the same reaction condition with CD as the chiral additive, only 14.3% e.e. for the (*R*)-ethyl lactate product was obtained, while the TOF only reached to 9.5 h^{-1}. These results support that the observed induction of enantioselectivity depends on how these chiral CD molecules aggregate on the surface of solid support around

the catalytic functionality. We envision that our study could serve as a new design principle for heterogeneous catalysis of various asymmetric reactions.

Introduction

The rapidly growing demand in chemical and pharmaceutical industries for optically pure compounds and their limited natural resources have led to an increasing interest in asymmetric catalysis.[1] To date, the field of asymmetric catalysis has been dominated by homogeneous asymmetric catalysis with transition metal-chiral ligand complexes because of their high activities and excellent enantioselectivities for various reactions.[2] However, the advantages of heterogeneous catalysis,[3] such as easy separation, efficient recycling, and superior control of handling and processing, have inspired researchers worldwide to design various materials for stereoselective catalysis on solid surfaces.

Literature-reported asymmetric heterogeneous catalyst systems mostly took advantage of surface-immobilized chiral organometallic complexes[4-6] and chiral agents adsorbed transition metal particles.[4,7-9] Most catalytic systems of surface-immobilized chiral organometallic complexes were based on those well-studied homogeneous transition metal complex catalysts that exhibit both high enantioselectivity and reactivity. These selected complexes with chiral first coordination environment were then immobilized onto some insoluble supports by adsorption, encapsulation, or tethering using a covalent bond and/or electrostatic interaction.[6,10]

In contrast to these synthetic asymmetric catalysts with chiral ligands, many enzymes could achieve very high enantioselectivity and reactivity by arranging an achiral catalytic functional group in conjunction with nearby chiral residues in the three-dimensionally controlled active site. Apparently, the success of transferring this biological design principle to artificial catalytic systems hinges upon the ability to spatially organize chiral moieties three-dimensionally around the achiral catalyst in a close proximity and orientation. Recently, a series of enantioselective Aza-Baylis-Hillman reactions catalyzed by an achiral catalyst in homogenous medium of pure chiral agents was reported.[11] Also, recent demonstrations on the matrix enhancement effect on the asymmetric catalysis induced by the

immobilization of chiral organometallic catalysts inside of structurally ordered mesoporous silicas[12,13] further highlighted the potential of this kind of biomimetic approach for designing effective heterogeneous enantioselective catalysts.

Results and Discussions

Herein, we report on the synthesis of an asymmetric hydrogenation catalytic system, where a Wilkinson-type achiral rhodium(I)-phosphine complex was covalently tethered on the surface of highly ordered, MCM-41 type mesoporous silica nanoparticles surface (**RhPMSN**). Interestingly, also for the first time, we demonstrated that the enantioselectivity of the hydrogenation of ethyl pyruvate could be induced and tuned by introducing different concentrations of a chiral molecule, (-)-cinchonidine (**CD**), to the mesopores of RhPMSN. In contrast, no enantioselectivity could be observed in homogeneous solutions of same concentrations of Wilkinson's catalyst ($RhCl(TPP)_3$, TPP: triphenylphosphine) and CD as depicted in Figure 6-1.

To ensure the homogeneous distribution of the rhodium-phosphine complex catalyst on the mesoporous silica surface, we first synthesized a 2-(diphenylphosphino)-ethyltriethoxy-functionalized, MCM-41 type mesoporous silica nanoparticle (PMSN) via a co-condensation method that we had previously developed and reported.[14-20] The experimental procedures for the synthesis and characterization of PMSN are detailed in the Supporting Information (SI). $[RhCl(COD)_2]_2$ (130.8 mg, 0.26 mmol) was added to a 20 mL THF suspension of PMSN (1.0 g) at room temperature and stirred under argon for 12 h. The resulting yellow solid was isolated by filtration, washed with excess THF, and dried at 90 °C under vacuum to yield the rhodium(I)-phosphine complex-functionalized RhPMSN material. The structure of RhPMSN was characterized by powder X-ray diffraction measurement, N_2 sorption analysis, and transmission electronic microscopy (TEM) as detailed in SI. Our results indicated that RhPMSN is comprised of short rod-shaped particles of 200 nm with a typical MCM-41 type of hexagonally packed, channel-like mesoporous structure with a total surface area of ca. 800 m^2/g and an average BJH pore diameter of ca. 2.4 Å. These results were further confirmed by the images of TEM (Figure 6-2a) and scanning electronic microscopy (SEM) (Figure S6-8). As described in SI, the amounts of phosphine and rhodium

were measured to be ca. 0.78 mmol/g and 0.25 mmol/g, respectively (P/Rh = 3.1) by energy dispersive X-ray (EDX). The distinct peak at 39.5 ppm of the ^{31}P solid-state NMR spectrum of RhPMSN confirmed the coordination bond of Rh-P suggesting the catalytic group is indeed a Wilkinson-type rhodium-phosphine complex.

To investigate whether RhPMSN could effectively catalyze the asymmetric hydrogenation of ethyl pyruvate in the presence of different amounts of CD, RhPMSN (20.0 mg, containing 5.0 μmol Rh) was added to a 10 mL THF solution of ethyl pyruvate (1.0 mmol) with different concentrations (0 to 21 mM) of CD. The reaction mixture was pressurized to 300 psi with H_2 at 40 °C. After 6 h, the products were isolated and analyzed. To compare the catalytic property of RhPMSN with that of the Wilkinson catalyst in homogeneous solution, we examined the hydrogenation of ethyl pyruvate catalyzed by $RhCl(TPP)_3$ (5.0 mg, 5.0 μmol) with CD (0 to 21 mM) in THF under the same reaction condition. As shown in Figure 3a, the reactions catalyzed by RhPMSN/CD and $RhCl(TPP)_3$/CD gave very different results in terms of enantioselectivity. In the case of $RhCl(TPP)_3$/CD, a turnover frequency (TOF) of 31 h^{-1} was observed with no enantioselectivity even when we introduced a high concentration (21 mM) of CD in THF. In contrast, the MSN-immobilized counterpart, RhPMSN/CD, gave rise to a TOF of 37 h^{-1} and 50% enantiomeric excess (e.e.) for the (*R*)-ethyl lactate product with only 1.6 mM of CD introduced in solution. The MSN surface-adsorbed CD (ca. 0.05 mmol/g) was measured by the thermogravimetric analysis (TGA) of RhPMSN/CD after reaction as described in the SI (Figure S6-12 and S6-13). This result indicated that the surface coverage of CD is approximately 6.4% when the e.e. reached to the maximum level (Scheme S6-1).

While more CD could be adsorbed by the RhPMSN material as shown in Figure 3b and S11, the e.e. did not further increased (Figure 6-3a and S6-13). Both the TOF and enantioselectivity of RhPMSN/CD leveled at 35 h^{-1} and 22% e.e., respectively, when the solution concentration of CD exceeded 6.5 mM, i.e., 0.11 mmol/g of CD (14.1% surface coverage) was adsorbed by RhPMSN. As shown in the ^{31}P solid-state NMR spectra (Figure 2b and c), the chemical shifts of the free phosphine linker (-12.0 ppm) and the rhodium-phosphine complex (+39.5 ppm) on the surface of RhPMSN were not altered after the hydrogenation reaction in the presence of CD. This result strongly suggested that the

observed enantioselectivity in the RhPMSN/CD system was not induced by the ligand exchange between the surface-bound phosphine linker and the solution CD. Therefore, it is reasonable to hypothesize that the surface-adsorption of CD in the mesoporous silica channels of MSN was responsible for the observed enantioselectivity. As shown in Figure 6-3a and discussed previously, the degree of e.e. was affected by the concentration of CD. Apparently, the enantioselectivity of RhPMSN is dictated by the self-assembled surface adsorption of CD in the structurally ordered, porous cavity of MSN for creating an efficient chiral environment around the rhodium-phosphine complex for the asymmetric hydrogenation.

To investigate whether this unprecedented chiral induction effect depends on the structural uniformity of MSN solid support, we immobilized the same rhodium-phosphine catalyst on the surface of an amorphous silica material (RhPNPS) with the BET total surface area of 60 m^2/g. Under the same reaction condition with CD as the chiral additive, only 14.3% e.e. for the (*R*)-ethyl lactate product was obtained (Figure 6-3a), while the TOF only reached to 9.5 h^{-1}. Also, only a small quantity (< 0.03 mmol/g) of CD was adsorbed by RhPNPS (Figure 6-3b). These results further support that the observed induction of enantioselectivity indeed depends on how these chiral CD molecules aggregate on the surface of solid support around the catalytic functionality.

Conclusions

While the detailed mechanism for the surface adsorption and conformational arrangement of CD molecules on the mesoporous surface of RhPMSN are still under investigation, we have demonstrated that the enantioselectivity of the hydrogenation of ethyl pyruvate catalyzed by the achiral RhPMSN material could be induced and tuned by introducing a surface-adsorbing chiral agent, (-)-cinchonidine. We envision that our study could serve as a new design principle for heterogeneous catalysis of various asymmetric reactions.

Acknowledgment

This research was supported at by the Office of Basic Energy Science, U.S. Department of Energy, under the contract No. DE-AC02-07CH11358.

Reference

(1) Noyori, R. *Asymmetric Catalysis in Organic Synthesis*; Wiley & Sons: New York, **1994**.

(2) *Catalytic asymmetric synthesis*; Ojima, I., Ed.; Wiley-VCH: New York, **2000**.

(3) Thomas, J. M.; Thomas, W. J. *Principles and Practice of Heterogeneous Catalysis*; Wiley-VCH: Weinheim, **1997**.

(4) Baiker, A. *Curr. Opin. Solid State Mater. Sci.* **1998**, *3*, 86-93.

(5) Murzin, D. Y.; Maki-Arvela, P.; Toukoniitty, E.; Salmi, T. *Catal. Rev.* **2005**, *47*, 175-256.

(6) McMorn, P.; Hutchings, G. J. *Chem. Soc. Rev.* **2004**, *33*, 108 - 122.

(7) Bein, T. *Curr. Opin. Solid State Mater. Sci.* **1999**, *4*, 85-96.

(8) *Chiral Catalysis Immobilization and Recycling*; Vos, D. E. D.; Vankelecom, I. F. J.; Jacobs, P. A., Eds.; Wiley-VCH: Weinheim, **2000**.

(9) Mallat, T.; Orglmeister, E.; Baiker, A. *Chem. Rev.* **2007**, *107*, 4803-4890.

(10) Heitbaum, M.; Glorius, F.; Escher, I. *Angew. Chem. Int. Ed.* **2006**, *45*, 4732-4762.

(11) Gausepohl, R.; Buskens, P.; Kleinen, J.; Bruckmann, A.; Lehmann, C. W.; Klankermayer, J.; Leitner, W. *Angew. Chem. Int. Ed.* **2006**, *45*, 3689-3692.

(12) Jones, M. D.; Raja, R.; Thomas, J. M.; Johnson, B. F. G.; Lewis, D. W.; Rouzaud, J.; Harris, K. D. M. *Angew. Chem. Int. Ed.* **2003**, *42*, 4326-4331.

(13) Thomas, J. M.; Raja, R. *Acc. Chem. Res.* **2008**, *41*, 708-720.

(14) Dufaud, V.; Beauchesne, F.; Bonneviot, L. *Angew. Chem. Int. Ed.* **2005**, *44*, 3475-3477.

(15) Chen, H.-T., Huh, S., Wiench, J. W., Pruski, M., Lin, V. S.-Y. *J. Am. Chem. Soc.* **2005**, *127*, 13305-13311.

(16) Huh, S.; Chen, H.-T.; Wiench, J. W.; Pruski, M.; Lin, V. S.-Y. *Angew. Chem. Int. Ed.* **2005**, *44*, 1826-1830.

(17) Huh, S.; Wiench, J. W.; Yoo, J.-C.; Pruski, M.; Lin, V. S.-Y. *Chem. Mater.* **2003**, *15*, 4247-4256.

(18) Huh, S. C., H.-T.; Wiench, J. W.; Pruski, M.; Lin, V. S.-Y. *J. Am. Chem. Soc.* **2004**, *126*, 1010-1011.

(19) Radu, D. R.; Lai, C.-Y.; Huang, J.; Shu, X.; Lin, V. S.-Y. *Chem. Commun.* **2005**, 1264-1266.

(20) Lin, V. S.-Y.; Radu, D. R.; Han, M.-K.; Deng, W.; Kuroki, S.; Shanks, B. H.; Pruski, M. *J. Am. Chem. Soc.* **2002**, *124*, 9040-9041.

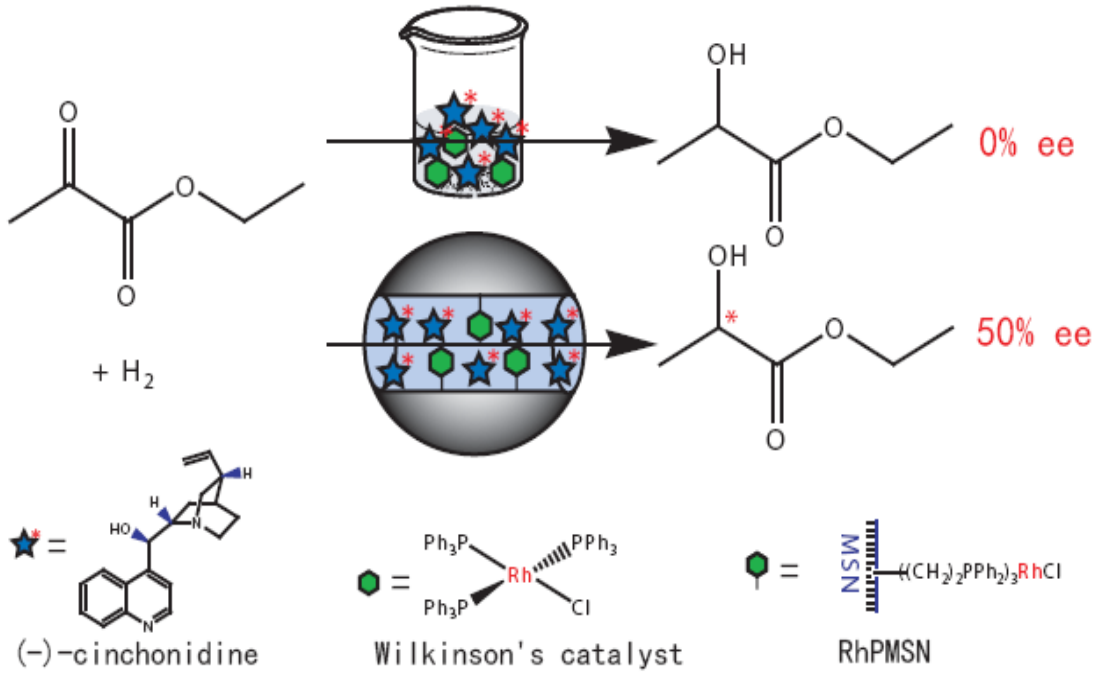

Figure 6-1. Schematic representation of asymmetric hydrogenation of ethyl pyruvate catalyzed by homogeneous $RhCl(TPP)_3$/CD and heterogeneous RhPMSN/CD systems.

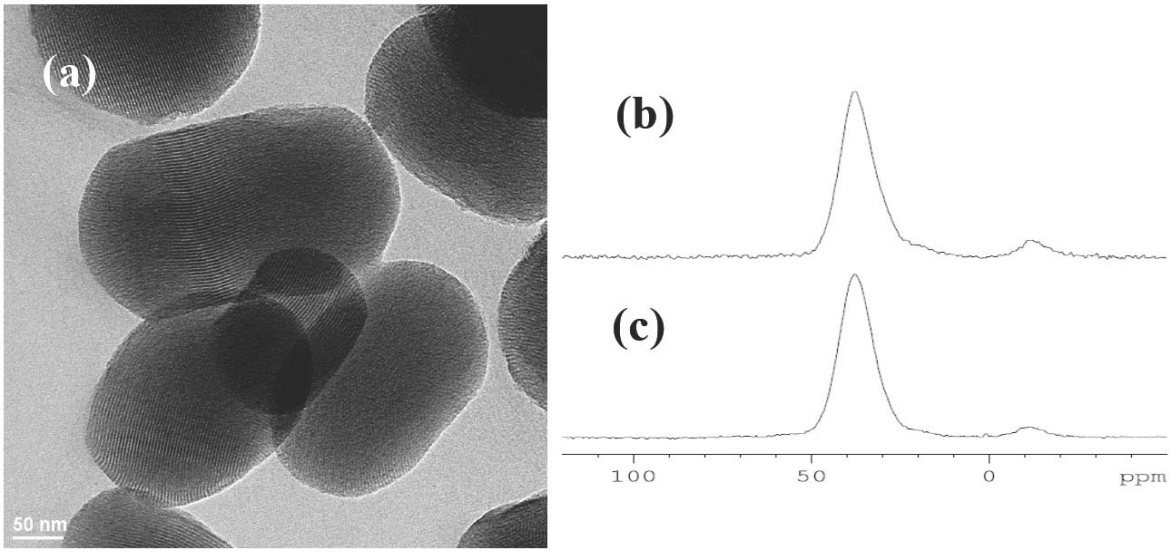

Figure 6-2. **(a)** Transmission electron micrograph of **RhPMSN** and ^{31}P solid-state NMR of **RhPMSN** before **(b)** and after **(c)** reaction

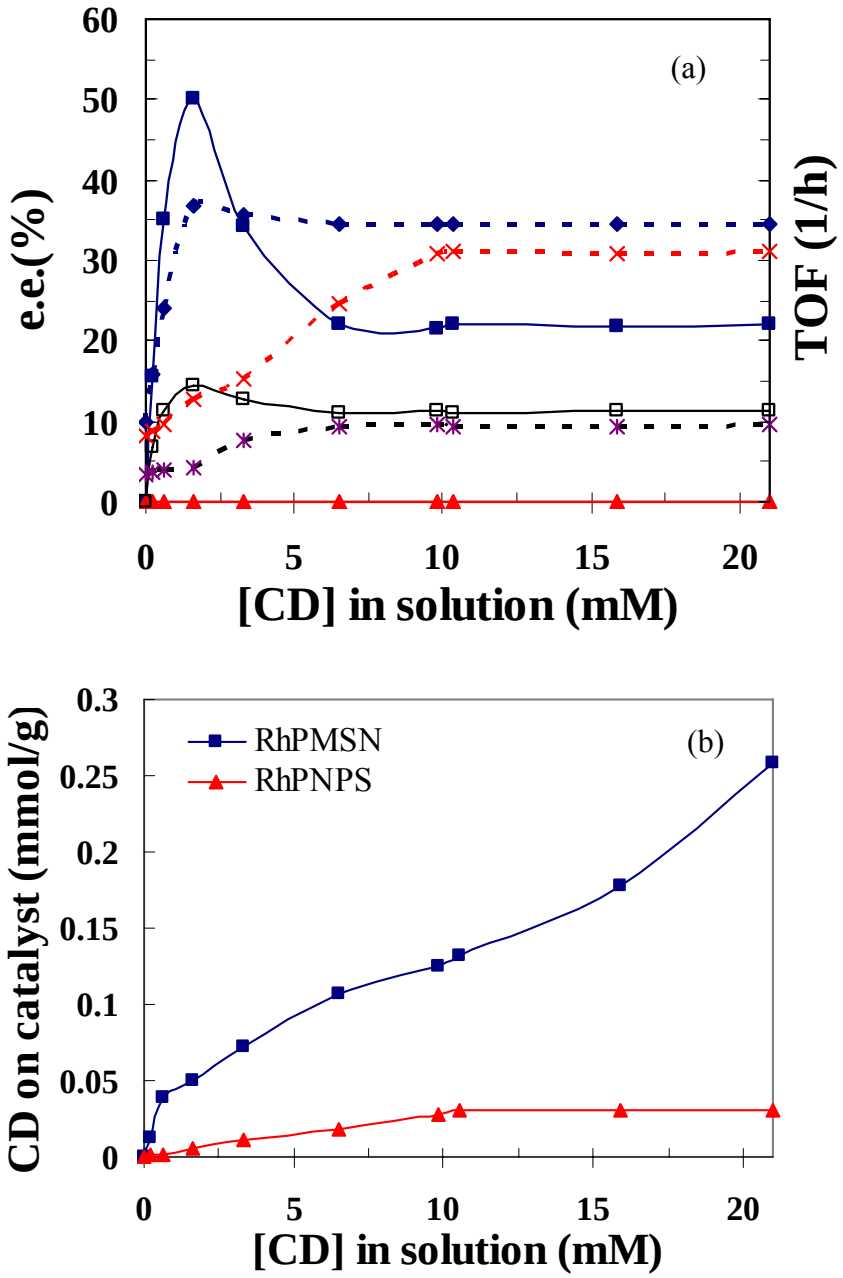

Figure 6-3. **(a)** Comparison of enantioselectivities of RhPMSN/CD and $RhCl(TPP)_3$/CD in hydrogenation of ethyl pyruvate (■: e.e. of RhMSN/CD, ▲: e.e. of $RhCl(TPP)_3$/CD, ◆: TOF of RhMSN/CD, x: TOF of $RhCl(TPP)_3$/CD, □: TOF of RhPNPS/CD, *: e.e. of RhPNPS/CD). **(b)** Comparison of adsorbed CD on RhPMSN and RhPNPS.

Supporting Information

1. Synthesis of phosphine-functionalized mesoporous silica nanoparticles (PMSN)

In order to distribute the functional group homogeneously on the mesoporous silica surface, co-condensation method was used. All the following reactions and manipulations were carried out under argon. A mixture of CTAB (2.0 g, 5.49 mmol), 2.0 M of NaOH (aq) (7.0 mL, 14.0 mmol) and H2O (480 g, 26.67 mol) was heated at 80 ºC for 30 min. To this clear solution, TEOS (9.34 g, 44.8 mmol) and 2-(diphenylphosphino)ethyltriethoxysilane (1.0 mL, 3.0 mmol) were added rapidly via injection, yielding an opaque reaction mixture. The white solid products of synthesis were observed after vigorous stirring of the mixture for ~2 min. The as-synthesized phosphine-functionalized mesoporous materials were obtained after additional 2 hours of heating at 80 ºC, followed by hot filtration, washing with excess of water and methanol, and drying under vacuum. An acid extraction of the CTAB surfactant was performed at 60 ºC, by placing 1.0 g of the as-synthesized material in a mixture of methanol (100 mL) and hydrochloric acid (0.5 mL) for 6 h. The resulting surfactant-removed solid products were filtered and washed with excess water and methanol and then dried under vacuum for several hours at 90 ºC. The highly ordered mesoporous structure of PMSN was characterized by nitrogen sorption isotherms (BET surface area: 827.1 m^2/g, pore size: 2.3 nm) (Figure S6-1), powder X-ray diffraction (XRD) (Figure S6-2), scanning electron microscopy (SEM) (Figure S6-3), and transmission electron microscopy (TEM)(Figure S6-4). The amount of phosphine in PMSN was determined by energy dispersive X-ray (EDX) and was around 0.80 mmol per gram particle. ^{31}P solid-state NMR (Figure S6-5) proved that most of the phosphine ligands on PMSN material are still P(+3) whose chemical shift is around -12.0 ppm and the oxidation of phosphine (P(+5), +33.0 ppm) was very limited here through our synthesis of this material.

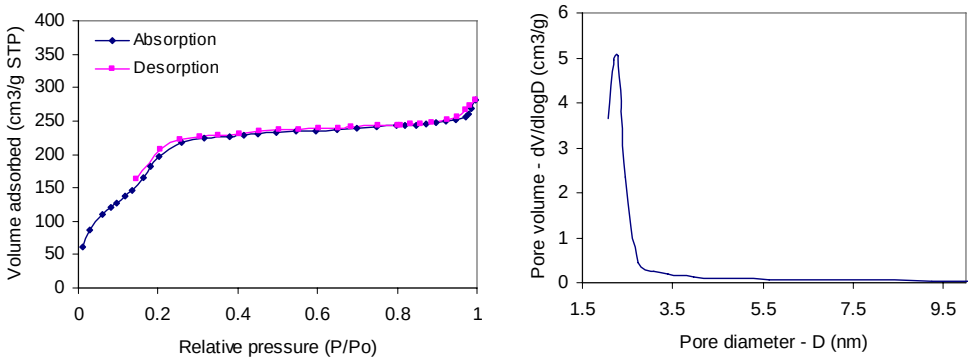

Figure S6-1. BET isotherms and BJH pore size distribution curve of PMSN.

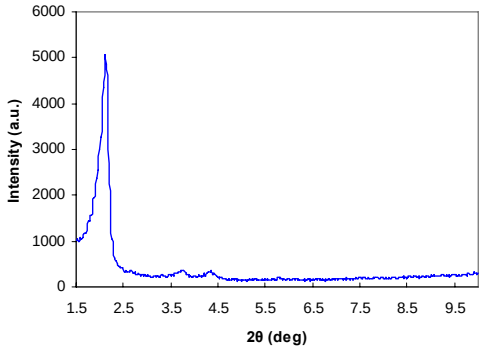

Figure S6-2. XRD of PMSN.

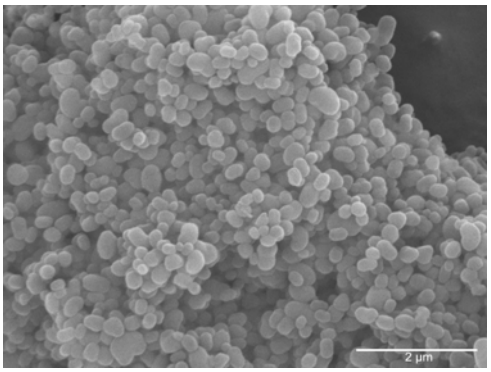

Figure S6-3. SEM image of PMSN.

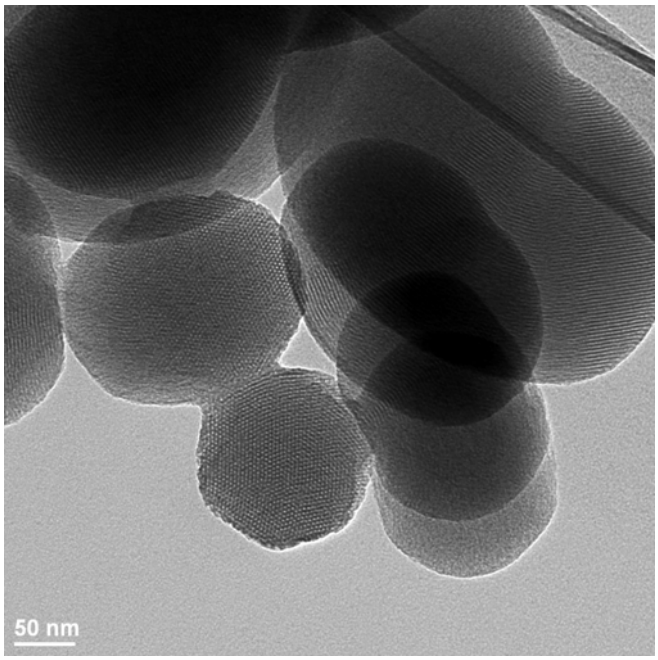

Figure S6-4. TEM image of PMSN.

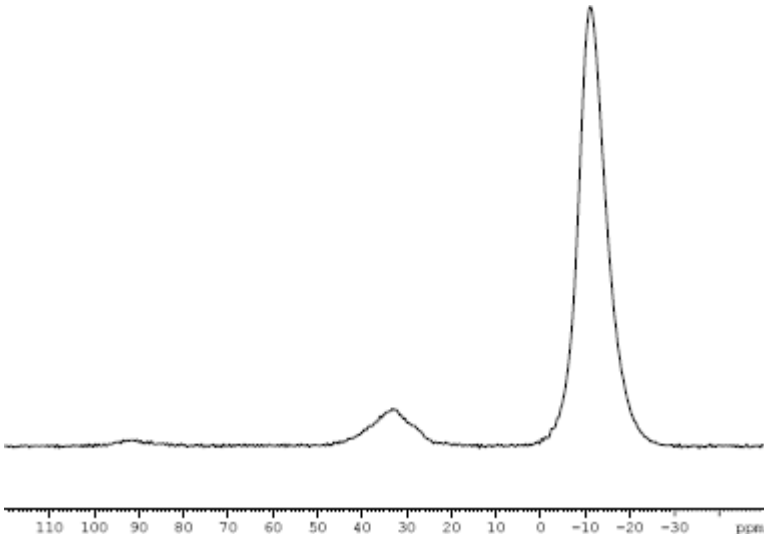

Figure S6-5. ^{31}P solid-sate NMR spectrum of PMSN.

2. Synthesis of catalyst RhPMSN

Under argon, $[RhCl(COD)_2]_2$ (130.8 mg, 0.26 mmol) was stirred with 1.0 g PMSN (including 0.80 mmol phosphine ligand) in 20 mL THF at room temperature overnight. The produced yellow solid was separated by filtration, washed with excess THF, and dried at 90 ^{o}C under vacuum for several hours. The mesoporous structure of RhPMSN was characterized

by nitrogen sorption isotherms (BET surface area: 813.7 m^2/g, pore size: 2.3 nm) (Figure S6-6), powder X-ray diffraction (XRD)(Figure S6-7), scanning electron microscopy (SEM)(Figure S6-8), and transmission electron microscopy (TEM). Amounts of phosphine and rhodium in RhPMSN was determined by energy dispersive X-ray (EDX) and was around 0.78 mmol per gram particle and 0.25 mmol per gram particle prospectively (P/Rh = 3.1). The chemical structure of RhPMSN was confirmed by ^{29}Si solid-state NMR (Figure S6-9), ^{13}C solid-state NMR (Figure S6-10), ^{31}P CP MAS NMR (Figure 6-2b).

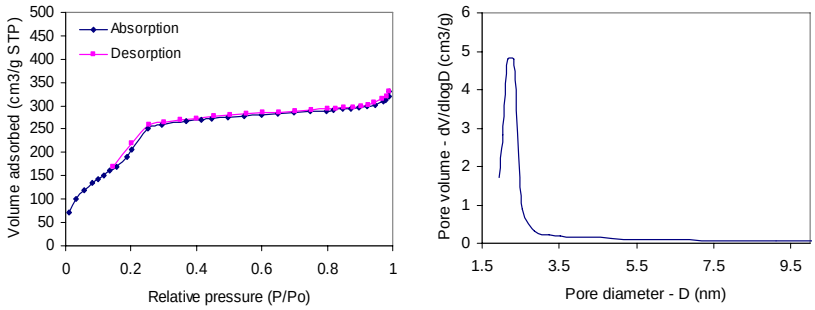

Figure S6-6. BET isotherms and BJH pore size distribution curve of RhPMSN.

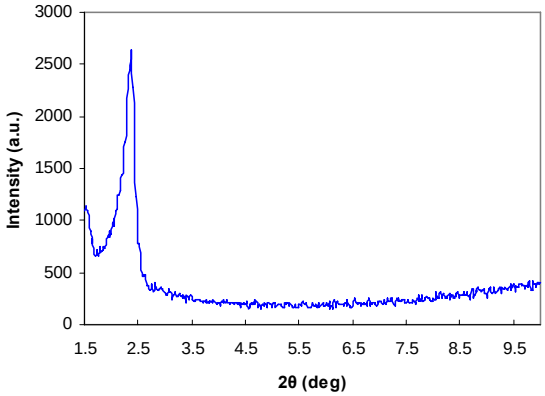

Figure S6-7. XRD of catalyst RhPMSN.

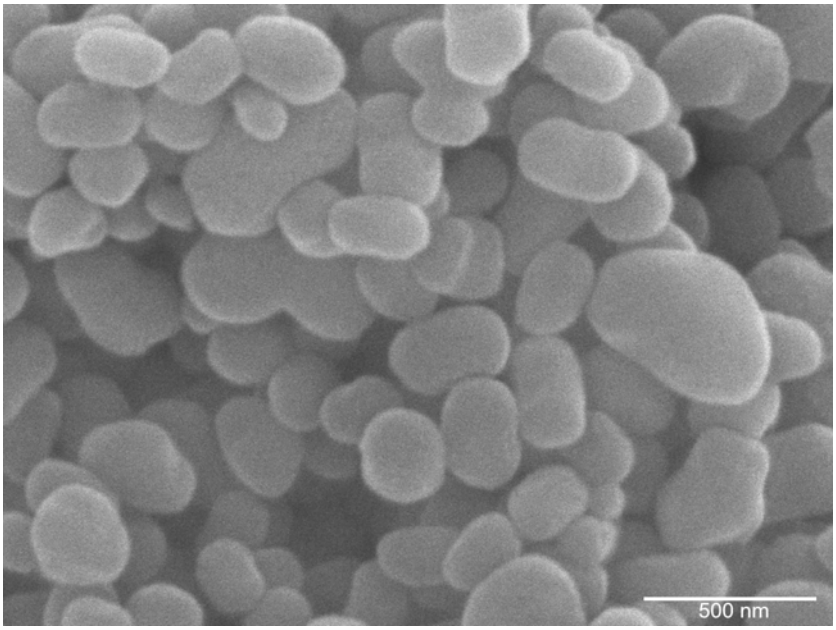

Figure S6-8. Scanning electron microscopy (SEM) of RhPMSN.

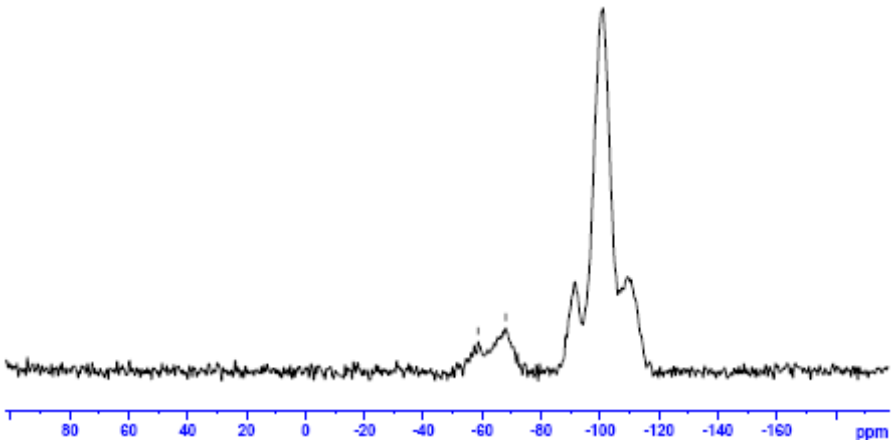

Figure S6-9. ^{29}Si solid-sate NMR spectrum of RhPMSN.

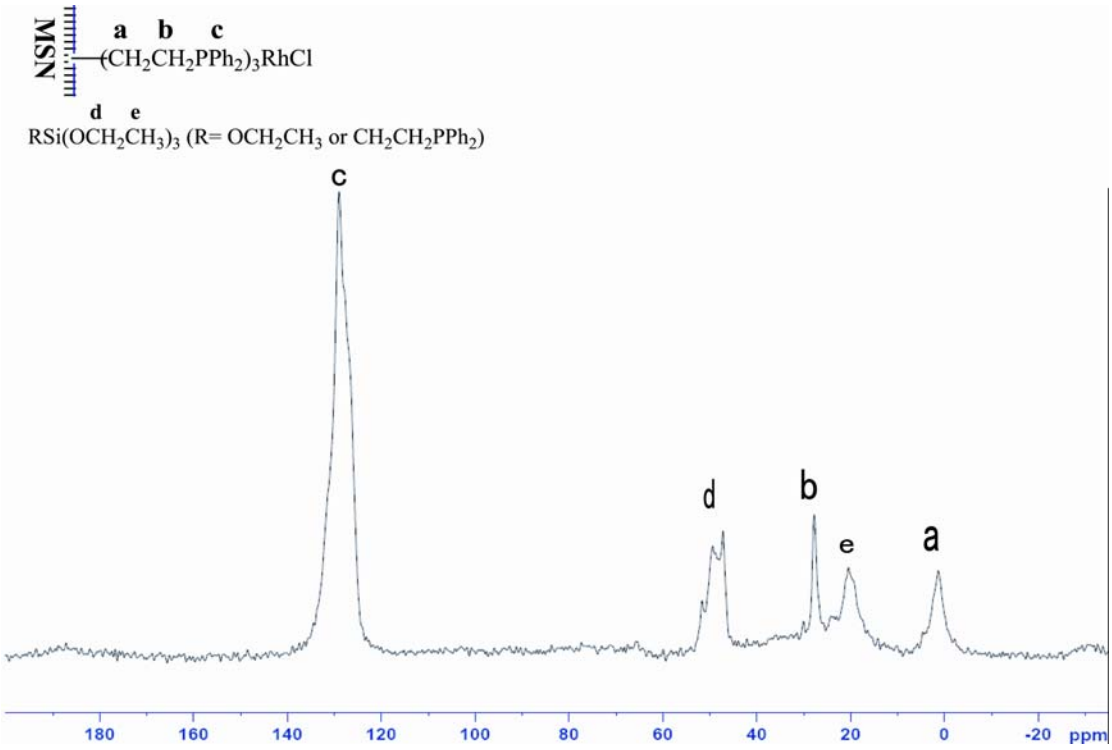

Figure S6-10. ^{13}C solid-state NMR spectrum of RhPMSN.

3. Catalytic hydrogenation of ethyl pyruvate

3.1. Hydrogenation of ethyl pyruvate catalyzed by Wilkinson's catalyst/(-)-cinchonidine

Wilkinson's catalyst ($RhCl(TPP)_3$, 5.0 mg, 0.005 mmol), cinchonidine (its amount was changed in different test), 10 mL THF, ethyl pyruvate (0.1 mL, 1.0 mmol) were loaded in a 25 mL autoclave. After purged several times with hydrogen, the autoclave was pressurized to 300 psi with H_2. After 6.0 hours at 40 ^oC with stirring, reaction was stopped. The solution was analyzed by Varian 3900 GC with chiral capillary column (CP-ChiralSil-Dex CB, 25 m × 0.25 mm × 0.25 μm).

3.1. Asymmetric hydrogenation of ethyl pyruvate catalyzed by RhPMSN/(-)-cinchonidine

RhPMSN (20 mg, including 0.005 mmol Rh), cinchonidine (its amount was changed in different test), 10 mL THF, ethyl pyruvate (0.1 mL, 1.0 mmol) were loaded in a 25 mL autoclave. After purged several times with hydrogen, the autoclave was pressurized to 300 psi with H_2. After 6.0 hours at 40 ^oC with stirring, reaction was stopped. The solution was

separated by filtration and centrifuge before the supernatant was analyzed by Varian 3900 GC with chiral capillary column (CP-ChiralSil-Dex CB, 25 m × 0.25 mm × 0.25 μm).

4. Characterization of (-)-cinchonidine adsorbed on RhPMSN surface

After hydrogenation of ethyl pyruvate, the solid was separated from the tetrahydrofuran solution by centrifuge, washed with tetrahydrofuran and dried under vacuum at 70 ^{o}C overnight. The amount of (-)-cinchonidine was detected by TGA (Thermogravimetric Analysis). As shown in Figure S6-11, the amount of (-)-cinchonidine on catalysts surface increased with its increasing concentration in solution. However, enantioselectivity of hydrogenation of ethyl pyruvate increased with (-)-cinchonidine concentration in solution as well as (-)-cinchonidine on catalyst surface before enantioselectivity reached its highest point (50.0 % e.e.) and then went down back and be stabilized at 22.0 % e.e. with higher (-)-cinchonidine concentration in solution and catalyst surface (Figure S6-12 and S6-13).

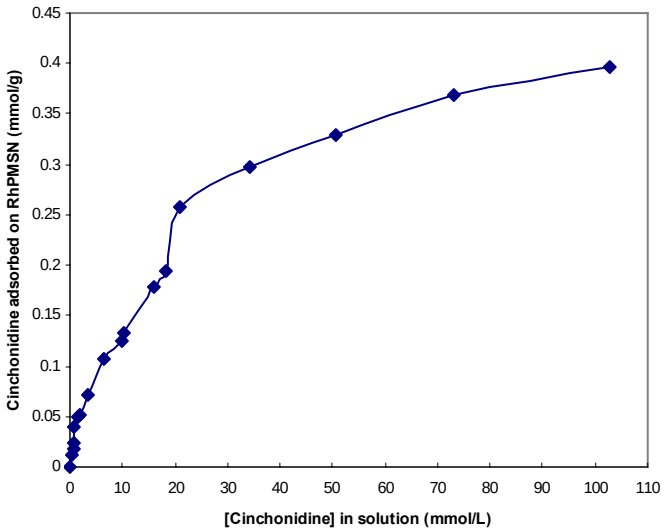

Figure S6-11. Effect of (-)-cinchonidine in solution on (-)-cinchonidine adsorbed on RhPMSN surface.

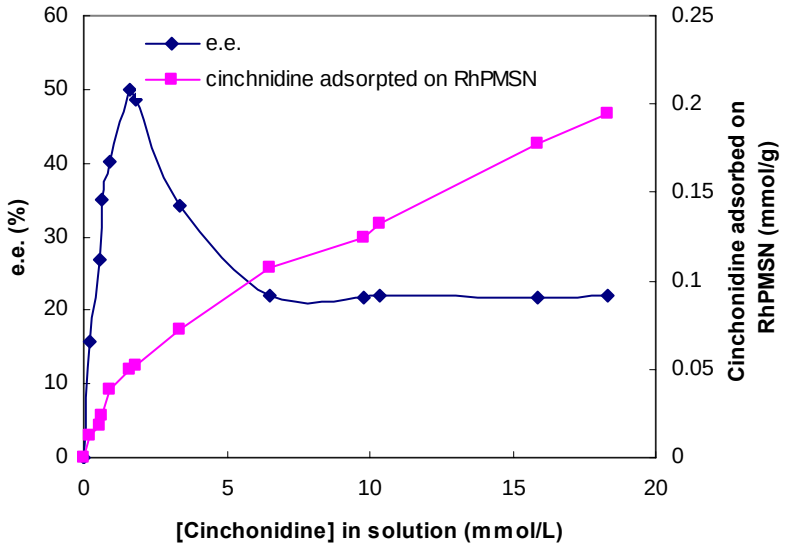

Figure S6-12. Effect of (-)-cinchonidine in solution on enantioselectivity.

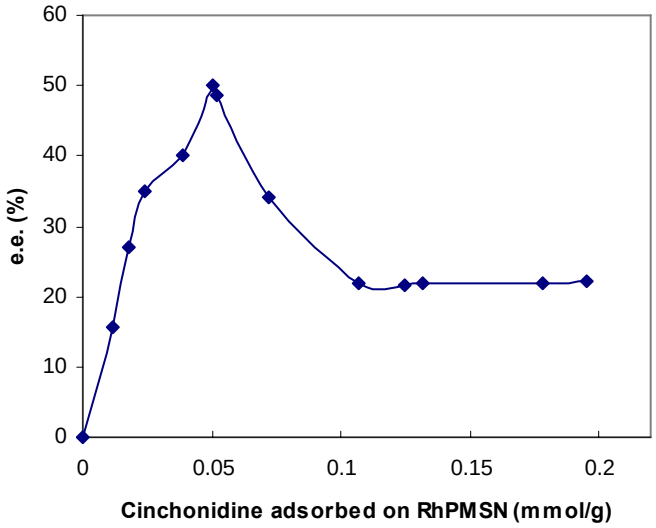

Figure S6-13. Effect of RhPMSN-adsorbed (-)-cinchonidine on enantioselectivity.

From Figure S6-12 and S6-13, it was found that e.e. was increased with the CD on RhPMSN before $[CD]_{solution}$ was 1.63 mmol/L, where 0.05 mmol CD was adsorbed on per gram RhPMSN surface, which means enantioselectivity is the best here with $[CD]_{RhPMSN}$ /Rh = 0.2.

The coverage of RhPMSN-adsorbed cinchonidine is about 6.4 % when e.e. reaches to the highest point, where 800 m^2/g is the BET surface area of RhPMSN (see Scheme S6-1).

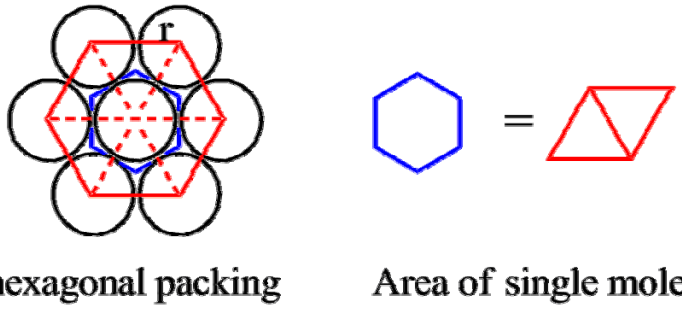

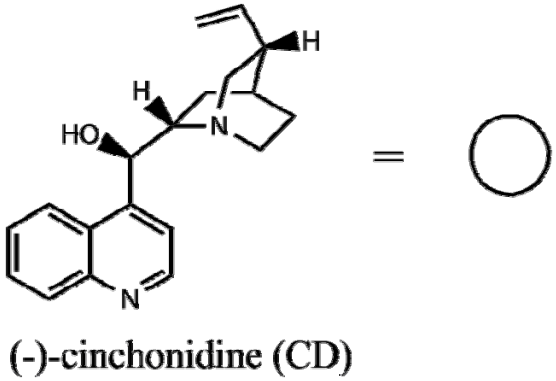

Area of *CD* = $(2\sqrt{3})\ r^2 = 1.7 \times 10^{-18}\ m^2$, where r is ~6.9Å.

Area of 0.05 mmol of *CD* = $0.05 \times (6.02 \times 10^{23}) \times$ (Area of *CD*) = 51.3 m^2

Total BET surface area of RhPMSN = 800 m^2/g

The % surface coverage of 0.05 mmol of *CD* adsorbed on 1 g of RhPMSN is:

$(51.3\ m^2)/(800\ m^2) \times 100 = 6.4\%$

Scheme S6-1. Estimation of the surface coverage of adsorbed (-)-cinchonidine on RhPMSN.

CHAPTER 7. A SOLID-STATE NMR INVESTIGATION OF THE STRUCTURE OF MESOPOROUS SILICA NANOPARTICLE SUPPORTED RHODIUM CATALYSTS

A paper published in *Solid State Nuclear Magnetic Resonance* **2009**, 35, 82-86.

Jennifer L. Rapp [a], **Yulin Huang** [c], Michael Natella [b], Yang Cai [c], Victor S.-Y. Lin [a,c,]*, Marek Pruski [a,c,]*

[a] *US DOE Ames Laboratory, Iowa State University, Ames, IA 50011, USA*

[b] *Ecole Nationale Superieure des Ingenieurs en Arts Chimiques et Technologiques, Toulouse 31077, France,* [c] *Department of Chemistry, Iowa State University, Ames, IA 50011, USA*

*Corresponding authors.

Abstract

A detailed study of the chemical structure of mesoporous silica catalysts containing rhodium ligands and nanoparticles (RhPMSN) was carried out by multi-dimensional solid-state NMR techniques. The degree of functionalization of the rhodium-phosphinosilyl complex to the surface of the RhPMSN channels was determined by ^{29}Si NMR experiments. The structural assignments of the rhodium-phosphinosilyl complex were unambiguously determined by employing the novel, indirectly detected heteronuclear correlation (^{13}C-^{1}H and ^{31}P-^{1}H idHETCOR) techniques, which indicated that oxidation of the attached phosphinosilyl groups and detachment of Rh was enhanced upon syngas conversion.

Introduction

Mesoporous silica nanoparticles (MSNs) have a wide range of applications, due to their high surface area and controllable morphology.[1,2] The characteristics of MSNs are highly dependent upon the synthetic conditions used, especially the silica source, type and ionic strength of the surfactant, pH of the reaction mixture, temperature and reaction time.[3-14] Functionalization of the MSN surfaces with organic or inorganic

groups, as well as incorporation and immobilization of metal complexes (e.g., containing Pt, Pd, Rh) via organic ligands, is a common practice towards obtaining MSN materials for uses in biotechnology[15-21] and catalysis[22-34]. Phosphine ligands have received much interest in the binding of metal complexes to silica supports, as they form strongly anchored and stable structures, are easily and inexpensively synthesized, and are useful for a variety of catalytic applications.[32,35-41] In particular, rhodium-phosphine complexes immobilized on silica surfaces (RhPMSN), typically synthesized via a co-condensation reaction in an acidic medium,[42] are of interest due to their excellent catalytic activity and selectivity in hydroformylation[30,40] and hydrogenation processes[41].

Numerous analytical tools are used to investigate the morphology and other characteristics of mesoporous materials, including SEM, TEM, N_2-adsorption, FTIR, XRD, TGA, and EDX. Solid-state NMR (SSNMR), however, has proven to be a very powerful technique in the determination of the bulk and surface structures of these materials, by providing detailed information about the local molecular environments.[43] Silicon-29 SSNMR, in particular, is used to characterize mesoporous silica materials. Utilizing cross-polarization (CP) and direct-polarization (DP) excitation methods in concert with magic-angle spinning (MAS), qualitative and quantitative information about the silicon functionalities can be readily obtained.[16,44] Two-dimensional heteronuclear correlation (2D HETCOR) SSNMR techniques involving ^{1}H, ^{29}Si, ^{13}C and other nuclei can provide more detailed structural information about these materials. We have recently demonstrated numerous advantages of using fast MAS (at 40 kHz) with ^{1}H-^{13}C and ^{1}H-^{29}Si HETCOR NMR of such systems.[45-50] In particular, a large sensitivity gain has been achieved by using the so-called indirect detection method, i.e., the detection of high-g (^{1}H) rather than low-g (^{13}C, ^{15}N, etc.) nuclei.[48] This type of data acquisition has been hitherto impractical due to the lack of adequate ^{1}H decoupling schemes. Herein, we employ these methods to detail the structure of MSNs functionalized with rhodium-phosphine ligands ($Ph_2P(CH_2)_2Si(OCH_2CH_3)_3)_3RhCl$) under basic conditions. By using the rhodium-phosphine complex as the precursor, we aimed to develop mesoporous silica supported Rh catalytic systems for the selective production

of ethanol and other alcohols from syngas. Rhodium nanoparticles, which are known to be very good catalysts for the production of bio-fuels from syngas, were detected after the functionalized MSNs were used for the selective production of ethanol from syngas. Understanding the ligands' structure in unreacted and reacted catalysts will help to determine whether their role is solely as a precursor for the formation of nanoparticles, or if they directly affect the catalytic performance. The activity and selectivity of these catalysts is currently being investigated in our laboratory.

Experimental

The rhodium phosphine mesoporous silica catalysts (RhPMSN) were synthesized via a co-condensation process inwhich1.0 mL (3.0 mmol) of 2-(diphenylphosphino)-ethyltriethoxysilane and 10 mL tetraethoxysilane (TEOS) were injected into 480 mL aqueous solution of 2.0 g cetyltrimethylammonium bromide(CTAB) and 14 mmol NaOH at 80 ^{o}C, under vigorous stirring in a 2 L flask. The solid product was isolated by filtration after 2 h, washed with excess methanol and dried under vacuum. Metallation was conducted by stirring the resulting phosphinoalkyl-functionalized mesoporous silica material in dry THF with $[Rh(COD)Cl]_2$ under Ar at room temperature for 12 h (P/Rh = 3.1). The solid was then isolated by filtration, washed with excess THF and MeOH and dried at 90 1C under vacuum. The syngas reaction was carried out in a bench top high pressure reactor at 280 ^{o}C under 450 psi with a 2:1 ratio of H_2:CO. The unreacted (as-synthesized) and reacted (in a syngas conversion process) materials are referred to as RhPMSN and RhPMSN*, respectively. Rhodium nanoparticles with an average size of 5 nm, embedded in the channel walls of RhPMSN* were detected via SEM and TEM measurements.

Solid-state NMR experiments were performed at 9.4 T and 14.1 T on a Chemagnetics Infinity spectrometer and a Varian NMR system 600 spectrometer, equipped with 3.2 and 1.6 mm MAS double-tuned probes, respectively. ^{29}Si, ^{13}C, and ^{1}H chemical shifts were all referenced with respect to tetramethylsilane (TMS) at 0 ppm and ^{31}P chemical shifts were referenced with respect to 85% H_3PO_4 at 0 ppm. The experimental conditions are listed

below with the following denotations of B_0, ν_R, ν_{RF}^H, ν_{RF}^X, τ_{RD}, τ_{CP} and NS representing the static magnetic field, the rate of sample rotation, magnitude of radiofrequency magnetic field applied to ^{1}H and X spins, the relaxation delay, the cross polarization time, and the number of scans, respectively.

^{1}H MAS: B_0 = 14.1 T; ν_R = 25-35 kHz; ν_{RF}^H = 62.5-65 kHz; τ_{RD} = 2 s; NS = 4 (RhP and RhPMSN) and 32 (RhPMSN*).

^{1}H-^{13}C CP/MAS: For RhP and RhPMSN: B_0 = 9.4 T; ν_R = 20 kHz; ν_{RF}^H during excitation = 112 kHz; ν_{RF}^H during CP = 30 kHz; ν_{RF}^H during TPPM decoupling = 78 kHz; ν_{RF}^C = 50 kHz; τ_{RD} = 5 s; τ_{CP} = 1 ms; NS = 8640. For RhPMSN*: B_0 = 14.1 T; ν_R = 25 kHz; ν_{RF}^H during excitation = 87.5 kHz; ν_{RF}^H during CP = 87 kHz; ν_{RF}^H during TPPM decoupling = 6 kHz; ν_{RF}^C = 68 kHz; τ_{RD} = 2 s; τ_{CP} = 1.5 ms; NS = 16384.

^{1}H-^{29}Si CP/MAS: B_0 = 9.4 T; ν_R = 20 kHz; ν_{RF}^H during excitation = 76 kHz; ν_{RF}^H during CP = 65 kHz; ν_{RF}^H during TPPM decoupling = 50 kHz; ν_{RF}^{Si} = 45.5 kHz; τ_{RD} = 1 s; τ_{CP} = 6 ms; NS = 16384 (RhPMSN) and 8192 (RhPMSN and RhPMSN*).

^{1}H-^{31}P CP/MAS: For RhP and RhPMSN: B_0 = 9.4 T; ν_R = 20 kHz; ν_{RF}^H during excitation = 109 kHz; ν_{RF}^H during CP = 30 kHz; ν_{RF}^H during TPPM decoupling = 83 kHz; ν_{RF}^P = 50 kHz; τ_{RD} = 5 s; τ_{CP} = 1.5 ms; NS = 1024. For RhPMSN*: B_0 = 14.1 T; ν_R = 25 kHz; ν_{RF}^H during excitation = 62.5 kHz; ν_{RF}^H during CP = 62.5 kHz; ν_{RF}^H during TPPM decoupling = 133 kHz; ν_{RF}^P = 85 kHz; τ_{RD} = 2 s; τ_{CP} = 1.5 ms; NS = 24576.

^{13}C-^{1}H indirect detection HETCOR (idHET): B_0 = 14.1 T; ν_R = 35 kHz; ν_{RF}^H during excitation = 62.5 kHz; ν_{RF}^H during CP = 54 kHz; ν_{RF}^H during π-decoupling = 62.5 kHz; ν_{RF}^C during CP = 81 kHz; ν_{RF}^C during SPINAL-64 decoupling = 9 kHz; τ_{RD} = 1 s; τ_{CP} = 1 ms; NS = 32; rows = 160; t_1 increments = 25 μs.

^{31}P-^{1}H indirect detection HETCOR (idHET): B_0 = 14.1 T; ν_R = 35 kHz; ν_{RF}^{H} during excitation = 65 kHz; ν_{RF}^{H} during CP = 65 kHz; ν_{RF}^{H} during π-decoupling = 9 kHz; ν_{RF}^{P} during CP = 100 kHz; ν_{RF}^{P} during SPINAL-64 decoupling = 180 kHz; τ_{RD} = 2 s; τ_{CP} = 1.5 ms; NS = 64 (RhPMSN*) and 128 (RhP and RhPMSN); rows = 128 (RhP and RhPMSN) and 350 (RhPMSN*); t_1 increments = 20 μs.

^{29}Si, ^{13}C, and ^{1}H chemical shifts were all referenced with respect to tetramethylsilane (TMS) at 0 ppm and ^{31}P chemical shifts were referenced with respect to 85% H_3PO_4 at 0 ppm.

Results and discussions

The ^{29}Si CPMAS NMR spectra of RhPMSN and RhPMSN* are shown in Figure 7-1a and b. Represented in the spectra are silicon sites of the types Q, T and M. The Q sites form the framework of the MSNs, with the wall core comprised of Q^4-type silicon atoms ($(SiO)_4Si$) and the surface containing Q^2 ($(SiO)_2Si(OH)_2$) and Q^3 ($(SiO)_3Si(OH)$) sites. The resonances representing Q^4, Q^3 and Q^2 sites are typically found near 110, 100, and 90 ppm, respectively.[16, 51-55] The sites denoted as T^2 and T^3, observed at approximately 58 and 68 ppm, are assigned to $(SiO)_2Si(R')R$ and $(SiO)_3SiR$ functionalities, where R represents the attached functional groups and R' = OC_2H_5 or OH. The presence of T sites indicates that functionalization of the MSN surfaces has indeed occurred. We will later demonstrate that the functional groups in RhPMSN correspond to rhodium phosphine complexes. The M sites ($(SiO\text{-}Si\text{-}(CH_3)_3$) are observed at around 13 ppm, in agreement with earlier reports.[42] These sites result from silylation (''capping''), a process by which surface hydroxyl hydrogens are substituted by trimethylsilyl groups.[23,52,56,57] Indeed, the RhPMSN sample which was not silylated did not exhibit this resonance (Figure 7-1c). Silylation was carried out using TMS-Cl ($(CH_3)_3SiCl$), prior to CTAB extraction, to increase the stability of the RhPMSN structure. Closer examination of the ^{29}Si spectra reveals that broadening of individual Q^n resonances occurs upon reaction of RhPMSN with syngas. It affected mainly the resonances representing the surface sites in RhPMSN* (i.e. the resonance representing Q^3 sites in Figure 1b was

broadened by roughly 15%) and to a lesser extent (5%), the Q^4 sites. It is well known that the range of line widths in ^{29}Si MAS spectra is associated with the degree of structural disorder. In an earlier study of cab-o-sil, increased ^{29}Si line widths were observed in both CP and DPMAS SSNMR spectra, compared to the silica gels.[58] This effect was attributed to a wider distribution of bond distances and angles formed at higher temperatures used in the production of cab-o-sil. A similar broadening due to heat treatment was also observed in the dehydration of silica gels.[52,59] The observed broadening of the resonances representing the Q sites in the spectrum of RhPMSN* (Figure 7-1b) results from additional heating during the syngas reaction at 280 ^oC.

The relative concentrations of silicon sites in the RhPMSN were found via deconvolution and integration of the resonances in the ^{29}Si DPMAS spectrum of Figure 7-1c-d. Due to slow spin-lattice relaxation of ^{29}Si nuclei, the DPMAS experiment required more experimental time (see the experimental section), but provided relative peak intensities that are not distorted by the ^1H-^{29}Si CP process. An overall T site concentration of 3.7(±0.5)% was determined, which correlates well with the result obtained from EDX measurements of the same sample (3.8%). The other samples were not examined via DPMAS, however, valid trends can be observed in the CPMAS spectra because they were all acquired under similar conditions. First, partial dehydroxylation of RhPMSN has occurred upon syngas conversion, as evidenced by the lower concentrations of Q^2 and Q^3 sites in RhPMSN*(compare Figure 7-1a and b). Although the overall concentration of T sites remained unchanged, it appears that partial conversion of T^2 to T^3 silicon sites has occurred upon reaction with syngas, although the exact concentration of T^2 sites is difficult to estimate without using much longer acquisition of data. Most likely, this process occurred via cleavage of the ethoxy groups together with dehydroxylation of the neighboring Q sites. Finally, the observed concentration of M sites is greater than in previously studied rhodium phosphinosilyl functionalized MSNs.[42] The ^{13}C-^1H idHETCOR spectra of RhPMSN and RhPMSN* are nearly identical, thus only the spectrum of RhPMSN is shown in Figure 7-2, along with the corresponding 1D ^{13}C CPMAS and ^1H DPMAS results. The observed correlations can be assigned to various

components of the phosphine ligands, as shown in the figure. The resonances representing CTAB have not been detected, which proves that it has been completely removed.[45,46] However, weak resonances from the ethoxy groups are observed, which confirms the aforementioned incomplete cleavage of ethoxysilane species.

The 1D ^{31}P CPMAS NMR spectra of unreacted (RhPMSN) and reacted (RhPMSN*) rhodium-phosphine MSN complexes are shown in Figure 7-3a and b. Due to the substantial breadth of the 1D spectra relative to the differences in chemical shifts, the ^{31}P-^{1}H idHETCOR experiment was employed to offer additional information about the phosphorus species. The 2D spectra of RhPMSN and RhPMSN* are shown in Figure 4a and b, respectively. Also shown, in Figure 3c, is a spectrum of MSNs functionalized with phosphine ligands without rhodium.

The 1D and 2D ^{31}P spectra of RhPMSN exhibit a broad nonsymmetrical resonance centered at 39 ppm, with a less intense contribution at 36 ppm. The ^{31}P-^{1}H idHETCOR spectrum reveals strong correlations between ^{31}P and methylene (2.5 ppm), as well as aromatic (7.5 ppm) protons, and somewhat weaker correlations to the methylene protons near the T sites. As expected, protons associated with M sites and the ethoxy groups, which dominated the ^{1}H MAS spectrum shown in the top part of Figure 7-2, do not correlate with phosphorus. Upon reaction with syngas, the ^{31}P resonance maximum shifts slightly upfield from 39 to 36 ppm (Figure 7-3b and 6-4b), while exhibiting the same correlation to the ^{1}H nuclei. By deconvoluting the ^{1}P spectra before and after the syngas conversion, the relative intensity of resonances at 36 ppm in unreacted and reacted samples was estimated to be 45(±5)% and 60(±5)%, respectively.

To assign the ^{31}P spectra, we first note that the surface-bound ligand without Rh yielded a peak at 12 ppm (Figure 7-3c), in accordance with earlier studies,[36,60,65] whereas the non-attached (free) ligands ($Ph_2P(CH_2)_2Si(OCH_2CH_3)_3$), with a ^{31}P resonance expected at 8.4 ppm,[32,42] have not been detected in any of the studied samples. The ^{31}P peak at 39 ppm is thus assigned to the silica-bound phosphine complex coordinated to rhodium. While several previous solid and liquid state NMR studies of silica catalysts containing transition metal complexes, including rhodium phosphine complexes, have reported two different ^{31}P NMR resonances assigned to the cis- and

trans-geometry around the metal center,[32,36,61-65] the chemical shift differences between these two confirmations are much greater (10 ppm) than the 3 ppm difference observed in Figure 7-3a and 6-3b and 6-4a and 6-4b. A more reasonable explanation for the downfield shift is oxidation of the phosphine complex. Indeed, it is known that in the case of phosphine ligands immobilized on silica surfaces, the ^{31}P chemical shift changes from -10 (±5) to 40(±5) ppm upon oxidation.[36,60,65] For example, a ^{31}P resonance at 38ppm was observed in oxidized phosphine complexes immobilized on capped (silylated) silica surface.[36,65,66] When the supported phosphine ligands are coordinated with metals, their oxidation causes detachment of the metal and a slight upfield shift of the ^{31}P peak.[38,65] Note that we have observed a peak at 36 ppm in MSN functionalized with phosphine alone (Figure 7-3c). Therefore, we conclude that the observed change of the chemical shift of the ^{31}P resonance in the 2D ^{31}P-^{1}H idHETCOR spectrum of RhPMSN* is indeed due to the oxidation of the phosphine group and the detachment of rhodium. Our studies indicated that the formation of 5 nm Rh nanoparticles is accompanied by oxidation of phosphine ligands on the support. These Rh nanoparticles showed good product selectivity for alcohol production at low temperature (< 200 ^{o}C). The additional role that the oxidation-induced detachment of rhodium played in the product selectivity of these catalytic systems is currently under investigation.

Conclusions

An in-depth solid-state NMR study of mesoporous silica nanoparticles (MSNs) functionalized with rhodium phosphine ligands has been presented. Functionalization of the ligand was confirmed by the presence of T sites in the ^{29}Si CPMAS NMR spectrum and quantification of these sites was achieved via integration of the ^{29}Si DPMAS NMR spectrum, in which the percent of T sites was found to be 3.7%. Both 1D and 2D SSNMR experiments showed that covalent attachment of the rhodium-phosphine ligand to the MSN surfaces was successful, as well as provided structural assignments of the ligand and the MSNs themselves. Both ^{13}C-^{1}H and ^{31}P-^{1}H idHETCOR experiments provided

structural details of oxidized and non-oxidized phosphine species, otherwise indiscernible in conventional 1D CPMAS NMR experiments.

Acknowledgments

This research was supported at the Ames Laboratory by the US Department of Energy, Office of Basic Energy Sciences, under Contract no. DE-AC02-07CH11358. The authors thank Dr. J. Wiench and Dr. Xu Shu for their helpful assistance with the measurements of NMR spectra.

References

(1) Giraldo, L. F.; López, B. L.; Pérez, L.; Urrego, S.; Sierra, L.; Mesa, M. *Macromol. Symp.* **2007**, *258*, 129–141.

(2) Stein, A. *Adv. Mater.* **2003**, *15*, 763-775.

(3) Stoeber, W.; Fink, A.; Bohn, E. *J. Colloid Interface Sci.* **1968**, *26*, 62-69.

(4) Davidson, A. *Curr. Opin. Colloid Interface Sci.* **2002**, *7*, 92-106.

(5) Cai, Q.; Luo, Z. S.; Pang, W. Q.; Fan, Y. W.; Chen, X. H. *Chem. Mater.* **2001**, *13*, 258-263.

(6) Lin, H. P.; Kao, C. P.; Mou, C. Y.; Liu, S. B. *J. Phys. Chem. B* **2000**, *104*, 7885-7894.

(7) Sierra, L.; Guth, J.-L. *Microporous Mesoporous Mater.* **1999**, *27*, 243-253.

(8) Corma, A.; Kan, Q.; Navarro, M. T.; Perez-Pariente, J.; Rey, F. *Chem. Mater.* **1997**, *9*, 2123-2126.

(9) Sayari, A.; S.; Hamoudi, S. *Chem. Mater.* **2001**, *13*, 3151-3168.

(10) Lei, J.; Fan, J.; Yu, C.; Zhang, L.; Jiang, S.; Tu, B. ; Zhao, D. *Microporous Mesoporous Mater.* **2004**, *73*, 121-128.

(11) Kruk, M.; Jaroniec, M.; Antochshuk, V.; Sayari, A. J. *Phys. Chem. B* **2002**, *106*, 10096-10101.

(12) Kresge, C.t.; Leonowicz, M. E.; Roth, W. J.; Vartuli, J. C.; Beck, J. S. *Nature* **1992**, *359*, 710-712.

(13) Huo, Q.; Margolese, D. I.; Ciesla, U.; Feng, P.; Gier, T. E.; Sieger, P.; Leon, R.; Petroff, P. M.; Schüth, F.; Stucky, G. D. *Nature* **1994**, *368*, 317-321.

(14) Monier, A.; Schüth, F.; Huo, Q.; Kumar, D.; Margolese, D.; Maxwell, R. S.; Stucky, G. D.; Krishnamurty, M.; Petroff, P.; Firouzi, A.; Janicke, M.; Chmelka, B. F. *Science* **1993**, *261*, 1299-1303.

(15) Huh, S.; Wiench, J. W.; Yoo, J. –C.; Trewyn, B. G.; Song, S.; Pruski, M.; Lin, V. S.-Y. *Chem. Commun. (Camb.)* **2003**, *18*, 2364-2365.

(16) Huh, S.; Wiench, J. W.; Yoo, J. –C.; Pruski, M.; Lin, V. S. –Y. *Chem. Mater.* **2003**, *15*, 4247-4256.

(17) Radu, D. R.; Lai, C. –Y.; Huang, J.; Shu, X.; Lin, V. S. –Y. *Chem. Commun.* **2005**, *10*, 1264-1266.

(18) Trewyn, B. G.; Slowing, I. I.; Giri, S.; Chen, H. –T.; Lin, V. S. –Y. *Acc. Chem. Res.* **2007**, *40*, 846-853.

(19) Giri, S.; Trewyn, B. G.; Lin, V. S. –Y. *Nanomedicine* **2007**, *2*, 99-111.

(20) Slowing, I. I.; Trewyn, B. G.; Giri, S.; Lin, V. S. –Y. *Adv. Funct. Mater.* **2007**, *17*, 12225-1236.

(21) Evans, J.; Zaki, A. B.; El-Sheikh, M. Y.; El-Safty, S. A. *J. Phys. Chem. B* **2000**, *104*, 10271-10281.

(22) Huh, S.; Chen, H. –T.; Wiench, J. W.; Pruski, M.; Lin, V. S. –Y. *J. Am. Chem. Soc.* **2004**, *126*, 1010-1011.

(23) Sutra, P.; Fajula, F.; Brunel, D.; Lentz, P.; Daelen, G.; Nagy, J. B. *Colloids Surf., A* **1999**, *158*, 21-27.

(24) Czakova, M.; Caka, M. *J. Mol. Catal.* **1981**, *11*, 313-322.

(25) Allum, K. G.; Hancock, R. D.; Howell, I. V.; Lester, T. E.; McKenzie, S.; Pitkethyl, R. C.; Robinson, P. J. *J. Organometal. Chem.* **1976**, *107*, 393-405.

(26) Michalska, Z. M.; Capka, M.; Stoch, J. *J. Mol. Catal.* **1981**, *11*, 323-330.

(27) Kimura, T.; Saeki, S.; Sagahara, Y.; Kuroda, K. *Langmuir* **1999**, *15*, 2794-2798.

(28) Brunel, D.; Bellocq, N.; Sutra, P.; Cauvel, A.; Laspéras, M.; Moreau, P.; Di Renzo, F.; Galarneau, A.; Fajula, F. *Coord. Chem. Rev.* **1998**, *178-180*, 1085-1108.

(29) Hernan, P.; Pino, C.; Huitzky, E. R. *Chem. Mater.* **1992**, *4*, 49-55.

(30) Sutra, P.; Brunel, D. *Chem. Commun.* **1996**, 2485-2486.

(31) Yang, C. –M.; Lin, H. –A.; Zibrowius, B.; Spliethoff, B.; Schüth, F.; Liou, S. –C.; (32) Kröcher, O.; Köppel, R. A.; Frōba, M.; Baiker, A. *J. Catal.* **1998**, *178*, 284-298.

(33) Pugin, B.; Müller, M.. *Stud. Surf. Sci. Catal.* **1993**, *78*, 107-114.

(34) Jorna, A. M. J.; Boelrijk, A. E. M.; Hoorn, H. J.; Reedijk, J. *React. Funtional. Polym.* **1996**, *29*, 101-114.

(35) Albert, K.; Bayer, E. *J. Chromatoghr.* **1991**, *544*, 345-370.

(36) Bemi, L.; Clark, H. C.; Davies, J. A.; Fyfe, C. A.; Wasylishen, R. *J. Am. Chem. Soc.* **1982**, *104*, 438-445.

(37) Gáti, T.; Simon, A.; Tóth, G.; Magiera, D.; Moeller, S.; Duddeck, H. *Magn. Reson. Chem.* **2004**, *42*, 600-604.

(38) Li, Z.; Peng, Q.; Yuan, Y. *Appl. Catal., A* **2003**, *239*, 79-86.

(39) Yan, L.; Ding, Y. J.; Zhu, H. J.; Xiong, J. M.; Wang, T.; Pan, Z. D.; Lin, L. W. *J. Molec. Catal. A* **2005**, *234*, 1-7.

(40) Bourque, S. C.; Maltais, F.; Xiao, W. –J.; Tardif, O.; Alper, H.; Arya, P.; Manzer, L. E. *J. Am. Chem. Soc.* **1999**, *121*, 3035-3038.

(41) Ezhova, N. N.; Kolesnichenko, N. V.; Bulygin, A. V.; Slivinskii, E. V.; Han, S. *Russ. Chem. Bull., Int. Ed.* **2002**, *51*, 2165-2169.

(42) Dufaud, V.; Beauchesne, F.; Bonneviot, L. *Angew. Chem. Int. Ed.* **2005**, *44*, 3475-3477.

(43) Bell, A. T.; Pines, A., *NMR Techniques in Catalysis*. Marcel Dekker, Inc.: New York, **1994**; Vol. 55.

(44) Mijatovic, J.; Binder, W. H.; Gruber, H. *Microchim. Acta* **2000**, *133*, 175-181.

(45) Trébosc, J.; Wiench, J. W.; Huh, S.; Lin, V. S. –Y.; Pruski, M. *J. Am. Chem. Soc.* **2005**, *127*, 3057-3068.

(46) Trébosc, J.; Wiench, J. W.; Huh, S.; Lin, V. S. –Y.; Pruski, M. *J. Am. Chem. Soc.* **2005**, *127*, 7587-7593.

(47) Chen, H. –T.; Huh, S.; Wiench, J. W.; Pruski, M.; Lin, V. S. –Y. *J. Am. Chem. Soc.* **2005**, *127*, 13305-133011.

(48) Wiench, J. W.; Bronnimann, C. E.; Lin, V. S.-Y.Pruski, M. *J. Am. Chem. Soc.* **2007**, *129*, 12076-12077.

(49) Wiench, J. W.; Avadhut, Y. S.; Maity, N.; Bhaduri, S.; Lahiri, G. K.; Pruski, M.; Ganapathy, S. *J. Phys. Chem. B* **2007**, *111*, 3877-3885.

(50) Maciel, G. E; Sindorf, D. W. *J. Am. Chem. Soc.* **1980**, *102*, 7606-7607.

(51) Wiench, J. W.; Pruski, M.; Lin, V. S.-Y. *J. Magn. Reson.* **2008**, 193, 233-242.

(52) Sindorf, D. W.; Maciel, G. E. *J. Am. Chem. Soc.* **1983**, *105*, 1487-1493.

(53) Maciel, G. E. In *Encyclopedia of Nuclear Magnetic Resonance*: Grant, D. M., Harris, R. K., Eds.: John Wiley & Sons Ltd: Chichester, 1996; Vol. 7, 4370-4386.

(54) Engelhardt, G.; Michel, D. *High Resolution Solid State NMR of Silicates and Zeolites*: John Wiley & Sons: Chichester, 1987.

(55) Lidner, E.; Schneller, T.; Auer, F.; Mayer, H. A. *Angew. Chem. Int. Ed.* **1999**, *38*, 2155-2174.

(56) Sindorf, D. W.; Maciel, G. E. *J. Phys. Chem.* **1983**, *87*, 5516-5521.

(57) Tao, T.; Maciel, G. E. *J. Am. Chem. Soc.* **2000**, *122*, 3118-3126.

(58) Liu, C. C.; Maciel, G. E. *J. Am. Chem. Soc.* **1996**, *118*, 5103-5119.

(59) Sindorf, D. W.; Maciel, G. E. *J. Phys. Chem.* **1983**, *86*, 5208-5219.

(60) Rudzinski, W. E.; Montgomery, T. L.; Frye, J. S.; Hawkins, B. L.; Maciel, G. E. *J. Catal.* **1986**, *98*, 444-456.

(61) Pregosin, P. S.; Kunz, R. W. *^{31}P and ^{13}C NMR of Transition Metal Phosphine Complexes*: Springer-Verlag: Berlin, 1979.

(62) Grim, S. O.; Keiter, R. L.; McFarlane, W. *Inorg. Chem.* **1967**, *6*, 1133-1137.

(63) Grim, S. O.; Keiter, R. L. *Inorg. Chim. Acta* **1970**, *4*, 56-60.

(64) Grim, S. O.; Ference, R. A. *Inorg. Chem.* **1970**, *4*, 277-282.

(65) Komoroski, R. A.; Magistro, A. J.; Nicolas, P. P. *Inorg. Chem.* **1986**, *25*, 3917-3925.

(66) Bemi, L.; Clark, H. C.; Davies, J. A.; Drexler, D.; Fyfe, C. A.; Wasylishen, R. *J. Organomet. Chem.* **1982**, *224*, C5-C9.

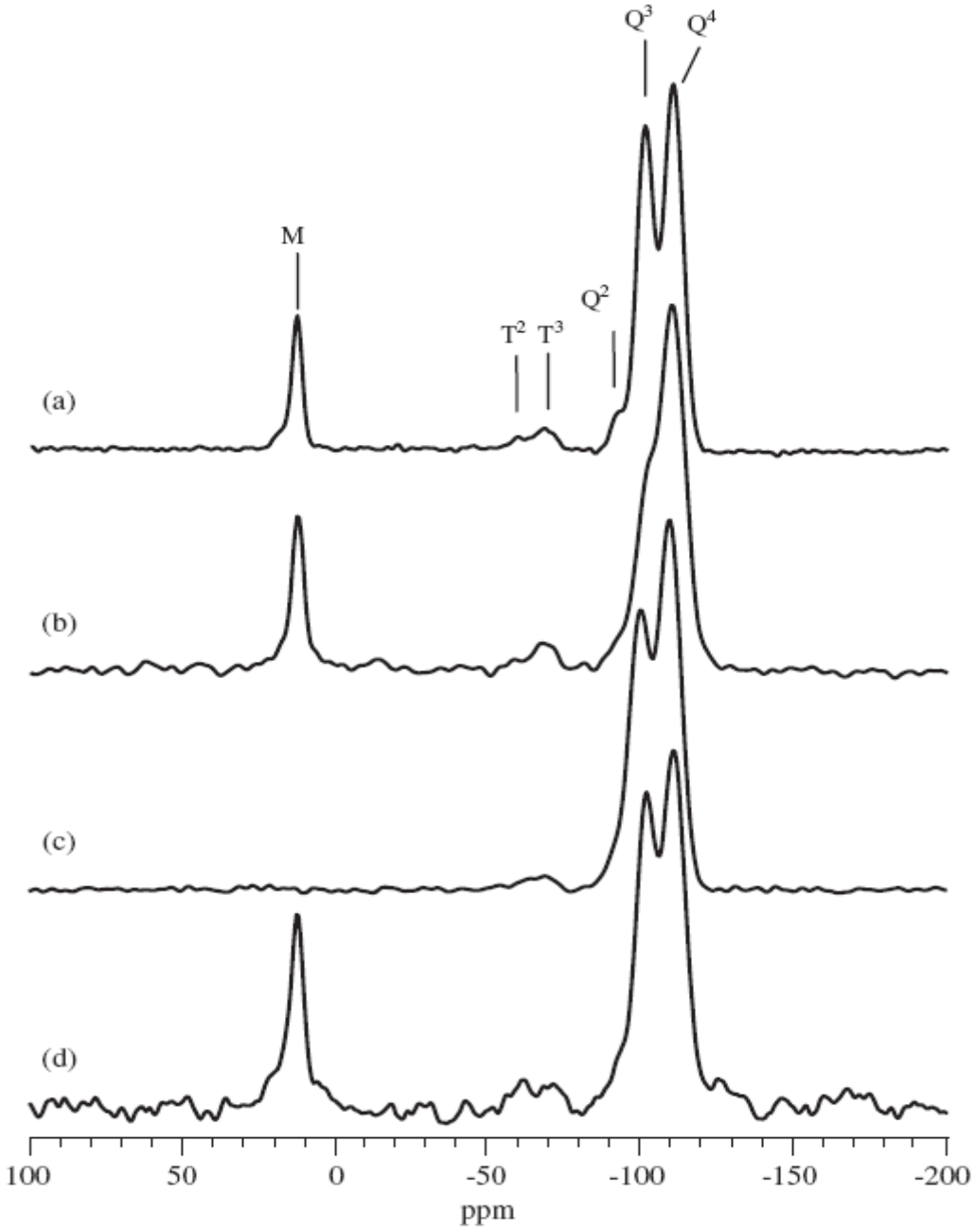

Figure 7-1. ^{29}Si CP/MAS NMR spectra of mesoporous silica nanoparticles functionalized with rhodium-phosphine ligands: a) unreacted catalyst (RhPMSN) and b) catalyst reacted with syngas (RhPMSN*).

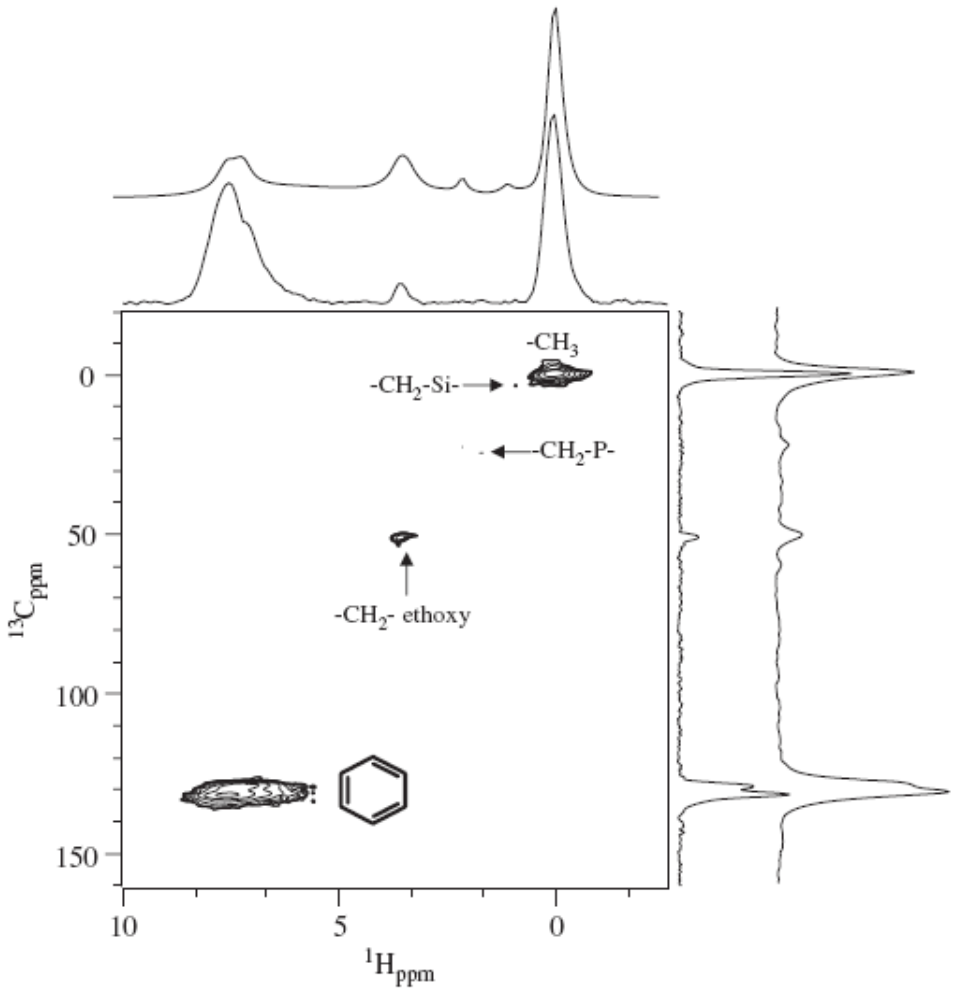

Figure 7-2. Two-dimensional ^{13}C-^{1}H indirectly detected HETCOR spectrum of RhPMSN. The weak correlation representing the CH3 peak of the ethoxy group is not labeled.

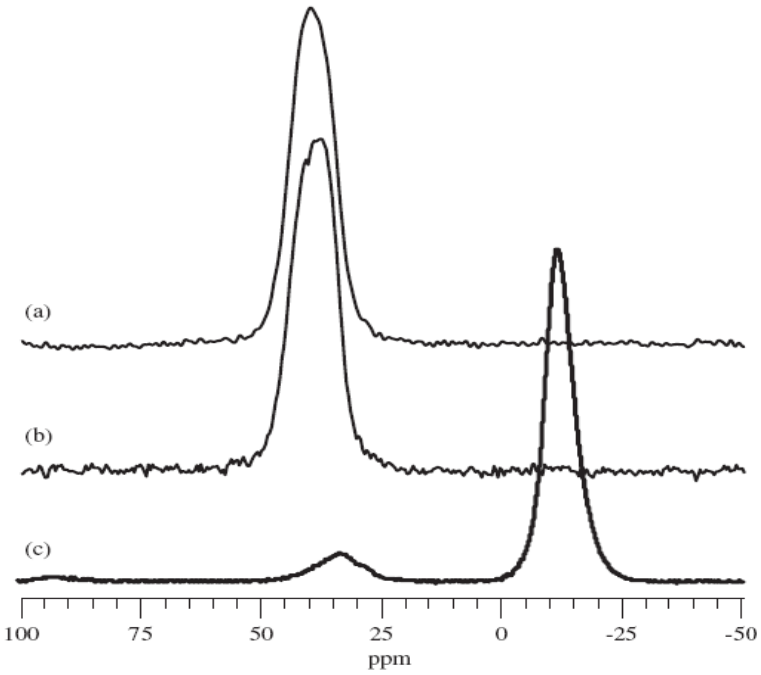

Figure 7-3. ^{1}H-^{31}P CP/MAS spectra of a) RhPMSN and b) RhPMSN* and c) Phosphinosilyl groups covalently attached to MSN surfaces.

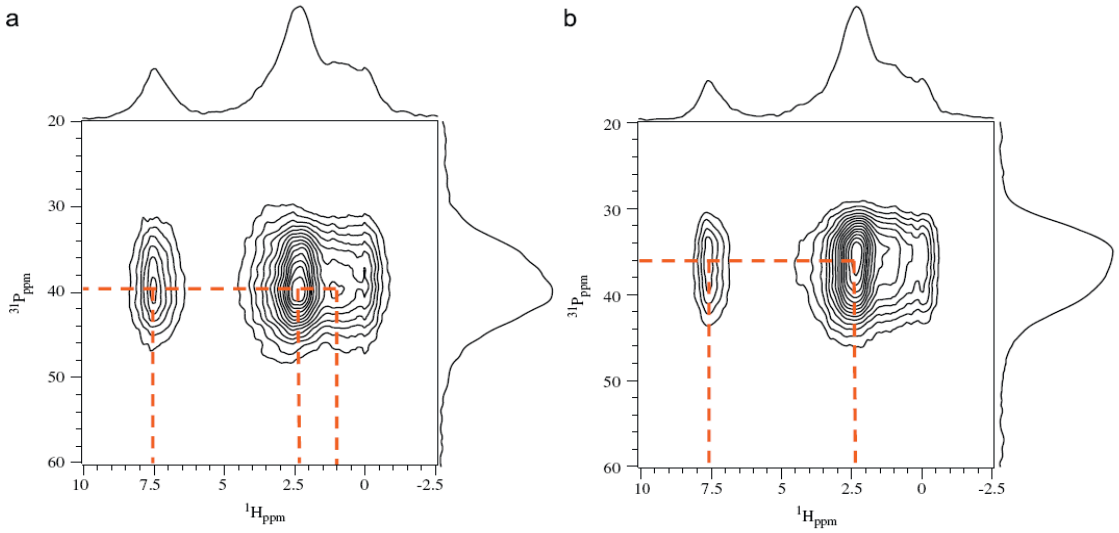

Figure 7-4. Two-dimensional 31P–1H indirectly detected HETCOR spectra of (a)RhPMSN and (b)RhPMSN*.

CHAPTER 8. KINETICS OF OXIDATION OF ORGANIC AMINE WITH A CR(V) SALEN COMPLEX IN HOMOGENEOUS AQUEOUS SOLUTION AND ON THE SURFACE OF MESOPOROUS SILICA

A paper published in *Dalton Transactions*, **2009**, 3237-3246.

Ewa Szajna-Fuller, **Yulin Huang**, Jennifer Rapp, Gezahegn Chaka, Victor S. Y. Lin*, Marek Pruski* and Andreja Bakac*

Ames Laboratory and Chemistry Department, Iowa State University, Ames, IA 50011

*Corresponding authors.

Abstract

A comparative study of catalytic activity under homogeneous and heterogeneous conditions was carried out using the (salen)Cr^{III}-catalyzed oxidation of tetramethylbenzidine (TMB) with iodosobenzene as a model reaction. The oxidation of TMB with iodosobenzene using MSN-(salen)Cr^{III} as a heterogeneous catalyst exhibited both similarities and differences with the analogous homogeneous reaction using (salen)Cr^{III}(H2O)+ as a catalyst in aqueous acetonitrile. In the presence of 0.10M HClO4, the two catalytic reactions proceeded at similar rates and generated the doubly oxidized product TMB^{2+}. In the absence of acid, the radical cation $TMB^{\bullet+}$ was produced. The kinetics of the heterogeneous reaction in the absence of added acid responded to concentrations of all three reagents, *i. e.* (salen)Cr^{III}, TMB, and PhIO.

Introduction

One of the important features of heterogeneous catalysis is the ease of separation and reuse of the catalyst. Homogeneous catalysis, on the other hand, appears to offer faster kinetics and better control of both kinetics and products, although this could be an incorrect perception arising from the better insight into homogeneous catalysis in general. Ideally, the ease of separation, large rates, and product selectivity should all be combined in a single,

heterogeneous catalyst. Comparative studies of catalytic reactions under homogeneous and heterogeneous conditions are therefore necessary to get detailed mechanistic information, to extract the roles of various parameters and conditions in different phases, and to use this knowledge in the building of the next generation of catalysts.

With this goal in mind we undertook a study of the oxidation of an organic amine, tetramethylbenzidine (TMB), with (salen)$Cr^{V}O^{+}$ under both homogeneous (aqueous acetonitrile) and heterogeneous (mesoporous-silica) conditions. Both the oxidant and the amine are well-defined and well-behaved species with excellent spectroscopic and redox properties to facilitate the detection and assignment of intermediates and individual reaction steps. Also, transition metal salen complexes have already found extensive use in synthesis and catalysis which makes them a worthwhile target for mechanistic studies. Among the metals, manganese and chromium appear to be the most widely used,[1-5] especially in the area of enantioselective catalysis,[6-9] although salen complexes of most of the transition metals are now known.[8,10,11]

Despite the great reactivity of (salen)$Cr^{v}O^{+}$ and ligand-substituted derivatives in several types of reactions, this molecule is quite stable in the absence of reactive substrates. Detailed spectroscopic, electrochemical, and crystallographic characterization has been carried out.[1,2,12] The one-electron reduction of (salen)$Cr^{v}O^{+}$ in acetonitrile has $E_{1/2}$ = 0.47 V against SCE,[2] which makes this Cr(V) complex a moderate 1-e oxidant. To the best of our knowledge, the 2-electron Cr^{V}/Cr^{III} potential has not been reported, but the process is clearly favorable thermodynamically, as shown by the successful oxygen atom transfer, a 2-e process, to various acceptors.

Even though a large volume of mechanistic work on (salen)$Cr^{V}O^{+}$ exists, challenges remain. For example, the distinction between 1-e and 2-e reduction is not always straightforward. Sometimes, conclusions reached in some laboratories[13] contradict those from others,[14] as in the oxidation of organic sulfides. Organic amines appear to have no consistent reactivity patterns, and both 1-e and 2-e reactions have been proposed depending on the choice of the amine and reaction conditions.[3] One would expect a straightforward chemistry with inorganic 1-e reductants, such as $V^{IV}O^{2+}$, but this, too is complicated by the formation of a dimetallic intermediate.[15]

The oxidation of TMB to its intensely absorbing, stable radical cation has made it useful as both a reagent and kinetic probe in mechanistic studies in aqueous and nonaqueous solvents.[16-20] TMB is also an efficient photosensitizer for reductions of various substrates in both solution and micelles.[21-24] These features seem well suited to address some of the key factors responsible for the kinetic and mechanistic differences, as well as similarities between homogeneous and heterogeneous electron transfer that we wish to discuss in this work.

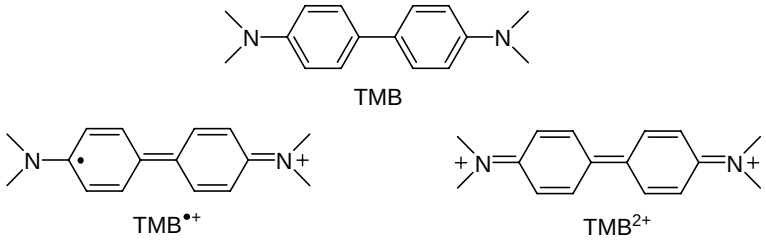

In our recent work on the reaction of (salen)$Cr^{V}O^{+}$ with another amine, tetramethylphenylene diamine (TMPD), we have unequivocally demonstrated an initial 2-e interaction followed by comproportionation with TMPD which yielded $TMPD^{\bullet+}$ as the ultimate product.[25] The assignment of the oxidation state to the initial product of the TMB reaction was initially thwarted by the widely disparate and sometimes conflicting spectral data[19,26-30] for the two oxidized forms, $TMB^{\bullet+}$, and TMB^{2+}. Part of the problem appears to lie in the similarity of the visible spectra of these two species, which has sometimes led to erroneous assignment of the reaction product.[26] We have therefore re-determined and assigned the UV-Vis spectra of TMB, $TMB^{\bullet+}$, and TMB^{2+} by a combination of spectral measurements and redox titrations with Cu^{2+} in CH_3CN/H_2O (9:1, v/v).

Experimental

Synthesis of amine-functionalized mesoporous silica nanoparticle. This material was synthesized by a co-condensation reaction.[31-33] A mixture of cetyltrimethylammonium bromide (CTAB, 5.49 mmol), 2.0 mol / L of aqueous NaOH (7 mL, 14 mmol) and water (480 mL, 26.67 mol) was heated at 80 ^{o}C for 30 min. Tetraethylorthosilicate (TEOS, 10 mL, 51.40 mmol) and 3-aminopropyltrimethoxysilane (2 mmol) were rapidly injected into the vigorously stirred solution, forming a solid white precipitate. After 2 hours, the precipitate was separated by hot filtration, washed with copious amount of methanol and dried under

vacuum overnight. Acid extraction was used to remove the surfactant (CTAB) by placing 1.0 gram of the solid material in methanol (100 mL)/ hydrochloride acid (1.0 mL) solution at 60 ^{o}C and vigorously stirring the suspension for 6 hours. The resulting AMSN was collected by hot filtration, washed with large amounts of water and methanol and dried at 90 ^{o}C under vacuum overnight.

Synthesis of MSN-(salen) and MSN-(salen)Cr^{III}. The synthetic procedure was derived from the literature[34,35] and is outlined in Figure 8-1. The notation MSN-(salen)Cr^{III} and MSN-(salen)Cr^{V}O will be used for the two oxidation states of chromium attached to the support. Even though the overall charges and the coordination sphere around the chromium are probably the same as for the solution species, that information could not be directly confirmed, which is why we use this less explicit notation for the supported species.

MSN-(salen). 1.0 g of aminopropyl-functionalized MSN was activated by heating at 120 ^{o}C under high vacuum overnight. The activated AMSN was stirred in 20 mL refluxing ethanol with 4-tert-butyl-2,6-diformylphenol (1.0 mmol) for 12 hours under N_2. The solid was separated by hot filtration and washed with copious amounts of ethanol and dried in air. The dried solid was stirred with 1,2-diaminoethane (1.0 mmol) in 20 mL ethanol at reflux for another 12 hours, separated by hot filtration and washed with excess ethanol. Following the separations and washing, the solid was stirred with 2-hydroxylbenzaldehyde (1.0 mmol) in refluxing ethanol for another 12 hours. After hot filtration and washing by ethanol, the solid (SalenMSN) was dried at 90^{o}C under high vacuum overnight.

MSN-(salen)Cr^{III}. MSN-(salen) (1.1g, including about 0.5 mmol salen ligand) was stirred with 1.25 equiv. $CrCl_2$ in 10mL dry THF at room temperature under N_2 for 6 hours and then stirred in air for another 3h.[34,35] The product MSN-(salen)Cr^{III} was filtered, washed with water and ethanol, and dried at 90^{o}C under vacuum overnight.

Characterization of MSN-(salen)Cr^{III}

Powder XRD experiments were performed on a Scintag XDS 2000 diffractometer using a Cu Kγ radiation source. Low angle diffraction with a 2θ range of 1 to 10° was used to investigate the long-range order of the materials (d_{100} = 38.40Å, d_{110} = 22.6Å, d_{200} = 19.30Å, Figure 8-2. The surface area (S_{BET} = 789.41m^2/g) and pore diameter (D_{BJH} =

22.40Å) were measured using N_2 adsorption/desorption measurements in a Micromeritics ASAP 2000 BET surface analyzer system, Figure 8-3. Data from powder XRD, BET isotherms and BJH pore size distribution show that MSN-(salen)Cr^{III} still has the typical MSN high surface area, narrow pore size distribution and ordered hexagonal pore structure, which were further confirmed by transmission electron microscopy (TEM) image shown in Figure 8-4. TEM results for MSN-(salen)Cr^{III} reveal that the parallel mesoporous channels, which are one of the specific features of MSN. The loadings of salen ligand and Cr-salen complex were determined via TGA and EDX respectively. Both measurements indicated that approximately 0.5 mmol/g of catalyst was loaded on the surface of MSN.

Solid-state NMR. The measurements were performed at 9.4 T and 14.1 T on a Chemagnetics Infinity spectrometer and a Varian NMR system 600 spectrometer, equipped with 5 mm and 3.2 mm MAS double-tuned probes, respectively. ^{13}C and ^{29}Si chemical shifts were all referenced with respect to tetramethylsilane (TMS) at 0 ppm. The experimental conditions are listed below with the following symbols: B_0 denotes the static magnetic field, ν_R the rate of sample rotation , ν_{RF}^H and ν_{RF}^X the magnitude of radio frequency magnetic fields applied to ^1H and X spins, τ_{RD} the relaxation delay, τ_{CP} the cross polarization time, and NS the number of scans.

^1H-^{13}C CP/MAS. For the salen ligand and MSN-(salen): B_0 = 9.4 T; ν_R = 10 kHz; ν_{RF}^H during excitation = 50 kHz; ν_{RF}^H during CP = 35 kHz; ν_{RF}^H during TPPM decoupling = ~42 kHz; ν_{RF}^C = 45 kHz; τ_{RD} = 2 s; τ_{CP} = 2 ms; NS = 256 and 8192 for the salen ligand and MSN-(salen), respectively. For MSN-(salen)-Cr^{III}: B_0 = 14.1 T; ν_R = 20 kHz; ν_{RF}^H during excitation = 84.7 kHz; ν_{RF}^H during CP = 70 kHz; ν_{RF}^H during TPPM decoupling = 84.7 kHz; ν_{RF}^C = 83 kHz; τ_{RD} = 1 s; τ_{CP} = 1.5 ms; NS = 34000.

^{29}Si DP/MAS. For MSN-(salen): B_0 = 9.4 T; ν_R = 8 kHz; ν_{RF}^{Si} = 62.5 kHz; ν_{RF}^H during TPPM decoupling = 35 kHz; τ_{RD} = 300 s; NS = 245. For MSN-(Salen)-Cr^{III}: B_0 = 14.1 T; ν_R = 20 kHz; ν_{RF}^{Si} = 58.8 kHz; ν_{RF}^H during TPPM decoupling = 6 kHz; τ_{RD} = 300 s; NS = 200.

Other reagents. Triflate salt of the chromium(V) complex, [(salen)$Cr^{V}(O)$](CF_3SO_3), was prepared by oxidation of the Cr(III) precursor[36] with iodosobenzene according to a literature procedure.[2,37] The concentration of (salen)$Cr^{V}(O)^{+}$ in aqueous or acetonitrile solutions was determined from the absorbance at 600 nm ($\varepsilon = 2 \times 10^3$ M^{-1} cm^{-1}).[37] Commercial (Aldrich) N,N,N',N'-tetramethylbenzidine (TMB) was purified by recrystallization from methanol.[38] Concentrations of $TMB^{\bullet+}$ ($\varepsilon_{470} = 4 \times 10^4$ M^{-1} cm^{-1})[30] and TMB^{2+} ($\varepsilon_{465} = 9 \times 10^4$ M^{-1} cm^{-1}) were determined from the spectral data obtained in this work, see later.

Kinetic samples of MSN-(salen)$Cr^{V}O$ were obtained by adding 1 mg of PhIO to a suspension of 4.5 mg of MSN-(salen)Cr^{III} in 10 mL of CH_3CN, stirring the suspension for 10 minutes, and allowing it to settle for 1 min. Each kinetic run required 3 mL of the decant that contained significant amounts of the solid (approximately 0.05 mM MSN-(salen)Cr^{III}). These kinetic samples also contained some unreacted MSN-(salen)Cr^{III} and some PhIO (dissolved and/or suspended). PhIO is unreactive toward TMB under our conditions, and thus caused no direct interference in the MSN-(salen)$Cr^{V}O$/TMB reaction. The background oxidation of MSN-(salen)Cr^{III} that was generated in the rapid MSN-(salen)$Cr^{V}O$/TMB stoichiometric reaction did, however, cause a follow-up catalytic oxidation of TMB to take place until one of the reagents was exhausted, see later. In some experiments, additional amounts of PhIO were introduced to examine the effect on reaction rates.

Kinetic studies. The experimental protocol was similar to that developed earlier in our work with supported UO_2^{2+} which demonstrated[38] that methods and techniques utilized in homogeneous solutions can be adapted for work with heterogeneous samples to yield reliable and reproducible data. Immediately upon transferring the MSN-(salen)$Cr^{V}O$ suspension (or salen)$Cr^{V}O^{+}$ solution) into a spectrophotometric cell, the reaction was initiated by adding TMB, and the absorbance was monitored at the visible absorption maxima of the radical cation $TMB^{\bullet+}$ or the dication, TMB^{2+}. The precision of the data was lower in the heterogeneous work, with an estimated standard deviation for the rates of about 50%. One source of error is associated with the difficulty in obtaining precise and reproducible amounts of the suspended particles, and thus MSN-(salen)Cr^{V}, in the kinetic samples. This was especially critical when excess Cr(V) was desired. Also, the presence of unreacted PhIO (see

above) caused some scattering the overall absorbance changes in the catalytic phase, but the kinetic data were reproducible and are considered reliable within the precision stated.

All the UV-Vis spectral and kinetic data were acquired with a Shimadzu 3101 PC instrument. In-house distilled and ion-exchanged water was further purified by passage through a Millipore Milli-Q water purification system. The fitting of the kinetic data was done with the program Kaleidagraph 3.6. Unless stated otherwise, all the kinetic and spectral work with TMB was carried out in the mixed CH_3CN/H_2O (9:1, v/v) solvent.

Results

^{13}C and ^{29}Si solid-state nuclear magnetic resonance (SSNMR) experiments were performed to provide structural information about the catalyst system under study and to determine the degree of functionalization of the MSN with the salen ligand. The ^{13}C SSNMR spectra obtained using $^{13}C\{^1H\}$ cross-polarization with magic angle spinning (CP/MAS) of as-synthesized salen ligand, salen ligand covalently attached to the silica surface (MSN-(Salen)) and salen ligand complexed with Cr^{III} covalently attached to the silica surface (Si(Salen)Cr^{III}) are shown in Figure 8-5. In all of the spectra, the peak assignments are indicated in reference to structures shown in Figure 8-6. The spectrum of salen ligand (Figure 8-5a) is consistent with that of salen containing two substituent groups, a carbonyl group attached to C(2) and a t-butyl group attached to C(4). The peak assignments are made following the previous reports on salen and μ-oxo-bis(disalicylideneiminatoiron) complexes.[39-42] The chemical shifts observed in the ^{13}C SSNMR spectrum of MSN-(salen) (Figure 8-5b) are primarily from the salen ligand attached to the MSN surface by amine linkers, as shown in Figure 8-6b. The covalent nature of the attachment is confirmed by the absence of the carbonyl resonance. Also present in spectrum *b* of Figure 5 are resonances from the residual ethoxy groups (underlying the C(9,18) and C(19) peaks),which result from washing the MSN-(salen) complex with ethanol during synthesis. The resonances denoted by '*' in Figure 8-5b are consistent with those observed earlier for unreacted surface-bound linkers.[31]

Coordination of metal species with salen-type complexes typically results in downfield chemical shifts of the imine, -N-CH_2- and C-O carbons, due to the deshielding effect from the metal.[39-43] Thus, the downfield chemical shifts of the resonances for C(7), C(8), and C(11), were observed in the spectrum of Figure 8-5c, whereas the peak representing C(9) shifted in the opposite direction. These results are consistent with coordination of Cr(III) to salen. It is also important to note that while there are unreacted amine linkers present in both MSN-(Salen) and Si(salen)Cr^{III} materials, all salen ligands were functionalized with the silica surface and all functionalized salen ligands were coordinated with Cr^{III}, as no resonances from free salen ligands or uncoordinated Cr^{III} salen ligands are present in the spectra of these materials. This is consistent with the above mentional results of TGA and EDX analysis, which yielded equal concentration of salen and Cr on the surface of MSN.

Further confirmation of the covalent attachment of the salen ligand is obtained from the ^{29}Si directly polarized (DP) MAS SSNMR spectra of MSN-(Salen) and Si(Salen) $Cr^{III}(H_2O)^+$ (Figure 8-7). The spectral region between -60 to -75 ppm represents silicon sites with covalently bound species, in positions T^3 [$(\equiv SiO)_3$**Si**R] and T^2 [$(\equiv SiO)_2$**Si**ROH]. The resonances in the chemical shift range of -90 to -130 ppm are consistent with those of typical Q-sites, representing the framework silica sites Q^4 [$(\equiv SiO)_4$**Si**] and Q^3 [$\equiv SiO)_3$**Si**(OH)]. The relative concentration of T-sites is determined via integration of the resonances and found to be 14 ±2%, in both MSN-(Salen) and Si(Salen) $Cr^{III}(H_2O)^+$ materials. The spectrum of the material containing coordinated Cr^{III} (Figure 8-7b) has the same line shape as spectrum α, again signifying that coordination of Cr^{III} does not affect the silica surface.

UV-Vis spectra of TMB, $TMB^{\bullet+}$, TMB^{2+}

The UV-Vis spectrum of TMB in CH_3CN/H_2O (9:1, v/v) exhibits λ_{max} at 310 nm ($\varepsilon_{310} = 4.5 \times 10^4$ M^{-1} cm^{-1}), Figure 8, trace *a*. In the presence of high acid concentrations (≤ 0.10 M $HClO_4$) both nitrogens of the amine are protonated. A sole maximum for $TMBH_2^{2+}$ appears at 250 nm ($\varepsilon_{250} = 2.9 \times 10^4$ M^{-1} cm^{-1}). At intermediate acid concentrations (1.0 mM), bands appear at 320 nm, believed to correspond to a combination of the singly and doubly protonated TMB, and 250 nm, where only $TMBH_2^{2+}$ absorbs. The absorbance at 250 nm was used to calculate the ratio $[TMBH_2^{2+}]/[TMBH^+] = 0.47$ at 1.0 mM $HClO_4$, and to obtain the

molar absorptivity of $TMBH^+$ at 320 nm, $\varepsilon_{320} = 3 \times 10^4\ M^{-1}\ cm^{-1}$. The observed species distribution at pH 3 leads to an apparent pK_{a1} of 2.7 in this solvent medium, close to the data reported in 1:1 CH_3OH/H_2O ($pK_{a1} = 3.1$, $pK_{a2} = 4.0$),[44] and, as expected, much smaller than in pure acetonitrile (where $pK_{a1} = 8.3$, $pK_{a2} = 10.3$).[27]

The spectra of $TMB^{\bullet+}$ and TMB^{2+} were obtained by controlled oxidation of TMB with Cu^{II} in the absence of added acid. The results of spectrophotometric titrations are shown in Figure 8-9**.** At low $[Cu^{2+}]/[TMB]$ ratios, the product exhibited a broad band around 800 nm, and a triplet-like feature with a maximum at 470 nm that is characteristic for $TMB^{\bullet+}$.[19,24,30] As the amount of Cu^{2+} increased past one equivalent, the 800 nm absorbance decreased, and the 470-nm maximum shifted to 465 nm and lost most of the triplet appearance. The titration plot at 470 nm, where both products absorb, is shown as inset *a* in Figure 9-9.

The plot of the absorbance at 520 nm against the ratio $[Cu^{2+}]/[TMB]$ shows even more clearly the successive generation of two products. The first oxidizing equivalent produces $TMB^{\bullet+}$ which is transparent at this wavelength. The addition of one more equivalent of copper converts $TMB^{\bullet+}$ to the absorbing TMB^{2+}. The chemistry of the two steps, with additional support for it described below, is shown in eq 7 and 8.

$$Cu^{2+} + TMB \rightarrow Cu^{+} + TMB^{\bullet+} \qquad (7)$$

$$Cu^{2+} + TMB^{\bullet+} \rightarrow Cu^{+} + TMB^{2+} \qquad (8)$$

From the 470-nm absorbance measured after the addition of one equivalent of Cu^{2+}, we obtained the molar absorptivity of $TMB^{\bullet+}$, $\varepsilon_{470} = 4 \times 10^4\ M^{-1}\ cm^{-1}$, in good agreement with some literature data[30], but larger than others.[27] The molar absorptivity of TMB^{2+} at its 465 nm maximum was calculated to be $9.0 \times 10^4\ M^{-1}\ cm^{-1}$, close to the reported data.[27]

Dramatic spectral changes took place upon the addition of acid, as shown in Figure 8-10. First, $TMB^{\bullet+}$ (spectrum *b*) was generated from TMB (0.017 mM, spectrum *a*) and a slight excess of Cu^{2+} (0.019 mM) in the absence of acid. Upon addition of enough 3 M $HClO_4$ to bring the acidity of the solution to 0.10 M, the spectrum of $TMB^{\bullet+}$ disappeared and was replaced with those of the doubly oxidized species (TMB^{2+}) and doubly protonated reduced form, $TMBH_2^{2+}$. Clearly, the acid caused the radical to disproportionate as in eq 9. The two products were formed in quantitative and equimolar amounts, as calculated from the

molar absorptivities determined above and summarized in Table 8-1. The reaction is reversible, so that the addition of solid $NaHCO_3$ to acidic mixtures of TMB^{2+} and $TMBH_2^{2+}$ regenerated the radical $TMB^{\bullet+}$. The identical spectra obtained for TMB^{2+} under neutral and strongly acidic conditions strongly argue that no protonation took place at high $[H^+]$. Thus, the spectral changes accompanying reactions of TMB^{2+} and $TMB^{\bullet+}$ under our conditions are believed to be associated with redox chemistry alone.

$$2TMB^{\bullet+} \underset{OH^-}{\overset{H^+}{\rightleftharpoons}} TMBH_2^{2+} + TMB^{2+} \qquad (9)$$

TMB/(salen)Cr^VO^+ reaction in solution

In these experiments, TMB (0.06-0.08 mM) was used in excess over the chromium complex (0.003-0.02 mM). The reaction was instantaneous on the time scale of conventional spectrophotometry (completion in ≤ 5 seconds), and generated different products depending on the concentration of H^+. In every case, the observations were identical regardless of whether the solution of (salen)Cr^VO^+ was prepared by dissolving the pure, independently synthesized material, or by *in situ* oxidation of Cr(III) with PhIO.

In the absence of added H^+, $TMB^{\bullet+}$ was produced according to the 2:1 stoichiometry of eq 10. Under identical conditions, except that the solvent was acidified to 0.10 M $HClO_4$, the stoichiometry changed to 1:1, and the product to doubly oxidized amine, eq 11. These results are displayed in Figure 8-11.

$$(salen)Cr^VO^+ + 2TMB\ (+\ 2\ H^+) \rightarrow (salen)Cr^{III}(H_2O)^+ + 2TMB^{\bullet+} \qquad (10)$$

$$(salen)Cr^VO^+ + TMB\ (+\ 2\ H^+) \rightarrow (salen)Cr^{III}(H_2O)^+ + TMB^{2+} \qquad (11)$$

TMB/MSN-(salen)Cr^VO – heterogeneous reaction

In 0.10 M $HClO_4$. The UV-Vis spectrum of MSN-(salen)Cr^{III} in CH_3CN exhibits a broad band at 455 nm, significantly red-shifted from the λ_{max} 420 nm in acetonitrile solution of (salen)Cr^{III}.[2] Since the coordination of chromium to salen has been unambigously confirmed by solid state NMR, the shift must be the result of a combination of factors and interactions (polar, hydrogen bonding) with the support.

After stirring the suspension with PhIO for 10 minutes, the 455-band was diminished but still present, as shown in Figure 8-11, indicating that only a fraction of Cr^{III} was

converted to Cr^{V}. No new features were observed around 600 nm, where MSN-(salen)$Cr^{V}O$ is expected to absorb, in analogy with the solution species. The reason, we believe, are the small concentrations of (salen)$Cr^{V}O$ produced, and some loss in signal quality caused by light scattering and by the fact that the 600-nm band is quite broad even in solution. Despite the lack of direct spectral evidence for MSN-(salen)$Cr^{V}O$, there is no doubt that the oxidized form was produced as shown by rapid formation (in mixing time) of $TMB^{\bullet+}$ when limiting amounts of TMB were added, eq 12. This behavior is qualitatively the same as that described above for the solution species under analogous conditions.

$$\text{MSN-(salen)}Cr^{V}O + 2TMB \rightarrow 2TMB^{\bullet+} + \text{MSN-(salen)}Cr^{III} \quad \text{fast} \quad (12)$$

With TMB in excess or comparable to MSN-(salen)$Cr^{V}O$, the radical $TMB^{\bullet+}$ was again formed, but now in two stages, as shown in Figure 8-12.

We attribute the fast initial absorbance jump to the reaction of the preformed Cr(V), and the slower step to the catalytic reaction, presumed to have the formation of MSN-(salen)$Cr^{V}O$ from PhIO and MSN-(salen)Cr^{III}, eq 13, as the rate-limiting step. The source of MSN-(salen)$Cr^{III}(H_2O)$ is either the starting material that had not been oxidized to MSN-(salen)$Cr^{V}O$ during the 10-min oxidation process, see Experimental, or that regenerated in reaction 12.

$$\text{MSN-(salen)}Cr^{III} + PhIO \rightarrow \text{MSN-(salen)}Cr^{V}O + PhI \quad (13)$$

The catalytic aspect of the slower stage was confirmed in an experiment starting with a much smaller amount of MSN-(salen)Cr^{III} (0.005 mM) and excess PhIO (0.02 mM), Figure 8-13. The reaction with excess TMB (0.03 mM) was monitored at 500 nm where the product has a molar absorptivity of 2.9×10^{4} M^{-1} cm^{-1}. Under these conditions, all of the oxidizing equivalents from PhIO were utilized to generate 0.02 mM TMB^{2+}, again in a kinetically clean but slower process, as expected for the conditions chosen.

In another set of experiments, the reaction was conducted side by side in solution and with the supported species. The results are displayed in Figure 8-15. Except for the ten times lower concentration of (salen)Cr(III) (0.005 mM) in solution, all the other conditions and concentrations are identical and given in the caption.

From the initial absorbance jump obtained for the supported material, trace *a* in Figure 8-14, the concentration of the initially present (salen)Cr^{V} was calculated as ~0.007

mM. The follow-up catalytic reaction accomplishes approximately two more cycles before all of the TMB is oxidized.

The lower concentration of the catalyst in the homogeneous solution resulted in a much smaller initial concentration of (salen)$Cr^{V}O^{+}$ (0.001 mM), requiring a larger number of cycles and longer times in the catalytic phase to complete the reaction, trace *b* in Figure 8-14**.** Overall, however, the times required for the completion of the two reactions were not greatly different. In fact, the initial rates in the catalytic phase, displayed in the inset to Figure 8-14, are quite similar, leading us to conclude that homogeneous catalysis is only slightly more efficient. With the estimated concentration of the active catalyst only about seven times larger under heterogeneous conditions, the efficacy of catalysis is certainly within the same order of magnitude as that in homogeneous solution.

In the absence of added acid. Unlike the homogeneous reaction, which was instantaneous under all of our conditions, the heterogeneous reaction became visibly slower when no acid was added. This is illustrated in Figure 8-15 where trace *a* denotes the reaction in 0.10 M $HClO_4$, and trace *b* in the absence of added H^{+}. In both experiments, (salen)$Cr^{V}O$ was generated from 0.047 mM MSN-(salen)Cr^{III} and PhIO in the absence of acid, as described in Experimental, followed by the addition of $HClO_4$ and TMB (in that order) in experiment a, or TMB only in experiment *b*. All the concentrations were identical in the two experiments, but the absorbance changes differ because different products are formed at the two acidities used, as already discussed and illustrated in Figure 8-12 Reaction *a* is decidedly faster than reaction *b*.

To determine whether the rate reduction in the absence of acid was caused by slower chemistry or by diminished amounts of the catalyst in the Cr(V) form, we interrupted experiment *b* (no $HClO_4$) by sudden addition of $HClO_4$, final concentration 0.10 M. As shown in trace *c* in Figure 8-15, the addition of acid failed to restore trace a*,* and instead caused only a small absorbance jump, showing that the concentration of MSN-(salen)Cr^{V} was smaller than in *a*. The subsequent catalytic step was also slower, which is now easily explained by the lower concentration of the active form of the catalyst.

The rates and product yields in the absence of added $HClO_4$ were examined as a function of concentrations/amounts within the experimentally allowed precision for all the

species involved. Table 2 summarizes the data. The rates responded to changes in all three concentrations, i. e. MSN-(salen)Cr^{III}, PhIO, and TMB. As was already clear from the data in Figure 8-15**,** no single kinetic step appears to be rate-controlling. Rather, a combination of the generation of the active catalyst (eq 13) and oxidation of TMB (eq 12) contribute to the observed rate. This results in an apparent third order reaction, eq 14, with $k_{14} = (7 \pm 4) \times 10^6$ M^{-2} s^{-1}.

$$\text{Rate} = k_{14}\,[\text{Catalyst}][\text{PhIO}][\text{TMB}] \qquad (14)$$

Discussions

We placed several requirements on the supported catalyst for this study. The complex had to be covalently bound to the silica surface to prevent leaching and interference from homogeneous chemistry. The surface sites containing the catalyst had to be equivalent chemically and structurally to allow equal access of reactants and departure of products. Ideally, the density of catalytic sites would be large enough to allow the chemistry to proceed rapidly, but low enough to avoid diffusional limitations, secondary chemistry, and nonbonding interactions between supported catalyst molecules.

Solid state NMR data and reactivity results show that the catalyst has indeed fulfilled these requirements. The covalent attachment of the salen ligand to the MSN surface (containing amine linkers), and coordination of metal to all the available salen sites were confirmed by NMR, as shown in the Result Section. The good quality of kinetic traces, especially under conditions (0.10 M $HClO_4$) having a well-defined rate determining step, from Figures 8-12 to Figure 8-14, strongly argues that the sought uniformity of catalytic sites has been achieved.

In acidic solutions, the results obtained with MSN-(salen)$Cr^{V}O$ are strikingly similar to those obtained in homogeneous solution under comparable conditions. In both cases, the oxidation of TMB with available Cr(V) was complete in mixing time. This was followed by a slower, catalytic phase that generated more product in a set of kinetically unresolved steps involving TMB, PhIO, and either suspended (Si(salen)Cr^{III}) or dissolved (salen)$Cr(H_2O)^{+}$) chromium complex. The similarity in behavior and reaction rates of the two systems in

Figure 8-14 shows the supported species to have the reactivity approaching that of the solution species to within less than an order of magnitude.

Qualitatively similar observations have been made recently for the oxidation of benzyl alcohol with H_2O_2 catalyzed by MSN-(salen)Cr^{III}. It was shown that both the conversion and selectivity to aldehyde increased relative to those obtained with the homogeneous (salen)Cr^{III}.[47] In that work, the attachment to the support was achieved through a ligand coordinated to the chromium, unlike in our case where a covalent C-Si bond has been established between the salen ligand and silica support. In several other reported cases, the activity of (salen)Cr^{III} on various supports also appeared acceptably close or better than the solution species in reactions such as CO_2 addition to epoxides,[48], asymmetric ring opening[49], enantioselective epoxidation[50], and others.[50] These studies provided useful and important phenomenological observations, although detailed kinetic and mechanistic data have not been obtained.

In the present work with the supported material in the absence of acid, a rate constant $k = 7.4 \times 10^6$ M^{-2} s^{-1} was determined over a moderate range of concentrations for the catalytic oxidation of TMB. We consider this value only an approximation that may or may not be valid outside of the range examined. None the less, having a rate law and a rate constant is extremely useful as it provides a quantitative standard against which one can gauge changes in catalyst performance.

One such change was observed when $HClO_4$ was added to the MSN-(salen)Cr^{III}-PhIO-TMB reaction. As shown in Figures 8-12, 8-13 and 8-14, the rates increased, and kinetic traces adopted the zero-order appearance expected for a catalytic reaction limited by the generation of the active form of the catalyst. The source of the acid dependence was traced to the greater concentration of the catalyst when $HClO_4$ was present. The reason for higher Cr(V) concentrations has not been established, but the results suggest that a greater concentration of H^+ at or close to the support surface may facilitate the approach of PhIO by hydrogen bonding or polar interactions, and promote the oxidation of Cr(III) to Cr(V).

A different effect of acid in this work is related to the reductant itself, and, in a more general sense, to the pH-induced changes in thermodynamics. Such phenomena play a role in the general area of energy storage and generation of kinetic (as opposed to thermodynamic

products). In the present work, the decrease in pH changes products from the radical cation to a mixture of reduced and doubly oxidized species. The relevant equilibria are shown in eq 15 and 16.

$$2TMB^{\bullet+} + 2H^{+} \rightleftharpoons TMBH_2^{2+} + TMB^{2+} \qquad \log K = +3.6 \qquad (15)$$

$$2TMB^{\bullet+} \rightleftharpoons TMB + TMB^{2+} \qquad \log K = -3.4 \qquad (16)$$

The equilibrium constants K_{15} and K_{16} can be calculated from the pKa for $TMBH_2^{2+}$ (3.1) and $TMBH^{+}$ (4.0) reported in 1:1 $MeOH/H_2O$,[44], and the reduction potentials for the singly and doubly oxidized TMB in acetonitrile[45]. The values obtained are log K = 3.6 for the disproportionation of $TMB^{\bullet+}$ according to eq 15, and -3.4[45] according to eq 16. The difference of about seven orders of magnitude in the equilibrium constant denotes great stability of the doubly oxidized form in acidic solutions, and provides thermodynamic explanation for the dramatic change in products of TMB oxidation with changes in $[H^{+}]$.

Similar calculations for the closely related TMPD (E_1 = 0.12 V *vs* SCE for $TMPD^{\bullet+}/TMPD$,[51] and E_2 = 0.72 V for $TMPD^{2+}/TMPD^{\bullet+}$, i. e. 0.6 V greater than E_1[52]) yielded log K = -10 for disproportionation of $TMPD^{\bullet+}$ in the absence of added acid, and -1.7 in the equivalent of eq 14 to yield TMPD and $TMPDH_2^{2+}$.[25] Clearly, even in acidic solutions the disproportionation is unfavorable, and the radical $TMPD^{\bullet+}$ is the expected and observed[25] product. In addition, the 1-e cross-reaction to give the radical and $(salen)Cr^{IV}O$ is downhill, at least in acetonitrile, based on $E_{1/2}$ = 0.47 V against SCE for $(salen)Cr^{V}O^{+}/(salen)Cr^{IV}O$ couple.[2]

This analysis makes the observed[25] single-step 2-e oxidation of TMPDeven more surprising, but the (unknown) 2-e reduction potential for $(salen)Cr^{V}O^{+}$ is clearly large enough to accomplish the reaction. Upon addition of one or more equivalents of TMPD, the rapid comproportionation step generates stoichiometric amounts of $TMPD^{\bullet+}$, in agreement with the thermodynamic predictions.

The mechanism of the TMB oxidation in either phase has not been established, but we favor a route similar to that used by TMPD in view of the fact that the 2-e reaction is thermodynamically much more favorable for TMB than for TMPD.

Conclusions

Chromium(III) salen-catalyzed oxidation of tetramethylbenzidine (TMB) with iodosobenzene was selected as a model reaction for a comparative study of catalytic activity under homogeneous and heterogeneous conditions. The kinetics of the heterogeneous reaction are well-behaved, as would be expected for a material having an easily accessible, well-defined chemical species, i.e.(salen)Cr^{III}, covalently attached inside the mesopore. Solid-state NMR data and well-behaved kinetics strongly argue for the chemical and structural uniformity of catalytic sites in the heterogeneous catalyst. The catalytic rates approach those observed in homogeneous solutions of (salen)Cr(H2O)$^{+}$ under comparable conditions. Reaction products are pH-dependent and change from the radical cation $TMPD^{\bullet+}$ in neutral solutions to the doubly oxidized $TMPD^{2+}$ at pH=1.

Acknowledgment

This manuscript has been authored under Contract No. DE-AC02-07CH11358 with the U.S. Department of Energy.

References

(1) Siddall, T. L.; Miyaura, N.; Huffman, J. C.; Kochi, J. K. *J. Chem. Soc., Chem. Commun.* **1983**, 1185-1186.

(2) Srinivasan, K.; Kochi, J. K. *Inorg. Chem.* **1985**, *24*, 4671-4679.

(3) Venkataramanan, N. S.; Kuppuraj, G.; Rajagopal, S. *Coord. Chem. Rev.* **2005**, *249*, 1249-1268.

(4) Rihter, B.; SriHari, S.; Hunter, S.; Masnovi, J. *J. Am. Chem. Soc.* **1993**, *115*, 3918-3924.

(5) Lane, B. S.; Burgess, K. *Chem. Rev.* **2003**, *103*, 2457-2473.

(6) Yoon, T. P.; Jacobsen, E. N. *Science* **2003**, *299*, 1691-1693.

(7) Jacobsen, E. N. *Acc. Chem. Res.* **2000**, *33*, 421-431.

(8) Baleizao, C.; Garcia, H. *Chem. Rev.* **2006**, *106*, 3987-4043.

(9) Bryliakov, K. P.; Talsi, E. P. *Inorg. Chem.* **2003**, *42*, 7258-7265.

(10) Zheng, X.; Jones, C. W.; Weck, M. *J. Am. Chem. Soc.* **2007**, *125*, 1105-1112.

(11) Canali, L.; Sherrington, D. C. *Chem. Soc. Rev.* **1999**, *28*, 85–93.

(12) Samsel, E. G.; Srinivasan, K.; Kochi, J. K. *J. Am. Chem. Soc.* **1985**, *107*, 7606-7617.

(13) Sevvel, R.; Rajagopal, S.; Srinivasan, C.; Alhaji, N. I.; Chellamani, A. *J. Org. Chem.* **2000**, *65*, 3334-3340.

(14) Lepage, C. R. J.; Mihichuk, L.; Lee, D. G. *Can. J. Chem.* **2003**, *81*, 75-80.

(15) Kanthimathi, M.; Nair, B. U.; Ramasami, T. *Transition Metal Chemistry (Dordrecht, Netherlands)* **2003**, *28*, 760-764.

(16) Neta, P.; Huie, R. E. *J. Phys. Chem.* **1985**, *89*, 1783-1787.

(17) Balla, J.; Espenson, J. H.; Bakac, A. *J. Phys. Chem. A* **1995**, *99*, 3598-3604.

(18) Chung, K.-T.; Chen, S.-C.; Wong, T. Y.; Li, Y.-S.; Wei, C.-I.; Chou, M. W. *Toxicological Sciences* **2000**, *56*, 351-356.

(19) Rao, P. S.; Hayon, E. *J. Phys. Chem.* **1975**, *79*, 1063-1066.

(20) Neta, P.; Huie, R. E.; Mosseri, S.; Shastri, L. V.; Mittal, J. P.; Maruthamuthu, P.; Steenken, S. *J. Phys. Chem.* **1989**, *93*, 4099-4104.

(21) Frank, A. J.; Graetzel, M. *Inorg. Chem.* **1982**, *21*, 3834-3837.

(22) Pan, Y.; Zhao, J.; Ji, Y.; Yan, L.; Yu, S. *Chemical Physics* **2006**, *320*, 125-132.

(23) Ranjit, K. T.; Kevan, L. *J. Phys. Chem. B* **2002**, *106* 9306-9312.

(24) Arce, R.; Kevan, L. *J. Chem. Soc., Faraday Trans. 1* **1985**, *81*, 1669-1676.

(25) Chaka, G.; Bakac , A. **2008**.

(26) Kiruthiga, K.; Aravindan, P.; Anandan, S.; Maruthamuthu, P. *Res. Chem. Intermed.* **2006**, *32*, 115-135.

(27) Saget, J. P.; Plichon, V. *Bull. Soc. Chim. France* **1969**, 1395-1401.

(28) Indelli, M. T.; Ballardini, R.; Scandola, F. *J. Phys. Chem.* **1984**, *88*, 2547-2551.

(29) Barek, J.; Berka, A.; Novakova, L. *Coll. Czech. Chem. Commun.* **1978**, *43*, 1597-1605.

(30) Guichard, V.; Bourkba, A.; Poizat, O.; Buntinx, G. *J. Phys. Chem.* **1989**, *93*, 4429-4435.

(31) Huh, S.; Wiench, J. W.; Yoo, J.-C.; Pruski, M.; Lin, V. S.-Y. *Chem. Mater.* **2003**, *15*, 4247-4256.

(32) Huh, S.; Wiench, J. W.; Trewyn, B. G.; Song, S.; Pruski, M.; Lin, V. S.-Y. *Chem. Comm.* **2003**, 2364-2365.

(33) Radu, D. R.; Lai, C.-Y.; Huang, J.; Shu, X.; Lin, V. S.-Y. *Chem. Comm.* **2005**, 1264-1266.

(34) Kim, G.-J.; Shin, J.-H. *Catal. Lett.* **1999**, *63*, 205-212.

(35) Baleizao, C.; Gigante, B.; Sabater, M. J.; Garcia, H.; Corma, A. *Appl. Cat.* **2002**, *228*, 279-288.

(36) Yamada, S.; Iwasaki, K. *Bull. Chem. Soc. Japan* **1969**, *42*, 1463.

(37) Bakac, A.; Guzei, I. A. *Inorg. Chem.* **2000**, *39*, 736-740.

(38) Yang, H.; Wipf, D. O.; Bard, A. J. *J. Electroanal. Chem.* **1992**, *331*, 913-924.

(39) Aranha, P. E.; dos Santos, M. P.; Romera, S.; Dockal, E. R. *Polyhedron* **2007**, *26*, 1373-1382.

(40) Signorini, O.; Dockal, E. R.; Castellano, G.; Oliva, G. *Polyhedron* **1996**, *15*, 245-255.

(41) Bottino, F. A.; Finocchiaro, P.; Libertini, E. *J. Coord. Chem.* **1988**, *16*, 341-345.

(42) Murray, K. S. *J. Chem. Soc., Dalton Trans.* **1975**, 1538-1942.

(43) Luo, Y.; Lin, J. *Microporous Mesoporous Mater.* **2005**, *86*, 23-30.

(44) Beck, S. M.; Brus, L. E. *J. Am. Chem. Soc.* **1983**, *105*, 1106-1111.

(45) Kratochvil, B.; Zatko, D. A. *Anal. Chem.* **1968**, *40*, 422-424.

(46) Bock, C. R.; Connor, J. A.; Gutierrez, A. R.; Meyer, T. J.; Whitten, D. G.; Sullivan, B. P.; Nagle, J. K. *J. Am. Chem. Soc.* **1979**, *101*, 4815-4824.

(47) Wang, X.; Wu, G.; Li, J.; Zhao, N.; Wei, W.; Suna, Y. *J. Mol. Cat. A* **2007**, *276*.

(48) Alvaro, M.; Baleizao, C.; Das, D.; Carbonell, E.; García, H. *J. Catal.* **2004**, *228*, 254–258.

(49) Dioos, B. M. L.; Geurts, W. A.; Jacobs, P. A. *Catal. Lett.* **2004**, *97*, 125-129.

(50) Heckel, A.; Seebach, D. *Helv. Chim. Acta* **2002**, *85*, 913 - 926.

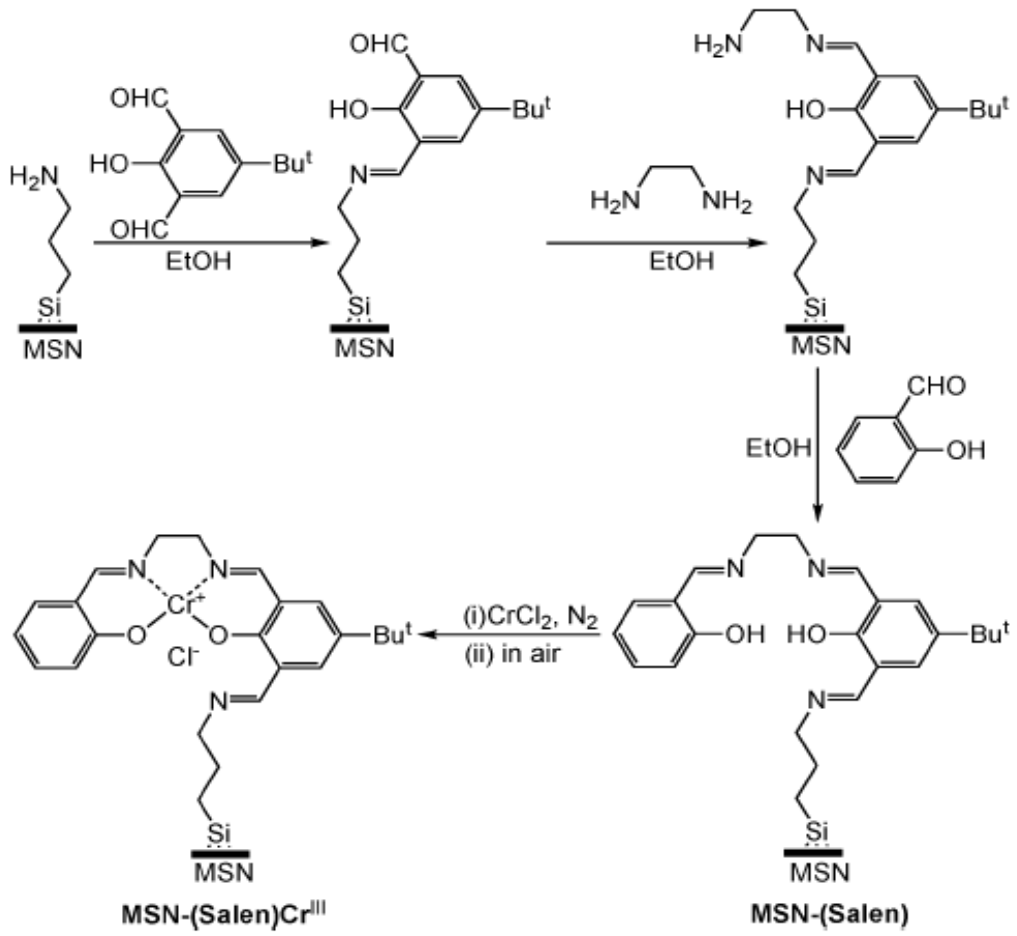

Figure 8-1. Synthetic procedure for the preparation of MSN-(salen) and MSN-(salen)Cr^{III}.

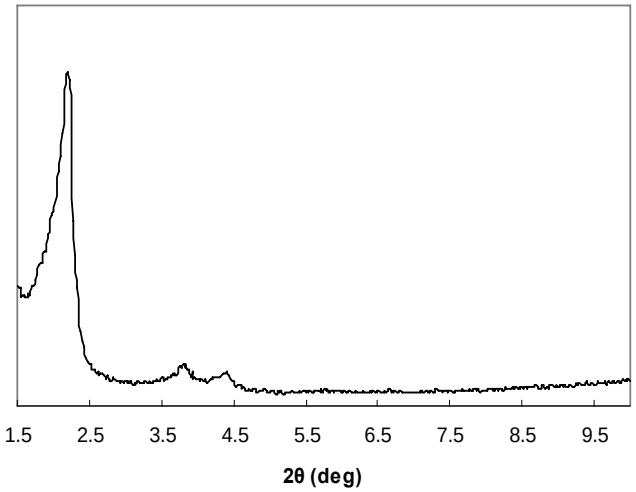

Figure 8-2. Powder XRD pattern of MSN-(salen)Cr^{III}.

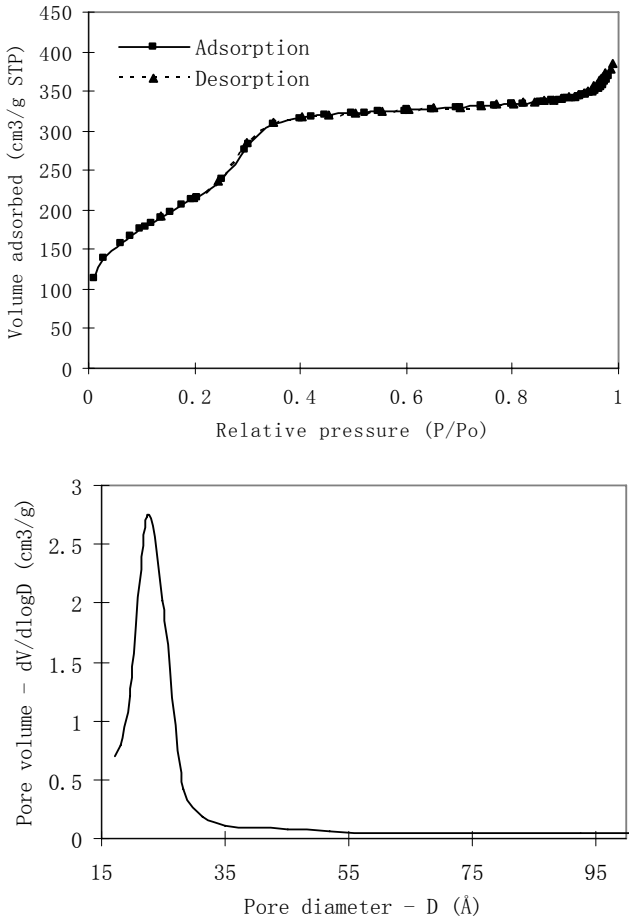

Figure 8-3. BET isotherms (above) and BJH pore size distributions (bottom) of MSN-(salen)Cr^{III}.

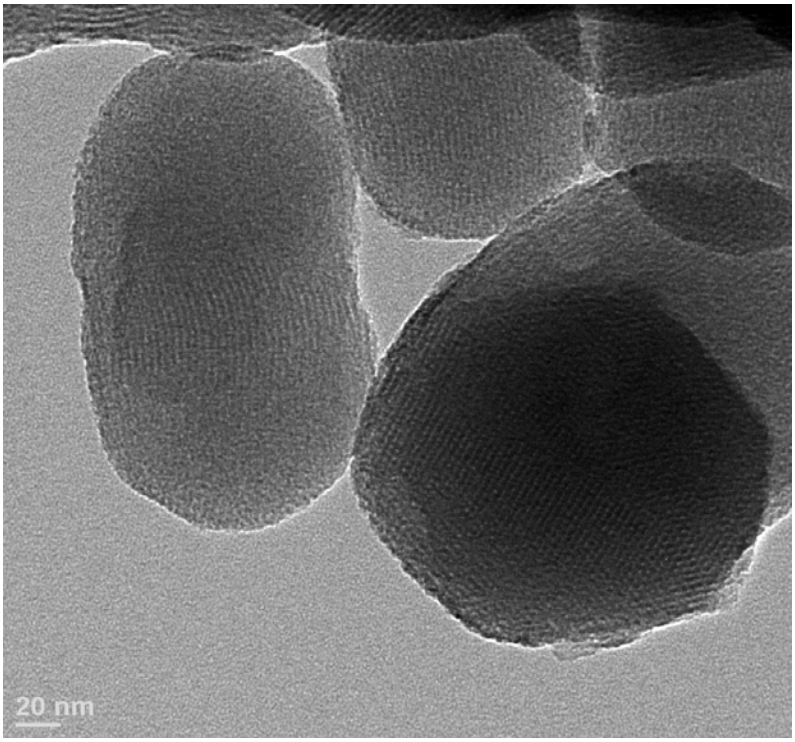

Figure 8-4. TEM image of Cr^{III}SalenMSN.

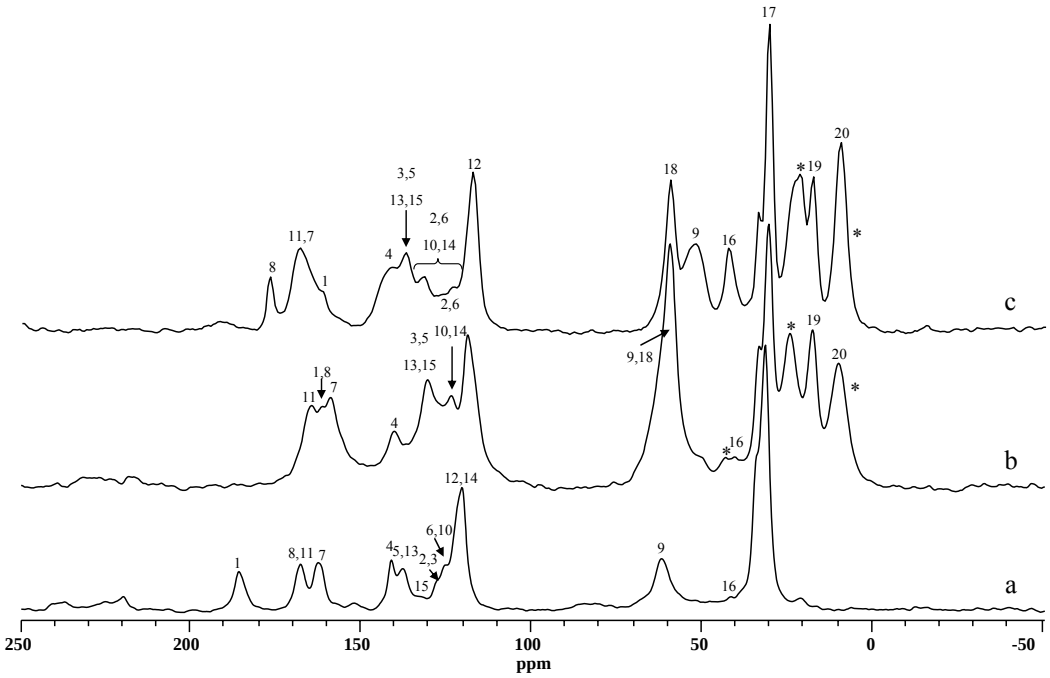

Figure 8-5. ^{13}C CP/MAS solid-state NMR spectra of: (a) as-synthesized salen ligand, (b) salen ligand covalently attached to the surface of MSN (MSN-(Salen) and (c) salen ligand complexed with Cr^{III} and covalently attached to the surface of MSN (Si(salen)Cr^{III}. The asterisks denote resonances due to unreacted amine linkers.

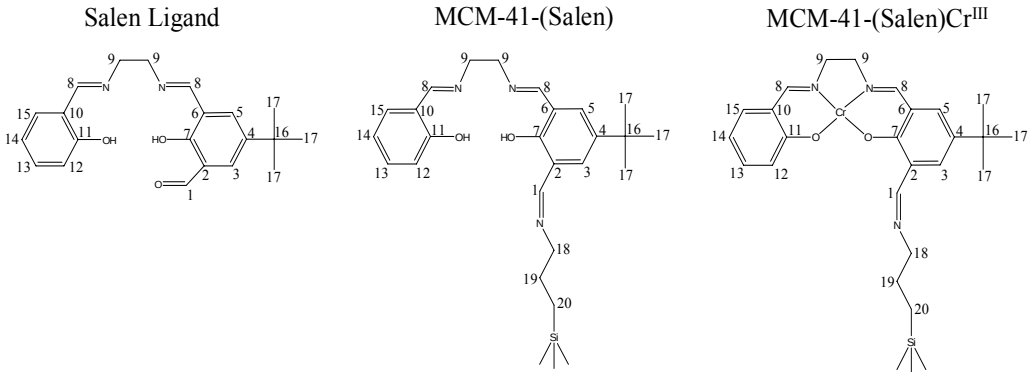

Figure 8-6. Structures of the salen complexes with carbon sites numbered for ^{13}C NMR analysis and assignments.

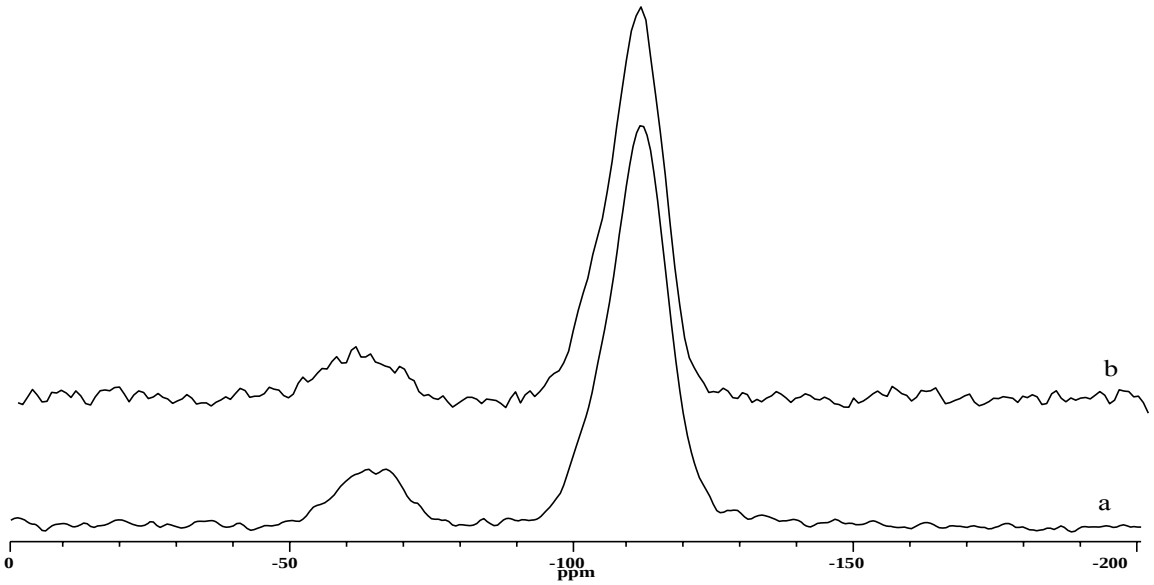

Figure 8-7. ^{29}Si DP/MAS solid-state NMR spectra of (a) salen ligand covalently attached to the surface of MSN (MSN-(Salen) and (b) salen ligand complexed with Cr^{III} and covalently attached to the surface of MSN ($Si(Salen)Cr^{III}(H_2O)^{+}$).

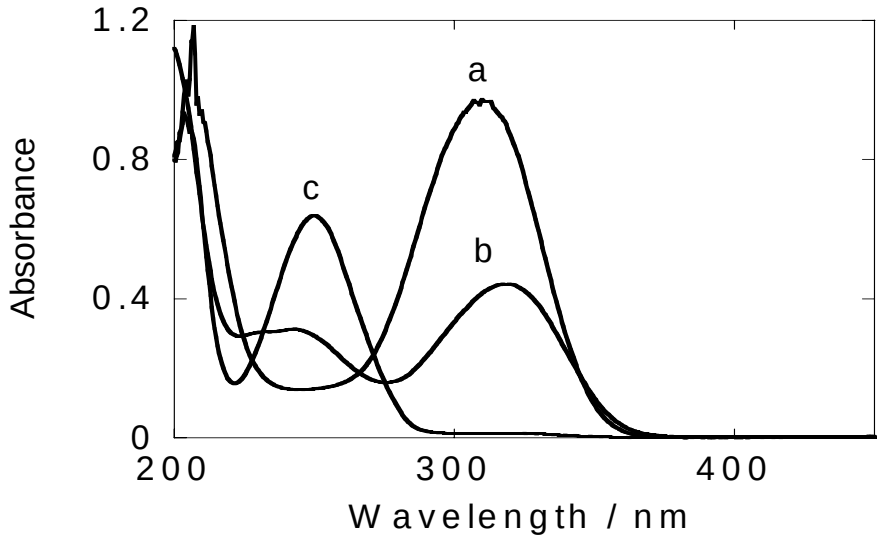

Figure 8-8. Uv-Vis spectra of TMB (0.022 mM) in CH_3CN/H_2O (9:1) with no acid added (a), 1.0 mM $HClO_4$ added (b), and 0.10 M $HClO_4$ added (c). Spectrum *b* is a mixture of 0.015 mM $TMBH^{+}$ and 0.007 mM $TMBH_2^{2+}$.

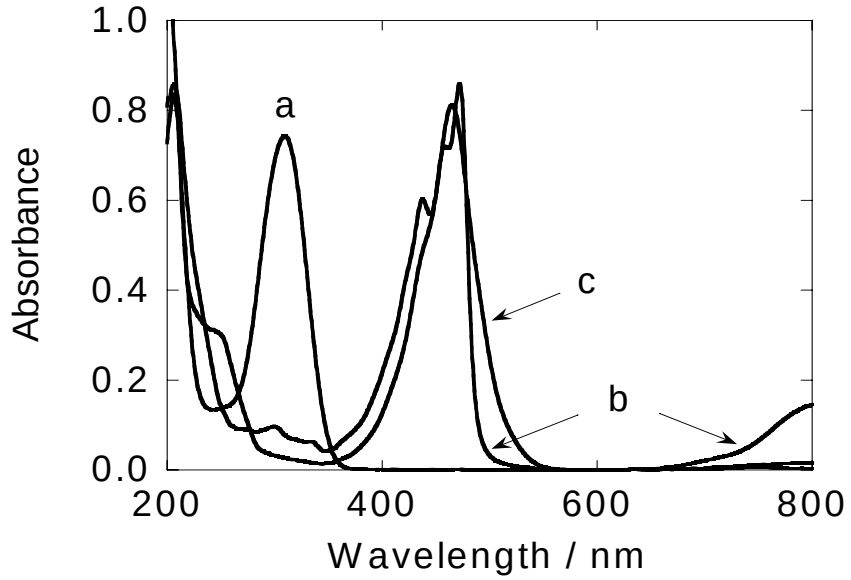

Figure 8-9. Titration of TMB (1.7×10^{-5} M) with $Cu(ClO_4)_2$. Insets: plots of absorbance vs. $[Cu^{2+}]/[TMB]$at 470 nm (a) and 520 nm (b).

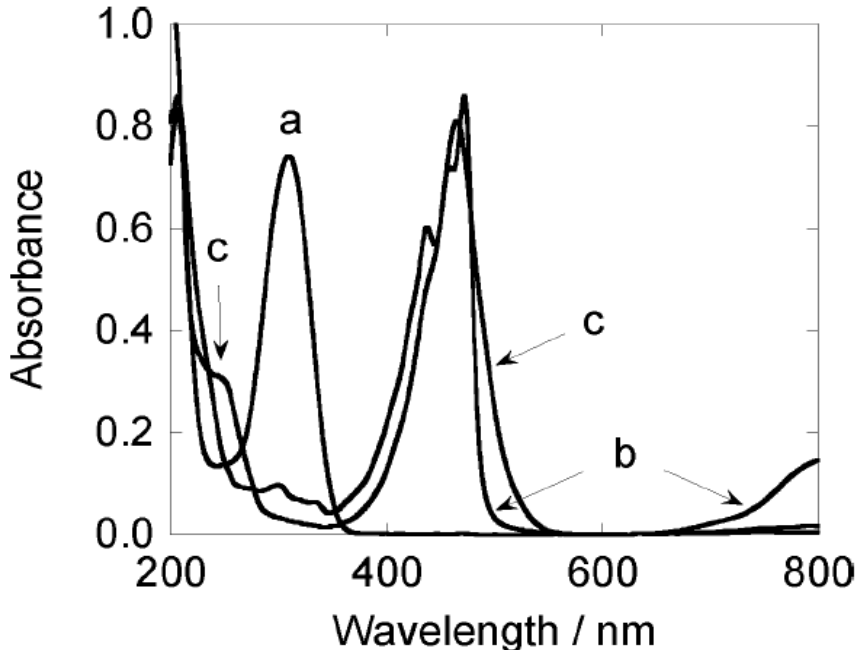

Figure 8-10. UV-vis spectra of: (a) TMB (0.017 mM) in CH_3CN/H_2O (9:1), (b) $TMB^{\bullet+}$ obtained by addition of 0.019 mM $Cu(ClO_4)_2$ to *a*; and (c) mixture of TMB^{2+} and $TMBH_2^{2+}$ generated by acidifying solution *b* to 0.10 M $HClO_4$.

Table 8-1. Summary of Spectral, pKa, and Electrochemical Data for TMB

Species	λ_{max}/nm	$\varepsilon/10^4$ M^{-1} cm^{-1}	E/V (reference)	Source
TMB	310	4.5		
$TMBH^+$	320	~3.0		
$TMBH_2^{2+}$	250	2.9		
$TMB^{\bullet+}$ [a, b]	470	4.0	0.10 ($Ag/AgNO_3$)	45
			0.115 (Ag/Ag^+)	27
			0.43 (SCE)	46
TMB^{2+}	465	9.0	0.30 ($Ag/AgNO_3$)	45
			0.305 (Ag/Ag^+)	27

[a] Reduction potentials in acetonitrile. [b] In water

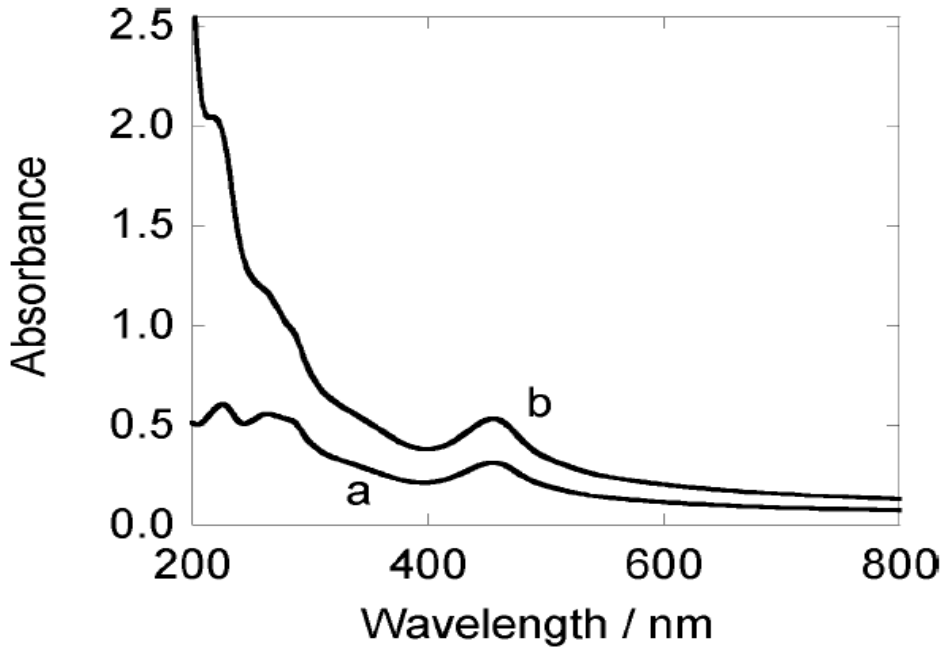

Figure 8-11. UV-vis spectrum of MSN-(salen)Cr^{III} in CH_3CN (a), and after oxidation with PhIO (b).

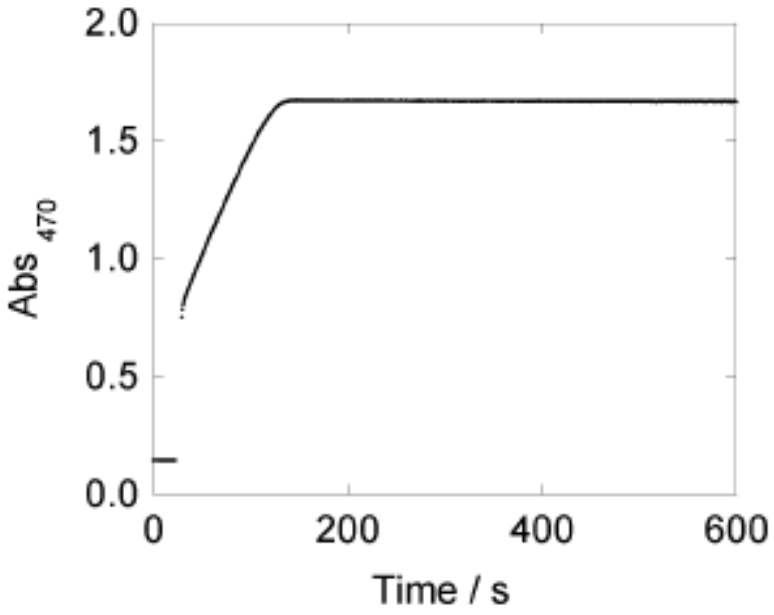

Figure 8-12. Kinetic traces at 470 nm for the reaction of MSN-(salen)Cr^{III} (0.05 mM) with PhIO (0.05 mM) in the presence of TMB (0.017 mM) in CH_3CN/H_2O (9:1) in 0.10 M $HClO_4$.

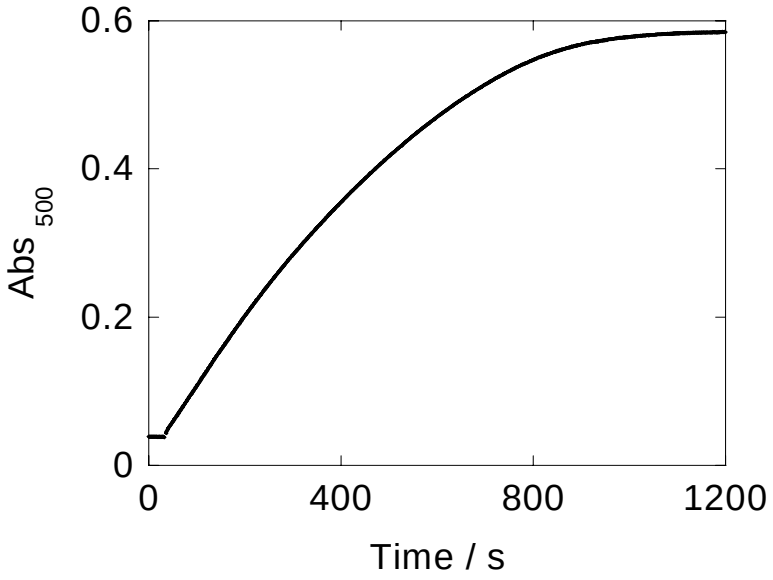

Figure 8-13. Kinetic traces at 500 nm for the reaction of MSN-(salen)Cr^{III} (0.005 mM) with PhIO (0.02 mM) in the presence of TMB (0.03 mM) in CH_3CN/H_2O (9:1) in 0.10 M $HClO_4$. ε_{500} (TMB^{2+}) = 2.9×10^4 M^{-1} cm^{-1}.

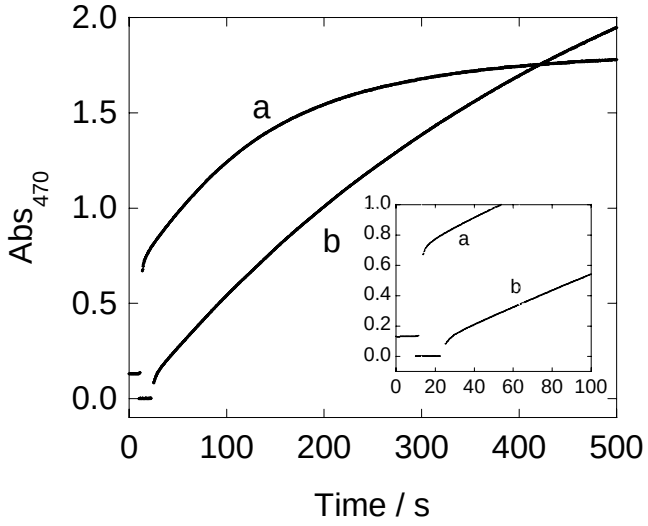

Figure 8-14. Kinetic traces at 470 nm for the reaction of MSN-(salen)Cr^{III} (0.05 mM, trace *a*) and (salen)Cr^{III} (0.005 mM, trace *b*) with PhIO (0.04 mM) in the presence of TMB (0.02 mM in trace *a*, 0.022 in trace *b*) in CH_3CN/H_2O (9:1) in 0.10 M $HClO_4$. Axis labels in the inset are the same as in main figure.

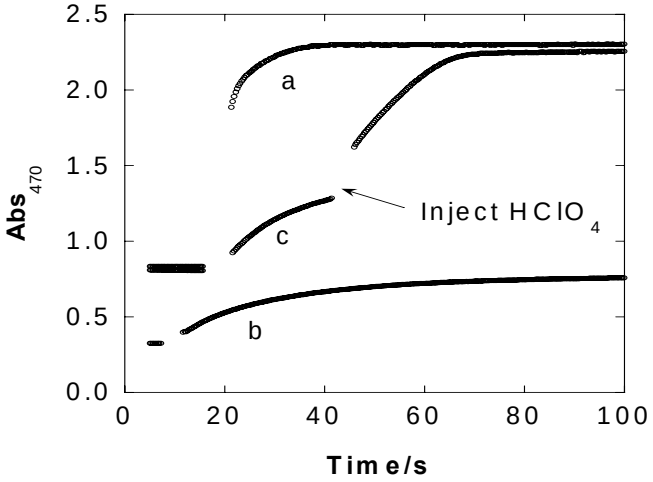

Figure 8-15. Kinetic traces at 470 nm for the reaction of MSN-(salen)Cr^{III} (0.047 mM) with PhIO (0.2 mM) in the presence of TMB (0.015 mM) in CH_3CN/H_2O (9:1) in 0.10 M $HClO_4$ (trace *a*), in the absence of added acid (trace *b*), and upon interruption of experiment *b* by addition of $HClO_4$ (trace *c*). The starting absorbance for experiments a and c is identical (0.8). Trace *b* was displaced downward for better visibility.

Table 2. Summary of Kinetic Data for the Oxidation of TMB with PhIO Catalyzed by MSN-(salen)Cr^{III} [a]

[PhIO] / mM	[TMB] / mM	v_i / M s^{-1} [b]	k / M^{-2} s^{-1}
0.04	0.008 – 0.034	c	1.4×10^{7} [d]
0.04	0.037	3.3×10^{-7}	4.7×10^{6}
0.04	0.073	6.2×10^{-7}	4.5×10^{6}
0.04	0.080	2.4×10^{-6}	1.4×10^{7}
0.04	0.130	2.1×10^{-6}	7.5×10^{6}
0.2	0.005	1.7×10^{-7}	3.6×10^{6}
0.2	0.013	4.8×10^{-7}	3.9×10^{6}
			$(7.4 \pm 4.5) \times 10^{6}$

[a][MSN-(salen)Cr^{III}] = 0.05 mM. [b] Initial rate. [c] In the range $(3.3 – 8.8) \times 10^{-7}$ M s^{-1}, depending on the concentrations. [d] Average of six determinations in the denoted range.

CHAPTER 9. SELECTIVE SEQUESTRATION OF CARBOXYLIC ACIDS FROM ANAEROBIC DIGESTION OF BIOMASS BY SURFACE-FUNCTIONALIZED MESOPOROUS SILICA NANOPARTICLES

A paper submitted to *Nano Letters*

Sang-Hyoun Kim,[1] **Yulin Huang**,[2] Chayanon Sawatdeenarunat,[3] Shihwu Sung,[3,*]
Victor S.-Y. Lin[2,*]

[1] *Green Process R&D Department, Korea Institute of Industrial Technology, Cheonan-si, Chungnam, 330-825, South Korea.*

[2] *Department of Chemistry, U.S. Department of Energy Ames Laboratory, Iowa State University, Ames, Iowa 50011-3111, U.S.A.*

[3] *Department of Civil, Construction, and Environmental Engineering, Iowa State University, Ames, Iowa 50011-3232, U.S.A.*

*Corresponding authors.

ABSTRACT

Carboxylic acids, such as acetic, propionic, *n*-butyric, and lactic acids, from biomass fermentation have attracted much attention recently as promising chemical feedstock for various applications. The feasibility of this bioconversion depends on the separation of carboxylic acids from the fermentation liquor. To selectively adsorb carboxylic acids, we synthesized an aminopropyl-functionalized mesoporous silica nanoparticle (MSN) material with the MCM-41 type, parallel channel porous structure via a co-condensation method that we previously developed and reported. The adsorption isotherms were analyzed with an extended Langmuir model using an overloading term. The highest acid adsorption capacity deduced was 3.38 mol/kg for 1:1 complexation at an amine density of 3.14 mol N kg^{-1}. Positive isosteric heat showed the reaction was exothermic and favored at low temperature. We demonstrated that the adsorption reaction between carboxylic acids and MSN was pH-dependent. Desorption/regeneration by increasing pH to 10.5 was completed within 1 min,

and the regenerated MSN showed adsorption capacity equivalent to the original. MSN had a high selectivity for carboxylic acid over ethanol, glucose, and protein. The pseudo-second-order rate constant for acetic acid adsorption on MSN was 0.41 kg/mol.min, significantly higher than that of an anion exchange resin (0.14 kg/mol.min) and activated carbon (0.06 kg/mol.min). We envision that the MSN material could serve as an efficient adsorbent for selective sequestration of carboxylic acids from anaerobic digestion of biomass for many different applications.

Introduction

The conversion of waste biomass into useful chemicals is an environmentally-sound, sustainable solution that can decrease fossil fuel dependency, reduce production of greenhouse gases and pollution in general.[1] A mixture of low-molecular weight carboxylic acids, such as acetic acid, propionic acid, butyric acid, and lactic acid, can be easily produced from various complex organic biomass by an indigenous mixed microbial community.[2, 3] The production of a mixture of carboxylic acids does not require a sterile environment, expensive tanks or purified enzymes. Efficient separation of carboxylic acids from fermented liquor would allow the thermochemical transformation of the acids to mixed alcohols and/or other liquid fuels.[4] Fermentation and extraction methods for selective organic acids with high commercial values from biomass also attracted much research attention recently.[1, 5]

Apparently, the economic feasibility of converting waste biomass to valuable chemicals is directly dependent on finding efficient and low-cost sequestration methods for the targeted, soluble products from the bulk solution. The conventional precipitation, adsorption, solvent extraction, pertraction, ion-exchange and electrodialysis have all been evaluated for the separation and purification of organic acids from fermentation mixtures.[5] Unfortunately, the high operational and/or capital costs of these methods are hindering the harvesting of organic acids from the fermentation of biomass in large scale.[1, 6]

The discovery of surfactant micelle-templated synthesis of mesoporous silica materials such as MCM-41/48, SBA-15, MSU-n, KIT-1, and FSM-16 enabled the use of

these structurally stable mesoporous solid materials with high surface areas (> 700 m^2/g) for catalysis, sensors, delivery, and adsorbents.[7] For example, amine-functionalized mesoporous silicas have been shown to adsorb heavy metals, pyruvic, and succinic acids from aqueous solutions.[8-11] In these studies, the performance of these amine-functionalized mesoporous silica adsorbents was shown to be dependent on the chemical accessibility and surface affinity determined by the structural and mass-transport properties of the materials, as well as the amine density.[8-11]

While the results in these recent literature reports are exciting, the question on how the selectivity and efficiency of using amine-functionalized mesoporous silicas as adsorbents for the sequestration of short-chain carboxylic acids, such as acetic, propionic, and *n*-butyric acids, would be affected in the presence of common chemicals, such as ethanol, glucose, and glutamate, in fermentation remains unanswered. Herein, we report on the design of a series of MCM-41 type amine-functionalized mesoporous silica nanoparticle (MSN) materials for the selective sequestration of the aforementioned carboxylic acids. We synthesized the MSN materials via a co-condensation method that we previously developed and reported.[7, 12, 13] As demonstrated in the following sections, the degree of amine-functionalization in these MSN particles is tunable without creating a non-homogenous surface coverage or distorting the porous structure at high-functional-group density. We investigated the structure and carboxylic acids adsorption capacity of MSN with different amine densities ranging from 0.84 to 3.65 mol N kg^{-1}. Based on the adsorption isotherms and kinetics at different pH and temperatures, and the results of competitive adsorption study with several common coexisting chemicals, such as amino acids, ethanol, and glucose, in fermentation, we found that MSN exhibited a superior adsorption efficiency and selectivity in comparison with several other conventional adsorbents, such as anion exchange resins and activated carbon.

Results and Discussions

MSN was synthesized via a sodium hydroxide-catalyzed co-condensation reaction of tetraethoxysilane (TEOS) with 3-aminopropyltrimethoxysilane (APTMS) in the presence of cetyltrimethylammonium bromide (CTAB) as the structure-directing template. Pure MSN without any organic functional group and five MSN materials with different amine densities

(0.84, 2.35, 3.14, 3.49, and 3.65 mol N kg^{-1} basing on elemental analysis) were made according reference.[7, 12, 13] These materials were characterized by N_2 adsorption/desorption (Figure 9-1), powder X-ray diffraction (XRD) (Figure S9-1) and transmission electron microscope (TEM) (Figure 9-2). The degree of amine functionalization and the structural properties, i.e., surface area, pore size, and pore volume of MSN materials are summarized in Table 1. As the loading of amine functional group increased from 0.0 to 3.7 mol N kg^{-1} (determined by the elemental analysis), the surface areas and pore volumes of MSN materials decreased from 1043 to 330 m^2/g, respectively. While the total surface area decreased significantly, all MSN samples exhibited the type IV nitrogen sorption isotherm and narrow BJH pore size distribution (Figure 9-1), indicating that these materials have the MCM-41 type, highly ordered 2-dimensional mesoporous structure even with the high amine density.[14-16] Transmission electron microscopy (TEM) (Figure 9-2) and the powder X-ray diffraction (XRD) analyses (Figure S9-1) further confirmed the highly-ordered mesoporous channel structure of these MSN materials. The mesoporous channels of these materials are indeed accessible to the targeted carboxylic acids in bulk solution while encountering little or no diffusion limitations.

With acetic acid as the first targeted organic acid, the maximum adsorption capacities of these MSN materials for acid at pH 3.5 to 4.0 (Table 9-1) and their corresponding adsorption isotherms (Figure S9-2) showed that the adsorption capacity increases proportionally with the degree of amine functionalization. The results suggested that the aminopropyl functional groups were converted to ammoniums under this acidic condition, which could serve as primary adsorption sites for acetic acid. The facile ion-exchange process between the surface bound ammonium functional groups and acetic acid molecules in aqueous solution under pH < 4.75 is described in Eq. (1). In contrast, the protonated silicate (silanol) of MSN materials could only weakly interact with acetic acid under the same condition as outlined in Eq. (2) and could only act as the secondary adsorption sites.[17]

$$\{\text{-}NH_3^+Cl^-\} + HOAc \rightarrow \{\text{-}NH_3^+OAc^-\} + HCl \quad (1)$$

$$\{\text{-Si-OH}\} + HOAc \rightarrow \{\text{-Si-OH}\cdot HOAc\} \quad (2)$$

Furthermore, the experimental data resembled the typical Langmuir-type isotherms with single linear increases and saturation limits. However, the calculated maximum

adsorption capacities using the Langmuir model were larger than the actual amine densities of MSN (Table S9-1) due to the adsorption data at high equilibrium acid concentrations. Even assuming the silanols in the amine-functionalized MSN have the same adsorption capacity of non-functionalized MSN (0.33 mol HOAc kg^{-1}), the adsorption capacities are still higher, implying that more than one acetic acid molecule could be adsorbed per surface site on MSN at high acetic acid load. Empirical approaches, such as the Freundlich and Sips equations, have been used to deal with the "overloading" phenomena.[18, 19] However, the semi-empirical equations developed for adsorbent with complex pore and surface structure like activated carbon might not be appropriate to MSN, where the mesoporous structure are highly ordered in two dimensions. Instead, we used an extended Langmuir isotherm model as shown in Eq. (3), which is based on an additional 2:1 adsorption by hydrogen bonding of a second acetic acid to the carbonyl oxygen of the first acetic acid bound to the adsorbent:[10]

$$Q_{EQ} = \frac{Q_{Max}(b_1 C_{EQ} + 2b_2 C_{EQ}^{\ 2})}{1 + b_1 C_{EQ} + b_2 C_{EQ}^{\ 2}} \qquad (3)$$

where Q_{EQ} (mol L^{-1}) is the equilibrium amount of carboxylic acid adsorbed on the adsorbent, Q_{Max} (mol kg^{-1}) is the maximum adsorption capacity for 1:1 complexation, C_{EQ} (mol L^{-1}) is the equilibrium concentration of unionized carboxylic acid, b_1 is the apparent equilibrium constant (L mol^{-1}) for 1:1 complexation and b_2 is the apparent equilibrium constant for 2:1 adsorption (overloading) (L^2 mol^{-2}). As shown in Table 9-1 and supplementary material (Figure S9-2), the extended Langmuir isotherm model explained the data with reasonable Q_{EQ} values. Acid adsorption capacity increased with the amine densities up to 3.14 mol N kg^{-1}. The calculated maximum adsorption capacity for 1:1 complexation was 3.38 mol HOAc kg^{-1}. At higher amine densities, the acid adsorption did not increase. Table 9-1 shows that the maximum capacity per surface area increased as the amine density became larger. This result suggested that the decrease of surface area would limit the efficiency. However, the ratios of adsorbed acetic acid to the amount of aminopropyl group on MSN remain no less than 0.83 mol HOAc per mol of amino group, because the accessibility of acid molecules to the surface ammonium sites was not significantly hindered. As discussed in the previous section, all MSN materials are with the same mesoporous structure regardless the degree of aminopropyl-functionalization. The apparent equilibrium

constants, b_1 and b_2, indicated how strong the adsorbate molecule is attached onto the primary and the secondary adsorption sites, respectively.[18] As the adsorption sites were the same at the amine-MSN, the values of the constants were little influenced by the amine density. It should be noted that the overloading term, $b_2C_{EQ}^2$ was negligible at a low equilibrium acid concentration. For acetic acid adsorption onto MSN with 3.14 mol N kg^{-1}, the difference between the two models was <6% at the equilibrium unionized acid concentration (<100 mM (6 g L^{-1})) as shown in Supporting Information (Figure S9-3).

Figure 9-3 depicts that isotherms of propionic, *n*-butyric, and lactic acids were not significantly different from that of acetic acid, indicating the carboxylic group would be the active functionality that is responsible for the adsorption to MSN surfaces. As acetic, propionic, *n*-butyric, and lactic acids are the main carboxylic acids in fermentation of waste biomass, this result showed that the adsorption data obtained using acetic acid could be representative for the carboxylic acid from the fermentation of waste biomass.[2, 3]

As we knew, isosteric heat of adsorption is one of the key thermodynamic variables for the design of an adsorption process.[20] Acid adsorption on our MSN materials was found to be favored at low temperature (Figure S9-5). The isosteric heat could be calculated using Clausius-Clapeyron equation as Eq (4).

$$-\Delta H_{ads} = -R \left. \frac{d(\ln C_{EQ})}{d(1/T)} \right|_{Q_{EQ}} \tag{4}$$

where ($-\Delta H_{ads}$) is the isosteric heat of adsorption (kJ mol^{-1}), R is the ideal gas constant (8.314 J mol^{-1} K^{-1}), and T is the thermodynamic temperature (K). Figure 9-4 shows plots of the isosteric heats of adsorption with adsorbed amounts of acetic acid. The isosteric heat values varied from 36.9 to 15.8 kJ mol^{-1} with adsorbed acetic acid amounts from 0.5 to 3.5 mol HOAc kg^{-1}. The positive isosteric heats (negative enthalpy) indicate that the adsorption reaction of acetic acid on MSN was exothermic. The heat values decreased with the adsorbed amount of acetic acid confirming that there were finite specific surface adsorption sites for acetic acid, which were the surface-bound ammonium groups in this case.[18]

Since the concentration of the unionized carboxylic acid molecules is a function of pH, adsorption would indeed depend on pH. At low carboxylic acid loading where b_2C_{Eq} is negligible, the effects of pH on adsorption would be predicted using Eq. (5):

$$Q_{EQ} = \frac{Q_{Max} b_1 \frac{C_{Eq,T}}{1+10^{pH-pK_a}}}{1+b_1 \frac{C_{Eq,T}}{1+10^{pH-pK_a}}} = \frac{Q_{Max} b_1 \frac{C_{int}-rQ_{EQ}}{1+10^{pH-pK_a}}}{1+b_1 \frac{C_{int}-rQ_{EQ}}{1+10^{pH-pK_a}}} \quad (5)$$

where $C_{EQ,\ T}$ (mol L^{-1}) is the equilibrium concentration of total (unionized + ionized) carboxylic acid, pK_a is carboxylic acid dissociation constant, C_{int} (mol L^{-1}) is the initial concentration of carboxylic acid, and r is the adsorbent-to-solution ratio (kg L^{-1}). The prediction was well agreed with the experimental data at the initial acid concentration of 50 mM (R^2 = 0.9533, Figure S4).

Figure 9-4 illustrates that more than 98% of adsorbed acetic acid desorbed from MSN within 1 min upon adjusting pH to 10.5. The desorbed MSN samples could be reused for carboxylic acids. Interestingly, these recycled MSN samples showed adsorption capacity as high (> 98%) as those of the freshly prepared materials. The results further confirmed that the regeneration of MSN and the extraction of adsorbed organic acid could indeed be achieved by a simple pH change.

We note that, in addition to the ionization equilibrium of acetic acid at pH between 6-10, the silanol groups of MSN would also be deprotonated yielding the anionic silicates (Si-O^-) on the mesopore surface. The surface-bound ammonium groups would likely be the only adsorption sites for the acetate (OAc^-) anions (Eq. (6)), given the fact that the silicate sites would not be attractive to acetate because of the charge repulsion (Eq. (7)).

$$\{\text{-}NH_3^+Cl^-\} + OAc^- \rightarrow \{\text{-}NH_3^+OAc^-\} + Cl^- \quad (6)$$

$$\{\text{-Si-}O^-\} + OAc^- \rightarrow \text{No reaction} \quad (7)$$

These interactions could explain the rapid decrease in adsorption capacity (Q_{EQ}) when pH increased from 4 to 7.5 as depicted in Figure S9-4, as the adsorption between these species would be governed by the equilibrium of the ionization of acetic acid.

The suppression on carboxylic acid adsorption by co-existing chemicals in the bulk solution is another important factor in evaluating the applicability of adsorbents. The effects of common organic and inorganic chemicals in fermentation were investigated at 10-100 times higher than the normal concentrations as depicted in Figure 5. Interestingly, the

aminopropyl-functionalized MSN materials have very high selectivity for carboxylic acids. The sequestration was unaffected by the presence of other organic chemicals. Ethanol (at the initial concentration ≤133.3 mM or 6.1 g L^{-1}) and glucose (at the initial concentration ≤33.3 mM or 24.0 g L^{-1}) did not affect the adsorption of acetic acid. Glutamate, an amino acid with two carboxylic groups, slightly decreased the adsorption of acetic acid only at a very high initial concentration ≥40 mM (5.9 g L^{-1} or 560 mg TKN L^{-1}). At 54.4 mM (8.0 g L^{-1}, 761 mg TKN L^{-1}), near the maximum solubility of the amino acid (0.1 g g^{-1} H_2O), the adsorption capacity remained high (84%) in comparison with the control. The carboxylic group in the amino acid would be adsorbed onto the amine group of MSN. As glutamate is one of only two amino acids among 20 having two carboxylic groups, the suppression effect of protein/amino acids in usual fermentation broth would be much less than that of glutamate that we had tested here. The inorganic anions chloride (at the initial concentration ≥15 mM or 533 mg L^{-1}), sulfate (at the initial concentration ≥5 mM or 160 mg S L^{-1}), and phosphate (at the initial concentration ≥15 mM or 465 mg P L^{-1}) retarded acetic acid adsorption at an initial acetic acid level of 50 mM as illustrated in Figure 5(b). Inorganic anions are regarded to be adsorbed onto an ammonium group at pH 3.5 to 4 as illustrated in Eq. (8).

$$\{\text{-}NH_3^+\} + A^- \rightarrow \{\text{-}NH_3^+A^-\} \quad (8)$$

We used a competitive Langmuir adsorption isotherm as Eq. (9) to express the suppression by co-existing anions when b_2C_{Eq} was negligible[19]

$$Q_{EQ} = \frac{Q_{Max} b_1 C_{EQ}}{1 + b_1 C_{EQ} + b_i \gamma_i C_{EQ,i}} \quad (9)$$

where $C_{EQ,i}$ (mol L^{-1}) is the equilibrium concentration of a competitor, b_i is the apparent equilibrium constant of a competitor, and γ_i is the activity coefficient of the competitor calculated using the extended DeBye-Hückel law. Apparent equilibrium constants of chloride, sulfate, and phosphate were 69.7, 159.8, 65.0 L mol^{-1}, respectively (Figure S6). We recommend considering the suppression effect when designing an adsorption process using MSN for fermentation liquor at high salt levels. It should be noted that the competitive isotherms were based on the equilibrium activity, which is quite lower than the initial anion concentration.

In order to describe the adsorption efficiency of our MSN materials, we adopted the pseudo-second-order absorption kinetic model (Eq. 10), which has been widely used for many chemisorption reactions.[21]

$$Q_t = \frac{k_2 Q_{EQ}^2 t}{1 + k_2 Q_{EQ} t} \qquad (10)$$

where Q_t (mol kg^{-1}) is the solid-phase loading of organic acids at time t, k (kg mol^{-1} min^{-1}) is the pseudo-second-order rate constant and t is time (min). Figure 9-6 shows the acetic acid adsorption kinetics on MSN with 3.14 mol N kg^{-1}, the weak base anion exchange resin, and the powdered activated carbon at initial acetic acid concentration of 0.05 M. The results were well-fitted to the pseudo-second-order model ($R^2 > 0.89$). For MSN with 3.14 mol N kg^{-1}, the adsorption reached a steady state within 10 min. The pseudo-second-order rate constant of MSN was 0.41 kg mol^{-1} min^{-1}, which was higher than that of the anion exchange resin (0.14 kg mol^{-1} min^{-1}) or the activated carbon (0.06 kg mol^{-1} min^{-1}). These results indicate that the uniformed mesoporous structure of MSN indeed would result in a faster adsorption.

Conclusions

A series of MCM-41 type, aminopropyl-functionalized mesoporous silica (MSN) materials was synthesized by a co-condensation method for the sequestration of carboxylic acids in biomass fermentation. The highest acid adsorption capacity was 3.38 mol/kg for 1:1 complexation plus overloading phenomenon at an amine loading of 3.14 mol N kg^{-1}. Desorption/regeneration by increasing pH to 10.5 was accomplished within 1 min, and the regenerated MSN showed adsorption capacity compatible to that of the original material. MSN also exhibited a very high selectivity to carboxylic acid over ethanol, glucose, and protein. And the highly ordered mesoporous structure of MSN enabled a faster reaction rate than those of anion exchange resin and activated carbon. We envision that the aminopropyl-functionalized mesoporous silica would be an efficient adsorbent for the selective sequestration of carboxylic acids from biomass fermentation for many energy and chemical applications.

Acknowledgement

This study was supported by research grand from the Iowa Energy Center (IEC), Ames, IA, U.S.A (No. 07-02) and the U.S. Department of Energy under contract (No. DE-FG26-0NT08854).

References

1. Angenent, L. T.; Karim, K.; Al-Dahhan, M. H.; Wrenn, B. A.; Domiguez-Espinosa, R. *Trends Biotechnol.* **2004,** 22, (9), 477-485.
2. Thanakoses, P.; Black, A. S.; Holtzapple, M. T. *Biotechnol. Bioeng.* **2003,** 83, (2), 191-200.
3. Wang, J.-Y.; Liu, X.-Y.; Kao, J. C. M.; Stabnikova, O. *J. Chem. Technol. Biotechnol.* **2006,** 81, (3), 345-351.
4. Aiello-Mazzarri, C.; Agbogbo Frank, K.; Holtzapple Mark, T. *Bioresour Technol* **2006,** 97, (1), 47-56.
5. Wu, Z.; Yang, S.-T. *Biotechnol. Bioeng.* **2003,** 82, (1), 93-102.
6. Bungay, H. R. *Trends Biotechnol.* **2004,** 22, (2), 67-71.
7. Huh, S.; Wiench, J. W.; Yoo, J.-C.; Pruski, M.; Lin, V. S.-Y. *Chem. Mater.* **2003,** 15, 4247-4256.
8. Algarra, M.; Jimenez, M. V.; Rodriguez-Castellon, E.; Jimenez-Lopez, A.; Jimenez-Jimenez, J. *Chemosphere* **2005,** 59, (6), 779-786.
9. Jun, Y.-S.; Huh, Y. S.; Park, H. S.; Thomas, A.; Jeon, S. J.; Lee, E. Z.; Won, H. J.; Hong, W. H.; Lee, S. Y.; Hong, Y. K. *J. Phys. Chem. C* **2007,** 111, (35), 13076-13086.
10. Huang, S.; Qin, W.; Dai, Y. *J. Chem. Technol. Biotechnol.* **2008,** 83, (5), 683-687.
11. Jang, M.; Park, J. K.; Shin, E. W. *Microporous Mesoporous Mater.* **2004,** 75, (1-2), 159-168.
12. Huh, S.; Wiench, J. W.; Trewyn, B. G.; Song, S.; Pruski, M.; Lin, V. S.-Y. *Chem. Commun.* **2003**, (18), 2364-2365.

13. Huang, Y.; Trewyn, B. G.; Chen, H.-T.; Lin, V. S.-Y. *New J. Chem.* **2008,** 32, (8), 1311-1313.
14. Beck, J. S.; Vartuli, J. C.; Roth, W. J.; Leonowicz, M. E.; Kresge, C. T.; Schmitt, K. D.; Chu, C. T. W.; Olson, D. H.; Sheppard, E. W.; et al. *J. Am. Chem. Soc.* **1992,** 114, (27), 10834-43.
15. Kresge, C. T.; Leonowicz, M. E.; Roth, W. J.; Vartuli, J. C.; Beck, J. S. *Nature (London)* **1992,** 359, (6397), 710-12.
16. Sing, K. S. W.; Everett, D. H.; Haul, R. A. W.; Moscou, L.; Pierotti, R. A.; Rouquerol, J.; Siemieniewska, T. *Pure Appl. Chem.* **1985,** 57, (4), 603-19.
17. Do, D. D., *Adsorption Analysis: Equilibria and Kinetics*. Imperial College Press: London, 1998.
18. Kanazawa, N.; Urano, K.; Kokado, N.; Urushigawa, Y. *J. Colloid Interface Sci.* **2001,** 238, (1), 196-202.
19. Srivastava, V. C.; Mall, I. D.; Mishra, I. M. *Chem. Eng. J. (Amsterdam, Neth.)* **2007,** 132, (1-3), 267-278.
20. Xiao, B.; Thomas, K. M. *Langmuir* **2004,** 20, (11), 4566-4578.
21. Jang, M.; Shin, E. W.; Park, J. K.; Choi, S. I. *Environ. Sci. Technol.* **2003,** 37, (21), 5062-5070.

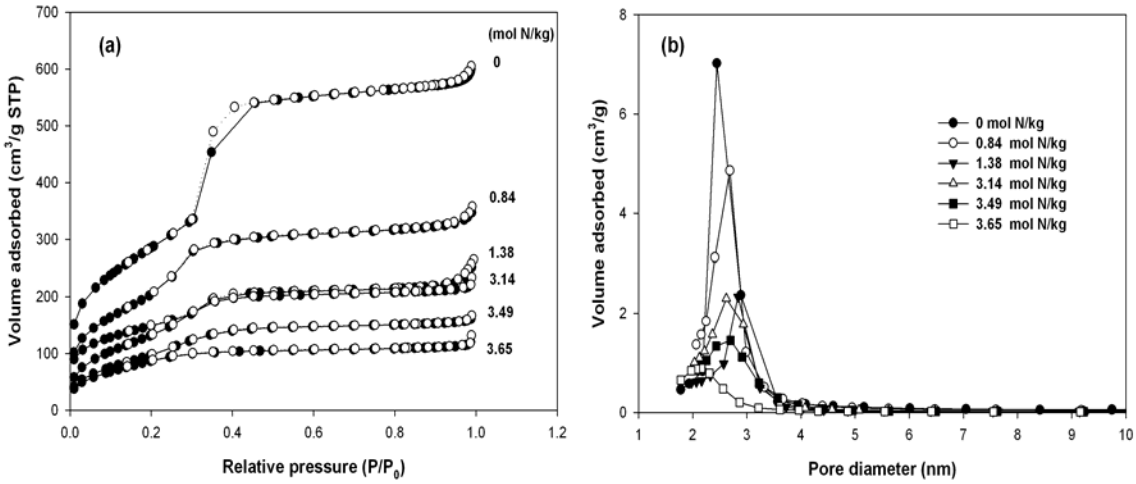

Figure 9-1. (a) BET isotherm and **(b)** BJH pore distribution of aminopropyl-functionalized MSN and pure MSN.

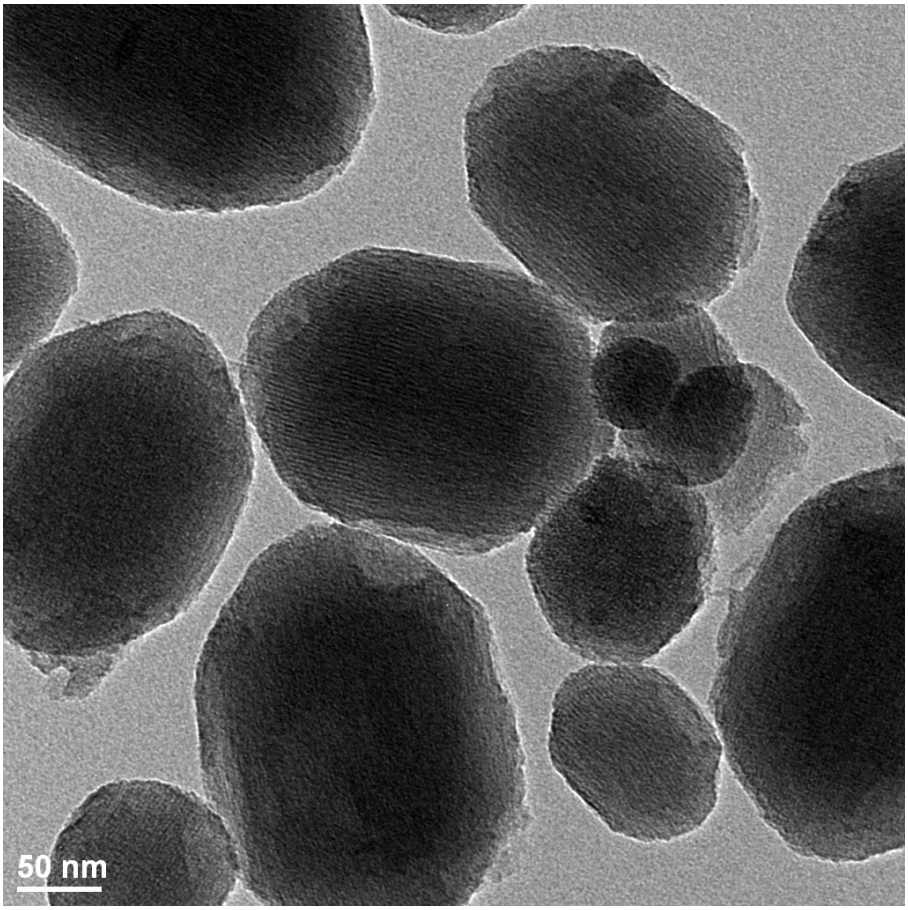

Figure 9-2. TEM image of a typical aminopropyl-functionalized MSN with 3.14 mmol N/g.

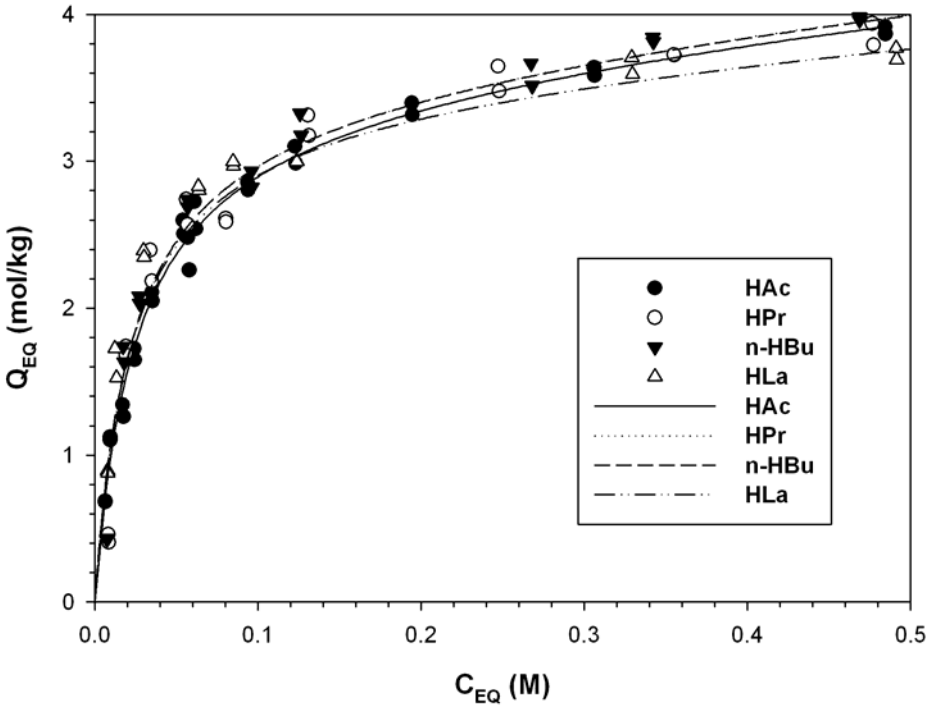

Figure 9-3. Adsorption isotherms of acetic, propionic, n-butyric, and lactic acids onto the 3.14 mol N/kg MSN at 35°C. The symbol and line are experimental data and the extended Langmuir model, respectively.

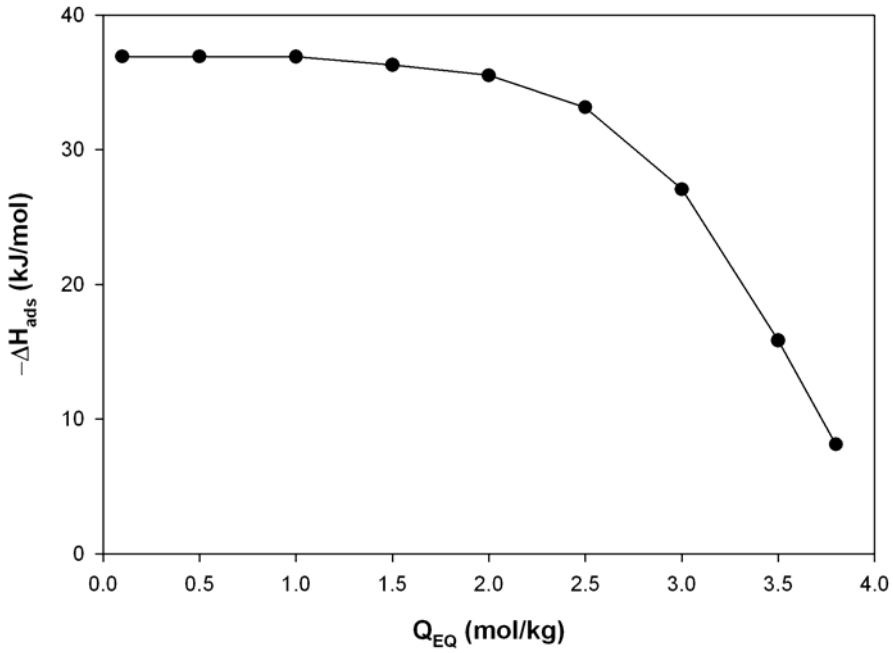

Figure 9-4. Isosteric heat of acetic acid adsorption onto the 3.14 mol/kg MSN.

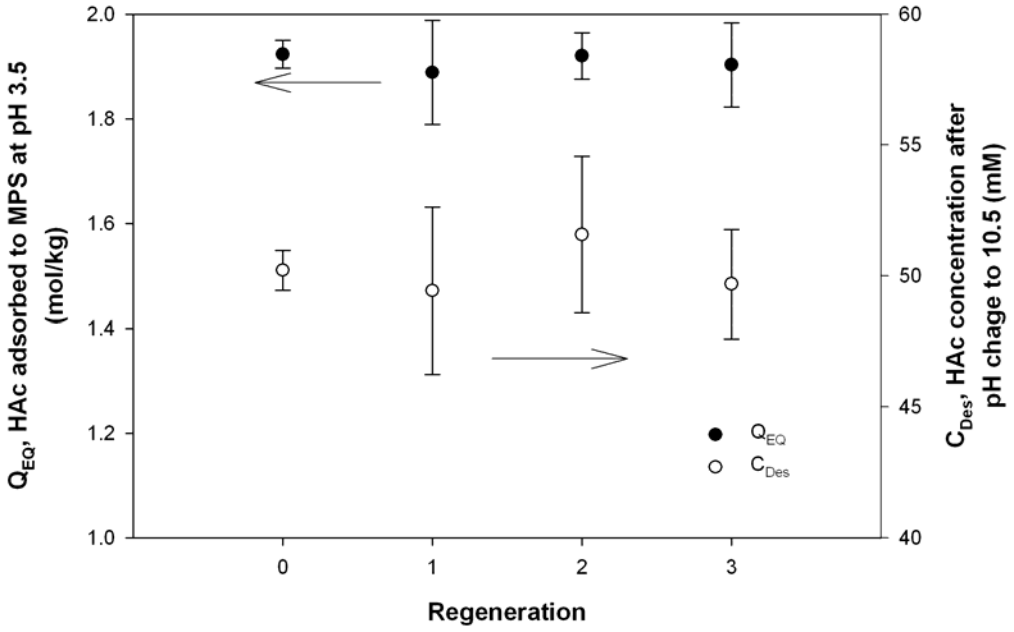

Figure 9-5. Acetic acid adsorption to regenerated the 3.14 mol N/kg MSN and desorbed acetic acid concentration by pH change.

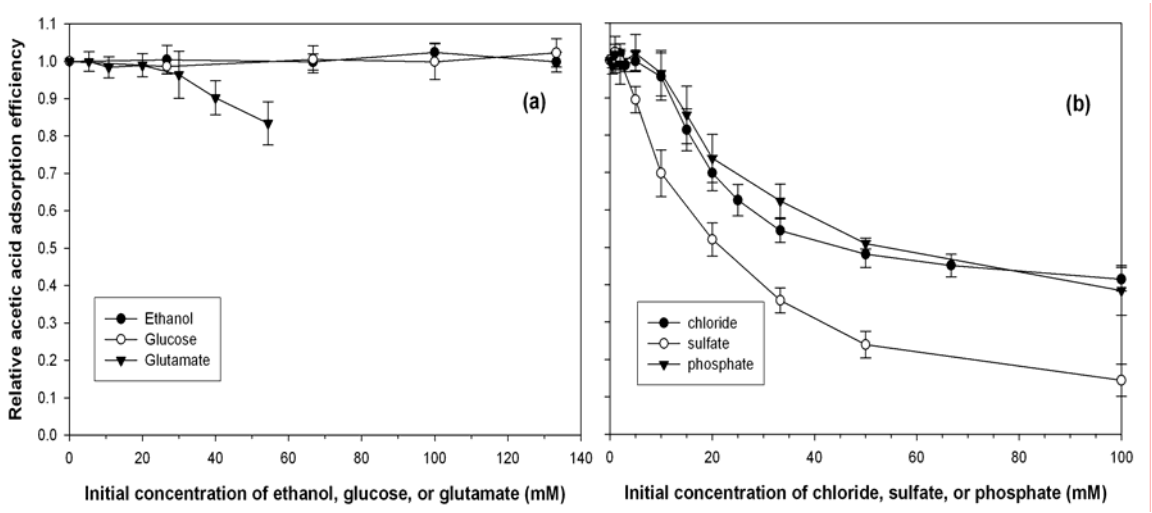

Figure 9-6. Effect of coexisting chemicals on acetic acid adsorption onto the 3.14 mol N/kg MSN at initial acetic acid concentration of 50 mM. (a) ethanol, glucose, and glutamate; (b) chloride, sulfate, and phosphate.

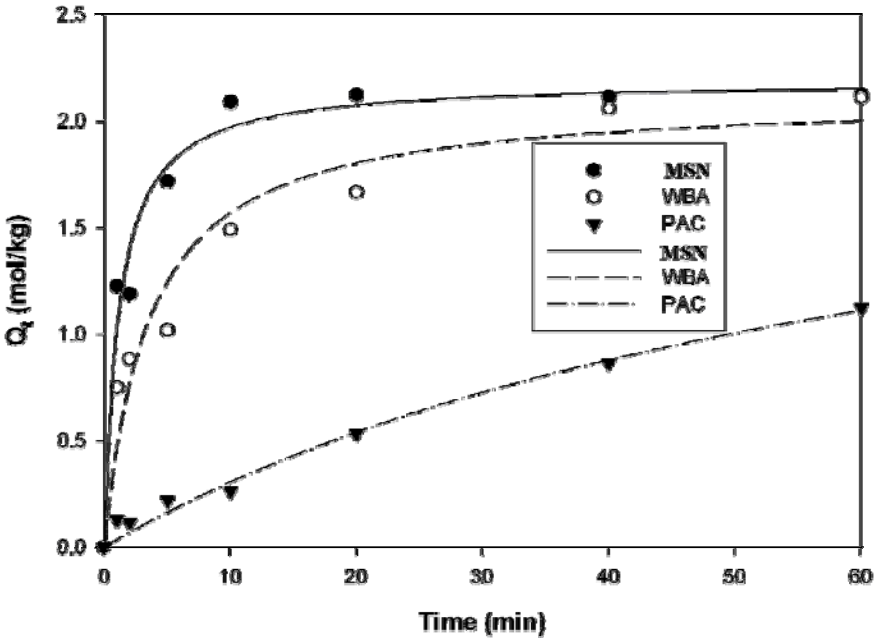

Figure 9-7. Kinetics of acetic acid adsorption at 35°C and initial acetic acid of 50 mM with the 3.14 mol N/kg MSN, a weak base anion exchange resin (WBA), and a powered activated carbon (PAC). The symbol and line are experimental data and the pseudo-second-order kinetic model, respectively.

Table 9-1. Structural properties and extended Langmuir isotherm parameters for acetic acid adsorption at 35°C of aminopropyl-functionalized MSN and pure MSN

Amine density (mol N/kg)	Structural properties			Extended Langmuir isotherm parameters					
	S_{BET} (m^2/g)	D_{BJH} (nm)	V_{pore} (cm^3/g)	Q_{Max}, Maximum adsorption capacity for 1 to 1 complexation			Apparent equilibrium constant (L/mol)		R^2
				mol/kg	mol/mol N [a]	mol/mm^2	b_1, 1 to 1	b_2, 2 to 1	
0	1043	2.5	0.91	0.24	-	0.23	27.8	27.0	0.979
0.84	755	2.7	0.52	0.91	0.80	1.20	58.8	59.9	0.983
1.38	531	2.8	0.36	1.21	0.70	2.27	66.0	234.8	0.989
3.14	502	2.6	0.33	3.38	1.00	6.73	42.1	22.3	0.990
3.49	337	2.6	0.24	3.31	0.88	9.83	39.5	16.3	0.988
3.65	330	2.2	0.18	3.26	0.83	9.87	43.2	24.2	0.933

[a] Assuming that silica atoms in aminopropyl-functionalized MSN had same adsorption capacity of pure MSN.

Supporting Information

Synthesis of amine-functionalized mesoporous silica nanoparticle (MSN)

MSN was synthesized via a sodium hydroxide-catalyzed co-condensation reaction of tetraethoxysilane (TEOS) with 3-aminopropyltrimethoxysilane (APTMS) in the presence of cetyltrimethylammonium bromide (CTAB) as the structure-directing template. The mixture of CTAB (2.0 g, 5.5 mmol), 2.0 M of NaOH (aq) (7.0 mL, 14.0 mmol), and H_2O (480.0 g, 26.7 mol) was heated at 80 °C for 30 min. Then, TEOS (9.3 g, 44.8 mmol) and

organoalkoxysilane (APTMS (0 to 40.0 mmol)) were injected sequentially. The solution was stirred at 550 rpm and 80 °C for 2 h yielding the crude MSN products, which were isolated via a hot filtration. The resulting solids were washed with water and methanol extensively and dried under vacuum. The purified materials were added to a 1% (v/v) HCl-methanol solution at 60 °C for 6 h to remove the CTAB surfactant molecules. The surfactant-removed solid products were filtered and washed with copious water and methanol, and then dried under vacuum. Five types of MSN materials with different amine densities (0.84, 2.35, 3.14, 3.49, and 3.65 mol N kg^{-1}) were synthesized. A pure inorganic MSN without any organic functional group was also prepared as a reference sample for the carboxylic acid adsorption studies.

Carboxylic acid adsorption study

The highest capacity MSN was determined using adsorption isotherms of the six MSN materials at 35 °C and a final pH between 3.5 and 4.0. Acetic acid was chosen as the first targeted organic acid. We poured stock solutions of acetic acid (500.0 mM) into capped glass bottles at 35 °C. Predetermined volumes of the stock solution for the target initial acetic acid concentration (3.3 to 500.0 mM) were transferred to 25-mL Erlenmeyer flasks in a gyratory water bath at 35 °C (Model G76, New Brunswick Scientific, Inc., NJ). Flasks were filled to 10.0 mL with nanopure water and pH-adjusted with 2 N HCl or 2 N NaOH. Then 50.0 mg of MSN was added, and the flasks sealed using parafilm (Pechiney, WI). After shaking at 190 rpm for 2 h, the solution was filtered through a 0.2-μm filter and the filtrate was evaluated for pH and soluble chemical. The same procedures were used in isotherm studies for other organic acids (propionic, *n*-butyric, and lactic acids) and temperature ranges (20 and 55 °C) using MSN with 3.14 mol N kg^{-1}.

The pH dependence (2.3 to 9.4, final value) of carboxylic acid adsorption was investigated at the initial acetic acid concentration of 50.0 mM. The pH dependence of carboxylic acid desorption and media regeneration was also studied in 15-mL centrifuge tubes at an initial acetic acid of 50.0 mM. After 2 h of shaking at pH 4.0, the sample was removed from two tubes, and the pH of the other tubes was increased to 10.5 using 2 N NaOH. The tubes were then shaken again for 1 min. The sample was removed from another

two tubes, and the remaining tubes were centrifuged at 2,000 rpm for 5 min to separate the supernatant and the regenerated MSN. The addition of acetic acid, pH adjustment to 4.0, adsorption, desorption by pH adjustment to 10.5, and centrifugation were repeated three times.

The effects of individual coexisting chemicals in fermentation liquor were investigated at initial acetic acid levels of 10.0 to 50.0 mM. Chloride, sulfate and phosphate were selected as representative anions. NaCl, Na_2SO_4, or $NaH_2PO_4 \cdot H_2O$ was added into acetic acid solution to provide the corresponding Cl^- of 1.0 to 20.0 mM (35.5 to 710.0 mg L^{-1}), SO_4^{2-} of 0.5 to 20.0 mM (16.0 to 640.0 mg L^{-1}), or PO_4^{2-} of 0.5 to 20.0 mM (15.5 to 620.0 mg L^{-1}). Suppression by organic chemical was studied using 26.7 to 133.3 mM (1.23 to 6.14 g L^{-1}) ethanol, 26.7 to 133.3 mM (4.8 to 24.0 g L^{-1}) glucose, and 5.4 to 54.4 mM (0.8 to 8 g L^{-1}) glutamate, representing alcohols, carbohydrates, and amino acids, respectively, in the fermentation effluent of waste biomass.

Adsorption kinetics data were obtained at an initial acetic acid level of 50.0 mM, where 3.14 mol N/kg MSN, powdered activated carbon (PAC) (Aqua Nuchar®, MeadWestvaco Co., VA), and a weak base anion exchange resin (Dowex® Marathon® WBA, Sigma-Aldrich, MO) were used as adsorbents. Samples were taken at 0.5 to 120 min intervals over the period of 4 h.

Structural analysis of MSN materials

The surface area and pore diameter were quantified using N_2 adsorption/desorption measurements with a Micromeritics ASAP 2000 system. The data were evaluated using the Brunauer-Emmett-Teller (BET) and Barrett-Joyner-Halenda (BJH) methods to calculate the surface area and pore volume/pore size distribution, respectively. Samples were prepared by degassing at 90 °C for 1 h and then at 150 °C for 4 h. Powder X-ray diffraction (XRD) experiments were performed on a Scintag XDS2000 diffractometer using a Cu Kα radiation source. Low angle diffraction with a 2θ range of 1 to 10° was used to investigate the long-range order of the mesoporous structures of MSN materials. Particle morphology and mesoporous structure of these materials were also examined by using a Tecnai G_2-F20 transmission electron microscope (TEM) with a 200 kV acceleration voltage. Carboxylic acid

concentration was measured by a high-performance liquid chromatograph HPLC (GP40, Dionex, CA) with an absorbance detector (AD20, Dionex) and a 300 mm × 7.8 mm Metacarb 67H column (Varian, CA) using 0.05 M H_2SO_4 as mobile phase. Anions were measured by the same chromatograph with a conductivity detector (CD20, Dionex) and a 250 mm × 4.6 mm AN1 column (Varian, CA) using carbonate buffer (1.7 mM $NaHCO_3$ + 1.8 mM Na_2CO_3) as mobile phase. pH values of samples were measured by a dual channel pH/ion meter (AR25, Fisher Scientific).

Table S9-1. Langmuir isotherm parameters for acetic acid adsorption at 35°C of amine-functionalized MSN and pure MSN

N density (mol N/kg)	Q_{Max}[a]		b (L/mol)[a]	R^2
	(mol/kg)	(mol/mol N)[b]		
0	0.33	-	15.8	0.972
0.84	1.18	1.01	33.2	0.958
1.38	2.06	1.25	24.0	0.974
3.14	3.98	1.16	30.1	0.984
3.49	3.81	1.00	30.5	0.973
3.65	3.85	0.97	30.7	0.921

[a] $$Q_{EQ} = \frac{Q_{Max} b C_{EQ}}{1 + b C_{EQ}}$$

where Q_{EQ} (mol L^{-1}) is the equilibrium amount of carboxylic acid adsorbed in the adsorbate, Q_{Max} (mol kg^{-1}) is the maximum adsorption capacity, C_{EQ} (mol L^{-1}) is the equilibrium concentration of unionized carboxylic acid, and b is the apparent equilibrium constant (L mol^{-1}).

[b] Assuming that silica atoms in amine-functionalized MSN had same adsorption capacity of pure MSN.

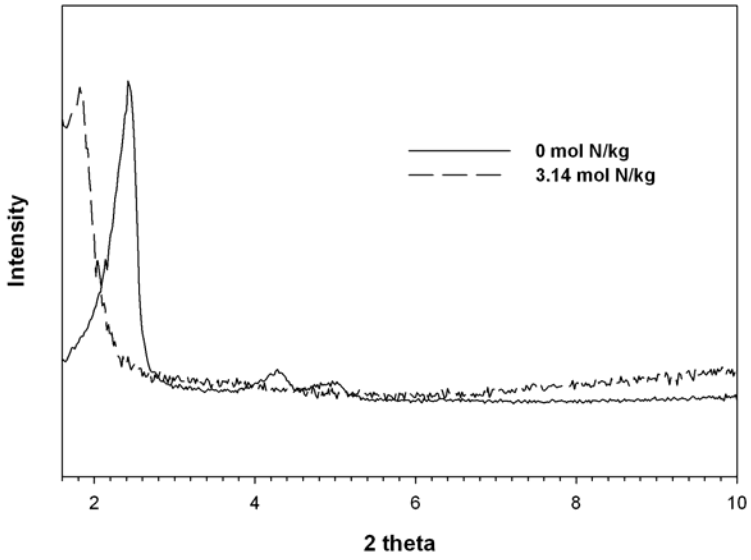

Figure S9-1. X-ray diffraction patterns of MSN before and after functionalization with aminopropyl group.

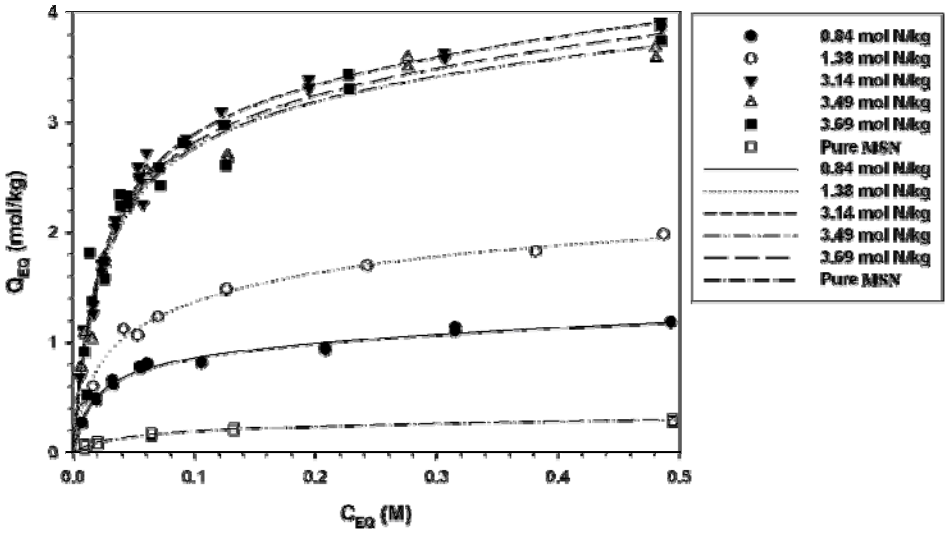

Figure S9-2. Acetic acid adsorption isotherms of MSN at 35°C. The symbol and line are experimental data and the extended Langmuir model, respectively.

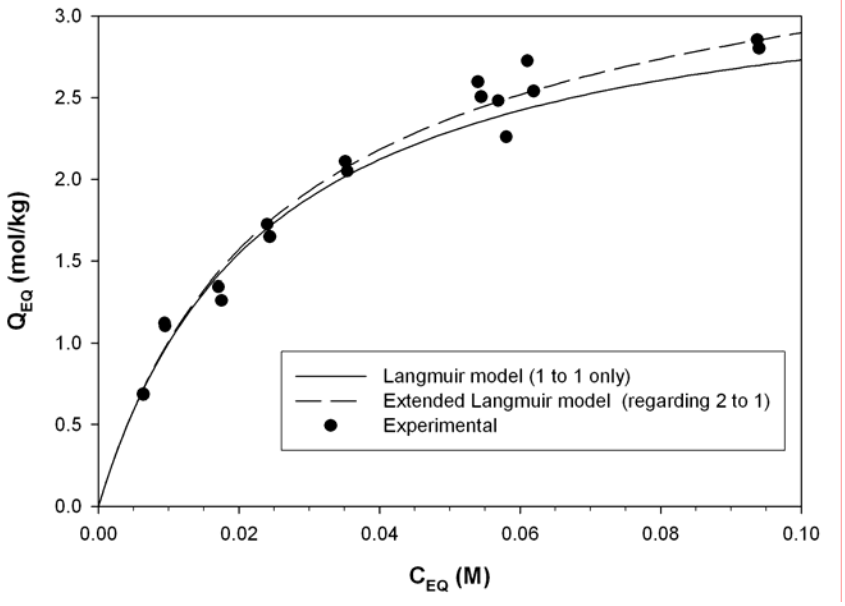

Figure S9-3. Comparison of Langmuir models with or without regarding 2 to 1 complexation for acetic acid adsorption onto the 3.14 mol N/kg MSN at 35°C.

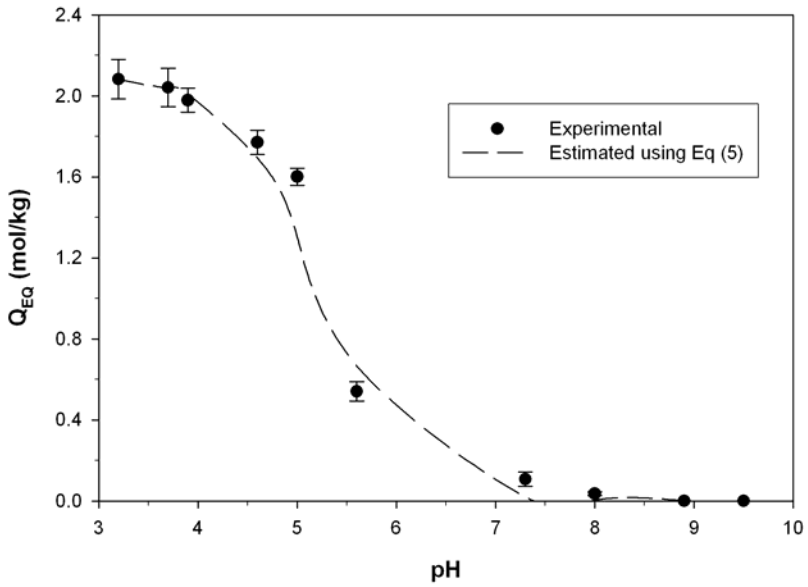

Figure S9-4. Effect of pH on acetic acid adsorption at initial acetic acid concentration of 50 mM.

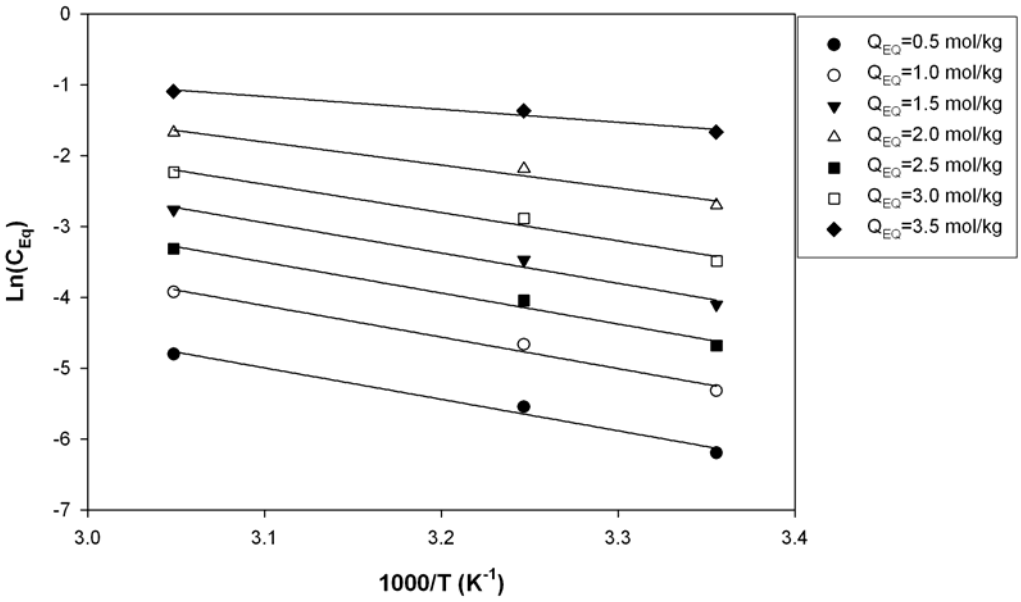

Figure S9-5. Effect of temperature on acetic acid adsorption onto the 3.14 mol N/kg MSN.

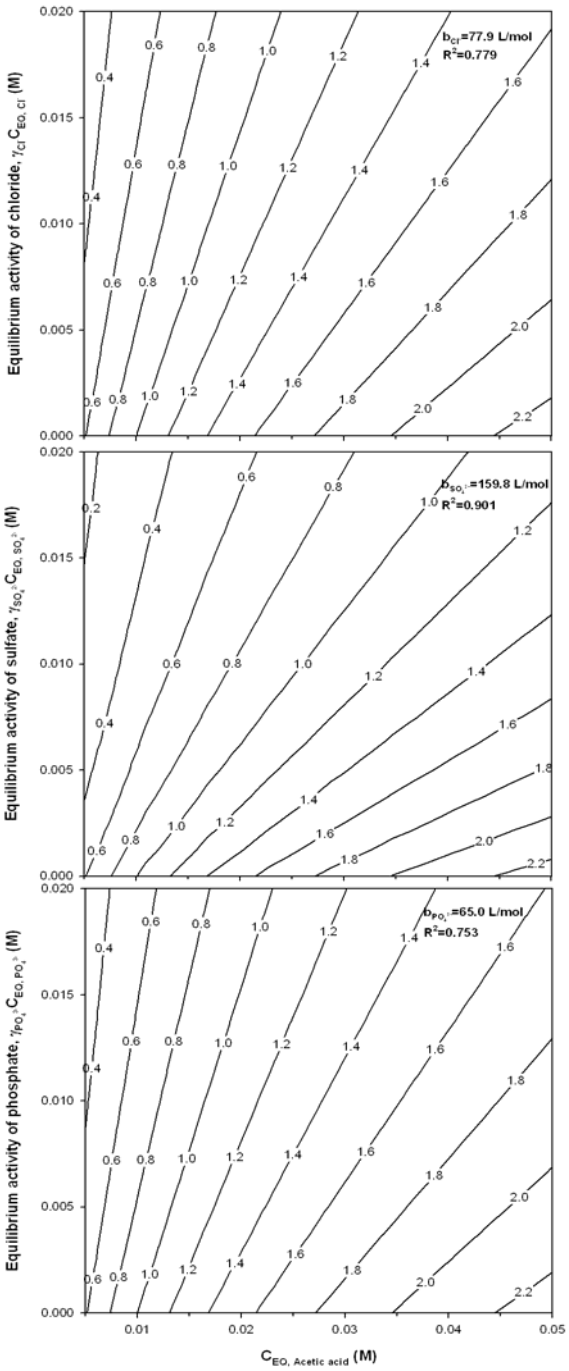

Figure S9-6. Contour lines of constant acetic acid adsorption onto the 3.14 mol N/kg MSN vs. equilibrium concentration of acetic acid and equilibrium activity of chloride, sulfate, and phosphate.

CHAPTER 10. GENERAL CONCLUSIONS

Mesoporous silica nanoparticles (MSN) with high surface area, tunable pore size and very narrow pore size distribution were functionalized by organic acid, organic base, metallic nanoparticles and organometallic complexes through co-condensation methods and/or post-synthesis grafting methods. And these surface-functionalized mesoporous materials were used as heterogeneous catalysts in organocatalysis, metallic catalysis, organometallic catalysis and used for selective sequestration of carboxylic acids as well.

Organocatalysis. First, sulfonic acid functionalized MSN (SAMSN) and aminopropyl functionalized MSN (APMSN) were synthesized by co-condensation methods where both the Brönsted acid and base were confined into the mesoporous channels of MSN materials. It was proved that they could co-exist as compatible catalysts for one-pot reaction cascades without neutralization each other because they were physically particle-separated in different MSN particles' channels (Figure 10-1).

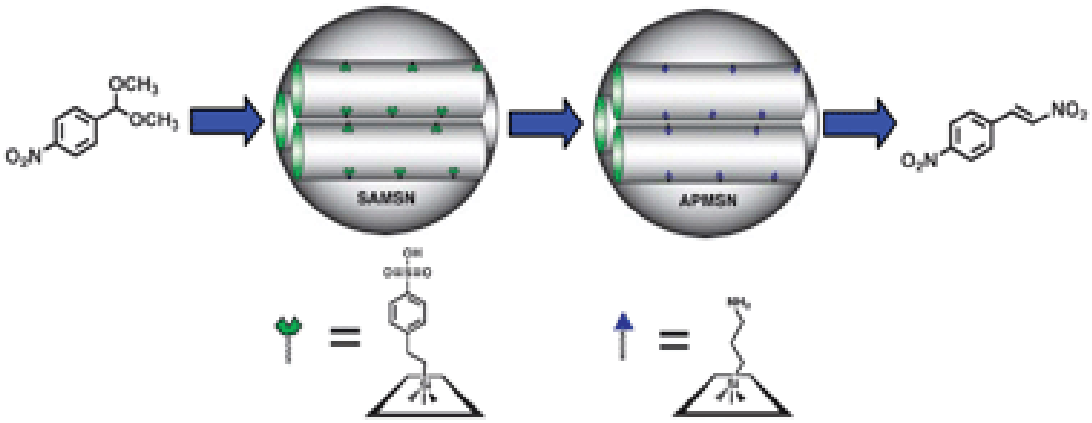

Figure 10-1. One-pot reaction cascades catalyzed by SAMSN and APMSN.

I also succeeded in site-separating Brönsted acid and base by MSN's internal surface and external surface through co-condensation method to functionalize MSN's internal surface followed by grafting method to functionalize MSN's external surface and using these internal and external surface separated Brönsted acid and base as compatible catalysts in one-pot reaction cascades too (Figure 10-2). In the kinetic studies, it was found that the activity of catalyst on the surface mesoporous silica nanoparticle was proportional to the coverage of catalyst on MSN surface.

Following these two successful approaches, we would further develop them into a general design principle for mimicking biological systems, in which a series of reactions are catalyzed by different enzymes in a precise sequence.

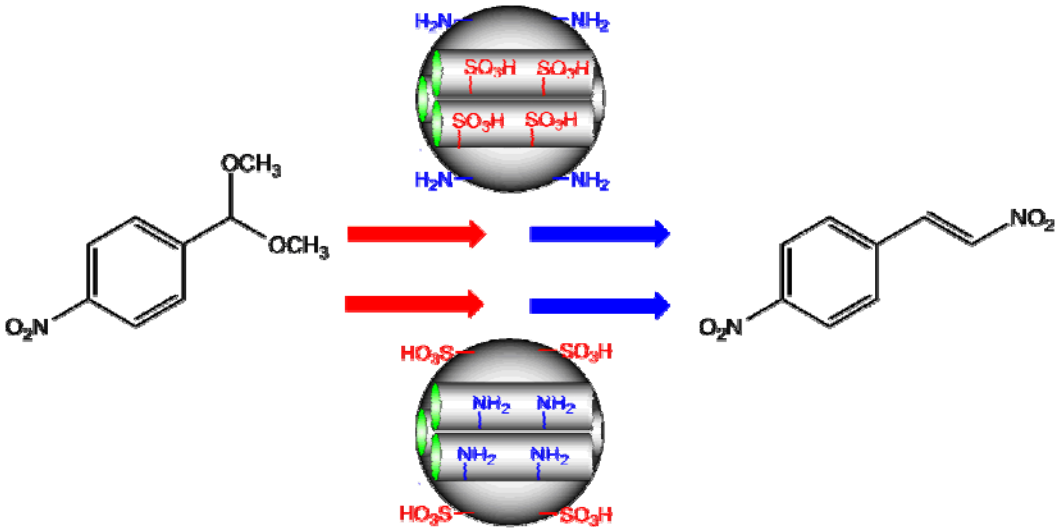

Figure 10-2. One-pot reaction cascades catalyzed by SAMSN-AP and APMSN-SA.

Metallic catalysis. Water-soluble rhodium nanoparticles with well defined particle size were synthesized and immobilized on MSN during *in situ* MSN's synthesis. The obtained material (MSNRhNPs) had homogeneous rhodium nanoparticle size, homogeneous rhodium nanoparticle distribution in MSN, with typical MSN's highly ordered structure and

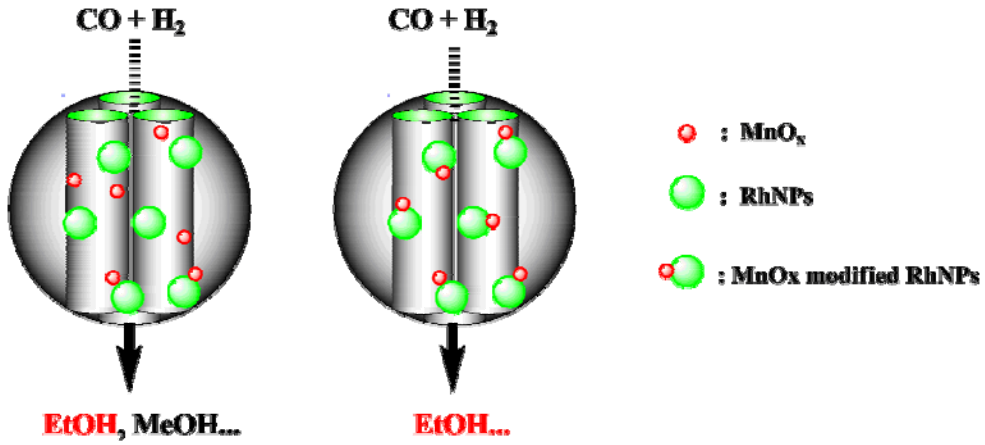

Figure 10-3. CO hydrogenation catalyzed by MSNRhNPs-Mn and MSNRhNPsMn.

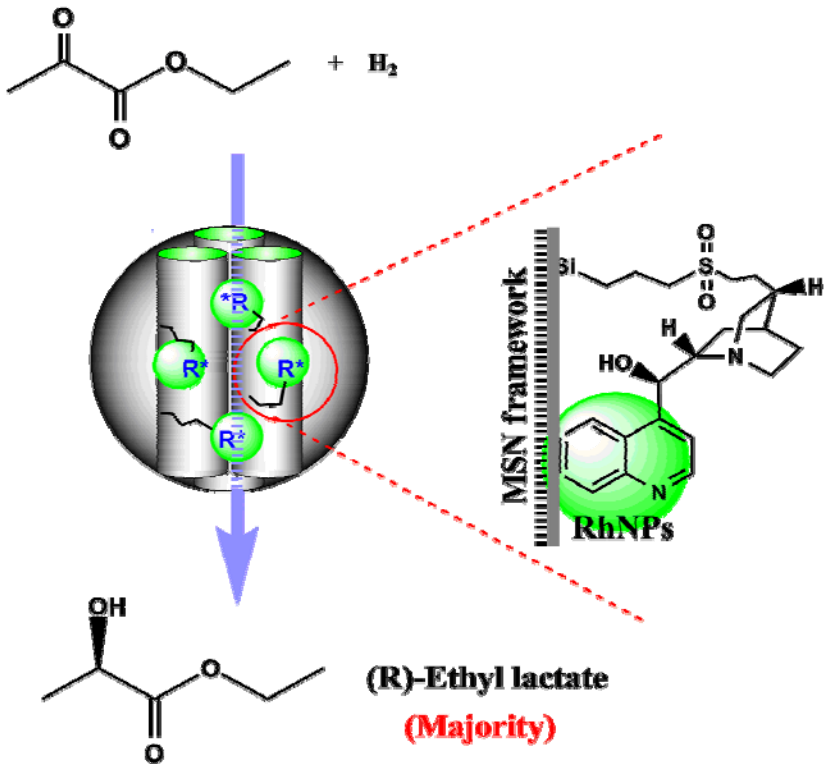

Figure 10-4. Enantioselective hydrogenation catalyzed by MSNRhNPsCD.

surface area and narrow pore size distribution as well. For the first time, I succeeded in distributing rhodium nanoparticles in MSN and modifying rhodium nanoparticles by manganese oxide during the formation of MSN. After MSNRhNPs were modified by manganese oxide efficiently (MSNRhNPsMn), MSNRhNPsMn could catalyze the hydrogenation of CO to produce the renewable energy alternative - ethanol with high selectivity and the by-product methanol could be suppressed dramatically (Figure 10-3).

Additionally, after MSNRhNPs were functionalized by some chiral agents such as (-)-cinchonidine, it can used as a solid chiral catalyst which can recycled and reused without any loss of reactivity and enantioselectivity (Figure 10-4). Here I opened a new strategy in heterogeneous catalysis to stabilize and homogeneously distribute metal nanoparticle catalysts in mesoporous silica nanoparticle during MSN formation.

Organometallic catalysis. Wilkinson-type rhodium phosphine complex was homogeneously immobilized on MSN surface by co-condensation method followed by coordination reaction. This MSN immobilized rhodium phosphine complex (RhPMSN) had a new and total different catalytic performance when (-)-cinchonidine was adsorbed on MSN surface. RhPMSN could enantioselectively catalyze the hydrogenation of pyruvate with surface-adsorbed (-)-cinchonidine with around 50% e.e. although its counterpart, $RhCl(TPP)_3$, in homogeneous system could not be chirally induced by (-)-cinchonidine (Figure 10-5). Here I hope a new door or field of asymmetric catalysis catalyzed by achiral catalysts was opened.

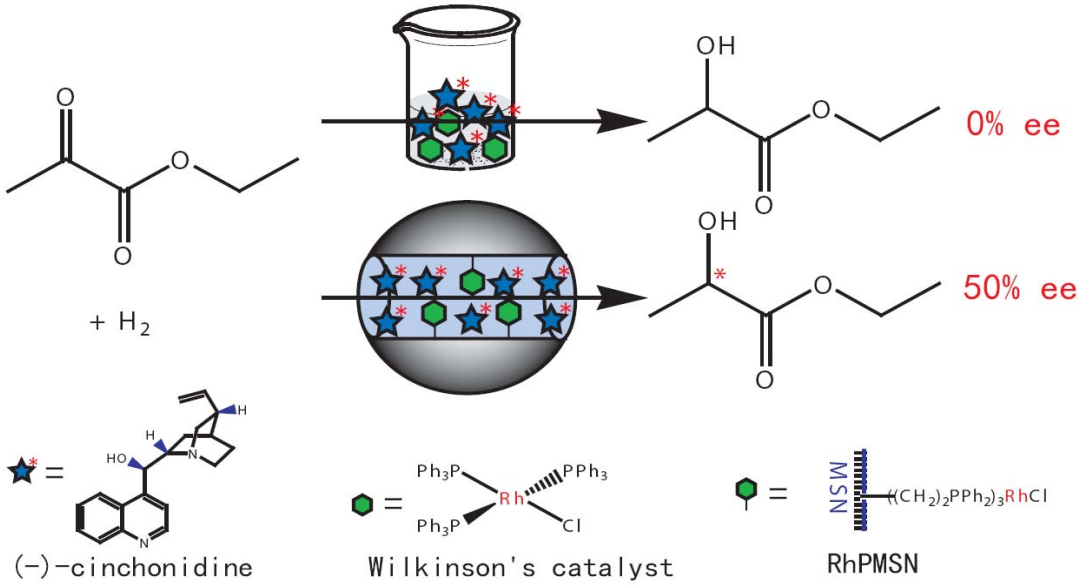

Figure 10-5. Asymmetric hydrogenation of ethyl pyruvate catalyzed by homogeneous $RhCl(TPP)_3$/(-)-cinchonidine and heterogeneous **RhPMSN**/(-)-cinchonidine.

During the in-depth solid-state NMR study of RhPMSN, functionalization of MSN by 2-(diphenylphosphino)ethyl groups was confirmed by the presence of T sites in the ^{29}Si CPMASNMR spectrum and quantification of these sites was achieved via integration of the ^{29}Si DPMAS NMR spectrum, in which the percent of T sites was found to be 3.7%. Both 1D and 2D SSNMR experiments showed that covalent attachment of the rhodium– phosphine ligand to the MSN surfaces was successful, as well as provided structural assignments of the ligand and the MSNs themselves. Both ^{13}C–^{1}H and ^{31}P–^{1}H idHETCOR experiments provided structural details of oxidized and non-oxidized phosphine ligands, otherwise indiscernible in a conventional 1D CPMAS NMR experiments. It was also found that oxidation of the attached 2-(diphenylphosphino)ethyl groups and detachment of Rh was enhanced at higher temperature even under CO and H_2.

Furthermore, I also synthesized organometallic complex (salen)Cr on MSN and applied it in the oxidation of tetramethylbenzidine (TMB) with iodosobenzene. And the reaction using MSN(salen)Cr^{III} as a heterogeneous catalyst exhibited both similarities and

differences with the analogous homogeneous reaction using (salen)$Cr^{III}(H_2O)^+$ as catalyst in aqueous acetonitrile (10% H_2O).

Selective sequestration of carboxylic acids. Aminopropyl-functionalized MSN could serve as an efficient adsorbent for selective sequestration of carboxylic acids. Aminopropyl-functionalized MSN with a designed loading of functional groups had a very high selectivity for carboxylic acid instead for ethanol, glucose, and protein. The regeneration of aminopropyl-functionalized MSN could be done easily by increasing pH to 10.5 because the adsorption reaction between carboxylic acids and MSN was pH-dependent. And the regenerated MSN showed adsorption capacity equivalent to the original (Figure 10-6). I believe this study provides a new approach that can serve a general principle for designing new nanoparticle-based adsorbent for selective sequestration of valuable chemicals from biomass fermentation with high efficiency.

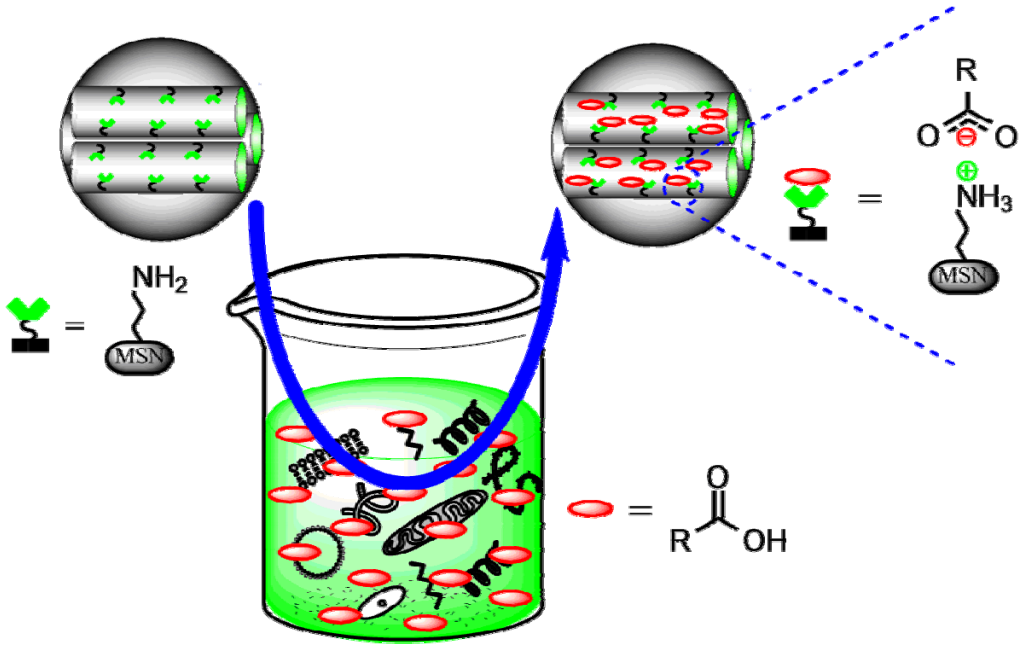

Figure 10-6. Selective sequestration of carboxylic acids by aminopropyl-functionalized MSN.

ACKNOWLEDGEMENTS

I would like to take this special opportunity to express my thanks to those who helped me during conducting research and writing of this dissertation.

First and foremost, I would like to thank my major advisor, Professor Dr. Victor S.-Y. Lin for his guidance and support throughout my Ph.D. study at Iowa State University. Without his help and scientific discussion, I would not be able to finish those projects and have current achievements.

I would also like to thank my committee members for their help and time to this work: Dr. Amy H. Andreotti, Dr. Nikki L. Pohl, Dr. Marek Pruski, Dr. Aaron D. Sadow.

I additionally would like to thank Dr. Robert Angelici, Dr. Andreja Bakac, Dr. Shihwu Sung, Dr. Shu Xu, Dr. Wehua Deng, Dr. Sang-Hyoun Kim, Dr. Jennifer L. Rapp and Dr. Ewa Szajna-Fuller for their valuable discussions and suggestions during my thesis work.

I also would like to thank our past and current group members for their help and suggestions.

Furthermore I would like to thank my wife Dr. Lie Min and my cute daughter Anna W. Huang for always cheering me up, sharing my joy and giving me emotional support. I also would like to thank my parents for their support and encouragement.

I also would like to express thanks to my friends who I met in China, UK and USA for their friendship.